# Nanostructured catalytic architectures for CO oxidation and reduction

---

**A thesis submitted in partial fulfilment of the requirements**

**for the Degree of Doctor of Philosophy**

**in Chemical and Process Engineering**

**in the University of Canterbury**

**New Zealand**

---

**Wasim Ullah Khan**

**2019**

"*Read in the name of your Lord who created, created man from clinging substance. Read and your Lord is the most Generous who taught by the Pen. Taught man that he knew not." (Al-Qura'n 96:1–5)*

*"Seeking knowledge is an obligation upon every Muslim." (Prophet Muhammad ﷺ)*

*To my parents, brothers, sister, all my family and friends who always stand by me. Also to you for adding colours to my life.*

# Abstract

The urbanization and increasing demand of transport vehicles have significant contribution in the emissions of carbon monoxide (CO) which is detrimental to humans, animals and environment. Hence, the conversion of CO either by oxidation or hydrogenation has gained attention in recent years. CO oxidation reaction plays an important role in air purification and vehicle exhaust treatment. CO oxidation also serves as a model reaction for basic studies of more complicated reactions such as methanol synthesis, water gas shift reaction or Fischer-Tropsch Synthesis (FTS). CO hydrogenation or syngas conversion via FTS process was first studied in the early $20^{th}$ century. Natural gas, biomass, coal and organic wastes are the sources to obtain syngas mixture. The FTS process generates value-added products with wide range of olefins, paraffins and oxygenates. Four types of active metals including ruthenium, nickel, iron and cobalt are mostly reported for the FTS process in the literature. Among these catalysts, iron and cobalt based catalysts are promising and utilized on the industrial scale.

In this research work, the copper and cobalt based catalysts were developed with a focus on their utilization for CO oxidation and hydrogenation/reduction via the FTS process. The novel hexameric copper nanoclusters were successfully synthesized and anchored over titanium dioxide ($TiO_2$-P25). The as-synthesized catalysts (with Cu contents varied between 0.15 and 5 wt%) were tested for CO oxidation reaction to find the size-activity threshold. The turnover number results for 8 h time-on-stream revealed that the copper contents up to 0.30 wt% resulted in size-activity threshold above which catalysts showed deactivation due to sintering. The higher dispersion and copper surface area along with strong metal-support interaction were among the factors of the stable performance of lower copper loading (0.15 and 0.30 wt%) catalysts.

The oxide support offers unique features to the catalyst including surface area, porosity, and metal dispersion and these parameters later play their role in the catalytic activity. Hence, the next phase was focused on the preparation of titanium dioxide nanotubes/nanorods. The synthesis parameters such as hydrothermal treatment duration (24-72 h) and temperature (130-150°C) were optimized to achieve nanostructures of wide aspect ratio. The hydrothermal temperature of 150°C for 44 h duration were chosen as optimum operating conditions. The effect of calcination temperature between

400 and 800℃ showed that mixture of nanotubes and nanoparticles were obtained at calcination temperature of 400 and 600℃ while calcination temperature of 800℃ produced uniform titania nanorods (TNRs).

In order to demonstrate the role of the catalytically active interfaces between copper and TNRs in CO oxidation reaction, the next phase was planned to anchor copper nanoparticles over TNRs synthesized in the last phase. Copper contents varied from 2.5 to 12.5 wt% showed an optimum of 7.5 wt% and the catalytic activity was assigned to the formation of suitable interface between copper and TNRs and presence of copper in the form of layers over the surface of TNRs. The effect of various oxide supports including $TiO_2$-P25, silica and alumina revealed that TNR supported Cu catalyst had higher rate of reaction as compared with the other oxide supports.

Syngas conversion into hydrocarbons via FTS process is reported to utilize cobalt based catalysts which are prone to deactivation. Hence, the addition of small fractions of second metal as promoter and/or to form synergistic bimetallic catalyst influences the catalytic performance and product selectivity. Therefore, the final phase of this project presented the role of base and Cu promoted Co/TNRs catalysts for hydrocarbons production via FTS. The optimum metal loading of 7.5 wt%, found in the last phase, was chosen as basis to synthesize catalysts. The amount of Cu promoter was varied from 1.5 to 6 wt% and the testing of as-synthesized catalysts for the FTS process showed that Cu promotion in smaller fraction (1.5 wt%) presented improved reducibility and CO and $H_2$ adsorption capacities which boosted CO conversion (16.8%) of this catalyst in comparison with base catalyst (9.4%). The increase in reaction temperature over the best catalyst from 240 to 300℃ revealed enhanced CO conversion (25%) but methane and $CO_2$ selectivity was also found to be increased in agreement with previous reports.

# Acknowledgements

The doctoral research is a unique journey which cannot be accomplished without the support of some of the amazing human beings around us. There are heaps of people who have been so supportive throughout my research work. First and the foremost, I am immensely pleased to express my gratitude to my supervisor, Dr. Alex Chi Kin Yip, for his guidance, encouragement, support, and friendly attitude towards conducting research as I believe these are the pillars in building an efficient research team. I would like to extend my gratitude to my co-supervisor, Assoc. Prof. Vladimir Golovko, for supporting through ideas and providing research resources in chemistry.

I would like to thank Chemical and Process Engineering (CAPE) department for providing me the financial support to conduct my doctoral research and also making me feel like staying home although being so far away from my home town. There are so many incredible people in CAPE staff and postgrads to whom I am indebted to say thanks. Among the staff, I would like to thank Prof. Peter Gostomski whose advice at the very start helped me a lot throughout my stay in a multi-cultural work environment like CAPE. Among technical staff, all of them are awesome, always helpful and approachable specially Leigh Richardson, Stephen Beuzenberg, Glen Wilson, Michael Sandridge, Rayleen Fredericks, Graham Furniss, Frank Weerts, Graham Mitchell, Stephen Hood, Garrick Thorn and Kun Zhao. I would like to thank Ranee Hearst for being so kind, friendly and supportive for administrative affairs till her retirement and lately Joanne Pollard for her kindness and help. Technical staff outside CAPE including Mike Flaws, Dr. Matthew Polson and Rob McGregor have always been there whenever needed, heaps of thanks to all of you. I would also like to thank intern student from Germany Felicitas Jansen, for helping in synthesis of copper nanoclusters and Siriluck Tesana (Mai) for her support during my work in Chemistry.

Last but not the least everyone at CAPE postgraduate office; from Von Haast to CAPE new building, each and every person has added value to my stay in CAPE. So I would like to thank each and every one of you. Thank you for making me laugh. Thank you for bearing my sarcasm and most importantly thank you for standing by me at hard times. All of you are amazing and I wish all the very best for all of your future endeavours.

Deputy Vice-Chancellor's Office
Postgraduate Research Office

UNIVERSITY OF CANTERBURY
*Te Whare Wānanga o Waitaha*
CHRISTCHURCH NEW ZEALAND

## Co-Authorship Form

This form is to accompany the submission of any thesis that contains research reported in co-authored work that has been published, accepted for publication, or submitted for publication. A copy of this form should be included for each co-authored work that is included in the thesis. Completed forms should be included at the front (after the thesis abstract) of each copy of the thesis submitted for examination and library deposit.

| |
|---|
| Please indicate the chapter/section/pages of this thesis that are extracted from co-authored work and provide details of the publication or submission from the extract comes:<br>*The results in Chapter 3 are in the submission process to the Journal of Hazardous Materials.* |

| |
|---|
| Please detail the nature and extent (%) of contribution by the candidate:<br>*The candidate is the first author of this article, have conducted 100% of the experimental work and written most of the text.* |

**Certification by Co-authors:**

If there is more than one co-author then a single co-author can sign on behalf of all

The undersigned certifies that:

- The above statement correctly reflects the nature and extent of the Doctoral candidate's contribution to this co-authored work
- In cases where the candidate was the lead author of the co-authored work he or she wrote the text

| | | |
|---|---|---|
| Name: *Alex Yip* | Signatu  | Date: *25 November, 2019* |

Deputy Vice-Chancellor's Office
Postgraduate Research Office

UNIVERSITY OF CANTERBURY
*Te Whare Wānanga o Waitaha*
CHRISTCHURCH NEW ZEALAND

# Co-Authorship Form

This form is to accompany the submission of any thesis that contains research reported in co-authored work that has been published, accepted for publication, or submitted for publication. A copy of this form should be included for each co-authored work that is included in the thesis. Completed forms should be included at the front (after the thesis abstract) of each copy of the thesis submitted for examination and library deposit.

| Please indicate the chapter/section/pages of this thesis that are extracted from co-authored work and provide details of the publication or submission from the extract comes: |
|---|
| *The results in Chapter 5 have been submitted to Nano Research and the article is currently under revision.* |

| Please detail the nature and extent (%) of contribution by the candidate: |
|---|
| *The candidate is the first author of this article, have conducted 95% of the experimental work and written most of the text.* |

**Certification by Co-authors:**

If there is more than one co-author then a single co-author can sign on behalf of all

The undersigned certifies that:

- The above statement correctly reflects the nature and extent of the Doctoral candidate's contribution to this co-authored work
- In cases where the candidate was the lead author of the co-authored work he or she wrote the text

| Name: *Alex Yip* | Signatu  | Date: *25 November, 2019* |
|---|---|---|

# List of Figures

# List of Tables

# Table of Contents

# Chapter 1 Introduction

## 1.1 The environmental impact of carbon monoxide

The urbanization, over a period of time, have increased the amounts of toxic gases being released into the atmosphere mainly due to enhanced number of vehicles in the recent years. The number of cars being manufactured has recently touched 70 million in 2016 (from 50 million in 2011) and over a billion motor vehicles are globally on road [1, 2]. The fossil fuel consumption in motorized vehicles releases tons of exhaust gases which are detrimental from environmental viewpoint. The exhaust gas contains primarily oxides of carbon and nitrogen including carbon monoxide (CO), nitrogen oxides ($NO_x$) and unburned hydrocarbons (HCs) [3]. The main source of CO in urban areas is the vehicle exhaust which contributes to over half of anthropogenic emissions [4]. The statistical data of anthropogenic emissions in US is given in Figure 1.1. The bar chart shows the contribution of various sectors in gas emissions. The industrialization and power plants have had significant impact on the environmental pollution. The high emissions of CO, emitted from different sources, are alarming for both humans and animals [5]. CO also negatively influences vegetation by interfering with nitrogen fixation and plant respiration. CO has an indirect impact on global warming and ozone depletion. Insolubility of CO in water also hinders its elimination from air. In conclusion, CO levels are one of the measures to assess the air quality of a region.

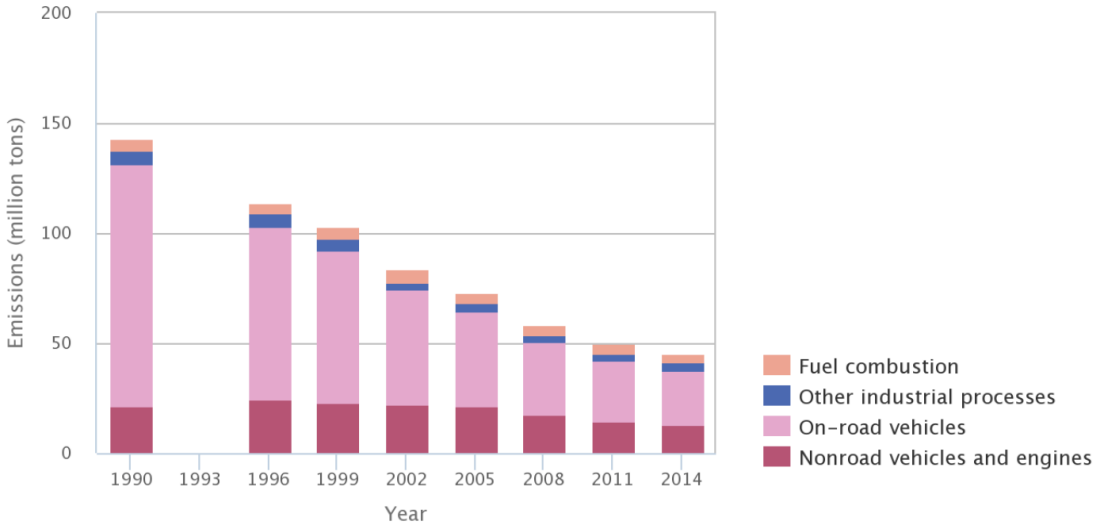


**Figure 1.1.** Anthropogenic emissions in the US by source category, 1990-2011 [6]

It is interesting to note the regulations have been implemented over the years to control the emissions and the emission standards applied in US are given in Table 1.1.

**Table 1.1** The US emission standards in cars [7]

| Emission standard | Implementation year | Emissions limit at 80,500 km CO (mg/km) | Emissions limit at 161,000 km CO (mg/km) |
|---|---|---|---|
| *Federal emission standards* | | | |
| **Tier 0** | 1987 | 2112 | - |
| **Tier 1** | 1994-1999 | 212 | 2600 |
| **NLEV** | 1999-2004 | 2112 | 2600 |
| **Tier 2/ Bin 9** | 2004-2010 | 2112 | 2174 |
| **Tier 3** | 2017-2025 | 870 | 1740 |
| *California emission standards* | | | |
| **Tier 1** | 1994-1999 | 2112 | 2600 |
| *LEV I* | | | |
| **TLEV** | 1999-2003 | 2112 | 2600 |
| **LEV** | | 2112 | 2600 |
| **ULEV** | | 1056 | 1300 |
| *LEV II* | | | |
| **LEV** | 2004-2010 | 2112 | 2200 |
| **ULEV** | | 1056 | 1100 |
| **SULEV** | | - | 520 |
| *LEV III* | | | |
| **LEV 160** | 2015-2025 | - | 1740 |
| **ULEV 125** | | | 870 |
| **ULEV 70** | | | 704 |
| **ULEV 50** | | | 704 |
| **SULEV 30** | | | 414 |
| **SULEV 20** | | | 414 |

NLEV: national low emission vehicles; TLEV: transitional low emission vehicles; LEV: low emission vehicles; ULEV: ultra-low emission vehicles; SULEV: super ultra-low emission vehicles.

Keeping in mind the impact of CO emissions on the daily life and environment, the necessary steps are required to be taken to minimize this detrimental impact of CO. The statistical data presented in Figure 1.1 demands developing the innovative ways to cope with this issue. Oxidation and hydrogenation of CO are some of the ways to utilizing CO to generate environmentally friendly products.

## 1.2 The research motivation and objectives

Despite the control measures, ever increasing number of on-road vehicles and use of fossil fuels still contributes significantly in increasing CO emissions in the air. The CO treatment or removal is essential for both humans and vegetation and this can be achieved by various ways such as CO methanation, adsorption or oxidation. CO oxidation is one of the effective ways of CO removal and many studies have been reported on CO oxidation. The reaction is described below:

$$CO + \frac{1}{2}O_2 \rightarrow CO_2 \qquad \Delta H^0_{298} = -293\ kJ/mol \qquad (1.1)$$

Numerous catalysts including noble metal and non-noble metal based have been reported for CO oxidation reaction. Palladium (Pd), platinum (Pt), and rhodium (Rh) are among the noble metals that have been extensively investigated and more recently gold (Au) and silver (Ag) are also part of the study in the form of nanoparticles or nanoclusters [8-11]. The transition metals including cobalt (Co), copper (Cu), and iron (Fe) have been presented as a cheap alternative to expensive noble metals with comparable activities for CO oxidation [12-14]. In addition to metal, the oxide support also plays a vital role during CO oxidation reaction. The metal-support interaction and interface are important parameters influencing the catalytic performance. Various oxide supports including alumina ($Al_2O_3$), silica ($SiO_2$), ceria ($CeO_2$), zirconia ($ZrO_2$) and titania ($TiO_2$) have been studied for this reaction [15-17].

Considering the importance of active metal and oxide support, this thesis is focused on the investigation of the role of Cu as active metal in the oxidation of CO. The recent developments in the characterization techniques such as microscopic and spectroscopic tools, the detailed catalyst performance can be investigated. The nanostructured catalytic architectures offer surface structure and interface which act as active sites while their porosity controls the reactant diffusion. The data obtained from these tools help in fine-tuning the catalysts at its interface or structure level to predict its

performance during reaction. Thus this thesis is focused upon the role of the structure of Cu nanoclusters to define the size-activity threshold in CO oxidation. Cu nanoclusters are emerging field in the heterogeneous catalysis, their performance in CO oxidation real time application is barely studied. Hence, one chapter of this thesis presents the preparation, characterization and testing of Cu nanoclusters anchored over $TiO_2$ for CO oxidation. The nanostructure support, in particular nanorods of $TiO_2$ (TNRs), significantly influences the catalytic CO oxidation activity. This thesis also elaborates the implication of the interface between Cu and $TiO_2$ nanorods. The main idea of this chapter is to validate the hypothesis that the change in copper contents over TNRs influences the interfacial active sites which play its role in controlling the catalytic activity performance.

In addition to CO oxidation, CO hydrogenation/reduction or syngas conversion to hydrocarbons *via* Fischer-Tropsch synthesis (FTS) has gained much attention in recent years due to the fact that the FTS produces wide range of value added products. The reactions involved in the FTS are given as:

$$2(n+1)H_2 + nCO \rightarrow C_nH_{2n+2} + nH_2O \quad (1.2)$$

$$2nH_2 + nCO \rightarrow C_nH_{2n} + nH_2O \quad (1.3)$$

$$CO + H_2O \rightarrow CO_2 + H_2 \quad (1.4)$$

$$2nH_2 + nCO \rightarrow C_nH_{2n+2}O + (n-1)H_2O \quad (1.5)$$

$$2CO \rightarrow C + CO_2 \quad (1.6)$$

$$CO + 3H_2 \rightarrow CH_4 + H_2O \quad (1.7)$$

Among these reactions, reactions (1.2) – (1.4) represent alkane, alkene production and water gas shift (WGS) reaction respectively, while side reaction (1.5) produces alcohols. Reaction (1.6) and (1.7) are Boudouard reaction (which generates carbon that deactivates the catalyst) and methanation reaction respectively. The catalysts based on cobalt and iron are widely utilized for the FTS process. The monometallic cobalt based catalysts are prone to deactivation which can be prevented by adding promoter or second metal to cobalt based catalysts [18]. The promoters are generally added in suitable amounts to boost the catalytic activity and product selectivity. Furthermore, the promoters influence the surface reducibility and number of active sites which contribute

towards activity during the FTS. In accordance with already reported research works highlighting the important aspects of promoter for the FTS process, this thesis presents the catalytic performance results of $TiO_2$ nanorods supported Cu and Co based catalysts.

This work fills the literature gap mainly associated with the real-time application of copper nanoclusters and catalytically active interfacial active sites between copper nanoparticles and titania nanorods. This thesis comprises seven chapters and a brief description of each chapter is given in the following paragraphs.

Chapter 1 provides brief introduction to CO oxidation and hydrogenation *via* the FTS. The research motivations, gap, the role of novel copper nanoclusters and titania nanorods and their background is presented.

The second chapter highlights the literature background of the current study with focus on research gap. The catalyst development, testing and characterization for CO oxidation and reduction are reviewed. The significance of the role of novel copper nanoclusters and titania nanorods is highlighted.

In chapter 3, the role of novel copper nanoclusters in thermal catalysis, copper nanoclusters are investigated. The catalysts with copper range of 0.15 to 5 wt% impregnated over $TiO_2$-P25 are tested for CO oxidation. The main focus of this work is to demonstrate the behavior of nanoclusters under CO oxidation reaction conditions (100 - 250 °C; 1 atm; 6000 mL/h. $g_{cat.}$) and investigate the influence of metal particle size on the catalytic performance. The metal-support interaction and catalyst deactivation are also discussed in this contribution. This chapter 3 sets basis for the synthesis of nanoparticles based catalysts which are discussed in subsequent chapters 5 and 6.

The development of metal oxide support and subsequently supported catalyst for a certain reaction requires the resulting catalyst to have intrinsic properties that may help in predicting the possible behaviour of the catalyst during reaction. For instance, some of the important factors in synthesizing one dimensional titanium dioxide nanostructures include choice of precursor, precursor particle size, concentration of alkaline solution, autoclave temperature and duration, washing (either with acidic solution or water) and calcination. In our work while synthesizing one dimensional

$TiO_2$ nanostructures, we have studied three parameters including autoclave temperature, duration and calcination temperature. The choice of autoclave temperature and time as well as the calcination temperature is presented. The details of one dimensional nanostructures formation are presented in chapter 4.

The synthesis of copper and cobalt nanoparticles were anchored over $TiO_2$ nanorods (TNRs) using deposition-precipitation is presented in chapter 5. This contribution focuses on metal-support interface active sites and their role during CO oxidation reaction. The change in particle size and metal-support interaction with increase in copper contents from 2.5 to 12.5 wt% are discussed in detail. Our work also elaborates how copper nanoparticles interact with various supports such as $TiO_2$-P25, alumina ($Al_2O_3$) and silica ($SiO_2$).

The chapter 6 focuses on the synthesis and testing of copper promoted TNRs supported cobalt based catalysts for syngas conversion into hydrocarbons using FTS process. The reduction properties are evaluated to understand the effect of Cu promotion over the reducibility of Co-based catalysts. CO and $H_2$ desorption profiles are discussed with their contribution in the catalytic performance. Finally, the activity and product selectivity data are analysed for base and Cu promoted Co/TNRs catalysts.

The concluding points are summarized in chapter 7 and recommendations are suggested for further research on this topic in the future.

### 1.3 The research publications

During the course of this research, following research articles have either been presented in conferences, published or in process of publication:

**Wasim Khan** and Alex C.K. Yip, Nanostructured copper-based catalytic particles for CO oxidation, Australasian Particle Technology Society Student Conference, Queenstown New Zealand (2018).

**Wasim Khan**, Vladimir Golovko and Alex C.K. Yip, Nanostructured copper particles for CO oxidation, Materials @ UC, University of Canterbury, Christchurch New Zealand (2018).

**Wasim Khan**, Xicheng Jia, Zhijie Wu, Jungkyu Choi and Alex C.K. Yip, Incorporating Hierarchy into Conventional Zeolites for Catalytic Biomass Conversions: A Review, Catalysts, 9 (2018) 127.

Xicheng Jia, **Wasim Khan**, Zhijie Wu, Jungkyu Choi and Alex C.K. Yip, Modern synthesis strategies for hierarchical zeolites: Bottom-up versus top-down strategies, Adv. Powder Technol., 30 (2019) 467-484.

**Wasim U. Khan**, Season S. Chen, Daniel C. W. Tsang, Xijun Hu, Frank L. Y. Lam, and Alex C.K. Yip, Catalytically active interfaces in titania nanorod-supported copper catalysts for CO oxidation, Nano Res., Under Review

**Wasim Ullah Khan**, Iris K. M. Yu, Daniel C. W. Tsang, Vladimir Golovko, Alex C. K. Yip, The supported Cu cluster size-activity threshold in CO oxidation, J. Hazard. Mater., in submission process

Qiqi Ding, **Wasim U. Khan**, Frank L. Y. Lam, Yongqing Zhang, Shuaifei Zhao, Alex C. K. Yip, Xijun Hu, Graphitic carbon nitride/copper-iron oxide composite for effective Fenton degradation of ciprofloxacin at near-neutral pH, in preparation

## References

[1] http://www.oica.net/category/production-statistics/2016-statistics/.

[2] H. Shinjoh, Noble Metal Sintering Suppression Technology in Three-way Catalyst: Automotive Three-way Catalysts with the Noble Metal Sintering Suppression Technology Based on the Support Anchoring Effect, Catal. Surv. Asia, 13 (2009) 184-190.

[3] R.M. Heck, R.J. Farrauto, Automobile exhaust catalysts, Appl. Catal. A-Gen., 221 (2001) 443-457.

[4] P. Flachsbart, W. Ott, Trends in passenger exposure to carbon monoxide inside a vehicle on an arterial highway of the San Francisco Peninsula over 30 years: A longitudinal study, J. Air. Waste Manage., 69 (2019) 459-477.

[5] G.M.S. Kumar, S.; Jeena, V.S.; Anjali, R., Carbon Monoxide Pollution Levels at Environmentally Different Sites, J. Indian Geophy. Union, 12 (2008) 31-40.

[6] https://cfpub.epa.gov/roe/indicator_pdf.cfm?i=10.

[7] K. Kuklinska, L. Wolska, J. Namiesnik, Air quality policy in the US and the EU - a review, Atmos. Pollut. Res., 6 (2015) 129-137.

[8] I. Miguel-Garcia, M. Navlani-Garcia, J. Garcia-Aguilar, A. Berenguer-Murcia, D. Lozano-Castello, D. Cazorla-Amoros, Capillary microreactors based on hierarchical $SiO_2$ monoliths incorporating noble metal nanoparticles for the Preferential Oxidation of CO, Chem. Eng. J., 275 (2015) 71-78.

[9] F. Morfin, T.S. Nguyen, J.L. Rousset, L. Piccolo, Synergy between hydrogen and ceria in Pt-catalyzed CO oxidation: An investigation on Pt-$CeO_2$ catalysts synthesized by solution combustion, Appl. Catal. B-Environ., 197 (2016) 2-13.

[10] T. Murayama, M. Haruta, Preparation of gold nanoparticles supported on $Nb_2O_5$ by deposition precipitation and deposition reduction methods and their catalytic activity for CO oxidation, Chinese J. Catal., 37 (2016) 1694-1701.

[11] E. Kolobova, A. Pestryakov, G. Mamontov, Y. Kotolevich, N. Bogdanchikova, M. Farias, A. Vosmerikov, L. Vosmerikova, V.C. Corberan, Low-temperature CO oxidation on Ag/ZSM-5 catalysts: Influence of Si/Al ratio and redox pretreatments on formation of silver active sites, Fuel, 188 (2017) 121-131.

[12] O.A. Kirichenko, N.A. Dayshan, E.A. Redina, G.I. Kapustin, I.V. Mishin, O.P. Tkachenko, A.V. Kucherov, L.M. Kustov, Gold nanoparticles in environmental catalysis: Influence of the Fe-modified alumina supports on the catalytic behavior of

supported gold nanoparticles in CO oxidation in the presence of ammonia, Chem. Eng. J., 292 (2016) 62-71.
[13] S. Royer, D. Duprez, Catalytic Oxidation of Carbon Monoxide over Transition Metal Oxides, Chemcatchem, 3 (2011) 24-65.
[14] G.J. Wu, N.J. Guan, L.D. Li, Low temperature CO oxidation on Cu-$Cu_2O/TiO_2$ catalyst prepared by photodeposition, Catal. Sci. Technol., 1 (2011) 601-608.
[15] M.M. Schubert, S. Hackenberg, A.C. van Veen, M. Muhler, V. Plzak, R.J. Behm, CO oxidation over supported gold catalysts-"inert" and "active" support materials and their role for the oxygen supply during reaction, J. Catal., 197 (2001) 113-122.
[16] D. Widmann, Y. Liu, F. Schuth, R.J. Behm, Support effects in the Au-catalyzed CO oxidation - Correlation between activity, oxygen storage capacity, and support reducibility, J. Catal., 276 (2010) 292-305.
[17] G.N. Li, B.H. Wu, L. Li, Surface-structure effect of nano-crystalline $CeO_2$ support on low temperature CO oxidation, J. Mol. Catal.A-Chem., 424 (2016) 304-310.
[18] N. E. Tsakoumis, M. Rønning, Ø. Borg, E. Rytter, A. Holmen, Deactivation of cobalt based Fischer–Tropsch catalysts: A review, Catal. Today 154 (2010) 162-182.

# Chapter 2 Literature Review

## 2.1 CO oxidation

CO oxidation is generally regarded as the most extensively studied reaction in heterogeneous catalysis [1]. On road vehicles are the main contributor in CO emissions. The cold start-up of a vehicle is mainly responsible for over 80% emission of CO and unprocessed hydrocarbons into the atmosphere. The increasing urbanization and ease of access of vehicles have enhanced threat of uncontrolled CO release to atmosphere, which needs to be addressed before it gets worse. This leads to the concept of catalytic converter that plays a vital role in CO abatement [1, 2].

In addition, CO oxidation is also widely used as a model reaction in heterogeneous catalysis to probe the fundamentals of reaction mechanism, nature and surface behaviour of the catalysts. Apart from air cleaning and automotive emissions control, CO oxidation finds its application in polymer electrolyte membrane fuel cell (PEMFC) to remove CO impurities from hydrogen [3-5]. The earliest commercial catalysts used for CO removal from air were Hopcalite catalysts, discovered in the 1920s [6, 7]. These catalysts were a complex mixture of copper and manganese oxides developed in the USA. However, the limitations of these catalysts such as low thermal stability, severe deactivation under sulphur and moisture environment and undesired behaviour during cycling conditions restricted their utilization and offered an opportunity for researchers to find an alternative catalyst [8, 9]. The researchers have been trying to explore the different strategies and metal/metal oxides supported on various materials to find better alternatives to such commercially available catalysts as Hopcalite catalysts.

Earlier noble metals were employed in catalytic converters. The development of catalytic converter offered the opportunity to utilize noble metals (Pd, Pt, Rh) for CO oxidation reaction in the 1970s and 1990s in the United States and Europe respectively. In the 1980s, the discovery of gold nanoparticles well dispersed over an inorganic oxide support showed excellent CO oxidation activity at low temperatures with better stability and resistance to water. The discovery of this catalyst made it a benchmark for low temperature CO oxidation reaction. However, the high cost and less abundance of these noble metals, together with the development in oxide catalysts have shifted the interest of the researchers from expensive noble metals to cheaper alternative *i.e.*, transition

metals and/or metal oxides. The transition metals with comparable activity and surface properties are the potential replacement of these noble metals based catalysts. Among transition metals, copper, iron and cobalt can be taken as better choice for both CO oxidation and reduction [10-13].

## 2.2 Nanostructured catalysts for CO oxidation

The metal-based catalysts, both on laboratory and industrial scales, are typically composed of metal nanoparticles. The role of active sites is crucial and vital to be defined as chemical reactions take place over active metal surface and/or the metal-support interfaces in case of supported metal catalysts [14-16]. Generally, the factors influencing the catalytic performance of metal nanoparticles-based catalysts include their size and shape, as well as metal-support interaction, which is related to their interfacial structure. These parameters can be easily examined by characterizing the catalysts before and after reaction. These structural features of metal nanoparticles-based catalysts are closely related to their catalytic activity, product selectivity and catalyst durability under reaction conditions [17-19].

### *2.2.1 Copper as active metal*

Both homo and heterogeneous catalysts have been part of fundamental research in CO oxidation. The choice of active metal is one of the vital the factors that influence the catalytic activity during reaction. The metal used either as homogeneous catalyst or heterogeneous supported catalyst has its significance in dictating the catalytic performance. As mentioned earlier, CO oxidation is extensively studied using noble metal catalysts but their high cost provides opportunity for transition metals as a potential alternative. CO oxidation has wide spectrum of transition metal choice utilized as homogeneous, supported or mixed oxides catalysts including copper, cobalt, iron, chromium and magnesium *etc*.

Copper-based nano-catalysts have been used in thermal catalysis for the CO oxidation [24-28]. It is noteworthy that copper easily oxidizes to $Cu(I)_2O$ or Cu(II)O [29-31] and the oxidation state of the copper defines the morphology of Cu species. Copper metal ($Cu^0$) and cuprous oxide ($Cu^+$) are reported to have cubic phase, while cupric oxide ($Cu^{2+}$) to have monoclinic phase [29, 30]. The synthesis ambience for Cu NPs formation requires an oxygen-free and/or reducing environment owing to the fact that the face

cubic centred (fcc) phase of copper is unstable under oxidative conditions. The morphology of Cu NPs might change even with the partial oxidation during the preparation [32].

*2.2.2 Nanoclusters versus nanoparticles*

In metals, the gap between atomic and larger nanoparticles is bridged by the metal nanoclusters, which comprise specific number of atoms within (typically) sub-nanometer cluster metal core [33]. The metal nanoclusters have exceptional physical, electrical and optical properties, which have recently been exploited by researchers in the fields of electronic devices, catalysis, chemical sensors and biological imaging [34-36]. The metal nanoclusters also offer the size tuning on atomic level and also the possibility to study the role of the addition of each atom into the catalyst. Since structure and interface are important features of nanostructured catalysts, the size of the active metal becomes vital in fine-tuning these features. These features vary based on the choice of nanoclusters and nanoparticles. The potential of metal nanoclusters has gained much research interest in recent years and the investigation of metal nanoclusters, particularly, in catalysis is increasing rapidly. The facile synthesis procedure and chemical stability are among the main factors behind extensive investigation of noble metal nanoclusters including mainly gold (Au) and silver (Ag) [37-39]. However, non-noble metal nanoclusters such as copper nanoclusters (CNCs), despite their promising features such as unique selectivity, have not received much attention. The precursors required for the synthesis of noble metal nanoclusters are more expensive than copper cluster precursors. Thus, copper nanoclusters stand as a competitive alternative for various applications as compared to noble metal nanoclusters. Despite offering exceptional size dependent optical and electronic properties and quantum size effect, CNCs also have some limitations. The role of ligand or capping agent becomes crucial specially when ligand removal is important for the reaction.

CNCs are novel idea in heterogeneous catalysis due to the fact that the size can be controlled on atomic level. Most of the research work on nanoclusters is based on density functional theory instead of real time catalytic application [40-50]. In addition, most of the research data published mainly focuses on synthesis of these clusters rather than the catalytic application. Noble metal based clusters have been reported for CO

oxidation reaction [1, 51-57]. The synthesis and theoretical studies of CNCs are extensively reported in the literature [58-69] and some of the CNCs based catalysts have been tested for real time catalytic applications such as methanol oxidation, oxidation and detection of hydrazine, and glucose sensing *etc*. [70-72]. Keeping in mind the advantages offered by nanoclusters, ***first phase*** of this research is focused on the synthesis of copper nanoclusters.

*2.2.3 Inorganic oxide support*

Standalone metal nanoparticles or nanoclusters are highly prone to agglomeration or sintering. When being used as a catalyst, the extent of agglomeration further enhances as the operating temperature increases during reaction. In order to overcome this problem, metal nanoparticles/nanoclusters are immobilized onto oxide supports. The anchoring of metal nanoparticles/nanoclusters onto a support material also has the advantages of offering a good dispersion of metal nanoparticles over the support surface and hence, is cost effective, as only a small amount of metal nanoparticles is required for the reaction as they are efficiently utilized.

The oxide support also plays a vital role during CO oxidation reaction. Therefore, the choice of support is also important since the intrinsic properties of support are known to have significant impact on the performance of the catalysts. These properties include surface area, porosity, dispersion, activity and selectivity [73-75]. The metal-support interaction and interface also influence the catalytic performance.

There is a range of oxide supports utilized in heterogeneous catalysis including silica ($SiO_2$), alumina ($Al_2O_3$), ceria ($CeO_2$), titania ($TiO_2$), and zirconium dioxide ($ZrO_2$) *etc.,* [12-14]. Some of these supports, such as silica, are inert supports and do not enhance performance of the metal anchored onto its surface while other supports do not only interact with the deposited metal but also enhance catalytic performance of metal species during reaction.

Among these oxide supports, titanium dioxide or titania is considered as one of the promising support for the application in heterogeneous catalysis. The main attributes of titania as support include its significant band gap, reducibility, low toxicity and environmental friendliness, and low price. The non-toxic nature, good effectiveness, good thermal and mechanical stabilities under oxidative and acidic conditions are

additional features for $TiO_2$ to be used as heterogeneous support. $TiO_2$ is mainly used in photo-catalysis, electro-catalysis and thermal catalysis due to above mentioned features. $TiO_2$ is found in three crystalline phases *i.e.*, brookite, anatase, and rutile. Anatase and rutile phases are most commonly used and crystalline size of anatase is always smaller than the rutile. Brookite phase usually in the form of orthorhombic structure is rarely used for any application [76-79]. Among the three phases, brookite and anatase are less thermally stable and start converting into rutile phase above 600 °C [77, 78]. Anatase comprises octahedral $TiO_6$ building blocks linked together in zigzag chains while rutile contains linear chains [78-81]. The arrangement of building blocks can be pictorially presented as shown in Figure 2.1.

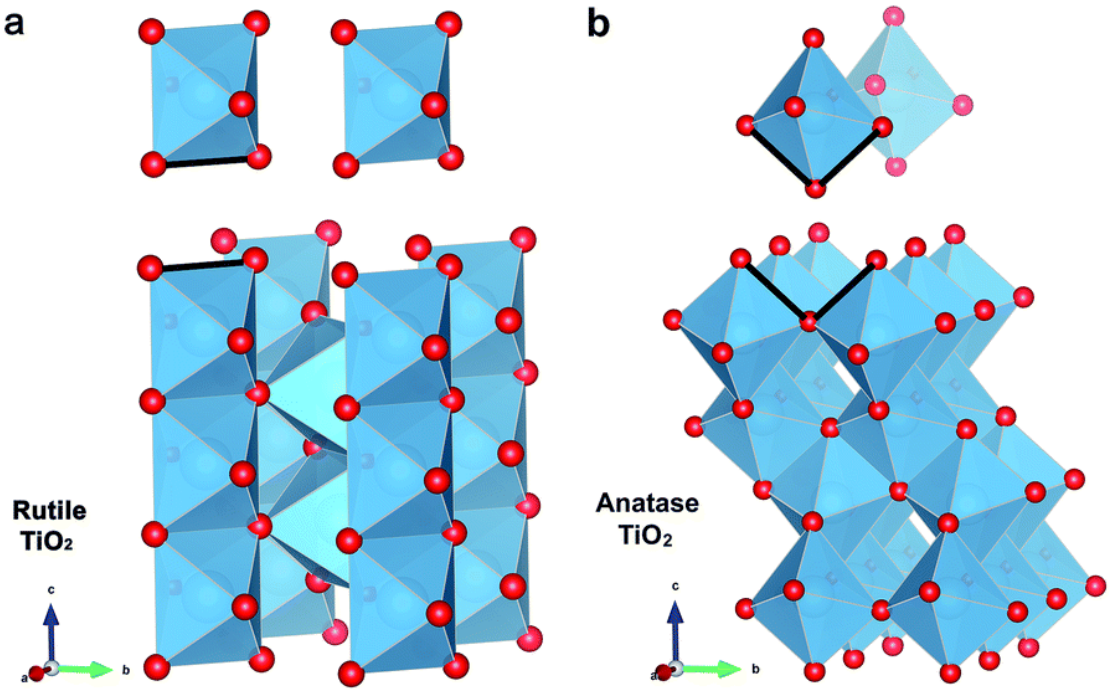


**Figure 2.1** The representation of octahedral $TiO_2$ building blocks in (a) rutile and (b) anatase $TiO_2$ [81].

$TiO_2$ has been reported to improve catalyst performance by modulating its performance in the reactions like thermal catalytic decomposition [82], water gas shift [83], hydrodesulphurization [84], and dehydrogenation [85, 86]. $TiO_2$, as a heterogeneous catalyst, also has some drawbacks including low adsorption abilities, low photocatalytic quantum efficiency and smaller surface areas [83, 84]. The hexameric copper nanoclusters were anchored over $TiO_2$ in the ***second phase*** of this research work and the catalysts were investigated for their catalytic performance in CO oxidation (Chapter 3).

The ***third phase*** of this research was focused on the successful preparation of one dimensional oxide support (Chapter 4). In recent years, one dimensional oxide nanostructures such as zinc oxide (ZnO), vanadium pentaoxide ($V_2O_5$), gallium oxide ($Ga_2O_3$), indium oxide ($In_2O_3$), and tin oxide ($SnO_2$) in the form of nanotubes, nanorods, nanowires and nanobelts have gained significant attention. The nanostructures have distinct physical and chemical properties. $TiO_2$ is used in different nanostructured forms like nanotubes (TNTs) or nanorods (TNRs) or nanobelts or nanowires. TNTs have been considered as a vital support in heterogeneous catalysis due to unique characteristics - large specific surface area, large pore volume, ion-exchangeability and rapid electron transport competency [87-89]. Importantly, TNRs and TNTs have high aspect ratio. TNTs/TNRs can be prepared using various techniques such as template method, anodic oxidation and hydrothermal synthesis. Among these methods, hydrothermal synthesis has the advantage of large scale production of materials with high length to diameter ratio and cation exchange capacity. The hydrothermal synthesis is a simple process in which various parameters can be changed to control the attributes of final product but hydrothermal synthesis also needs longer reaction times and concentrated NaOH. There are difficulties involved with hydrothermal synthesis which include controlling size uniformity and thermal stability. The high cost and use of highly toxic hydrofluoric acid make other two methods (template method and anodic oxidation) less favourable in comparison with hydrothermal synthesis [87, 90, 91]. Table 2.1 shows the advantages and limitations of various synthesis techniques of one dimensional titania nanostructures.

Kasuga *et al*. [92] were the first who discovered the hydrothermal synthesis of nanotubular shaped titania using alkaline media which later became a great deal of interest. The synthesis of one dimensional titania nanostructures using hydrothermal method involves many parameters which control the final product. These parameters include the size of titania precursor, the concentration of NaOH used, autoclave treatment temperature and duration, acid/water washing, and calcination temperature.

**Table 2.1.** Comparison between synthesis techniques for one dimensional titania nanostructures [93]

| Synthesis Technique | Advantages | Limitations | Internal diameter/length (nm/µm) |
|---|---|---|---|
| **Hydrothermal synthesis** | 1. Simple route for large scale production<br>2. Flexible and easily modifiable<br>3. High aspect ratio<br>4. High cation-exchange capacity | 1. Long reaction time<br>2. Highly concentrated NaOH required<br>3. Non-uniform size<br>4. Thermal instability | 3–10/50–500 |
| **Anodic oxidation** | 1. More suitable for practical applications<br>2. Ordered alignment with high aspect ratio<br>3. Viable for extensive applications | 1. Limited mass production<br>2. Utilization of highly toxic solvent e.g. HF<br>3. High production cost | 20–100/0.1–2.4 |
| **Template method** | 1. More suitable for practical applications<br>2. Controlled scale of products | 1. High production cost<br>2. Long term instability<br>3. High production cost<br>4. Complicated production process | 2.5–6000/0.05–200 |

The procedure reported by Kasuga *et al*. [92] was adopted to prepare the one dimensional titania nanostructures for the utilization in the ***fourth phase*** of the research work. The effect of preparation parameters such as hydrothermal temperature, duration and calcination temperature was studied in detail to obtain the required properties of the synthesized one dimensional titania nanorods (TNRs). After successful synthesis of one dimensional titania nanorods, the next step *i.e.*, the ***fourth phase*** was deposition of active metals of choice *i.e.*, copper and cobalt onto these titania nanorods for further investigation of the resulting catalysts for CO oxidation and reduction.

*2.2.4 The supported catalysts*

The investigation of metal/metal oxide nanoparticles anchored over oxide support such as $TiO_2$, $CeO_2$ *etc*. in heterogeneous catalysis, is significantly important to understand the nature and extent of metal-support interaction which affects the catalytic activity and product selectivity [94, 95]. The preparation of heterogeneous catalyst involves different elevated temperature steps including oxidation and reduction which influence the morphology of the catalyst. The metal-support interaction also causes morphological changes like alloy formation, sintering of metal particles, inter-diffusion and encapsulation. Therefore, the preparation steps need to be optimized to have well dispersed metal nanoparticles anchored onto the oxide support.

The catalysts are prepared using different synthesis techniques including impregnation, co-precipitation (CP), deposition-precipitation (DP), photo-deposition (PD) and sol-gel *etc*. Each of these techniques have the advantages and limitations. PD is a simple process which requires a light source to prepare a well-defined catalyst. Moreover, PD does not require elevated temperatures and facilitates control of the nanoparticle size and oxidation state [96]. In addition, nanoparticle size distribution can potentially be varied by simply varying precursor concentration, wavelength of light source, pH and irradiation time [97].

Unlike CP, DP maintains the deposition of active metal on the support surface and prevents the interaction of active metal with the bulk of the support. The active metal is made to precipitate over the support surface by preventing the local high concentrations of alkali which could precipitate the active metal away from support surface [98]. The other advantage of DP is it provides narrow particle size distribution. DP technique is recommended when involving the supports with high surface areas [99].

*2.2.4.1 The ligand protected metal nanoclusters based catalysts*

The supported ligand protected metal nanoclusters based catalysts are novel idea in the heterogeneous catalysis. Generally, noble metals based nanoclusters have been reported as supported catalysts for CO oxidation reaction including density functional theory (DFT) or first principles based theoretical studies or real time catalytic performance [48, 51, 52, 57, 100-106]. Nie *et al*. [51] studied the oxide support effect on the catalytic

performance of gold nanoclusters in CO oxidation. The study of anchoring $Au_{25}(C_2H_4Ph)_{18}$ over $CeO_2$, $Fe_2O_3$ and $TiO_2$ revealed that $CeO_2$ supported catalyst exhibited more activity. The oxygen pre-treatment for 1.5 h at 150 ℃ showed that gold was intact as nanoclusters and its activity enhanced after pre-treatment. These results contradicted the general findings of activity enhancement after complete removal of ligands [100, 101] and revealed that gold nanoclusters formed perimeter interface active sites which behaved as active centres for CO oxidation reaction. One of the interesting findings of this work was the inactivity of gold supported on $TiO_2$ which is in striking contrast to gold nanoparticles supported $TiO_2$ catalysts [48, 102]. The lack of interfacial active sites was the main factor behind inactivity of gold nanoclusters supported on $TiO_2$.

The elucidation of interface engineering of gold nanoclusters by supporting series ($Au_{38}(SR)_{24}$, $Au_{36}(SR')_{24}$, $Au_{25}(SR'')_{18}$) of nanoclusters on ceria revealed that the presence of ligands at the cluster surface adversely affected CO oxidation activity [52]. It was found that for each series, the commonly believed carbon tails bulkiness did not affect CO adsorption over Au active sites. Rather, the ligands at the interface between thiolate, Au and ceria support caused the steric hindrance which prevented CO adsorption. The investigation of the catalysts was further extended to the comparison between nanoclusters of almost the same size *i.e.*, $Au_{38}(SR)_{24}$ and $Au_{36}(SR')_{24}$. The thermal pre-treatment at various temperatures between 100 and 225 ℃ revealed that $Au_{36}(SR')_{24}$ catalyst was insensitive to pre-treatment while $Au_{38}(SR)_{24}$ catalyst exhibited an optimum CO oxidation activity after thermal pre-treatment at 150 ℃. The difference in geometrical structure of these two catalysts was the main factor responsible for their corresponding catalytic activities. The bi-icosahedral structure in $Au_{38}(SR)_{24}$ catalyst remained stable until pre-treatment temperature of 150 ℃ above which its structure began to convert into face centred cubic structure of $Au_{36}(SR')_{24}$ catalyst and, thus, loss in activity was observed.

The ligand protected copper nanoclusters alone or as bimetallic with noble metal clusters are widely reported from theoretical calculations perspective using density functional theory (DFT) or first principles studies [107-111]. The real life applications of ligand protected copper nanoclusters based catalysts are scarce. There are some reports which have studied the roles of the unsupported and supported ligand protected copper nanoclusters for their catalytic applications including benzene oxidation to

phenol, $CO_2$ reduction to methanol, low temperature water gas shift reaction (LTWGS) and CO oxidation [112-117]. Recently, Baharudin *et al.* [116] investigated the surface chemisorption and CO temperature-programmed desorption (CO-TPD) of hexameric copper hydride ($Cu_6$) nanoclusters (0.5-15 wt%) supported on functional multi-walled carbon nanotubes (MWCNTs). The elementary steps in most common Langmuir-Hinshelwood mechanism for LTWGS in conjunction with the study of the interaction between active sites and CO using CO-TPD allows to predict the catalytic behaviour of as-synthesized catalysts. Cu dispersion, crystallite size, Cu surface area and amount of CO adsorbed as obtained from CO chemisorption were found to correlate with the hypothetical active sites. Among various Cu loading contents supported on carboxyl functionalized MWCNTs ($MWCNT_{COOH}$) studied, 1 wt% $Cu_6/MWCNT_{COOH}$ exhibited highest Cu dispersion, Cu surface area and CO adsorbed and found to be optimal Cu loading. The effect of support using non-functional MWCNTs and $Al_2O_3$, the comparative study between $Cu_6$ and Cu nanoparticles deposited over $MWCNT_{COOH}$ showed that 1 wt% $Cu_6/MWCNT_{COOH}$ is active for LTWGS with the operating temperature governed by Cu sintering and water dew point.

The same research group performed CO oxidation over carboxyl-modified and copper clusters supported pristine-MWCNTs [117]. The contaminated oxidation atmosphere as simulated by the carboxyl-modification of pristine-MWCNTs and anchoring copper cluster over pristine-MWCNTs as modelled pollutant showed an inhibition of CO oxidation activity. The CO oxidation onset temperature over unmodified pristine-MWCNTs is 150 ℃ and almost complete CO is converted at ~230 ℃. Carboxyl-modification of pristine-MWCNTs acts more like CO adsorbent with no $CO_2$ formation. The modification of pristine-MWCNTs with copper cluster as modelled pollutant containing PAHs, P and VOCs, promotes the formation of $CuCO_3$ during reaction below 330 ℃ and these carbonates decompose above 400 ℃ to generate $CO_2$. This study highlighted the significance of pre-treatment of flue gas prior to CO oxidation reaction at low temperatures.

*2.2.4.2 The $TiO_2$ supported metal nanoparticle-based catalysts*

$TiO_2$ supported copper catalysts are widely reported in heterogeneous catalysis, in particular, for CO oxidation reaction [24-26]. Most of the researchers have focused on anatase phase of $TiO_2$. Limited studies are aimed at the role of rutile $TiO_2$ in CO

oxidation. Furthermore, the study of the role of titania nanorods with dominant rutile phase is worth investigating to have an insight of these nanomaterials in CO oxidation reaction.

The ratio of anatase to rutile is one of the important factors which affects the catalytic activity during CO oxidation. The investigation of CuO anchored on pure anatase phase, pure rutile phase, 70% rutile phase and 70% anatase phase showed that the chemical, physical and catalytic properties of the catalyst strongly depend on the phase of $TiO_2$. It was found that CuO anchored over pure rutile phase (CuO/R) exhibited weaker interaction between metal and support. The high dispersion, more reducibility and presence of large amount of oxygen species enhanced the catalytic performance of CuO/R catalyst [118].

It has been reported that the active sites and oxidation states of copper species have strong impact on CO oxidation reaction rate [28, 119], but there is controversy about the exact nature of the active centre of copper species. Generally, catalytic activity depends upon the coexistence of $Cu^0$ and $Cu^{+1}$. Monolayer dispersion of 8wt% CuO supported on $TiO_2$ showed excellent activity for CO oxidation when copper loading was varied from 2 to 12 wt% [120].

The modification of $TiO_2$ by adding second oxide enhances the catalytic performance of resulting catalysts. The influence of cerium dioxide ($CeO_2$) addition over $CuO/TiO_2$ catalysts showed that the thermal stability of anatase phase improved with the modification of $TiO_2$ with $CeO_2$. The stabilization of $Ce^{+3}$ and $Cu^{+1}$ in the inter-domain boundaries of anatase in the modified catalyst improved the thermal stability of the catalysts which was intact even at higher calcination temperature of 700 ℃. The catalytic activity of modified catalysts outperformed $CuO/TiO_2$ catalysts. For instance, $T_{50}$ for the modified catalyst (5wt%Cu on 5 wt% $CeO_2$-95 wt% $TiO_2$) decreased to 135 ℃ from $T_{50}$ of 187 ℃ for unmodified catalyst (5 wt% $CuO/TiO_2$) [121].

$TiO_2$ modification with $SnO_2$ was investigated for copper based catalysts [122]. The various amounts of copper (2-20 wt%) were anchored over the modified support. The catalysts with unmodified supports *i.e.,* $TiO_2$ and $SnO_2$ were also synthesized for comparison. It was found that the catalytic activity of catalysts made using modified support was higher than that of catalysts made using unmodified support. CO conversion of ~100% was achieved at 80, 110 and 130 ℃ for 8 wt% $Cu/TiO_2$-$SnO_2$, 8

wt% Cu/$TiO_2$ and 8 wt% Cu/$SnO_2$ respectively. It can be inferred from experimental results that CuO species act as active centres which had significant impact on the catalytic activity. Moreover, synergy between $SnO_2$ and $TiO_2$ in modified 8 wt% Cu/$SnO_2$-$TiO_2$ catalyst was among the main contributing factors towards higher activity of this catalyst.

Recently, Tang *et al*. [27] performed *in situ* Fourier transform infrared (FTIR) spectroscopy study of copper oxide supported on $TiO_2$. The easily reduced $Cu^{+2}$ and $Cu^{+1}$ were well dispersed on rutile surface and showed excellent activity. The presence of surface oxygen vacancy at the rutile phase catalyst surface also enhanced the catalytic performance. Cu supported on rutile exhibited threefold CO conversion as compared with anatase supported catalyst. CO reaction mechanism showed that in rutile supported Cu catalyst, CO mainly adsorbed on $Cu^{+1}$ while oxygen adsorbed on surface oxygen vacancies. The adsorbed CO reacted with dissociatively adsorbed oxygen to generate $CO_2$.

The reduction of $Cu^{+1}$ and electronic interaction between copper and $TiO_2$ also play a role in CO oxidation reaction. The study of the effect of $Ti^{+3}$ on copper supported over $TiO_2$ catalysts utilized for CO oxidation showed that even smaller copper loading of 3.4 wt% exhibited higher turnover frequency (3.7 $s^{-1}$) than Pt (3-5%) supported on $TiO_2$ (1.5-1.8 $s^{-1}$) and bimetallic CuO/ZnO/$Al_2O_3$ catalyst (0.3 $s^{-1}$). The presence of $Cu^{+1}$ species, high dispersion of copper species, and strong electron interaction between copper species and $TiO_2$ support were the factors responsible for excellent activity of 3.4 wt% Cu/$TiO_2$ catalyst [123].

The comparison study between $TiO_2$ nanopowder and nanotubes (NTs) for copper based catalyst for CO oxidation inferred the role of different morphologies and surface areas during reaction. It was observed that CuO/$TiO_2$-NTs outperformed CuO/$TiO_2$ and light off temperatures were 90 and 144 ℃ respectively. The catalytic performance of nanotubes supported catalyst was ascribed to the higher surface area of $TiO_2$-NTs, better dispersion of CuO over $TiO_2$-NTs support surface and stronger interaction between CuO and $TiO_2$-NTs [124].

Considering the significance of both copper and titania nanostructures, the next step of the ***fourth phase*** of this research work is focused on the study of interface between

copper and titania nanorods (synthesized in the first stage of ***fourth phase***) and their role in CO oxidation reaction. This study is thoroughly discussed in chapter 5.

*2.2.5 The proposed reaction mechanism*

The interaction of gas molecules at the catalyst surface, including the adsorption of reactants, their interaction with each other to yield product and the desorption of products, are described by the reaction mechanism. Generally, three types of mechanisms are proposed and discussed for CO oxidation reaction *i.e.*, Langmuir-Hinshelwood (LH) mechanism, Eley-Rideal (ER) mechanism and Mars and Van Krevelen (MVK) mechanism. In LH mechanism, the adsorption of both the reactants takes place over the catalyst surface, followed by the reaction between the adsorbed molecules which is facilitated by the surface diffusion. Finally, the products desorb from the surface. In LH mechanism, the highest reactivity is achieved by the adsorption of stoichiometric amounts of reactants as well as full dispersion and good diffusion of reactants over the catalyst surface. Most of the catalytic systems are reported to follow LH mechanism. An example is the oxidation of CO on Cu-based catalyst [27].

The adsorption of only one of the reactants at the surface happens in case of ER mechanism. The second reactant interacts/reacts with the adsorbed reactant directly from the gas phase followed by the desorption of the product. The higher reactivity in ER mechanism is achieved by increased coverage of the reactant being adsorbed and by the higher pressure or concentration of the second reactant. The $CO_2$ hydrogenation during formate synthesis is an example of a reaction following the ER mechanism [125].

MVK mechanism mainly involves metal oxide catalysts which are defined by its reducibility or tendency to donate oxygen. MVK mechanism over reducible oxides is different than over the metal anchored on the oxide supports. The presence of metal/oxide interface, in case of supported catalysts, also influences the surface oxygen reactivity. In the MVK mechanism over reducible metal oxides, one of the reactants chemisorbs on the metal oxide catalyst surface and forms a thin layer of reactant-metal oxide. The reaction takes place between the surface/lattice oxygen and surface chemisorbed species. Consequently, the product desorption leaves behind a vacancy in the surface which is filled again by the second reactant. The oxidation of CO on platinum under high oxygen pressure is an example of the MVK reaction mechanism

in which surface oxide formed interacts with the gas phase CO [126]. The different aspects of MVK mechanism over reducible oxides and supported catalysts are discussed in [126].

### 2.3 CO reduction *via* Fischer-Tropsch synthesis (FTS)

Carbon monoxide (CO) can be hydrogenated to valuable products using different processes including methanol synthesis, Fischer-Tropsch synthesis (FTS), and higher alcohol synthesis [127]. The high energy demands and depletion of fossil fuels have attracted the intentions and interest of the researchers in the FTS technology [128]. It is generally accepted that the FTS technology plays major role, in gas to liquid technology, in serving as a bridge between inorganic and organic chemistry [129-132]. In the FTS process, syngas generated from partial oxidation, gasification or steam reforming of natural gas, coal, biomass or shale gas, is converted to linear hydrocarbons [132, 133]. Cobalt, iron or ruthenium are common metals to be utilized for the FTS process [134-137]. The FTS process can also lead to the production of oxy-compound products and lower olefins [138-141]. Therefore, it can be inferred that the FTS process is environmentally friendly alternative to synthesize olefins, transportation fuels, value-added chemicals and oil products [142-144].

The FTS is a polymerization process which involves adsorption of CO, chain initiation and termination of the chain growth. The mechanistic pathway of chain initiation and chain growth can be schematically presented in the Figure 2.1.

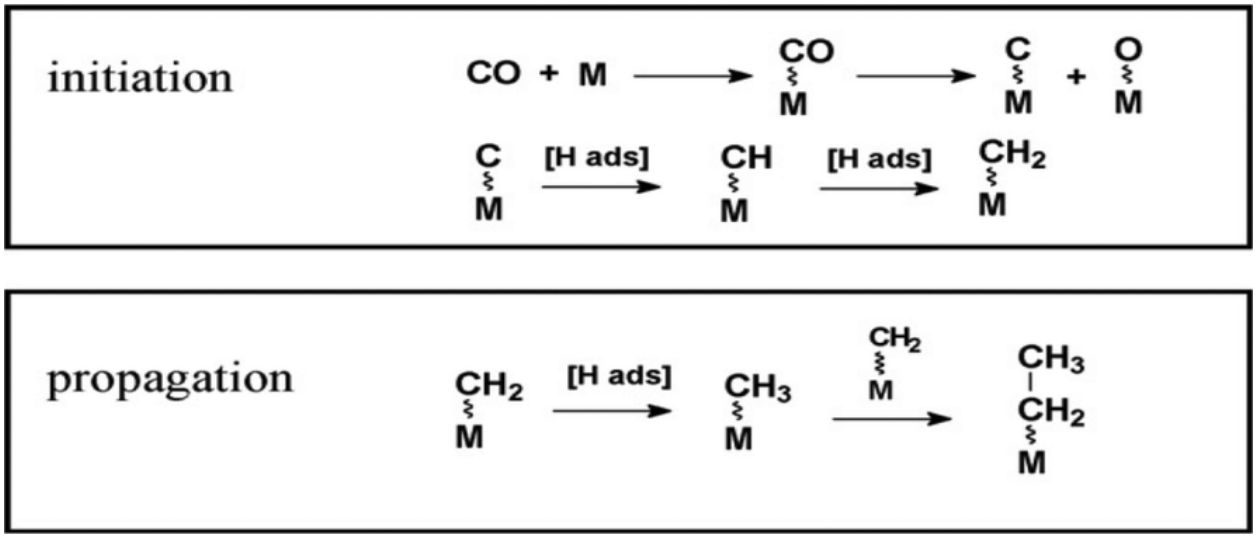


**Figure 2.2.** Mechanistic pathway for the FTS process [145]

The CO adsorption occurring over the catalyst surface leads to the stepwise growth process. The dissociative adsorption of CO is followed by the hydrogenation of CO which results in the formation of $CH_2$ units and these units act as "monomers" for the chain propagation process. In the next step, the adsorbed monomers can proceed to either desorb from the catalyst surface or form FT products *via* further hydrogenation and this process continues until termination reaction. The termination reaction follows two possible pathways *i.e.*, hydrogenation and hence producing paraffin products or dehydrogenation leading to the synthesis of olefin products. Additionally, the alcohols and aldehydes are also formed *via* insertion of oxygenated species into alkyl functional group grown over the catalyst surface [146]. CO insertion into alkyl functional groups at the end of the growing chain terminates the reaction with the production of α-olefins and normal paraffin as major products [147].

The ***fifth phase*** of the proposed project work was focused on CO hydrogenation over cobalt and copper based mono and bimetallic catalysts *via* the FTS to produce long chain hydrocarbons. The cobalt based catalysts have attracted the attention of scientists in recent decades for the FTS process due to their higher activity towards olefins production, lower activity towards water gas shift and lower deactivation than iron and copper catalysts which favour water gas shift [148-152]. The copper based catalysts are not reported for the FTS process due to their very low or no activity while copper has been reported as promoter over cobalt and iron based catalysts [153, 154]. Intensive research is in progress during recent years to improve the performance of commercially used cobalt based catalysts to find a suitable mono and/or metal promoted/bimetallic catalyst, which would be active, selective and stable for linear hydrocarbons.

## 2.4 Nanostructured catalysts for the FTS

Since the FTS process generates wide range of products including olefins, paraffins, and oxygenates, the design of the catalyst depends upon its physical, mechanical and chemical properties. The catalyst composition, structure and physico-chemical properties play significant role in the selectivity of the products. Generally, four types of catalysts are used in the FTS including cobalt (Co), nickel (Ni), iron (Fe) and ruthenium (Ru) due to their dissociative adsorption of CO and $H_2$ [155]. These catalysts behave differently under reaction conditions and their selectivity varies for reactions (mentioned in chapter 1 *i.e.*, reactions 1.2-1.7). Among these catalysts, Ni is more

selective towards methane formation under reaction conditions [156] while the rest of the catalysts promote the formation of olefins and paraffins. Ru is less selective to the methane, promotes the synthesis of $C_{5+}$ hydrocarbons [157] and is expensive to be utilized commercially. Hence, Co- and Fe-based catalysts are promising and widely used for the FTS process on commercial scale [158, 159]. The cost of Co-based catalysts is more than that of the Fe-based catalysts, but Co-based catalysts are more resistant to deactivation. In addition, the productivity of Co-based catalysts is also higher than that of the Fe-based catalysts despite having almost similar activities.

Fe-based catalysts are more prone to carbon deposition and, thus, catalyst deactivation as compared with Co-based catalysts. Fe also forms nitrides and carbides, which also play their role in the FTS process and, as mentioned earlier, Fe favours WGS reaction while Co-based catalysts are reported to exhibit WGS activity only at higher temperatures [160-162]. Fe-based catalysts produce huge amounts of oxygenates in contrast to Co-based catalysts, which generate straight chain hydrocarbons as major products. The operating temperatures and pressures for Co-based catalysts are within a narrow range in contrast to Fe-based catalysts, which produces oxygenates and hydrocarbons at different temperatures (up to ~350 °C) and pressures. The increase in operating temperature in case of Co-based catalysts increase their selectivity towards methane. Fe-based catalysts are more selective to production of olefins than Co counterparts [161, 162]. The higher stability and productivity of Co-based catalysts make these catalysts optimal choice to be utilized in the FTS for long chain hydrocarbons production. The catalytic activity of Co-based catalysts for the FTS process depends upon various factors such as Co particle size and dispersion, catalyst synthesis technique, operating conditions, type of oxide support and type of promoters *etc*.

The fundamental role of the oxide support in the FTS catalysts is to facilitate metal particles dispersion and stability post hydrogen reduction. The physico-chemical properties of the oxide support also influence the properties of the final catalyst. For instance, porosity and surface structure of the support might affect the particle size of supported metal catalysts. The oxide support also offers unique features to the final catalyst, including improved surface area and porosity, enhanced active metal dispersion, control over metal particle size, reducibility and metal-support interaction, and improved mechanical properties [163-165].

The effect of several oxide supports on the performance of the catalysts during the FTS process has been extensively investigated and the oxide support is reported to have strong impact on the properties of the resulting catalysts [132, 164, 166]. Mostly oxide supports such as silica ($SiO_2$), alumina ($Al_2O_3$) and titania ($TiO_2$) are studied for the FTS process. Storsæter *et al*. [167] studied the influence of above mentioned oxide supports ($SiO_2$, $Al_2O_3$ and $TiO_2$) on the catalytic performance of Co-based catalysts in the FTS process. The increase in the average pore diameter of the support enhanced the Co particle size and reducibility. The size and the shape of the active metal particles was also significantly affected by the pore structure of the oxide support. The study of various oxide supports such as magnesia (MgO), $SiO_2$, $Al_2O_3$ and $TiO_2$ over the Co-based catalysts showed the activity performance was highest over $TiO_2$-supported Co catalyst while least activity was revealed over MgO-supported Co-based catalyst [166]. Iglesia *et al*. [132] investigated the effect of oxide supports on the catalytic performance of Ru- and Co-based catalysts under reaction conditions (203 °C; 5.5 bar; $H_2/CO = 2.1$) favourable for the formation of $C_{5+}$ hydrocarbons. It was found that hydrocarbons production rates were independent of the oxide supports for both Ru and Co-based catalysts at pressures greater than 5 bar.

Although the role of the promoters, despite extensive characterization studies, is not yet clear, the addition of promoters affects the catalytic activity of the FTS catalysts. Different types of promoters are used in the FTS catalysts including textural promoters, electronic promoters, structural promoters, poison-resistant promoters and stabilizers [168]. The structural promoters influence Co dispersion and metal-support interaction. By avoiding the formation of metal-support alloys or metal sintering, these promoters mainly enhance the number of active sites which may lead to improved catalytic activity and stability but these promoters have no role in affecting the product selectivity [168, 169]. The role of electronic promoters is more ambiguous and they primarily affect the surface properties or surface electron transfer. In electronic promotion of Co-based catalysts, promoter either forms an alloy with Co or decorates Co surface with its oxide to improve the activity and stability of the catalysts. Promoters can also have synergistic effect which may influence the overall the FTS reaction. Depending upon the promoter type, synergistic effect can promote water gas shift reaction, influence the alkane to alkene ratio, can cause $CO_2$ hydrogenation and can oxidize the carbon depositing on Co surface [168]. Both noble metal and non-noble metal promoters are used for the FTS

catalysis. The active metal dispersion, structure, product selectivities and reaction rates are strongly influenced by noble metal promoters including rhodium (Rh), platinum (Pt), palladium (Pd) and Ru. Furthermore, noble metal promoters facilitate easier metal oxide reduction, enhance active metal dispersion, alloy formation between promoter and active metal, improve resistance to catalyst deactivation and promote the intrinsic reactivity of the metal active sites on the catalyst surface [133].

The non-noble metal based promoters such as copper, potassium, manganese and sodium are also reported for the FTS catalysis [169-171]. The copper based catalysts are commonly utilized for low temperature water gas shift reaction. Copper, when added to iron as promoter, improves the reduction of iron and thus prevents sintering of iron [154]. Similarly, copper (Cu) can be used as promoter over Co-based catalysts and it is hypothesized that Cu addition to Co-based catalysts supported on titania nanorods could improve the reducibility and, hence, the activity and selectivity of the promoted and/or bimetallic catalysts.

## References


[1] A.D. Allian, K. Takanabe, K.L. Fujdala, X. Hao, T.J. Truex, J. Cai, C. Buda, M. Neurock, E. Iglesia, Chemisorption of CO and Mechanism of CO Oxidation on Supported Platinum Nanoclusters, J. Am. Chem. Soc., 133 (2011) 4498-4517.

[2] J.T. Kummer, Catalysts for Automobile Emission Control, Prog. Energy Combust., 6 (1980) 177-199.

[3] H.J. Freund, G. Meijer, M. Scheffler, R. Schlogl, M. Wolf, CO Oxidation as a Prototypical Reaction for Heterogeneous Processes, Angew. Chem. Int. Edit., 50 (2011) 10064-10094.

[4] M.V. Twigg, Progress and future challenges in controlling automotive exhaust gas emissions, Appl. Catal. B-Environ., 70 (2007) 2-15.

[5] K. Liu, A.Q. Wang, T. Zhang, Recent Advances in Preferential Oxidation of CO Reaction over Platinum Group Metal Catalysts, ACS Catal., 2 (2012) 1165-1178.

[6] A.B. Lamb, W.C. Bray, J.C.W. Frazer, The removal of carbon monoxide from air, J. Ind. Eng. Chem., 12 (1920) 213-221.

[7] D.R. Merrill, C.C. Scalione, The catalytic oxidation of carbon monoxide at ordinary temperatures, J. Am. Chem. Soc., 43 (1921) 1982-2002.

[8] C.H. Yoon, D.L. Cocke, The Design and Preparation of Planar Models of Oxidation Catalysts .1. Hopcalite, J. Catal., 113 (1988) 267-280.

[9] X.W. Xie, Y. Li, Z.Q. Liu, M. Haruta, W.J. Shen, Low-temperature oxidation of CO catalysed by $Co_3O_4$ nanorods, Nature, 458 (2009) 746-749.

[10] G.J. Wu, N.J. Guan, L.D. Li, Low temperature CO oxidation on Cu-$Cu_2O/TiO_2$ catalyst prepared by photodeposition, Catal. Sci. Technol., 1 (2011) 601-608.

[11] S. Lv, G.F. Xia, C. Jin, C.Y. Hao, L. Wang, J.L. Li, Y.H. Zhang, J.J. Zhu, Low-temperature CO oxidation by $Co_3O_4$ nanocubes on the surface of $Ca(OH)_2$ nanosheets, Catal. Commun., 86 (2016) 100-103.

[12] S. Royer, D. Duprez, Catalytic Oxidation of Carbon Monoxide over Transition Metal Oxides, Chemcatchem, 3 (2011) 24-65.

[13] O.A. Kirichenko, N.A. Dayshan, E.A. Redina, G.I. Kapustin, I.V. Mishin, O.P. Tkachenko, A.V. Kucherov, L.M. Kustov, Gold nanoparticles in environmental catalysis: Influence of the Fe-modified alumina supports on the catalytic behavior of supported gold nanoparticles in CO oxidation in the presence of ammonia, Chem. Eng. J., 292 (2016) 62-71.

[14] J. Dou, Z.C. Sun, A.A. Opalade, N. Wang, W.S. Fu, F. Tao, Operando chemistry of catalyst surfaces during catalysis, Chem. Soc. Rev., 46 (2017) 2001-2027.
[15] R. Ye, T.J. Hurlburt, K. Sabyrov, S. Alayoglu, G.A. Somorjai, Molecular catalysis science: Perspective on unifying the fields of catalysis, Proc. Natl. Acad. Sci. USA, 113 (2016) 5159-5166.
[16] Y. Zhou, Y. Li, W.J. Shen, Shape Engineering of Oxide Nanoparticles for Heterogeneous Catalysis, Chem-Asian J., 11 (2016) 1470-1488.
[17] B. Roldan Cuenya, F. Behafarid, Nanocatalysis: size- and shape-dependent chemisorption and catalytic reactivity, Surf. Sci. Rep., 70 (2015) 135-187.
[18] F. Tao, M. Salmeron, In Situ Studies of Chemistry and Structure of Materials in Reactive Environments, Science, 331 (2011) 171-174.
[19] S.R. Zhang, L. Nguyen, Y. Zhu, S.H. Zhan, C.K. Tsung, F. Tao, In-Situ Studies of Nanocatalysis, Acc. Chem. Res., 46 (2013) 1731-1739.
[20] D. Wang, D. Astruc, The recent development of efficient Earth-abundant transition-metal nanocatalysts, Chem. Soc. Rev., 46 (2017) 816-854.
[21] D. Das, Multicomponent Reactions in Organic Synthesis Using Copper-Based Nanocatalysts, ChemistrySelect, 1 (2016) 1959-1980.
[22] M.B. Gawande, A. Goswami, F.X. Felpin, T. Asefa, X.X. Huang, R. Silva, X.X. Zou, R. Zboril, R.S. Varma, Cu and Cu-Based Nanoparticles: Synthesis and Applications in Review Catalysis, Chem. Rev., 116 (2016) 3722-3811.
[23] B.C. Ranu, R. Dey, T. Chatterjee, S. Ahammed, Copper Nanoparticle-Catalyzed Carbon–Carbon and Carbon–Heteroatom Bond Formation with a Greener Perspective, Chemsuschem, 5 (2012) 22-44.
[24] P.O. Larsson, A. Andersson, Complete oxidation of CO, ethanol, and ethyl acetate over copper oxide supported on titania and ceria modified titania, J. Catal., 179 (1998) 72-89.
[25] O.V. Komova, A.V. Simakov, V.A. Rogov, D.I. Kochubei, G.V. Odegova, V.V. Kriventsov, E.A. Paukshtis, V.A. Ushakov, N.N. Sazonova, T.A. Nikoro, Investigation of the state of copper in supported copper-titanium oxide catalysts, J. Mol. Catal. A-Chem., 161 (2000) 191-204.
[26] T. Venkov, K. Hadjiivanov, FTIR study of CO interaction with $Cu/TiO_2$, Catal. Commun., 4 (2003) 209-213.

[27] Y.X. Tang, L.H. Dong, C.S. Deng, M.N. Huang, B. Li, H.L. Zhang, In situ FT-IR investigation of CO oxidation on $CuO/TiO_2$ catalysts, Catal. Commun., 78 (2016) 33-36.

[28] G.G. Jernigan, G.A. Somorjai, Carbon-Monoxide Oxidation over 3 Different Oxidation-States of Copper - Metallic Copper, Copper (I) Oxide, and Copper (II) Oxide-a Surface Science and Kinetic-Study, J. Catal., 147 (1994) 567-577.

[29] A.S. Barnard, L.Y. Chang, Thermodynamic Cartography and Structure/Property Mapping of Commercial Platinum Catalysts, ACS Catal., 1 (2011) 76-81.

[30] P. Lignier, R. Bellabarba, R.P. Tooze, Scalable strategies for the synthesis of well-defined copper metal and oxide nanocrystals, Chem. Soc. Rev., 41 (2012) 1708-1720.

[31] M. Yin, C.K. Wu, Y.B. Lou, C. Burda, J.T. Koberstein, Y.M. Zhu, S. O'Brien, Copper oxide nanocrystals, J. Am. Chem. Soc., 127 (2005) 9506-9511.

[32] C. Barriere, K. Piettre, V. Latour, O. Margeat, C.O. Turrin, B. Chaudret, P. Fau, Ligand effects on the air stability of copper nanoparticles obtained from organometallic synthesis, J. Mater. Chem., 22 (2012) 2279-2285.

[33] H.M. Lee, M.F. Ge, B.R. Sahu, P. Tarakeshwar, K.S. Kim, Geometrical and electronic structures of gold, silver, and gold-silver binary clusters: Origins of ductility of gold and gold-silver alloy formation, J. Phys. Chem. B, 107 (2003) 9994-10005.

[34] D.I. Gittins, D. Bethell, D.J. Schiffrin, R.J. Nichols, A nanometre-scale electronic switch consisting of a metal cluster and redox-addressable groups, Nature, 408 (2000) 67-69.

[35] L.B. Zhang, E.K. Wang, Metal nanoclusters: New fluorescent probes for sensors and bioimaging, Nano Today, 9 (2014) 132-157.

[36] X. Yuan, Z.T. Luo, Y. Yu, Q.F. Yao, J.P. Xie, Luminescent Noble Metal Nanoclusters as an Emerging Optical Probe for Sensor Development, Chem-Asian J., 8 (2013) 858-871.

[37] L. Shang, S.J. Dong, G.U. Nienhaus, Ultra-small fluorescent metal nanoclusters: Synthesis and biological applications, Nano Today, 6 (2011) 401-418.

[38] Y.Z. Lu, W. Chen, Sub-nanometre sized metal clusters: from synthetic challenges to the unique property discoveries, Chem. Soc. Rev., 41 (2012) 3594-3623.

[39] J.J. Li, J.J. Zhu, K. Xu, Fluorescent metal nanoclusters: From synthesis to applications, Trac-Trend. Anal. Chem., 58 (2014) 90-98.

[40] L.D. Socaciu, J. Hagen, T.M. Bernhardt, L. Woste, U. Heiz, H. Hakkinen, U. Landman, Catalytic CO oxidation by free $Au_2^-$: Experiment and theory, J. Am. Chem. Soc., 125 (2003) 10437-10445.

[41] I.N. Remediakis, N. Lopez, J.K. Norskov, CO oxidation on gold nanoparticles: Theoretical studies, Appl. Catal. A-Gen., 291 (2005) 13-20.

[42] H. Hakkinen, U. Landman, Gas-phase catalytic oxidation of CO by $Au_2^-$, J. Am. Chem. Soc., 123 (2001) 9704-9705.

[43] Y. Gao, N. Shao, S. Bulusu, X.C. Zeng, Effective CO oxidation on endohedral gold-cage nanoclusters, J. Phys. Chem. C, 112 (2008) 8234-8238.

[44] J.L.C. Fajin, M.N.D.S. Cordeiro, J.R.B. Gomes, DFT Study of the CO Oxidation on the Au(321) Surface, J. Phys. Chem. C, 112 (2008) 17291-17302.

[45] M.F. Camellone, S. Fabris, Reaction Mechanisms for the CO Oxidation on $Au/CeO_2$ Catalysts: Activity of Substitutional $Au^{3+}/Au^+$ Cations and Deactivation of Supported $Au^+$ Adatoms, J. Am. Chem. Soc., 131 (2009) 10473-10483.

[46] A. Roldan, J.M. Ricart, F. Illas, G. Pacchioni, $O_2$ Activation by $Au_5$ Clusters Stabilized on Clean and Electron-Rich MgO Stepped Surfaces, J. Phys. Chem. C, 114 (2010) 16973-16978.

[47] Y. Chen, P. Crawford, P. Hu, Recent advances in understanding CO oxidation on gold nanoparticles using density functional theory, Catal. Lett., 119 (2007) 21-28.

[48] M.C. Kung, R.J. Davis, H.H. Kung, Understanding Au-catalysed low-temperature CO oxidation, J. Phys. Chem. C, 111 (2007) 11767-11775.

[49] P. Frondelius, H. Hakkinen, K. Honkala, Formation of Gold(I) Edge Oxide at Flat Gold Nanoclusters on an Ultrathin MgO Film under Ambient Conditions, Angew. Chem. Int. Edit., 49 (2010) 7913-7916.

[50] F. Wang, D.J. Zhang, X.H. Xu, Y. Ding, Theoretical Study of the CO Oxidation Mediated by $Au_3^+$, $Au_3$, and $Au_3^-$: Mechanism and Charge State Effect of Gold on Its Catalytic Activity, J. Phys. Chem. C, 113 (2009) 18032-18039.

[51] X.T. Nie, H.F. Qian, Q.J. Ge, H.Y. Xu, R.C. Jin, CO Oxidation Catalyzed by Oxide-Supported $Au_{25}(SR)_{18}$ Nanoclusters and Identification of Perimeter Sites as Active Centers, ACS Nano, 6 (2012) 6014-6022.

[52] Y.W. Li, Y.X. Chen, S.D. House, S. Zhao, Z. Wahab, J.C. Yang, R.C. Jin, Interface Engineering of Gold Nanoclusters for CO Oxidation Catalysis, ACS Appl. Mater. Interfaces, 10 (2018) 29425-29434.

[53] J. Papavasiliou, Interaction of atomically dispersed gold with hydrothermally prepared copper-cerium oxide for preferential CO oxidation reaction, Catal. Today, (2019).

[54] X.T. Nie, C.J. Zeng, X.G. Ma, H.F. Qian, Q.J. Ge, H.Y. Xu, R.C. Jin, $CeO_2$-supported $Au_{38}(SR)_{24}$ nanocluster catalysts for CO oxidation: a comparison of ligand-on and -off catalysts, Nanoscale, 5 (2013) 5912-5918.

[55] Z.L. Wu, D.R. Mullins, L.F. Allard, Q.F. Zhang, L.S. Wang, CO oxidation over ceria supported $Au_{22}$ nanoclusters: Shape effect of the support, Chinese Chem. Lett., 29 (2018) 795-799.

[56] X. Zhao, Y.J. Hu, H. Jiang, J.R. Yu, R.X. Jiang, C.Z. Li, Engineering $TiO_2$ supported Pt sub-nanoclusters *via* introducing variable valence Co ion in high-temperature flame for CO oxidation, Nanoscale, 10 (2018) 13384-13392.

[57] W.L. Li, Q.J. Ge, X.G. Ma, Y.X. Chen, M.Z. Zhu, H.Y. Xu, R.C. Jin, Mild activation of $CeO_2$-supported gold nanoclusters and insight into the catalytic behavior in CO oxidation, Nanoscale, 8 (2016) 2378-2385.

[58] C.F. Albert, P.C. Healy, J.D. Kildea, C.L. Raston, B.W. Skelton, A.H. White, Lewis-Base Adducts of Group-11 Metal(I) Compounds .49. Structural Characterization of Hexameric and Pentameric (Triphenylphosphine)Copper(I) Hydrides, Inorg. Chem., 28 (1989) 1300-1306.

[59] A.W. Cook, T.A.D. Nguyen, W.R. Buratto, G. Wu, T.W. Hayton, Synthesis, Characterization, and Reactivity of the Group 11 Hydrido Clusters $[Ag_6H_4(dppm)_4(OAc)_2]$ and $[Cu_3H(dppm)_3(OAc)_2]$, Inorg. Chem., 55 (2016) 12435-12440.

[60] M.A. Walter, J.; Lopez-Acevedo, O.; Jadzinsky, P. D.; Calero, G.; Ackerson, C. J.; Whetten, R. L.; Grönbeck, H.; Häkkinen, H., A unified view of ligand-protected gold clusters as superatom complexes, Proc. Natl. Acad. Sci. USA, 105 (2008) 9157-9162.

[61] W.T. Wei, Y.Z. Lu, W. Chen, S.W. Chen, One-Pot Synthesis, Photoluminescence, and Electrocatalytic Properties of Subnanometer-Sized Copper Clusters, J. Am. Chem. Soc., 133 (2011) 2060-2063.

[62] N. Vilar-Vidal, J. Rivas Rey, M.A.L. Quintela, Green Emitter Copper Clusters as Highly Efficient and Reusable Visible Degradation Photocatalysts, Small, 10 (2014) 3632-3636.

[63] H. Oyanagi, Z.H. Sun, Y. Jiang, M. Uehara, H. Nakamura, K. Yamashita, Y. Orimoto, L. Zhang, C. Lee, A. Fukano, H. Maeda, Small copper clusters studied by X-ray absorption near-edge structure, J. Appl. Phys., 111 (2012).
[64] H. Oyanagi, Y. Orimoto, K. Hayakawa, K. Hatada, Z.H. Sun, L. Zhang, K. Yamashita, H. Nakamura, M. Uehara, A. Fukano, H. Maeda, Nanoclusters Synthesized by Synchrotron Radiolysis in Concert with Wet Chemistry, Sci. Rep., 4 (2014).
[65] V.L. Mazalova, A.V. Soldatov, S. Adam, A. Yakovlev, T. Moller, R.L. Johnston, Small Copper Clusters in Ar Shells: A Study of Local Structure, J. Phys. Chem. C, 113 (2009) 9086-9091.
[66] P.A. Montano, G.K. Shenoy, E.E. Alp, W. Schulze, J. Urban, Structure of Copper Microclusters Isolated in Solid Argon, Phys. Rev. Lett., 56 (1986) 2076-2079.
[67] T.A.D. Nguyen, B.R. Goldsmith, H.T. Zaman, G. Wu, B. Peters, T.W. Hayton, Synthesis and Characterization of a $Cu_{14}$ Hydride Cluster Supported by Neutral Donor Ligands, Chem-Eur. J., 21 (2015) 5341-5344.
[68] M.A. Huertos, I. Cano, N.A.G. Bandeira, J. Benet-Buchholz, C. Bo, P.W.N.M. van Leeuwen, Phosphinothiolates as Ligands for Polyhydrido Copper Nanoclusters, Chem-Eur. J., 20 (2014) 16121-16127.
[69] R.S. Dhayal, J.H. Liao, Y.R. Lin, P.K. Liao, S. Kahlal, J.Y. Saillard, C.W. Liu, A Nanospheric Polyhydrido Copper Cluster of Elongated Triangular Orthobicupola Array: Liberation of $H_2$ from Solar Energy, J. Am. Chem. Soc., 135 (2013) 4704-4707.
[70] R. Li, S.N. Li, Y. Liu, T. Ochiai, S.S. Latthe, K. Nakata, R.M. Xing, S.H. Liu, Polyelectrolyte-assisted soft reduced process for Pt-Cu nanoclusters with enhanced electrocatalytic activity for the methanol oxidation reaction, J. Phys. Chem. Solids, 124 (2019) 361-366.
[71] X.H. Gao, C. Du, C.M. Zhang, W. Chen, Copper Nanoclusters on Carbon Supports for the Electrochemical Oxidation and Detection of Hydrazine, Chemelectrochem, 3 (2016) 1266-1272.
[72] L.P. Mei, P. Song, J.J. Feng, J.H. Shen, W. Wang, A.J. Wang, X.X. Weng, Nonenzymatic amperometric sensing of glucose using a glassy carbon electrode modified with a nanocomposite consisting of reduced graphene oxide decorated with $Cu_2O$ nanoclusters, Microchim. Acta, 182 (2015) 1701-1708.
[73] A. Dobrzeniecka, P.J. Kulesza, Electrocatalytic Activity toward Oxygen Reduction of $RuS_xN_y$ Catalysts Supported on Different Nanostructured Carbon Carriers, ECS J. Solid State Sci. Technol., 2 (2013) M61-M66.

[74] D. Astruc, F. Lu, J.R. Aranzaes, Nanoparticles as recyclable catalysts: The frontier between homogeneous and heterogeneous catalysis, Angew. Chem. Int. Edit., 44 (2005) 7852-7872.

[75] C.M. Crudden, M. Sateesh, R. Lewis, Mercaptopropyl-modified mesoporous silica: A remarkable support for the preparation of a reusable, heterogeneous palladium catalyst for coupling reactions, J. Am. Chem. Soc., 127 (2005) 10045-10050.

[76] A. D'Agata, S. Fasulo, L.J. Dallas, A.S. Fisher, M. Maisano, J.W. Readman, A.N. Jha, Enhanced toxicity of 'bulk' titanium dioxide compared to 'fresh' and 'aged' nano-$TiO_2$ in marine mussels (Mytilus galloprovincialis), Nanotoxicology, 8 (2014) 549-558.

[77] Y.G. Guo, Y.S. Hu, W. Sigle, J. Maier, Superior electrode performance of nanostructured mesoporous $TiO_2$ (anatase) through efficient hierarchical mixed conducting networks, Adv. Mater., 19 (2007) 2087.

[78] J.L. Xu, K. Li, W.Y. Shi, R.J. Li, T.Y. Peng, Rice-like brookite titania as an efficient scattering layer for nanosized anatase titania film-based dye-sensitized solar cells, J. Power Sources, 260 (2014) 233-242.

[79] M.M. Chen, X. Sun, Z.J. Qiao, Q.Q. Ma, C.Y. Wang, Anatase-$TiO_2$ nanocoating of $Li_4Ti_5O_{12}$ nanorod anode for lithium-ion batteries, J. Alloys Compd., 601 (2014) 38-42.

[80] M. Fujimoto, H. Koyama, M. Konagai, Y. Hosoi, K. Ishihara, S. Ohnishi, N. Awaya, $TiO_2$ anatase nanolayer on TiN thin film exhibiting high-speed bipolar resistive switching, Appl. Phys. Lett., 89 (2006).

[81] J. Su and L. Guo, High aspect ratio $TiO_2$ nanowires tailored in concentrated HCl hydrothermal condition for photoelectrochemical water splitting, RSC Adv. 5 (2015) 53012-53018.

[82] H. Kominami, J. Kato, Y. Takada, Y. Doushi, B. Ohtani, S. Nishimoto, M. Inoue, T. Inui, Y. Kera, Novel synthesis of microcrystalline titanium(IV) oxide having high thermal stability and ultra-high photocatalytic activity: thermal decomposition of titanium(IV) alkoxide in organic solvents, Catal. Lett., 46 (1997) 235-240.

[83] S. Bagheri, K. Shameli, S.B. Abd Hamid, Synthesis and Characterization of Anatase Titanium Dioxide Nanoparticles Using Egg White Solution *via* Sol-Gel Method, J. Chem., (2013).

[84] R. Palcheva, L. Dimitrov, G. Tyuliev, A. Spojakina, K. Jiratova, $TiO_2$ nanotubes supported NiW hydrodesulphurization catalysts: Characterization and activity, Appl. Surf. Sci., 265 (2013) 309-316.

[85] G.F. Liang, L.M. He, H.Y. Cheng, W. Li, X.R. Li, C. Zhang, Y.C. Yu, F.Y. Zhao, The hydrogenation/dehydrogenation activity of supported Ni catalysts and their effect on hexitols selectivity in hydrolytic hydrogenation of cellulose, J. Catal., 309 (2014) 468-476.

[86] Q.Q. Luo, M. Beller, H.J. Jiao, Formic Acid Dehydrogenation on Surfaces-a Review of Computational Aspect, J. Theor. Comput. Chem., 12 (2013).

[87] X.B. Chen, S. Cao, X.L. Weng, H.Q. Wang, Z.B. Wu, Effects of morphology and structure of titanate supports on the performance of ceria in selective catalytic reduction of NO, Catal. Commun., 26 (2012) 178-182.

[88] F.J. Song, Y.X. Zhao, Q. Zhong, Adsorption of carbon dioxide on amine-modified $TiO_2$ nanotubes, J. Environ. Sci., 25 (2013) 554-560.

[89] M. Kim, S.H. Hwang, S.K. Lim, S. Kim, Effects of ion exchange and calcinations on the structure and photocatalytic activity of hydrothermally prepared titanate nanotubes, Cryst. Res. Technol., 47 (2012) 1190-1194.

[90] Y. Wu, L. Song, Y. Hu, Fabrication and Characterization of $TiO_2$ Nanotube-Epoxy Nanocomposites, Ind. Eng. Chem. Res., 50 (2011) 11988-11995.

[91] X.B. Chen, H.Q. Wang, S. Gao, Z.B. Wu, Effect of pH value on the microstructure and de$NO_x$, catalytic performance of titanate nanotubes loaded $CeO_2$, J. Colloid Interface Sci., 377 (2012) 131-136.

[92] T. Kasuga, M. Hiramatsu, A. Hoson, T. Sekino, K. Niihara, Formation of titanium oxide nanotube, Langmuir, 14 (1998) 3160-3163.

[93] N. Liu, X.Y. Chen, J.L. Zhang, J.W. Schwank, A review on $TiO_2$-based nanotubes synthesized *via* hydrothermal method: Formation mechanism, structure modification, and photocatalytic applications, Catal. Today, 225 (2014) 34-51.

[94] S.J. Tauster, S.C. Fung, R.T.K. Baker, J.A. Horsley, Strong-Interactions in Supported-Metal Catalysts, Science, 211 (1981) 1121-1125.

[95] T.S. Kim, J.D. Stiehl, C.T. Reeves, R.J. Meyer, C.B. Mullins, Cryogenic CO oxidation on $TiO_2$-supported gold nanoclusters precovered with atomic oxygen, J. Am. Chem. Soc., 125 (2003) 2018-2019.

[96] K. Wenderich, G. Mul, Methods, Mechanism, and Applications of Photodeposition in Photocatalysis: A Review, Chem. Rev., 116 (2016) 14587-14619.

[97] Y.F. Yang, P. Sangeetha, Y.W. Chen, Au/$TiO_2$ catalysts prepared by photo-deposition method for selective CO oxidation in $H_2$ stream, Int. J. Hydrogen Energy, 34 (2009) 8912-8920.

[98] G.C. Bond, D.T. Thompson, Catalysis by gold, Catal. Rev., 41 (1999) 319-388.
[99] M. Haruta, Novel catalysis of gold deposited on metal oxides, Catal. Surv. Asia, 1 (1997) 61-73.
[100] H.F. Yin, Z. Ma, M.F. Chi, S. Dai, Heterostructured catalysts prepared by dispersing Au@$Fe_2O_3$ core-shell structures on supports and their performance in CO oxidation, Catal. Today, 160 (2011) 87-95.
[101] N. Hickey, P.A. Larochette, C. Gentilini, L. Sordelli, L. Olivi, S. Polizzi, T. Montini, P. Fornasiero, L. Pasquato, M. Graziani, Monolayer protected gold nanoparticles on ceria for an efficient CO oxidation catalyst, Chem. Mater., 19 (2007) 650-651.
[102] M. Haruta, S. Tsubota, T. Kobayashi, H. Kageyama, M.J. Genet, B. Delmon, Low-Temperature Oxidation of CO over Gold Supported on $TiO_2$, Alpha-$Fe_2O_3$, and $Co_3O_4$, J. Catal., 144 (1993) 175-192.
[103] A.A. Herzing, C.J. Kiely, A.F. Carley, P. Landon, G.J. Hutchings, Identification of active gold nanoclusters on iron oxide supports for CO oxidation, Science, 321 (2008) 1331-1335.
[104] H. Kim, G. Henkelman, CO Oxidation mechanism on $CeO_2$-supported Au nanoclusters, Abstr. Pap. Am. Chem. Soc., 246 (2013).
[105] L. Zhang, H.Y. Kim, G. Henkelman, CO Oxidation at the Au-Cu Interface of Bimetallic Nanoclusters Supported on $CeO_2$(111), J. Phys. Chem. Lett., 4 (2013) 2943-2947.
[106] C.Y. Jia, W.H. Zhong, M.S. Deng, J. Jiang, CO oxidation on Ru-Pt bimetallic nanoclusters supported on $TiO_2$(101): The effect of charge polarization, J. Chem. Phys., 148 (2018).
[107] D.Y. Tang, J. Zhang, Theoretical investigation on CO oxidation catalysed by a copper nanocluster, RSC Adv, 3 (2013) 15225-15236.
[108] A.M. Joshi, M.H. Tucker, W.N. Delgass, K.T. Thomson, CO adsorption on pure and binary-alloy gold clusters: A quantum chemical study, J. Chem. Phys., 125 (2006).
[109] Y. Gao, N. Shao, Y. Pei, X.C. Zeng, Icosahedral Crown Gold Nanocluster $Au_{43}Cu_{12}$ with High Catalytic Activity, Nano Lett., 10 (2010) 1055-1062.
[110] W. Liu, Y.H. Zhao, R.Q. Zhang, Y. Li, E.J. Lavernia, Q. Jiang, Oxidation of CO Catalyzed by a Cu Cluster: Influence of an Electric Field, Chemphyschem, 10 (2009) 3295-3302.

[111] E. Fernandez, M. Boronat, A. Corma, Trends in the Reactivity of Molecular $O_2$ with Copper Clusters: Influence of Size and Shape, J. Phys. Chem. C, 119 (2015) 19832-19846.

[112] K. Basu, S. Paul, R. Jana, A. Datta, A. Banerjee, Red-Emitting Copper Nanoclusters: From Bulk-Scale Synthesis to Catalytic Reduction, ACS Sustain. Chem. Eng., 7 (2019) 1998-2007.

[113] X.L. You, Z.H. Wei, H.L. Wang, D.P. Li, J. Liu, B.B. Xu, X.M. Liu, Synthesis of two copper clusters and their catalysis towards the oxidation of benzene into phenol, RSC Adv., 4 (2014) 61790-61798.

[114] B. Yang, C. Liu, A. Halder, E.C. Tyo, A.B.F. Martinson, S. Seifer, P. Zapol, L.A. Curtiss, S. Vajda, Copper Cluster Size Effect in Methanol Synthesis from $CO_2$, J. Phys. Chem. C, 121 (2017) 10406-10412.

[115] C. Liu, B. Yang, E. Tyo, S. Seifert, J. DeBartolo, B. von Issendorff, P. Zapol, S. Vajda, L.A. Curtiss, Carbon Dioxide Conversion to Methanol over Size-Selected $Cu_4$ Clusters at Low Pressures, J. Am. Chem. Soc., 137 (2015) 8676-8679.

[116] L. Baharudin, A.C.K. Yip, V.B. Golovko, M.I.J. Polson, M.J. Watson, CO temperature-programmed desorption of a hexameric copper hydride nanocluster catalyst supported on functionalized MWCNTs for active site characterization in a low-temperature water-gas shift reaction, Chem. Eng. J. 377 (2019) 120278.

[117] L. Baharudin, A.C.K. Yip, V.B. Golovko, M.I.J. Polson, K.-F. Aguey-Zinsou, M.J. Watson, CO oxidation and the inhibition effects of carboxyl-modification and copper clusters on multi-walled carbon nanotubes, Appl. Catal. B-Environ., 262 (2020) 118265.

[118] M.Y. Kang, H.J. Yun, S. Yu, W. Kim, N.D. Kim, J. Yi, Effect of $TiO_2$ crystalline phase on CO oxidation over CuO catalysts supported on $TiO_2$, J. Mol. Catal. A-Chem., 368 (2013) 72-77.

[119] K. Nagase, Y. Zheng, Y. Kodama, J. Kakuta, Dynamic study of the oxidation state of copper in the course of carbon monoxide oxidation over powdered CuO and $Cu_2O$, J. Catal., 187 (1999) 123-130.

[120] J. Huang, S.R. Wang, Y.Q. Zhao, X.Y. Wang, S.P. Wang, S.H. Wu, S.M. Zhang, W.P. Huang, Synthesis and characterization of $CuO/TiO_2$ catalysts for low-temperature CO oxidation, Catal. Commun., 7 (2006) 1029-1034.

[121] A.A. Shutilov, G.A. Zenkovets, S.V. Tsybulya, V.Y. Gavrilov, G.N. Kryukova, Effect of the microstructure of the supported catalysts $CuO/TiO_2$ and $CuO/(CeO_2\text{-}TiO_2)$

on their catalytic properties in carbon monoxide oxidation, Kinet. Catal., 53 (2012) 409-418.

[122] K.R. Li, Y.J. Wang, S.R. Wang, B.L. Zhu, S.M. Zhang, W.P. Huang, S.H. Wu, A comparative study of $CuO/TiO_2$-$SnO_2$, $CuO/TiO_2$ and $CuO/SnO_2$ catalysts for low-temperature CO oxidation, J. Nat. Gas Chem., 18 (2009) 449-452.

[123] C.S. Chen, T.C. Chen, C.C. Chen, Y.T. Lai, J.H. You, T.M. Chou, C.H. Chen, J.F. Lee, Effect of $Ti^{3+}$ on $TiO_2$-Supported Cu Catalysts Used for CO Oxidation, Langmuir, 28 (2012) 9996-10006.

[124] B.L. Zhu, X.X. Zhang, S.R. Wang, S.M. Zhang, S.H. Wu, W.P. Huang, Synthesis and catalytic performance of $TiO_2$ nanotubes-supported copper oxide for low-temperature CO oxidation, Micropor. Mesopor. Mat., 102 (2007) 333-336.

[125] J. Ogawa, Eley-Rideal type mechanism for Formate Synthesis on a Cu(III) surface, Nippon Kagakkai Koen Yokoshu, 81 (2002) 270-276.

[126] A.R. Puigdollers, P. Schlexer, S. Tosoni, G. Pacchioni, Increasing Oxide Reducibility: The Role of Metal/Oxide Interfaces in the Formation of Oxygen Vacancies, ACS Catal., 7 (2017) 6493-6513.

[127] G.K. Ertl, H.; Schüth, F.; Weitkamp, J., Handbook of Heterogeneous Catalysis, 2008.

[128] J.P. den Breejen, A.M. Frey, J. Yang, A. Holmen, M.M. van Schooneveld, F.M.F. de Groot, O. Stephan, J.H. Bitter, K.P. de Jong, A Highly Active and Selective Manganese Oxide Promoted Cobalt-on-Silica Fischer-Tropsch Catalyst, Top. Catal., 54 (2011) 768-777.

[129] E. van Steen, M. Claeys, Fischer-Tropsch catalysts for the Biomass-to Liquid process, Chem. Eng. Technol., 31 (2008) 655-666.

[130] J.F. Li, X.F. Cheng, C.H. Zhang, W.S. Dong, Y. Yang, Y.W. Li, Comparative Study of Iron-Based Fischer-Tropsch Synthesis Catalysts Promoted with Strontium or Potassium, Catal. Lett., 146 (2016) 2574-2584.

[131] B. Qiu, C. Yang, W.H. Guo, Y. Xu, Z.B. Liang, D. Ma, R.Q. Zou, Highly dispersed Co-based Fischer-Tropsch synthesis catalysts from metal-organic frameworks, J. Mater. Chem. A, 5 (2017) 8081-8086.

[132] E. Iglesia, S.L. Soled, R.A. Fiato, Fischer-Tropsch Synthesis on Cobalt and Ruthenium - Metal Dispersion and Support Effects on Reaction-Rate and Selectivity, J. Catal., 137 (1992) 212-224.

[133] A.Y. Khodakov, W. Chu, P. Fongarland, Advances in the development of novel cobalt Fischer-Tropsch catalysts for synthesis of long-chain hydrocarbons and clean fuels, Chem. Rev., 107 (2007) 1692-1744.
[134] J.C. Kang, X.J. Wang, X.B. Peng, Y.D. Yang, K. Cheng, Q.H. Zhang, Y. Wang, Mesoporous Zeolite Y-Supported Co Nanoparticles as Efficient Fischer-Tropsch Catalysts for Selective Synthesis of Diesel Fuel, Ind. Eng. Chem. Res., 55 (2016) 13008-13019.
[135] C.X. Xiao, Z.P. Cai, T. Wang, Y. Kou, N. Yan, Aqueous-phase Fischer-Tropsch synthesis with a ruthenium nanocluster catalyst, Angew. Chem. Int. Edit., 47 (2008) 746-749.
[136] J. Xie, J. Yang, A.I. Dugulan, A. Holmen, D. Chen, K.P. de Jong, M.J. Louwerse, Size and Promoter Effects in Supported Iron Fischer-Tropsch Catalysts: Insights from Experiment and Theory, ACS Catal., 6 (2016) 3147-3157.
[137] W.Z. Li, J.X. Liu, J. Gu, W. Zhou, S.Y. Yao, R. Si, Y. Guo, H.Y. Su, C.H. Yan, W.X. Li, Y.W. Zhang, D. Ma, Chemical Insights into the Design and Development of Face Centered Cubic Ruthenium Catalysts for Fischer Tropsch Synthesis, J. Am. Chem. Soc., 139 (2017) 2267-2276.
[138] Y.J. Ding, $Co_2C$ nanoprisms for syngas conversion to lower olefins with high selectivity, Chinese J. Catal., 38 (2017) 1-4.
[139] Q.H. Zhang, J.C. Kang, Y. Wang, Development of Novel Catalysts for Fischer-Tropsch Synthesis: Tuning the Product Selectivity, Chemcatchem, 2 (2010) 1030-1058.
[140] Q.L. Yang, A. Cao, N. Kang, H.Y. Ning, J.M. Wang, Z.T. Liu, Y. Liu, Bimetallic Nano Cu-Co Based Catalyst for Direct Ethanol Synthesis from Syngas and Its Structure Variation with Reaction Time in Slurry Reactor, Ind. Eng. Chem. Res., 56 (2017) 2889-2898.
[141] D.D. Xu, H.T. Zhang, H.F. Ma, W.X. Qian, W.Y. Ying, Effect of Ce promoter on Rh-Fe/$TiO_2$ catalysts for ethanol synthesis from syngas, Catal. Commun., 98 (2017) 90-93.
[142] H. Du, H.J. Zhu, X.K. Chen, W.D. Dong, W. Lu, W.T. Luo, M. Jiang, T. Liu, Y.J. Ding, Study on CaO-promoted Co/AC catalysts for synthesis of higher alcohols from syngas, Fuel, 182 (2016) 42-49.
[143] N. Yamane, Y. Wang, J. Li, Y.L. He, P.P. Zhang, L. Nguyen, L. Tan, P.P. Ai, X.B. Peng, Y. Wang, G.H. Yang, N. Tsubaki, Building premium secondary reaction

field with a miniaturized capsule catalyst to realize efficient synthesis of a liquid fuel directly from syngas, Catal. Sci. Technol., 7 (2017) 1996-2000.
[144] P. Zhai, C. Xu, R. Gao, X. Liu, M.Z. Li, W.Z. Li, X.P. Fu, C.J. Jia, J.L. Xie, M. Zhao, X.P. Wang, Y.W. Li, Q.W. Zhang, X.D. Wen, D. Ma, Highly Tunable Selectivity for Syngas-Derived Alkenes over Zinc and Sodium-Modulated $Fe_5C_2$ Catalyst, Angew. Chem. Int. Edit., 55 (2016) 9902-9907.
[145] C. Perego, Development of a Fischer-Tropsch catalyst: From laboratory to commercial scale demonstration, Rend. Lincei-Sci. Fis., 18 (2007) 305.
[146] H.A.J.V. Dijk, The Fischer-Tropsch Synthesis: A mechanistic study using transient isotopic tracing, Proefschrift, Technische Universiteit Eindhoven, (2001).
[147] M.E. Dry, FT catalysts, In: A. Steynberg, M. E Dry (Eds.), Fischer Tropsch Technology, Stud. Surf. Sci. Catal. Elsevier, 152 (2004).
[148] W. Chu, L.N. Wang, P.A. Chernavskii, A.Y. Khodakov, Glow-discharge plasma-assisted design of cobalt catalysts for Fischer-Tropsch synthesis, Angew. Chem. Int. Edit., 47 (2008) 5052-5055.
[149] J.X. Liu, H.Y. Su, D.P. Sun, B.Y. Zhang, W.X. Li, Crystallographic Dependence of CO Activation on Cobalt Catalysts: HCP versus FCC, J. Am. Chem. Soc., 135 (2013) 16284-16287.
[150] A. Banerjee, V. Navarro, J.W.M. Frenken, A.P. van Bavel, H.P.C.E. Kuipers, M. Saeys, Shape and Size of Cobalt Nanoislands Formed Spontaneously on Cobalt Terraces during Fischer-Tropsch Synthesis, J. Phys. Chem. Lett., 7 (2016) 1996-2001.
[151] A. Griboval-Constant, A. Butel, V.V. Ordomsy, P.A. Chernavskii, A.Y. Khodakova, Cobalt and iron species in alumina supported bimetallic catalysts for Fischer-Tropsch reaction, Appl. Catal. A-Gen., 481 (2014) 116-126.
[152] H. Atashi, F. Rezaeian, Modeling of the Fischer-Tropsch process using a Fe-Cu-K catalyst, Petrol. Sci. Technol., 35 (2017) 1110-1116.
[153] M.K. Gnanamani, H. Hamdeh, G. Jacobs, W. Shafer, B. Davis, Fischer-Tropsch synthesis: Effect of Cu, Mn, and Zn addition on the activity and product selectivity of cobalt ferrite catalyst, Abstr. Pap. Am. Chem. Soc., 251 (2016).
[154] M.K. Gnanamani, H.H. Hamdeh, G. Jacobs, D.L. Qian, F. Liu, S.D. Hopps, G.A. Thomas, W.D. Shafer, Q.F. Xiao, Y.F. Hu, B.H. Davis, Fischer-Tropsch synthesis: effect of Cu, Mn and Zn addition on activity and product selectivity of cobalt ferrite, RSC Adv., 6 (2016) 62356-62367.

[155] P. Biloen, W.M.H. Sachtler, Mechanism of Hydrocarbon Synthesis over Fischer-Tropsch Catalysts, Adv. Catal., 30 (1981) 165-216.
[156] G.Y. Chai, J.L. Falconer, Alkali Promoters on Supported Nickel - Effect of Support, Preparation, and Alkali Concentration, J. Catal., 93 (1985) 152-160.
[157] M.A. Vannice, The Catalytic Synthesis of Hydrocarbon from $H_2$/CO Mixtures over the Group-VIII Metals. 1. The Specific Activities and Product Distributions of Supported Metals, J. Catal., 37 (1975) 449-461.
[158] M.E. Dry, Practical and theoretical aspects of the catalytic Fischer-Tropsch process, Appl. Catal. A-Gen., 138 (1996) 319-344.
[159] M.E. Dry, Fischer-Tropsch reactions and the environment, Appl. Catal. A-Gen., 189 (1999) 185-190.
[160] B. Jager, R. Espinoza, Advances in Low-Temperature Fischer-Tropsch Synthesis, Catal. Today, 23 (1995) 17-28.
[161] A.P. Steynberg, R.L. Espinoza, B. Jager, A.C. Vosloo, High temperature Fischer-Tropsch synthesis in commercial practice, Appl. Catal. A-Gen., 186 (1999) 41-54.
[162] R.L. Espinoza, A.P. Steynberg, B. Jager, A.C. Vosloo, Low temperature Fischer-Tropsch synthesis from a Sasol perspective, Appl. Catal. A-Gen., 186 (1999) 13-26.
[163] B. Jongsomjit, P. Praserthdam, P. Kaewkrajang, A comparative study on supporting effect during copolymerization of ethylene/1-olefins with silica-supported zirconocene/MAO catalyst, Mater. Chem. Phys., 86 (2004) 243-246.
[164] A.Y. Khodakov, A. Griboval-Constant, R. Bechara, V.L. Zholobenko, Pore size effects in Fischer Tropsch synthesis over cobalt-supported mesoporous silicas, J. Catal., 206 (2002) 230-241.
[165] A. Voss, D. Borgmann, G. Wedler, Characterization of alumina, silica, and titania supported cobalt catalysts, J. Catal., 212 (2002) 10-21.
[166] R.C. Reuel, C.H. Bartholomew, Effects of Support and Dispersion on the CO Hydrogenation Activity Selectivity Properties of Cobalt, J. Catal., 85 (1984) 78-88.
[167] S. Storsaeter, B. Totdal, J.C. Walmsley, B.S. Tanem, A. Holmen, Characterization of alumina-, silica-, and titania-supported cobalt Fischer-Tropsch catalysts, J. Catal., 236 (2005) 139-152.
[168] J. J. Spivey and K. M. Dooley, Promotion Effects in Co-based Fischer–Tropsch Catalysis, Catalysis, 19 (2006) 1-40.

[169] W. Warayanon, S. Tungkamani, H. Sukkathanyawat, M. Phongaksorn, T. Ratana, T. Sornchamni, Effect of Manganese Promoter on Cobalt Supported Magnesia Catalyst for Fischer-Tropsch Synthesis, Energy Proc., 79 (2015) 163-168.
[170] Z. Li, J. Wu, L. Wu, Effect of Zr, Ca and Mn as promoters on the Co/SiC catalysts for the Fischer–Tropsch synthesis, React. Kinet. Mech. Catal., 122 (2017) 887-900.
[171] Z. Tian, C. Wang, J. Yue, X. Zhang, L. Ma, Effect of a potassium promoter on the Fischer–Tropsch synthesis of light olefins over iron carbide catalysts encapsulated in graphene-like carbon, Catal. Sci. Technol., 9 (2019) 2728-2741.

# Chapter 3

# The supported Cu cluster size-activity threshold in CO oxidation

## 3.1 Introduction

The industrial growth, urbanization and increased demand of vehicles have caused damaging impacts on the environment in the recent years. Many industrial combustion processes and on-road cars consuming large amounts of gasoline have significant contribution in global pollutant emissions, particularly carbon monoxide (CO), nitrogen oxides (NOx) and unburned hydrocarbons [1]. Among all, CO is of particular concern because of its toxic nature as an odourless noxious gas [2]. It can be fatal to both humans and animals and can cause death in indoors. Almost one million children under the age of five die annually due to smoke from household solid fuel combustion as reported by World Health Organization (WHO) [3]. CO is also readily generated in confined environment. For example, CO generated from household fuels (gas or charcoal) for cooking or heating purposes, and second-hand smoke emitted from cigarettes [4].

To eliminate indoor CO, many approaches including ventilation, air purification/separation, and direct removal using low-cost adsorbents, such as activated carbon, have been adopted [4]. However, high electricity costs and complex design involved in ventilation, limited adsorption capacity of adsorbents and regular replacement of filters in air purification equipments limit these methods. Therefore, low-temperature catalytic reaction is considered the most effective approach to oxidize CO into $CO_2$ rapidly in a confined environment. Moreover, catalytic CO oxidation is an important step in many key industrial reactions, such as water-gas-shift reaction, production of pure hydrogen for proton-exchange membrane fuel cells, gaseous waste abatement in petrochemical industries and CO-coupled NO reduction [5-7].

Most reported CO oxidations to date are catalysed using noble or transition metal nanoparticles which show declining activity at low temperatures [4, 8-20]. In order to find whether CO oxidation is structure sensitive or not, many studies are reported for

nanoparticles based catalysts and mainly effect of metal particle size over the catalytic activity has been investigated to identify size-activity relationship [14-16, 21-25]. CO oxidation is reported to be significantly influenced by the change in catalyst crystal size and the catalytic activity is found to be increased with reduction in crystal size to a certain limit below which catalytic activity decreased [26, 27]. The change in crystal size alters the metal-support contact boundary which affects metal-support interaction, surface structure, oxidation state, electronic state and active surface oxide layer [27]. These factors have direct impact on the catalytic performance and therefore the crystal size is one of the most critical factors to define size-activity relationship.

Metal nanoclusters have drawn considerable interest in recent years mainly owing to their size dependent optical and electronic properties and quantum size effect [28-31]. The noble metal nanoclusters, such as Au and Ag, have shown superior catalytic activity in CO oxidation [32-34]; however, their high cost and less abundance are the limitations in their commercial application [35-41]. Copper nanoclusters (CNC) is a potential alternative to noble metals due to its low cost and ease of controlled synthesis [42-44].

In this paper, we successfully synthesized CNC supported on $TiO_2$ with various copper contents (0.15 to 5 wt%) and studied the stability of the resulting catalysts in CO oxidation at 200℃. The catalysts were characterized pre- and post-reaction to demonstrate the catalytic activity performance using x-ray diffraction (XRD), ultraviolet-visible diffuse reflectance spectroscopy (UV-Vis DRS), temperature programmed desorption using CO, $O_2$ and $CO_2$ (CO-, $O_2$- and $CO_2$-TPD), temperature programmed reduction using hydrogen (H2-TPR), CO chemisorption and thermo-gravimetric analysis (TGA). Specifically, the cluster size-activity threshold of the $TiO_2$-supported CNC catalysts have been elucidated.

## 3.2 Experimental

### *3.2.1 Catalyst preparation*

The details of the chemicals used are given in Appendix A. The $Cu_6$ nanoclusters (CNCs) were synthesized using the procedure reported by Albert *et al.* [47]. In a typical procedure, 0.5 g (0.005 mol) of copper(I) chloride and 1.3 g (0.005 mol) of triphenylphosphine ($PPh_3$) were added into a Schlenk flask attached to the Schelnk line

(synthesis performed under inert atmosphere) and subsequently 10 mL of tetrahydrofuran (THF) was added. A white precipitate was obtained upon stirring the mixture for half an hour. The mixture was placed in an ice bath and kept under continuous stirring and subsequently K-Selectride (5 mL of 1.0 M of THF, 0.005 mol) was added slowly using syringe. The white color of mixture turned into dark red. The mixture was kept under stirring for one hour after removing the ice bath. The resulting mixture was filtered and washed with THF (2 × 5 mL). The filtrate was reduced to 50% of its volume using vacuum. The filtrate was layered with the same volume of degassed hexanes for crystallization. Identity of product was confirmed by X-ray diffraction analysis of a single crystal. Prior to catalyst synthesis, $TiO_2$-P25 was pre-treated at 200 ℃ for 5 h under vacuum. The known amount of pre-treated $TiO_2$-P25 (on the basis of total catalyst mass of 1.1 g) was added into THF in a Schlenk flask under argon followed by the addition of CNC corresponding to 0.00165-0.055 grams of Cu to obtain copper loading ranging from 0.15 to 5 wt%. The sample was kept under stirring at room temperature overnight and was subsequently dried under vacuum until complete evaporation of solvent was achieved. The catalysts were designated as xCT, where x represents copper content (wt%) and T represents the $TiO_2$-P25 support. The as-synthesized catalysts were stored in capped sample bottles under ambient environment.

*3.2.2 Catalyst characterization*

X-ray diffraction (XRD) profiles were recorded using a SuperNova Agilent technologies instrument (Cu-Kα radiation source) and all measurements were conducted at room temperature. The recordings were obtained for scanning range of 20-80° using scanning step of 0.05° while X-ray diffraction (XRD) patterns were recorded using a Philips PW1700 X-ray diffractometer (Co-Kα radiation source). The recordings were obtained for scanning range of 20-80° using scanning step of 0.05°. MPI Jade® software was utilized for XRD data analysis. The average crystallite size of copper oxide was estimated using Scherrer equation ($d = \frac{K\lambda}{\beta Cos\theta}$) where d is the mean crystallite size, K is dimensionless shape factor, λ is the X-ray wavelength, β is the line broadening at full width half maximum (FWHM) of the peak and θ is Bragg angle.

The temperature-programmed desorption using CO and $O_2$ (CO-TPD and $O_2$-TPD, respectively) and CO chemisorption measurements were completed on a BELCAT II chemisorption apparatus. For these measurements, the catalyst surface was pre-treated

by keeping 25-30 mg of the catalyst sample at 150 and 200 ℃ for half an hour under inert atmosphere (helium (He) flow of 30 mL/min) for CO chemisorption and for CO- and $O_2$-TPD respectively. For CO- and $O_2$-TPD, the sample was subsequently cooled to ambient temperature and 10%CO/He (30 mL/min) and 5%$O_2$/He (30 mL/min) were injected for 1 hr followed by injection of He (30 mL/min) for 30 min to remove any remaining CO or $O_2$. Then, the sample temperature was raised to 500 ℃ at 10°C/min using 30 mL/min flow of He. In the case of CO chemisorption, 10%CO/He (30 mL/min) was injected in pulses until surface saturation was reached. Thermal conductivity detector (TCD) was used to monitor the outlet signal of BELCAT II.

Ultraviolet visible diffuse reflectance spectroscopy (UV-Vis DRS) measurements were performed using integrating sphere attachment in Cintra 404 (GBC Scientific Equipment) spectrophotometer with Spectralon as a reference.

*3.3.3 Catalytic activity*

The CO oxidation reaction was carried out in a fixed bed tubular reactor. The catalyst was placed in quartz wool, and the temperature of the catalyst bed was monitored using a k-type thermocouple. A total of 0.2 g of each catalyst was loaded into the reactor, and reaction feed gas (20 mL/min) containing 1% CO and 10% oxygen balanced with argon was flowed over the catalyst bed. The products and unconverted reactants were monitored by an online gas chromatograph (SRI Instruments) equipped with a flame ionization detector (FID) and a TCD (please refer to Appendix A for details). The CO conversion, rate of reaction and turnover number (TON) were calculated using the following equations:

$$CO\ Conversion\ (\%) = \frac{CO_{in} - CO_{out}}{CO_{in}} \times 100 \quad (3.1)$$

$$Rate\ = \frac{F_{CO} X_{CO}}{m} \quad (3.2)$$

$$TON = \frac{n_{CO2}}{n_{Cu}} \quad (3.3)$$

where $F_{CO}$ is the molar flow of CO (mol/h), $X_{CO}$ is the conversion of CO, m is the amount of the catalyst used (g), $r_{CO}$ is the rate of the reaction in $mol_{CO}/h.g_{Cat.}$, and TON is the ratio of the moles of $CO_2$ produced per mole of copper.

## 3.3 Results and Discussion

*3.3.1 Preparation and characterization of hexameric copper nanoclusters*

The $Cu_6$ nanoclusters (CNCs) were successfully prepared by following the already reported procedure of C.F. Albert [47]. The crystal structure was characterized using single crystal X-ray diffraction (SC-XRD) by selecting a single crystal of CNCs sample. The SC-XRD results of as-synthesized crystal were compared with the reported literature as shown in Table 3.1.

**Table 3.1** Comparison of single crystal XRD data of as-synthesized CNCs with data reported in the literature.

| | **$[(PPh_3)CuH]_6 \cdot 0.75THF$** (this work) | **$[(PPh_3)CuH]_6 \cdot 0.5THF$[a]** (literature) |
|---|---|---|
| **Formula** | $Cu_6P_6C_{111}H_{102}O_{0.75}$ | $Cu_6P_6C_{110}H_{100}O_{0.5}$ |
| **Formula weight** | 2014.9 | 1997.1 |
| **Crystal system** | monoclinic | monoclinic |
| **Temperature/K** | 120 | 295 |
| **Space group** | $P2_1$ | $P2_1$ |
| **a/Å** | 14.3 (10) | 14.5 (10) |
| **b/Å** | 16.0 (10) | 16.2 (9) |
| **c/Å** | 21.4 (10) | 21.5 (5) |
| **β/deg** | 92.1 (10) | 91.4 (3) |
| **V/Å$^3$** | 4888 (5) | 5049 (4) |
| **Dc/g cm$^{-3}$** | 1.4 | 1.3 |
| **μ/mm$^{-1}$** | 2.7 | 1.3 |

[a] Taken from Albert *et al*. [47]

It can be seen that crystal structure is different from the reported structure by means of the amount of THF. Using the same space group of $P2_1$, crystal parameters are

evaluated as a = 14.3 (10) Å, b = 16.0 (10) Å, c = 21.4 (10) Å, β = 92.1 (10)°, V = 4888.2 (5) $Å^3$, ρ = 1.4 $gcm^{-3}$, μ = 2.7 $mm^{-1}$. The difference between the literature [47] and the current findings is due to the temperature difference used for SC-XRD which is 120K in our case. The powder XRD (PXRD) of CNCs is shown in Figure A2 is supporting information. The CNCs were further subjected to thermal treatment using thermogravimetric analysis (TGA) to estimate the temperature needed for the removal and/or thermal stability of organic ligands attached to copper. Figure 3.1 shows the graph of weight loss versus temperature and it can be seen that the ligands are completely removed at a temperature above 250 °C. It is interesting to note that initially slight weight loss is observed at around 150 °C which depicts the removal of surface-bonded THF followed by removal of phosphine ligand. The slight increase at the end of the peak may be ascribed to nitride formation or oxidation which is not experimentally confirmed.

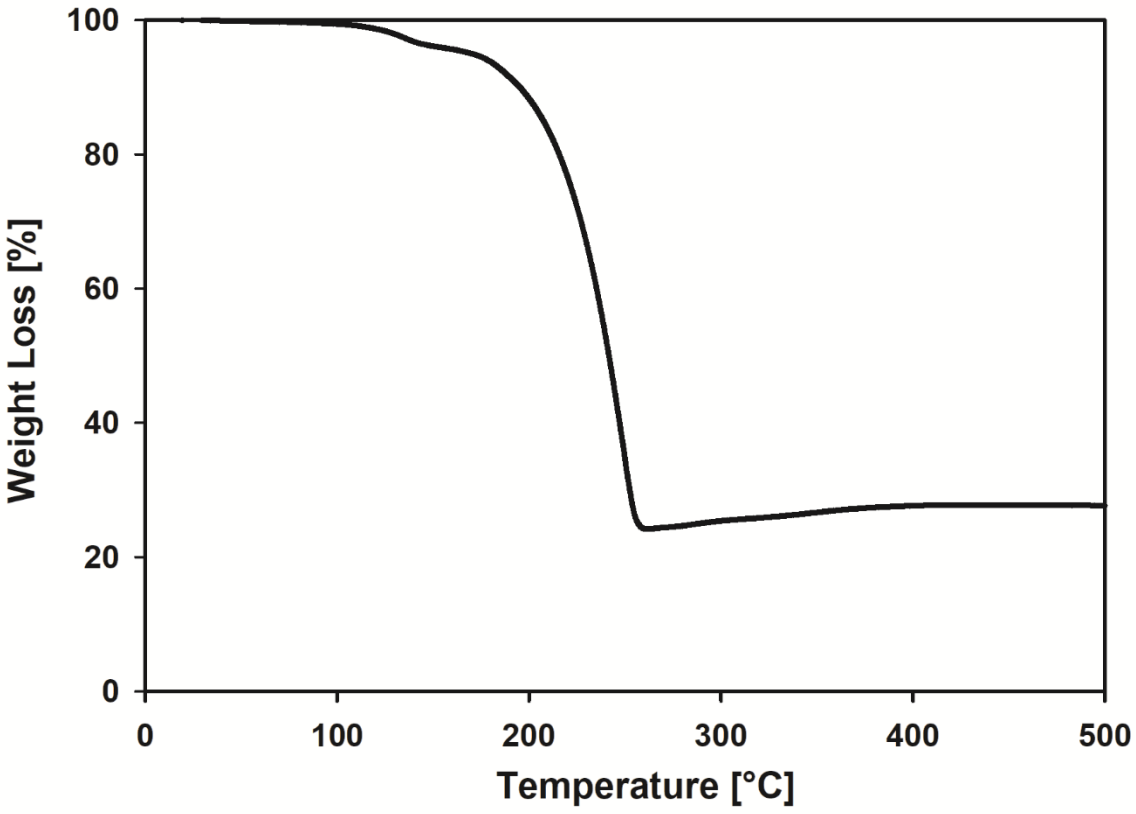


**Figure 3.1.** TGA profile for pure CNCs

*3.3.2 Characterization of catalysts before reaction*

In order to assess the thermal stability and loss of ligand under reaction conditions, the same concentration of air was used in the thermo-gravimetric analysis (TGA). Figure 3.2 shows that the increase in temperature under air showed slight weight loss for 0.15CT (~2%) and 0.75CT (4%) catalysts but a significant weight loss in case of 5CT (27%). The TGA results are reported from 120 to 400 °C to observe the thermal stability behaviour of the catalysts under air and more specifically ligand removal. The weight loss for all catalysts started above 200 °C which means at or below this temperature, the ligand was intact and catalysts had copper in the cluster form. Based on TGA results, it can be predicted that 0.15CT catalyst exhibits higher thermal stability as compared with the other counterparts.

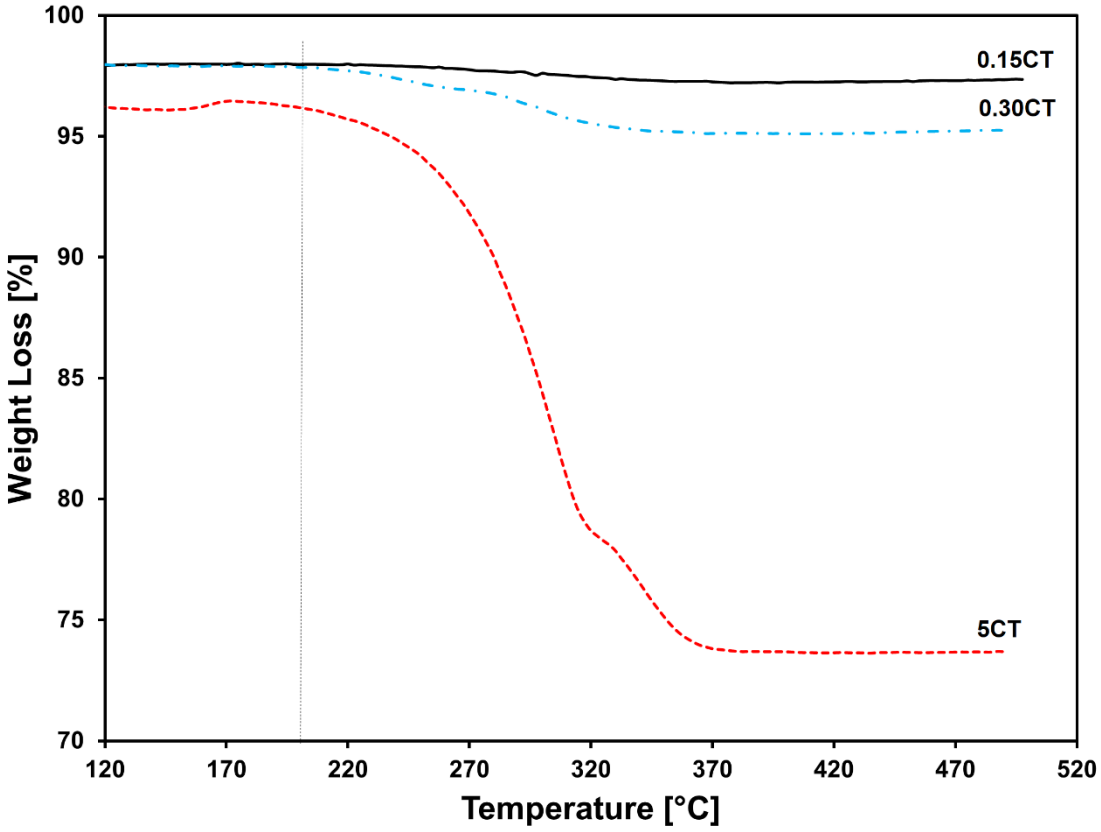


**Figure 3.2.** TGA profiles for xCT catalysts [x = 0.15-5 wt%Cu]

The identification of crystalline nature or phase of the as-synthesized catalysts, powder X-ray diffraction (PXRD) analysis was carried out. From PXRD patterns (Figure 3.3), the characteristic peaks of copper or copper oxide are not detected which is due to the smaller crystallite size and fine dispersion of CNCs over the support surface [48]. The

diffraction peaks at 2θ = 25, 37, 48, 54 and 56° are the characteristic peaks of anatase phase [49] and the peaks at 2θ = 28, 35, 42 and 63° are assigned to rutile phase of $TiO_2$ [50].

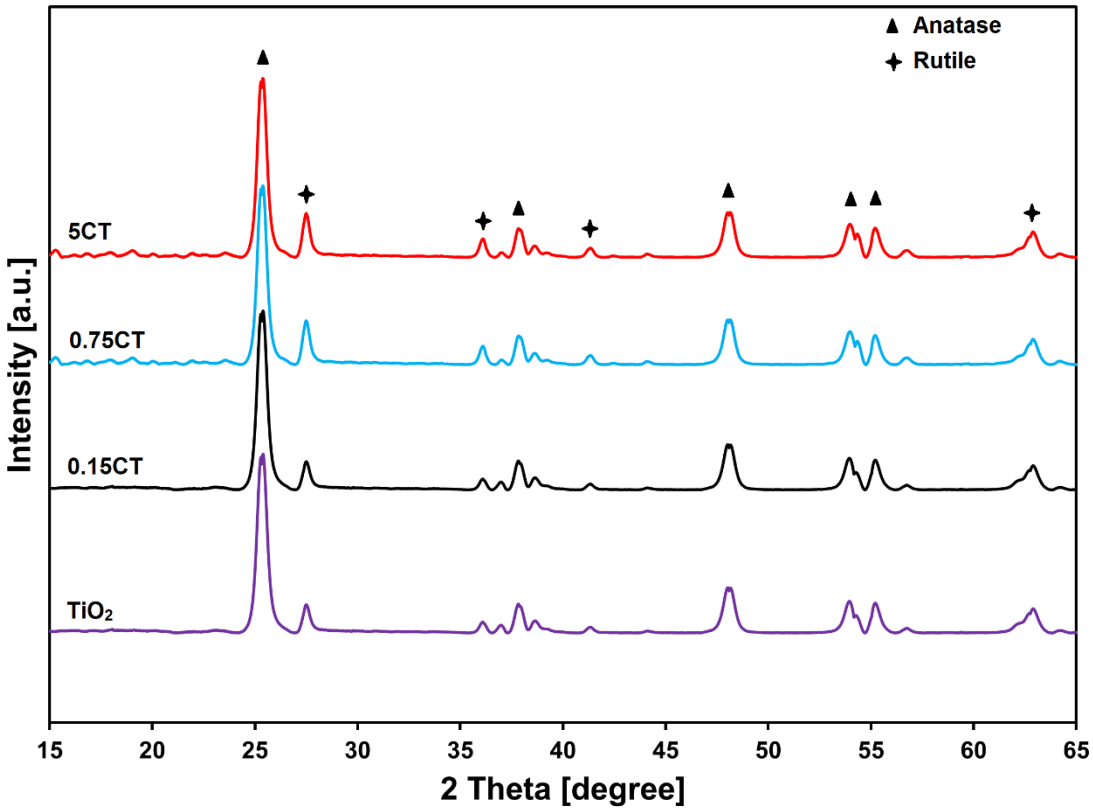


**Figure 3.3.** XRD patterns of xCT catalysts [x = 0.15-5 wt%Cu]

UV-Vis DRS results for CNC supported on $TiO_2$ are shown in Figure 3.4. The absorbance spectra (λ ~410 nm) for bare support and supported catalysts show that all the catalysts exhibited same capacity of visible light absorption.

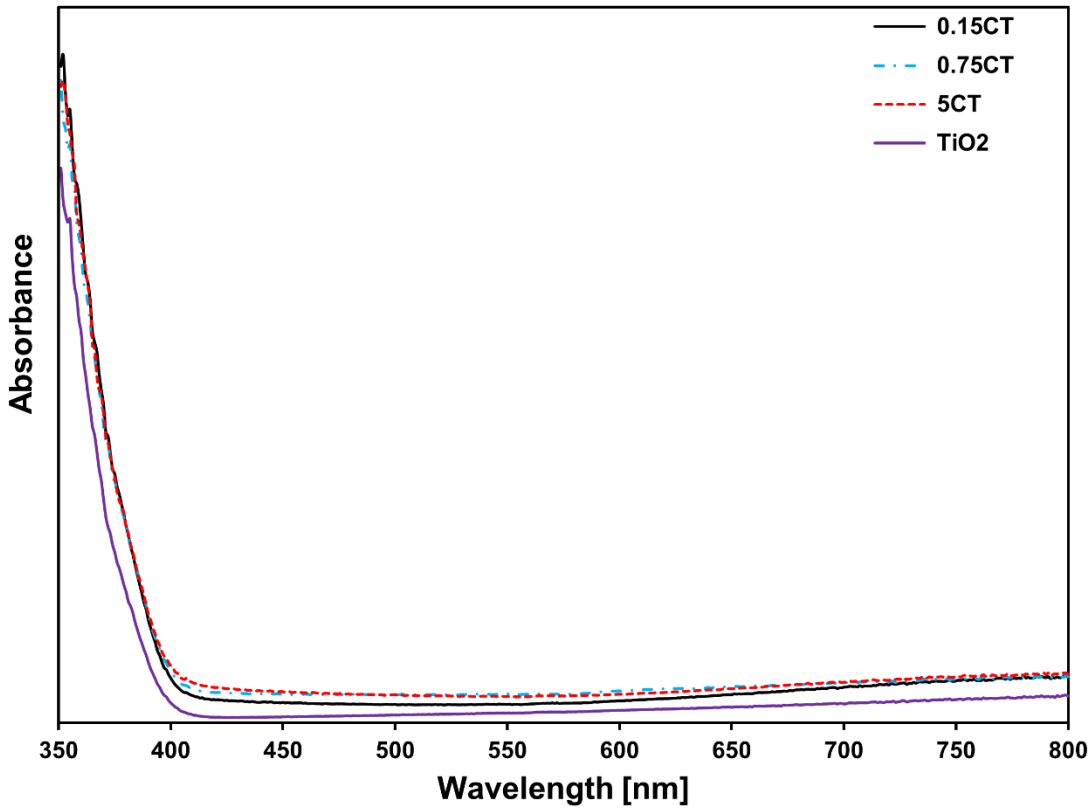


**Figure 3.4.** UV-Vis DR spectra for fresh xCT catalysts [x = 0.15-5 wt%Cu]

In addition to light absorption, the absorbance profiles also indicate the absence of typical surface plasmon resonance peak for nanoparticles, appearing at around 560 nm, for all the catalysts ruling out the presence of large copper nanoparticles after deposition of CNCs over $TiO_2$ support [51]. Despite high Cu loading contents (5CT), these results suggest that Cu active species are still in the form of nanoclusters.

The metal-support interaction is one of the important parameters which plays its role in catalytic performance and is depicted by temperature-programmed reduction using hydrogen ($H_2$-TPR). The $H_2$-TPR profiles of fresh catalysts did not show any reduction peak at lower copper loadings up to 0.30CT while 0.75CT catalyst presented one peak near 240 ℃ and 5CT catalyst exhibited three shoulders at around 185, 275 and 335 ℃.

The peak at 240 ℃ in case of 0.75CT catalyst corresponds to the reduction of crystalline CuO species [52]. It is interesting to note that this peak is shifted to higher temperature (275 ℃) when copper contents are further increased to 5 wt%. Furthermore, two additional peaks are observed for 5CT catalyst at 185 and 335 ℃. These peaks are assigned to the reduction of $Cu_2O$ species weakly interacting with the support [53] and bulk CuO species interacting strongly with the support [52].

The particle size, metal dispersion, and metal surface area are important factors influencing the catalytic performance of the catalysts during the reaction. These parameters are found using CO chemisorption by BELCAT II system. Generally, CO or $N_2O$ are used as probe gases to study chemisorption for Cu site measurements. $N_2O$ chemisorption requires oxygen uptake by $Cu^0$ sites and thus any unreduced Cu sites are not taken into account [54]. Moreover, the variations in (a) the temperature of copper oxide reduction to $Cu^0$ and (b) the temperature of $N_2O$ reduction *i.e.*, $Cu^0$ oxidation to $Cu^+$, affect the Cu sites measurements. These concerns limit the use of $N_2O$ as probe gas in our work and therefore, CO chemisorption was used for Cu site characterisation. The chemisorption results in Table 3.2 show that the increase in Cu contents, from 0.15 to 5 wt%, showed the decrease in copper dispersion and copper surface area per gram of copper. The 0.15CT catalyst exhibits Cu dispersion of 59.1% which is around 12 times higher than that of 5CT catalyst (5.1%). Furthermore, the average particle diameter for 0.15CT catalyst (1.77 nm) is around 5 times smaller than 0.75CT (9.59 nm) and this gap further increases when Cu loading is increased to 5 wt% (20.5 nm). The increase in copper particle diameter and reduction in dispersion with increase in Cu loading can be assigned to metal agglomeration.

The nature of metal-support interfacial sites and extent of interaction between CO and catalyst surface was measured using CO-TPD as shown in Figure 3.5. CO-TPD profiles for all catalysts can be divided into, at least, two regions *i.e.*, the low-temperature region (LTR) ranging from 60 to 245 °C and the high-temperature region (HTR) lies in the temperature array of 250 to 460 °C.

In the LTR, CO-TPD for 0.15CT catalyst exhibited broader desorption peak at around 155 ℃ and this peak shifts to ~175 ℃ when copper contents are increased from 0.15 to 0.75 wt%. It is interesting to note that the peak maximum is almost the same (~175 ℃) for 0.75 and 5CT catalysts which indicates the similar nature of the adsorption sites for both of these catalysts. The relatively lower desorption peak temperature (155 ℃) in case of 0.15CT implies that CO desorbs easily form the surface of this catalyst as compared with other catalysts and thus this catalyst offers weaker adsorption sites which could be assigned to smaller Cu particle size for this catalyst. The desorption peak temperature is an indication of desorption activation energy [55].

**Table 3.2** CO chemisorption data for $TiO_2$-supported CNCs catalysts before reaction.

| Sample | CO adsorbed amount [$cm^3$ STP] | Cu dispersion [%] | Cu surface area [$m^2/g_{cat.}$] | Cu surface area [$m^2/g_{Cu}$] | Average particle diameter [nm] |
|---|---|---|---|---|---|
| **0.15CT** | 0.0851 | 59.1 | 0.572 | 381.1 | 1.77 |
| **0.75CT** | 0.0381 | 10.8 | 0.526 | 70.1 | 9.59 |
| **5CT** | 0.0226 | 5.1 | 1.64 | 32.8 | 20.5 |
| **Spent 0.15CT** | 0.0073 | 53 | 0.513 | 341.9 | 1.97 (13.1)* |
| **Spent 0.75CT** | 0.0052 | 4.9 | 0.318 | 31.8 | 21.1 (26.3)* |
| **Spent 5CT** | 0.0041 | 1.7 | 0.533 | 10.7 | 63.1 (42.5)* |

*Average copper oxide ($Cu_2O$) crystallite size obtained from Scherrer equation

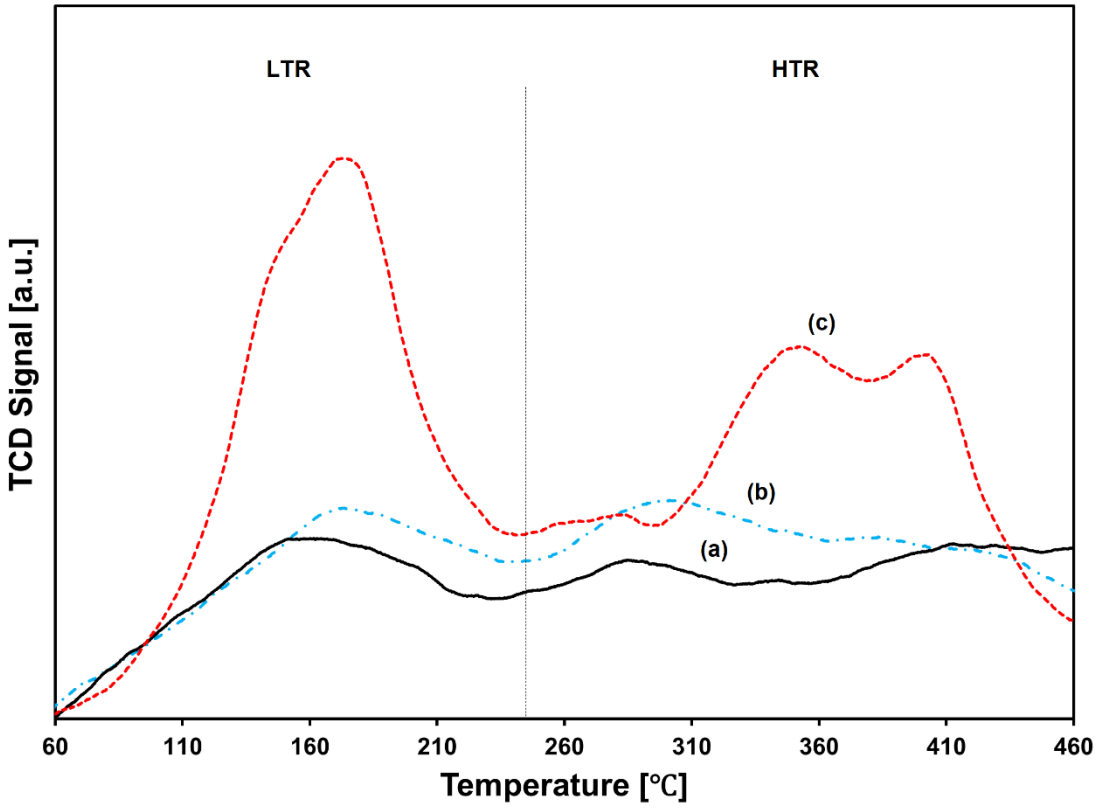


**Figure 3.5.** CO-TPD profiles for fresh (a) 0.15CT, (b) 0.75CT and (c) 5CT catalysts

The increase in desorption peak temperature for 0.75 and 5CT catalysts indicates that higher Cu contents enhanced the activation energy of CO desorption.

In the HTR, all the catalysts also exhibited desorption peak(s), which is assigned to CO adsorption on stronger adsorption sites. The desorption peak temperature follows the same trend as in the LTR and increases from 290 to 305 ℃ when Cu contents vary from 0.15 to 0.75 wt%. It is noteworthy that 5CT catalyst exhibited two desorption peaks at around 350 and 400 ℃ respectively, which can be assigned to the presence of more than one type of Cu active sites interacting differently with CO.

Overall, the area under the curve of CO-TPD represents the CO coverage *i.e.*, the amount of CO adsorbed. CO coverage is found to be increasing when copper contents are increased from 0.15 to 5 wt% (Table 3.3). For instance, 0.15CT catalyst showed CO uptake of 0.103 mmol/g in the LTR which increased to 0.226 mmol/g for 5CT catalyst. This increase in the CO coverage shows that more adsorption sites are generated with the increase of copper amount.

**Table 3.3** Quantitative results of CO- and $O_2$-TPD for xCT catalysts.

| Sample | CO uptake [mmol/g] | | $O_2$ uptake [mmol/g] |
|---|---|---|---|
| | LTR | HTR | |
| **0.15CT** | 0.103 | 0.179 | 0.19 |
| **0.75CT** | 0.135 | 0.226 | 0.17 |
| **5CT** | 0.226 | 0.277 | - |

$O_2$-TPD results shown in Figure 3.6 exhibit the adsorption behaviour of oxygen over catalysts. The catalysts have only one distinct peak in the temperature range of 60 to 310 °C. The 0.15CT catalyst exhibited broad desorption peak at around 180 °C. The 0.75CT catalyst showed distinct and broader desorption peak which shifted to slightly higher temperature *i.e.*, 190 °C. It can be assigned to oxygen species chemically adsorbed on the surface [56]. Interestingly, the peak height in case of 0.15CT catalyst is found to be more than that of 0.75CT catalyst, which demonstrates that more of $O_2$ was adsorbed onto 0.15CT catalyst. For instance, $O_2$ uptake of 0.17 mmol/g was observed on 0.75CT catalyst as compared to 0.19 mmol/g for 0.15CT catalyst.

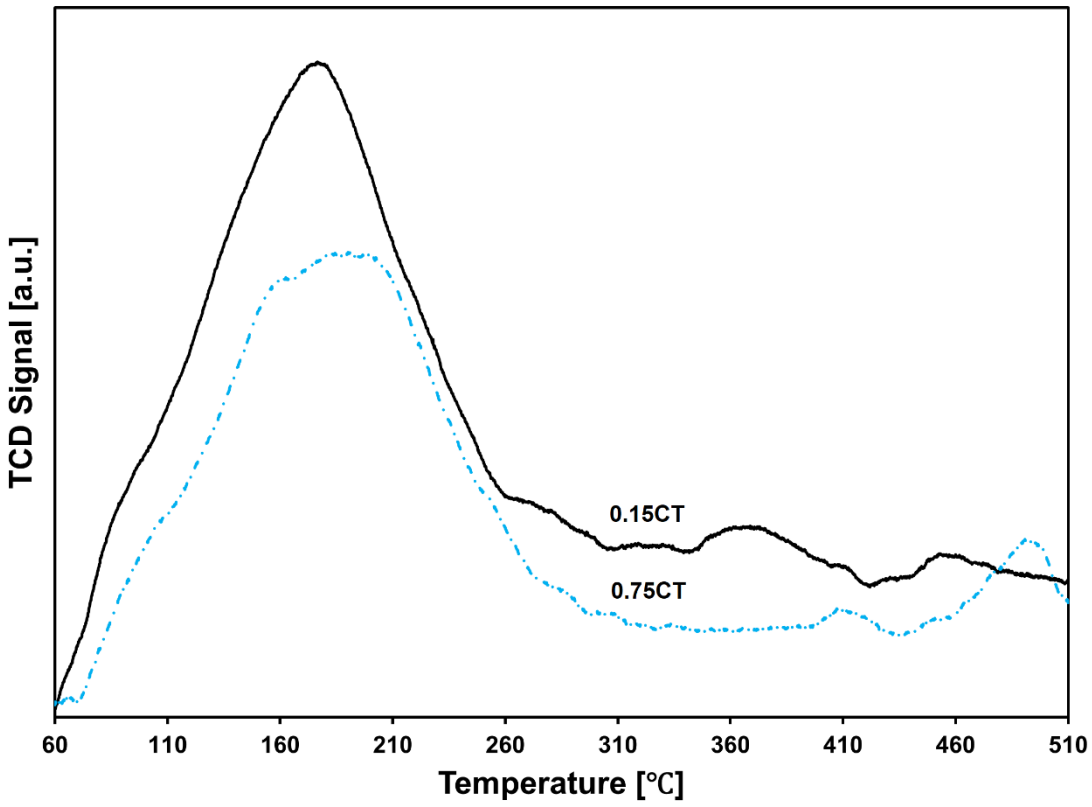


**Figure 3.6.** $O_2$-TPD profiles for fresh 0.15 and 0.75CT catalysts

The desorption of the $CO_2$ product is another important factor which influences the catalytic activity, reaction temperature or reaction mechanism [33, 57]. The study of product *i.e.*, $CO_2$ desorption, at least, within the reaction temperature range also gives an insight of catalyst affinity towards the product. $CO_2$-TPD results of 0.30CT and 0.75CT catalysts are shown in Fig. 3.7. It is obvious from desorption profiles that $CO_2$ starts desorbing from the catalyst surface at as low temperature as 60 ℃ for both catalysts. Both catalysts exhibit two desorption peaks between 60 to 360 ℃. The desorption peak maxima for 0.30CT catalyst is found to be 170 ℃ which shifts to lower temperature for 0.75CT catalyst depicting weaker adsorption of $CO_2$ over high loading catalyst. Similarly, the high temperature desorption peak presents maxima at 290 ℃ for 0.30CT catalyst which again shows the weaker adsorption for high loading catalyst (0.75CT) and peak maxima shifts to 285 ℃. It is reported that $CO_2$, when is weakly

adsorbed, do not influence the variation in reaction temperature [57]. $CO_2$ is also found to react with surface Cu nanoclusters oxide species and forms $CuCO_3$ which inhibits the CO oxidation reaction [33]. This discussion follows that weak $CO_2$ desorption facilitates CO oxidation reaction (which will be discussed later).

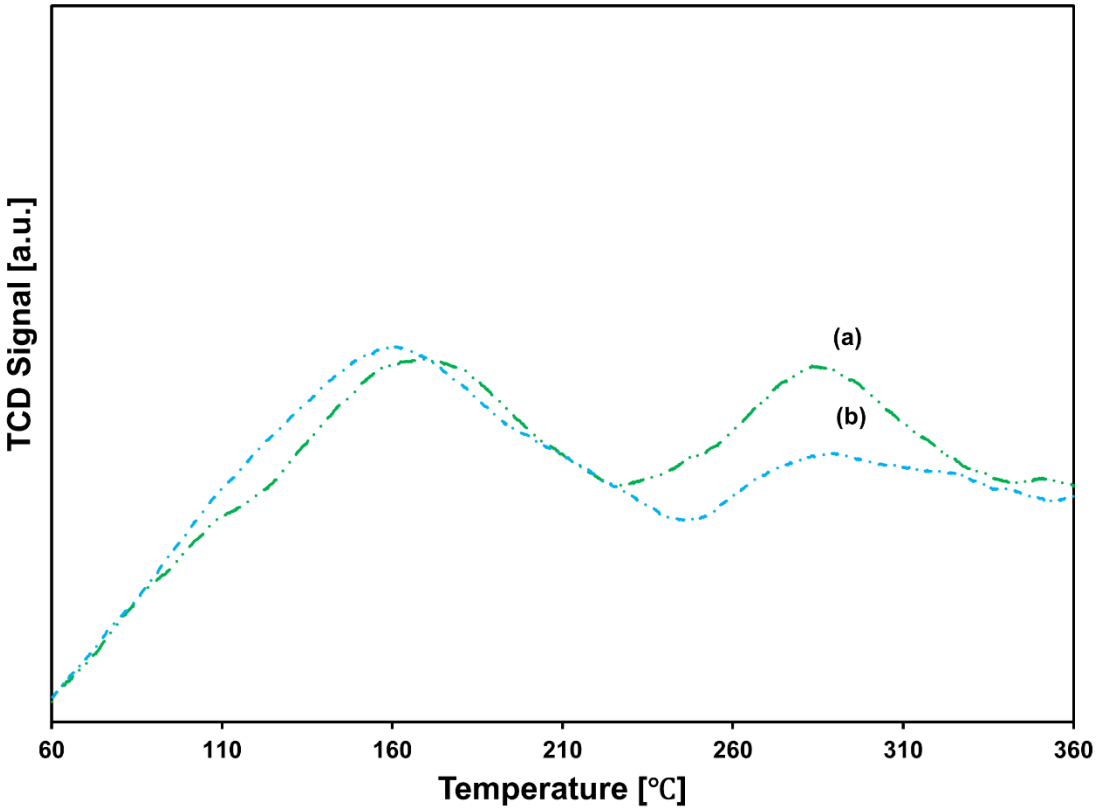


**Figure 3.7** $CO_2$-TPD profiles for fresh (a) 0.30CT and (b) 0.75CT catalysts

*3.3.3 CO oxidation reaction and kinetics over xCT catalysts*

Herein, we demonstrate the catalytic performance of these catalysts for CO oxidation at atmospheric pressure in the temperature range of 100 – 250 °C. The catalytic performance results are shown in terms of CO conversion and turnover number versus time in Figure 3.8 and 3.9, respectively. In our study, we focused on the effect of varying copper nanoclusters contents, from 0.15 to 5 wt%, on the activity performance of the catalysts in the CO oxidation reaction. The activity test performed using the bare support showed no CO conversion in the above-mentioned temperature range and therefore ruled out any role of support during the reaction. Moreover, instability of copper under the oxidative environment is well known [58] and thus unsupported CNC

cannot be tested for CO oxidation reaction. Interestingly, deposition of CNC onto $TiO_2$-P25 resulted in an increase in CO oxidation activity as compared with unmodified support. The catalytic performance in terms of CO conversion versus temperature showed the activity increased linearly with the increase in copper contents (Figure 3.8). For instance, at 188 °C, 0.15CT catalyst showed CO conversion of around 6%, while 5CT catalyst exhibited more than three-fold higher CO conversion of *cf.* 0.15CT. Interestingly, CNC anchoring onto $TiO_2$-P25 was so effective that even small contents of copper (0.15 wt%) exhibited a noticeable $CO_2$ formation. This significant increase in activity can be assigned to the formation of metal-support interface giving rise to active sites enhancing the conversion of CO into $CO_2$.

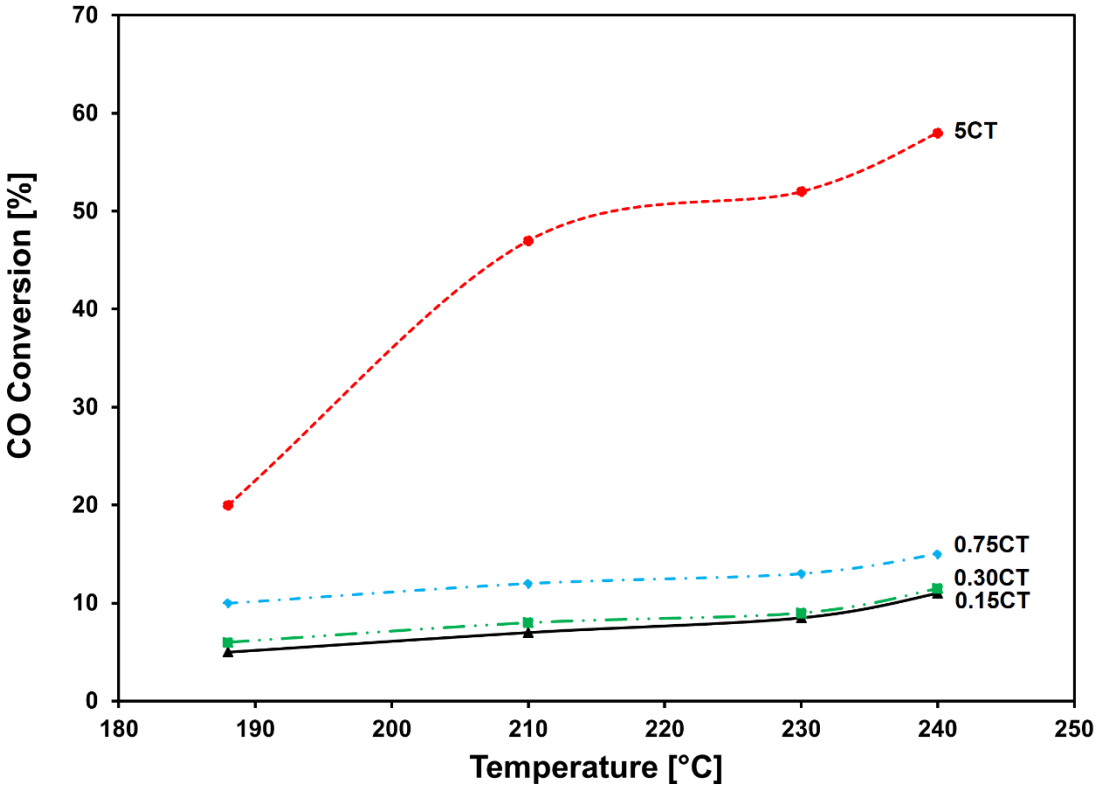


**Figure 3.8.** CO conversion versus temperature for xCT catalysts [x = 0.15-5 wt%Cu]

To further explore the effect of metal loading over time, the catalytic tests were conducted at 200 °C for 8 h time-on-stream. The activity results in terms of turnover number (TON), in Figure 3.9, clearly demonstrate the stability of catalysts with different loadings of copper. 0.15 and 0.30CT catalysts presented excellent stability for reaction duration of 8 h while higher loading catalysts *i.e.*, 0.75CT and 5CT catalysts showed deactivation over time. These results suggest that copper loading up to 0.30

wt% is the threshold limit for stable catalytic performance. The cause of deactivation is explored by the characterization of the catalysts after reaction as explained in section 3.4.

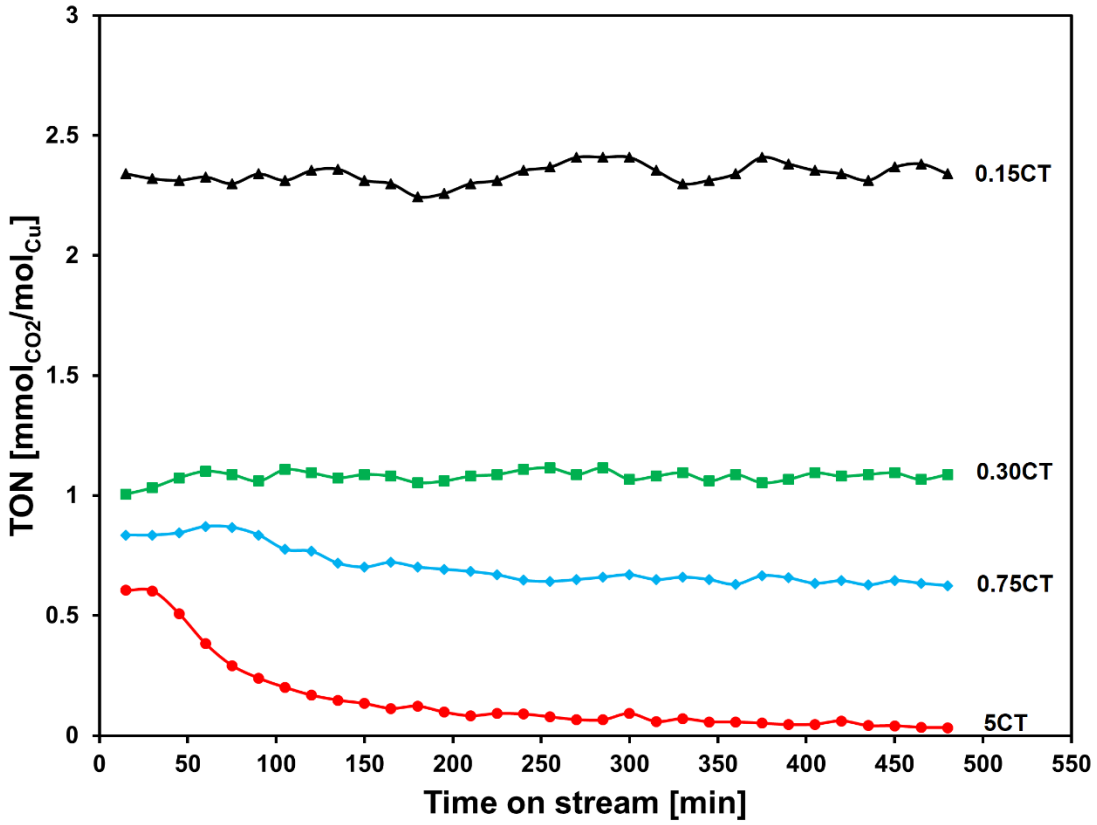


**Figure 3.9.** Turnover number versus time for xCT catalysts [x = 0.15-5 wt%Cu]

The kinetic study over 0.15 and 0.75CT catalysts was performed at 200°C. The logarithmic plots of rate of reaction versus partial pressures of CO and $O_2$ are demonstrated in Figure 3.10 (a) and (b) respectively. It can be observed that the rate of reaction increased with partial pressures of CO and $O_2$ in the feedstock for 0.15CT catalyst. 0.75CT catalyst, on the contrary, showed an increase in the rate of reaction with increase in initial partial pressure of $O_2$ but decrease in the rate of reaction with initial partial pressure of CO. The decrease in the rate of reaction with respect to CO in 0.75CT catalyst can be ascribed to stronger adsorption of CO with the catalyst surface and/or reduction of copper oxide species to metallic copper which might promote metal sintering and thus loss of activity. From the plots in Figure 3.10 (a) and (b), the order of reaction with respect to CO and $O_2$ could be evaluated. For 0.15CT catalyst, the orders were found to be 0.22 and 0.37 with respect to CO and $O_2$ respectively. On the contrary, 0.75CT catalyst presented the CO and $O_2$ kinetic orders of 0.19 and 0.30

respectively. The Arrhenius plot shown in Figure 3.10 (c) was used to calculate the apparent activation energies over 0.15CT and 0.75CT catalysts and values were found to be 14.1 and 27.9 kJ/mol respectively. These values are lower than the reported values in the literature for Cu supported on $TiO_2$ by photo-deposition (PD) and impregnation (IMP) techniques (33.1 and 59.2 kJ/mol for Cu-$TiO_2$-PD and Cu-$TiO_2$-IMP respectively) [59].

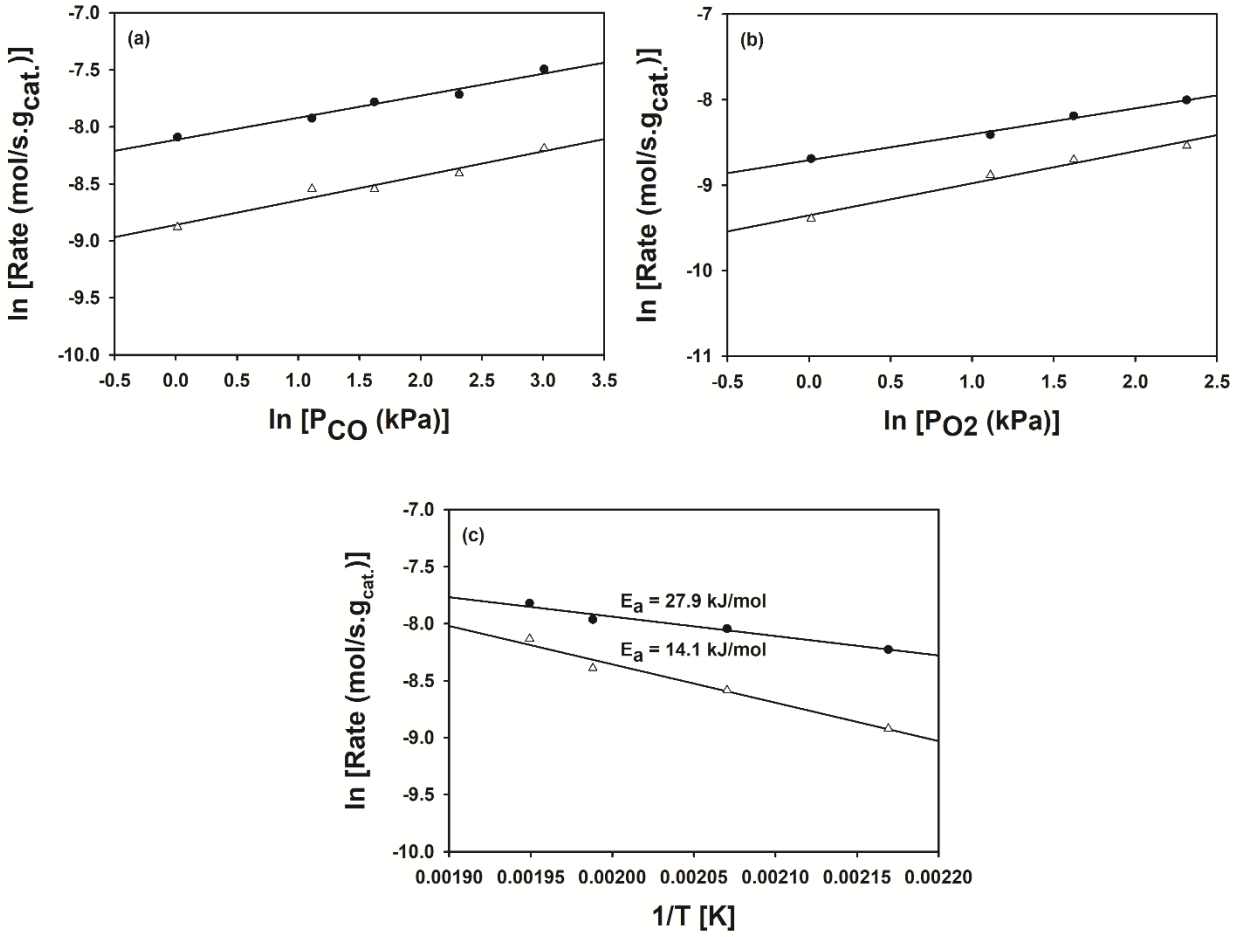


**Figure 3.10.** Kinetic results and Arrhenius plots for CO oxidation over 0.15CT (hollow symbols) and 0.75CT catalysts (filled symbols)

Based on the kinetic results, the reaction mechanism can be proposed for 0.15CT and 0.75CT catalysts. Generally, three reaction models are reported in the literature [60] including Mars van-Krevelen (MVK) model, Eley Rideal (ER) model and Langmuir-Hinshelwood (LH) model. Among these models, MVK model presents the rate equation which is 0 order with respect to $O_2$ partial pressure [61] while ER model presents the rate equation which is 1$^{st}$ order with respect to $O_2$ partial pressure [16]. Therefore, these models can be excluded as the kinetic results of this work, as obtained, are inconsistent

with these models. Moreover, in order to investigate the role of lattice oxygen of reducible $TiO_2$ support, these catalysts were tested without oxygen and results showed no formation of $CO_2$ despite loss in CO concentration *i.e.*, CO chemisorbed on the surface, but did not react with oxygen species from $TiO_2$ to form $CO_2$. Hence, LH model must be considered in which, assuming non-competitive adsorption, CO chemisorbs on Cu active sites while $O_2$ adsorbs on the support and both chemisorbed species react on the Cu-$TiO_2$ interface to form $CO_2$. The following steps can be proposed:

$$CO + Cu^* \rightarrow Cu^* - CO \tag{3.4}$$

$$O_2 + TiO_2{}^* \rightarrow TiO_2{}^* - O_2 \tag{3.5}$$

$$Cu^* - CO + TiO_2{}^* - O_2 \rightarrow Cu^* - CO_2 + TiO_2{}^* - O \tag{3.6}$$

$$Cu^* - CO + TiO_2{}^* - O \rightarrow Cu^* - CO_2 + TiO_2{}^* \tag{3.7}$$

$$Cu^* - CO_2 \rightarrow Cu^* + CO_2 \tag{3.8}$$

Among the steps (4) to (8), step (6) is the rate determining step (RDS). The chemisorption of CO or $O_2$ cannot be considered RDS as this would require rate expression to be first order with respect to CO or $O_2$ [48] which contradicts the kinetic findings in this work. The chemisorption of both CO and $O_2$ is confirmed by CO- and $O_2$-TPD. In order to ensure the surface reaction to be RDS, we varied initial partial pressure of CO and evaluated initial rate of reaction (IRR) (Figure A3 and A4 in the Appendix C). The graph between IRR and CO initial partial pressure elucidates whether the reaction is adsorption, desorption or surface reaction limited. It can be seen from Figure A5 (in the Appendix C) that the graphical trend depicts the reaction is surface reaction limited and hence rules out any role of adsorption or desorption to be RDS. It concludes that both the catalysts follow LH reaction mechanism.

### *3.3.4 Post-reaction Characterization*

In order to substantiate the argument of deactivation due to metal particles sintering during the reaction, the catalysts were characterized after reaction. CO chemisorption, UV-Vis DRS and XRD patterns of spent catalysts are shown in Table 3.2, Figure 3.11 and 3.12 respectively. CO chemisorption results of spent catalyst showed loss of dispersion and increase in particle size. The dispersion of 0.15CT catalyst decreased

from 59.1% to 53%. The particle size of 5CT (63.1 nm) catalyst after reaction increased three times that of the fresh catalyst (20.5 nm).

The surface plasmon resonance (SPR) peak, for copper nanoparticles, is reported to be in the wavelength range of 560-760 nm [51] while SPR peaks for $Cu_2O$ and CuO are found to be in the range of 540-750 and 540-860 nm respectively [62]. Moreover, the exact position of SPR peak depends upon the size and aspect ratio of the particle.

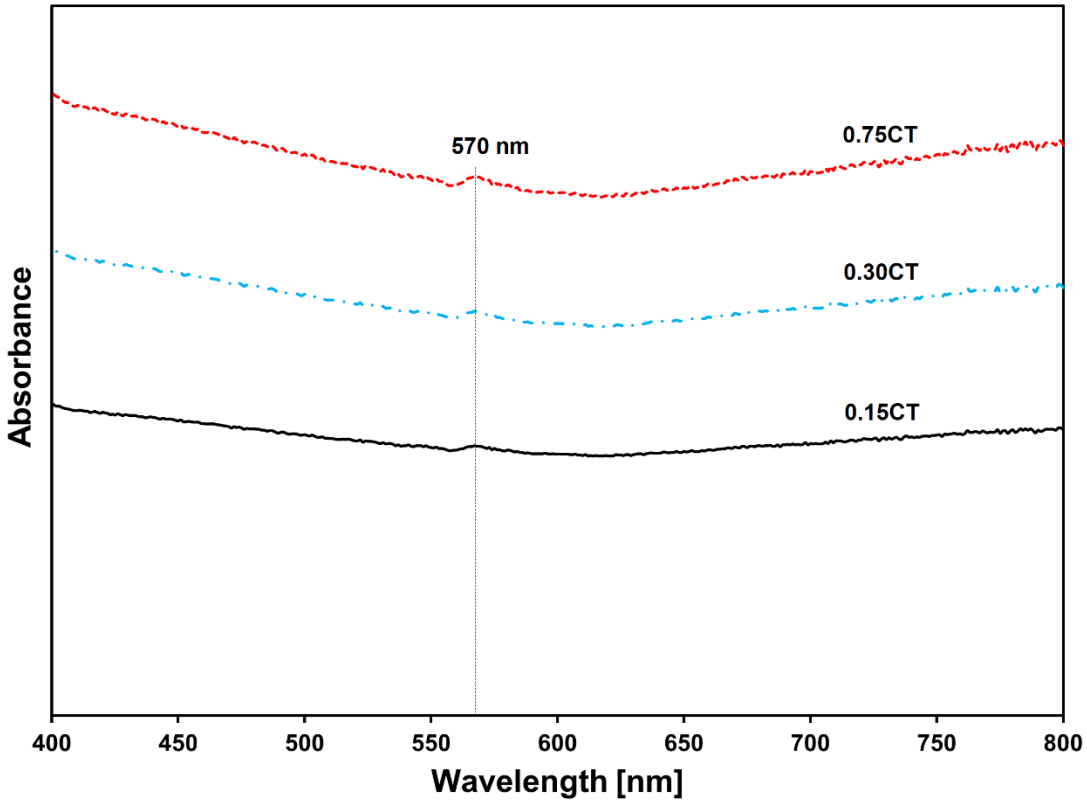


**Figure 3.11.** UV-Vis DR spectra for spent xCT catalysts [x = 0.15-5 wt%Cu]

The SPR peak at ~570 nm indicates the presence of larger, plasmonic nanoparticles as a result of sintering during reaction over all the catalysts. The identification of copper oxides in XRD of spent catalysts (Figure 3.12 discussed later) suggests that sintered nanoparticles are copper oxides. The intensity of surface plasmon resonance peak increases with increasing amount of copper depicting catalysts with higher copper contents (0.75 and 5 wt%) are more prone to sintering than lower loading catalysts (0.15 wt%).

XRD patterns of spent catalysts (Figure 3.12) show the presence of copper oxides unlike fresh catalysts confirming the agglomeration of copper oxide particles during

reaction. In addition to typical diffraction profiles of anatase and rutile, the peaks for $Cu_2O$ and CuO are also detected. The diffraction peak near 43° is difficult to distinguish between anatase (PDF# 21-1272) and $Cu_2O$ (PDF# 34-1354) but absence of CuO (PDF# 44-0706) peak in 0.15CT catalyst near 45° is obvious.

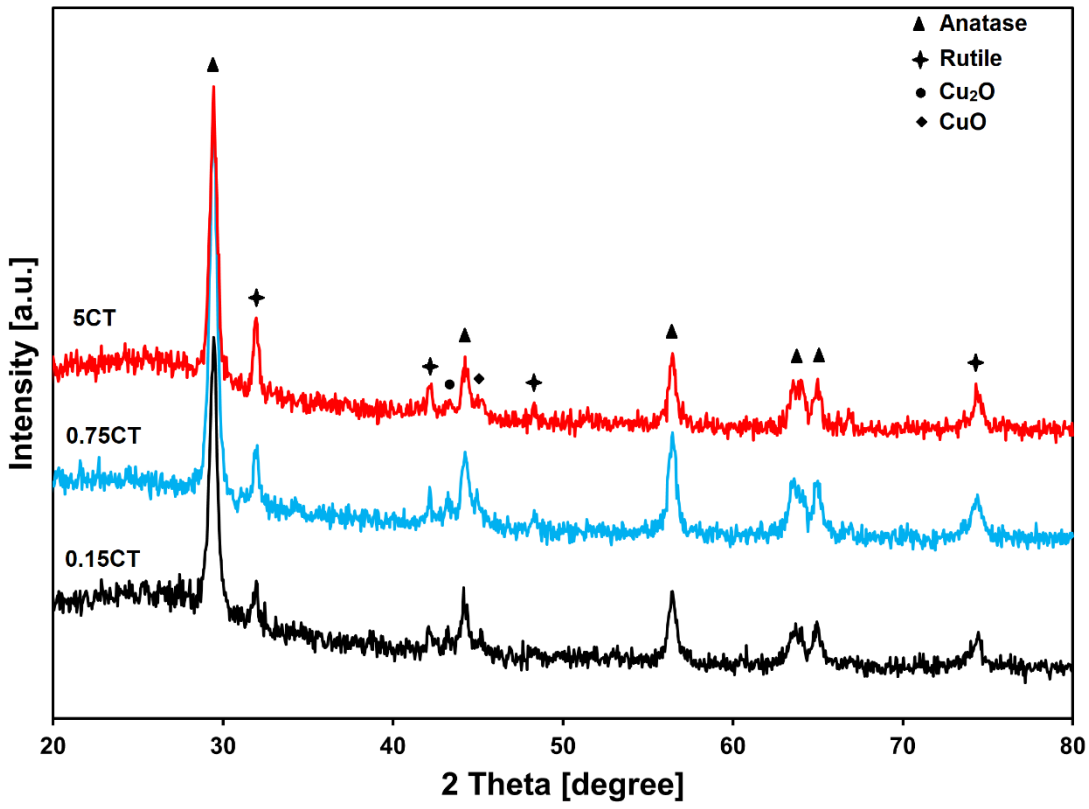


**Figure 3.12.** XRD patterns of spent xCT catalysts [x = 0.15-5 wt%Cu]

As mentioned earlier, pure CNCs are unstable under oxidative atmosphere and $TiO_2$-P25 support cannot convert CO into $CO_2$. The formation of the metal-support interface is most likely the active centre for the reaction to proceed [48, 63]. The CO chemisorption data shows that increase in copper contents from 0.15 to 5 wt% results in loss of dispersion which is ascribed to the metal agglomeration naturally occurring as metal particles are easily attracted to each other at higher metal loadings. Moreover, the Huttig temperature is the temperature which causes significant mobility of surface atoms [64, 65]. The Huttig temperature for copper oxide nanoparticles is 229 (502 K) and 260 ℃ (533 K) for $Cu_2O$ and CuO respectively [64]. Although the reaction temperature of 200 ℃ is below Huttig temperature of copper oxides, long term exposure at this temperature would tend nanoparticles to aggregate at higher copper loadings. It can also be seen from CO-TPD results that increase in copper content

showed an increase in CO adsorption due to the presence of more copper species in the case higher loaded catalysts and, thus, CO conversion increases with increase in copper content. The drawback of higher loading catalysts is the long term instability due to the as metal agglomeration becomes even more severe during the reaction. The characterisation using UV-Vis DRS and XRD after long term reaction test also show the increase in metal particle size. The crystallite size based on $Cu_2O$ peak, measured using Scherrer equation, is presented in Table 3.2 and increase in particle size is obvious. For instance, 0.15CT catalyst exhibits particle size of 1.97 nm after reaction and crystallite size of 13.1 nm as compared with 1.77 nm before reaction. It has been reported that the change in particle size affects the oxidation state of copper which in turn influences the distribution of these oxides on the surface of the catalyst [66]. The presence of CuO in 0.75CT and 5CT catalysts, as indicated in XRD patterns of used catalysts (Figure 3.12), is another factor behind the deactivation of these catalysts over time due to the fact that CuO is less active than $Cu_2O$ and $Cu^0$ for CO oxidation reaction [67].

The chemical adsorption of CO and $O_2$ found using CO- and $O_2$-TPD corroborates with the proposed kinetic model of LH which requires adsorption of both reactants before they react on the Cu-$TiO_2$ interface to generate $CO_2$. Moreover, the influence of CO and $O_2$ partial pressures over reaction rate revealed positive impact of both reactants over reaction rate of both 0.15CT and 0.75CT catalyst.

## 3.4 Conclusions

The investigation of novel catalysts - CNCs anchored on $TiO_2$-P25 for CO oxidation reaction revealed the significance of the size-activity threshold for the copper loading contents between 0.15 and 5 wt%. The excellent dispersion and high copper surface area, as depicted by CO chemisorption, UV-Vis DRS and XRD, remained key factors behind the stable catalytic performance of lower loading catalysts. 0.15 and 0.30CT catalysts remained stable over 8 h time-on-stream revealing copper size-activity threshold. The stability of these catalysts was assigned to the smaller particle size and stronger metal-support interaction which prevented particle agglomeration and growth. On the contrary, 0.75 and 5CT catalysts showed metal particles migration and sintering which eventually ended in catalyst deactivation. The metal particles' sintering was further confirmed by post-reaction CO chemisorption, UV-Vis DRS and XRD. The

presence of CuO over higher loading catalysts was found to be another factor behind deactivation of these catalysts over time. The kinetic study revealed that 0.15CT and 0.75CT catalysts followed LH mechanistic model. The reaction was surface reaction limited as confirmed by the experimental data obtained from initial reaction rates and initial CO partial pressures. The apparent activation energies and reaction orders with respect to CO and $O_2$ were found to be 14.1 kJ/mol, 0.22 and 0.37 (0.15CT catalyst); 27.9 kJ/mol, 0.19 and 0.30 (0.75CT catalyst) respectively.

## References


[1] R.M. Heck, R.J. Farrauto, Automobile exhaust catalysts, Appl. Catal. A-Gen., 221 (2001) 443-457.

[2] P.W. Seo, H.J. Choi, S.I. Hong, S.C. Hong, A study on the characteristics of CO oxidation at room temperature by metallic Pt, J. Hazard. Mater., 178 (2010) 917-925.

[3] B. Gordon, Mackay, R., Rehfuess, E., Inheriting the World: the Atlas of Children's Health and the Environment WHO, (2004).

[4] A.M. Harzandi, J.N. Tiwari, H.S. Lee, H. Jeon, W.J. Cho, G. Lee, J. Baik, J.H. Kwak, K.S. Kim, Efficient CO Oxidation by 50-Facet $Cu_2O$ Nanocrystals Coated with CuO Nanoparticles, ACS Appl. Mater. Interfaces, 9 (2017) 2495-2499.

[5] M. Setvin, M. Buchholz, W.Y. Hou, C. Zhang, B. Stoger, J. Hulva, T. Simschitz, X. Shi, J. Pavelec, G.S. Parkinson, M.C. Xu, Y.M. Wang, M. Schmid, C. Woll, A. Selloni, U. Diebold, A Multitechnique Study of CO Adsorption on the $TiO_2$ Anatase (101) Surface, J. Phys. Chem. C, 119 (2015) 21044-21052.

[6] F.F. Han, Y.H. Yang, J.Y. Han, O.Y. Jin, N. Na, Room-temperature cataluminescence from CO oxidation in a non-thermal plasma-assisted catalysis system, J. Hazard. Mater., 293 (2015) 1-6.

[7] S.H. Xie, H.X. Dai, J.G. Deng, H.G. Yang, W. Han, H. Arandiyan, G.S. Guo, Preparation and high catalytic performance of Au/3DOM $Mn_2O_3$ for the oxidation of carbon monoxide and toluene, J. Hazard. Mater., 279 (2014) 392-401.

[8] C.H. Tseng, T.C.K. Yang, H.E. Wu, H.C. Chiang, Catalysis of oxidation of carbon monoxide on supported gold nanoparticle, J. Hazard. Mater., 166 (2009) 686-694.

[9] A.K. Srivastava, A. Saxena, D. Shah, T.H. Mahato, B. Singh, A.R. Shrivastava, P.K. Gutch, C.P. Shinde, Catalytic removal of carbon monoxide over carbon supported palladium catalyst, J. Hazard. Mater., 241 (2012) 463-471.

[10] Z.Q. Zou, M. Meng, L.H. Guo, Y.Q. Zha, Synthesis and characterization of $CuO/Ce_{1-x}Ti_xO_2$ catalysts used for low-temperature CO oxidation, J. Hazard. Mater., 163 (2009) 835-842.

[11] T.C. Jones, L. Sementa, M. Stener, K.J. Gagnon, V.D. Thanthirige, G. Ramakrishna, A. Fortunelli, A. Dass, $Au_{21}S(SAdm)_{15}$: Crystal Structure, Mass Spectrometry, Optical Spectroscopy, and First-Principles Theoretical Analysis, J. Phys. Chem. C, 121 (2017) 10865-10869.

[12] M. Rambukwella, A. Dass, Synthesis of $Au_{38}(SCH_2CH_2Ph)_{24}$, $Au_{36}(SPhtBu)_{24}$, and $Au_{30}(StBu)_{18}$ nanomolecules and structural selectivity, Abstr. Pap. Am. Chem. Soc., 255 (2018).
[13] I. Diez, R.H.A. Ras, Fluorescent silver nanoclusters, Nanoscale, 3 (2011) 1963-1970.
[14] L. Shang, G.U. Nienhaus, Metal nanoclusters: Protein corona formation and implications for biological applications, Int. J. Biochem. Cell Biol., 75 (2016) 175-179.
[15] S. Roy, A. Baral, R. Bhattacharjee, B. Jana, A. Datta, S. Ghosh, A. Banerjee, Preparation of multi-coloured different sized fluorescent gold clusters from blue to NIR, structural analysis of the blue emitting $Au_7$ cluster, and cell-imaging by the NIR gold cluster, Nanoscale, 7 (2015) 1912-1920.
[16] A.S. Nair, K. Kimura, Charge Transport Behavior of N-(2-Mercaptopropionyl glycine)-Protected Gold Clusters with Temperature, Langmuir, 25 (2009) 1750-1756.
[17] U. Goswami, S. Basu, A. Paul, S.S. Ghosh, A. Chattopadhyay, White light emission from gold nanoclusters embedded bacteria, J. Mater. Chem. C, 5 (2017) 12360-12364.
[18] B.Y. Wu, C.W. Wang, P.C. Chen, H.T. Chang, Glutathione assisted preparation of gold nanoclusters using minimum amount of protein, Sens. Actuators B-Chem., 238 (2017) 1258-1265.
[19] L. Shang, S.J. Dong, G.U. Nienhaus, Ultra-small fluorescent metal nanoclusters: Synthesis and biological applications, Nano Today, 6 (2011) 401-418.
[20] Q.F. Yao, X. Yuan, V. Fung, Y. Yu, D.T. Leong, D.E. Jiang, J.P. Xie, Understanding seed-mediated growth of gold nanoclusters at molecular level, Nat. Commun., 8 (2017).
[21] H. Kondoh, R. Toyoshima, Y. Monya, M. Yoshida, K. Mase, K. Amemiya, B.S. Mun, In situ analysis of catalytically active Pd surfaces for CO oxidation with near ambient pressure XPS, Catal. Today, 260 (2016) 14-20.
[22] S. Fernandez-Garcia, S.E. Collins, M. Tinoco, A.B. Hungria, J.J. Calvino, M.A. Cauqui, X.W. Chen, Influence of {111} nanofaceting on the dynamics of CO adsorption and oxidation over Au supported on $CeO_2$ nanocubes: An operando DRIFT insight, Catal. Today, 336 (2019) 90-98.
[23] J.P.H. Li, Z.B. Liu, H. Wu, Y. Yang, Investigation of CO oxidation over $Au/TiO_2$ catalyst through detailed temperature programmed desorption study under low temperature and Operando conditions, Catal. Today, 307 (2018) 84-92.

[24] Z.G. Wang, Y. Xiong, S.V. Kershaw, B.K. Chen, X.M. Yang, N. Goswami, W.F. Lai, J.P. Xie, A.L. Rogach, In Situ Fabrication of Flexible, Thermally Stable, Large-Area, Strongly Luminescent Copper Nanocluster/Polymer Composite Films, Chem. Mater., 29 (2017) 10206-10211.
[25] X.F. Jia, X.A. Yang, J. Li, D.Y. Liab, E.K. Wang, Stable Cu nanoclusters: from an aggregation-induced emission mechanism to biosensing and catalytic applications, Chem. Commun., 50 (2014) 237-239.
[26] X.H. Gao, S.J. He, C.M. Zhang, C. Du, X. Chen, W. Xing, S.L. Chen, A. Clayborne, W. Chen, Single Crystal Sub-Nanometer Sized $Cu_6(SR)_6$ Clusters: Structure, Photophysical Properties, and Electrochemical Sensing, Adv. Sci., 3 (2016).
[27] Y.W. Li, Y.X. Chen, S.D. House, S. Zhao, Z. Wahab, J.C. Yang, R.C. Jin, Interface Engineering of Gold Nanoclusters for CO Oxidation Catalysis, ACS Appl. Mater. Interfaces, 10 (2018) 29425-29434.
[28] A.D. Allian, K. Takanabe, K.L. Fujdala, X. Hao, T.J. Truex, J. Cai, C. Buda, M. Neurock, E. Iglesia, Chemisorption of CO and Mechanism of CO Oxidation on Supported Platinum Nanoclusters, J. Am. Chem. Soc., 133 (2011) 4498-4517.
[29] X.T. Nie, H.F. Qian, Q.J. Ge, H.Y. Xu, R.C. Jin, CO Oxidation Catalysed by Oxide-Supported $Au_{25}(SR)_{18}$ Nanoclusters and Identification of Perimeter Sites as Active Centers, ACS Nano, 6 (2012) 6014-6022.
[30] W.L. Li, Q.J. Ge, X.G. Ma, Y.X. Chen, M.Z. Zhu, H.Y. Xu, R.C. Jin, Mild activation of $CeO_2$-supported gold nanoclusters and insight into the catalytic behaviour in CO oxidation, Nanoscale, 8 (2016) 2378-2385.
[31] H.Y. Kim, G. Henkelman, CO Oxidation at the Interface of Au Nanoclusters and the Stepped-$CeO_2$(111) Surface by the Mars-van Krevelen Mechanism, J. Phys. Chem. Lett., 4 (2013) 216-221.
[32] L. Baharudin, A.C.K. Yip, V.B. Golovko, M.I.J. Polson, M.J. Watson, CO temperature-programmed desorption of a hexameric copper hydride nanocluster catalyst supported on functionalized MWCNTs for active site characterization in a low-temperature water-gas shift reaction, Chem. Eng. J. 377 (2019) 120278.
[33] L. Baharudin, A.C.K. Yip, V.B. Golovko, M.I.J. Polson, K.-F. Aguey-Zinsou, M.J. Watson, CO oxidation and the inhibition effects of carboxyl-modification and copper clusters on multi-walled carbon nanotubes, Appl. Catal. B-Environ., 262 (2020) 118265.

[34] Y. He, J.C. Liu, L.L. Luo, Y.G. Wang, J.F. Zhu, Y.G. Du, J. Li, S.X. Mao, C.M. Wang, Size-dependent dynamic structures of supported gold nanoparticles in CO oxidation reaction condition, Proc. Natl. Acad. Sci. USA, 115 (2018) 7700-7705.
[35] W.Y. Song, E.J.M. Hensen, Structure Sensitivity in CO Oxidation by a Single Au Atom Supported on Ceria, J. Phys. Chem. C, 117 (2013) 7721-7726.
[36] B. Atalik, D. Uner, Structure sensitivity of selective CO oxidation over Pt/gamma-$Al_2O_3$, J. Catal., 241 (2006) 268-275.
[37] M. Bowker, Q.M. Guo, Y.X. Li, R.W. Joyner, Structure Sensitivity in CO Oxidation over Rhodium, Catal. Lett., 18 (1993) 119-123.
[38] M. Bowker, Q.M. Guo, Y.X. Li, R.W. Joyner, Structure Sensitivity of CO Oxidation over Rhodium - Reply, Catal. Lett., 22 (1993) 275-276.
[39] C.S. Chen, J.H. You, J.H. Lin, Y.Y. Chen, Effect of highly dispersed active sites of $Cu/TiO_2$ catalyst on CO oxidation, Catal. Commun., 9 (2008) 2381-2385.
[40] Tana, F.G. Wang, H.J. Li, W.J. Shen, Influence of Au particle size on $Au/CeO_2$ catalysts for CO oxidation, Catal. Today, 175 (2011) 541-545.
[41] M.M. Du, D.H. Sun, H.W. Yang, J.L. Huang, X.H. Jing, T. Odoom-Wubah, H.T. Wang, L.S. Jia, Q.B. Li, Influence of Au Particle Size on $Au/TiO_2$ Catalysts for CO Oxidation, J. Phys. Chem. C, 118 (2014) 19150-19157.
[42] F. Yang, M.S. Chen, D.W. Goodman, Sintering of Au Particles Supported on $TiO_2$(110) during CO Oxidation, J. Phys. Chem. C, 113 (2009) 254-260.
[43] N.K. Soliman, Factors affecting CO oxidation reaction over nanosized materials: A review, J. Mater. Res. Technol., 8 (2019) 2395-2407.
[44] B. Roldan Cuenya, Synthesis and catalytic properties of metal nanoparticles: Size, shape, support, composition, and oxidation state effects, Thin Solid Films, 518 (2010) 3127-3150.
[45] G. Bond and D. Thompson, Formulation of mechanisms for gold-catalysed reactions, Gold Bull., 42 (2009) 247-259.
[46] G. Bond, Source of the catalytic activity of gold nanoparticles, Gold Bull., 43 (2010) 88-93.
[47] C.F. Albert, P.C. Healy, J.D. Kildea, C.L. Raston, B.W. Skelton, A.H. White, Lewis-Base Adducts of Group-11 Metal(I) Compounds .49. Structural Characterization of Hexameric and Pentameric (Triphenylphosphine)Copper(I) Hydrides, Inorg. Chem., 28 (1989) 1300-1306.

[48] J.Q. Lu, C.X. Sun, N. Li, A.P. Jia, M.F. Luo, Kinetic study of CO oxidation over $CuO/MO_2$ (M = Si, Ti and Ce) catalysts, Appl. Surf. Sci., 287 (2013) 124-134.
[49] Y.L. Yu, Y. Tang, J.X. Yuan, Q. Wu, W.J. Zheng, Y.A. Cao, Fabrication of N-$TiO_2/InBO_3$ Heterostructures with Enhanced Visible Photocatalytic Performance, J. Phys. Chem. C, 118 (2014) 13545-13551.
[50] Y.L. Yu, J.S. Wang, W. Li, W.J. Zheng, Y. Cao, Doping mechanism of $Zn^{2+}$ ions in Zn-doped $TiO_2$ prepared by a sol-gel method, Crystengcomm, 17 (2015) 5074-5080.
[51] R. Li, S.K. Wu, X.Y. Wan, H.X. Xu, Y.J. Xiong, $Cu/TiO_2$ octahedral-shell photocatalysts derived from metal-organic framework@semiconductor hybrid structures, Inorg. Chem. Front., 3 (2016) 104-110.
[52] H.Q. Wan, Z. Wang, J. Zhu, X.W. Li, B. Liu, F. Gao, L. Dong, Y. Chen, Influence of CO pretreatment on the activities of CuO/gamma-$Al_2O_3$ catalysts in $CO+O_2$ reaction, Appl. Catal. B-Environ., 79 (2008) 254-261.
[53] J.L. Cao, Y. Wang, T.Y. Zhang, S.H. Wu, Z.Y. Yuan, Preparation, characterization and catalytic behavior of nanostructured mesoporous $CuO/Ce_{0.8}Zr_{0.2}O_2$ catalysts for low-temperature CO oxidation, Appl. Catal. B-Environ., 78 (2008) 120-128.
[54] A. Dandekar, R.T.K. Baker, M.A. Vannice, Carbon-supported copper catalysts I. Characterization, J. Catal., 183 (1999) 131-154.
[55] L.D. V. Rakić, Temperature-Programmed Desorption (TPD) Methods, in: Auroux A. (eds) Calorimetry and Thermal Methods in Catalysis, 154 (2013) 131-174.
[56] N.A. Merino, B.P. Barbero, P. Grange, L.E. Cadus, $La_{1-x}Ca_xCoO_3$ perovskite-type oxides: preparation, characterisation, stability, and catalytic potentiality for the total oxidation of propane, J. Catal., 231 (2005) 232-244.
[57] T. Baidya, T. Murayama, S. Nellaiappan, N.K. Katiyar, P. Bera, O. Safonova, M. Lin, K.R. Priolkar, S. Kundu, B.S. Rao, P. Steiger, S. Sharma, K. Biswas, S.K. Pradhan, N. Lingaiah, K.D. Malviya, M. Haruta, Ultra-Low-Temperature CO Oxidation Activity of Octahedral Site Cobalt Species in $Co_3O_4$ Based Catalysts: Unravelling the Origin of the Unique Catalytic Property, J. Phys. Chem. C, 123 (2019) 19557-19571.
[58] C. Barriere, K. Piettre, V. Latour, O. Margeat, C.O. Turrin, B. Chaudret, P. Fau, Ligand effects on the air stability of copper nanoparticles obtained from organometallic synthesis, J. Mater. Chem., 22 (2012) 2279-2285.
[59] G.J. Wu, N.J. Guan, L.D. Li, Low temperature CO oxidation on $Cu-Cu_2O/TiO_2$ catalyst prepared by photodeposition, Catal. Sci. Technol., 1 (2011) 601-608.

[60] S. Royer, D. Duprez, Catalytic Oxidation of Carbon Monoxide over Transition Metal Oxides, Chemcatchem, 3 (2011) 24-65.
[61] L.C. Loc, H.T. Cuong, N. Tri, H.S. Thoang, A study on the properties of modified CuO samples and the kinetics of carbon monoxide oxidation over the given catalysts, 6 (2011) 631-640.
[62] J.S. Sekhon and S.S. Verma, Cu, CuO, and $Cu_2O$ Nanoparticle Plasmons for Enhanced Scattering in Solar Cells, Renewable Energy and the Environment, OSA Technical Digest (CD) (Optical Society of America, 2011), paper JWE22.
[63] N. Li, Q.Y. Chen, L.F. Luo, W.X. Huang, M.F. Luo, G.S. Hu, J.Q. Lu, Kinetic study and the effect of particle size on low temperature CO oxidation over $Pt/TiO_2$ catalysts, Appl. Catal. B-Environ., 142 (2013) 523-532.
[64] T. Popa, G. Xu, T.F. Barton, M.D. Argyle, High temperature water gas shift catalysts with alumina, Appl. Catal. A-Gen., 379 (2010) 15-23.
[65] R. van den Berg, J. Zecevic, J. Sehested, S. Helveg, P.E. de Jongh, K.P. de Jong, Impact of the synthesis route of supported copper catalysts on the performance in the methanol synthesis reaction, Catal. Today, 272 (2016) 87-93.
[66] Z. He, H.Q. Lin, P. He, Y.Z. Yuan, Effect of boric oxide doping on the stability and activity of a $Cu\text{-}SiO_2$ catalyst for vapor-phase hydrogenation of dimethyl oxalate to ethylene glycol, J. Catal., 277 (2011) 54-63.
[67] T.J. Huang, D.H. Tsai, CO oxidation behaviour of copper and copper oxides, Catal. Lett., 87 (2003) 173-178.

# Chapter 4

# Synthesis of $TiO_2$ nanotubes and nanorods

## 4.1 Introduction

The study of nanomaterials with a focus on their shape, size, crystal structure and morphology and surface properties has been an area of recent research. The idea to study these parameters is to tailor these materials for specific applications. The other aspect of such materials is the difference of their chemical and physical properties from the bulk materials. The discovery of various nanomaterials including nanotubes, nanofibers, nanorods, nanowires and nanobelts based on different oxides such as tin oxide ($SnO_2$), zinc oxide (ZnO), indium oxide ($In_2O_3$), gallium oxide ($Ga_2O_3$) and vanadium oxide ($V_2O_5$), during the past decade has extraordinarily influenced researchers [1-9]. Titanium dioxide ($TiO_2$) is a material with unique characteristics and applicability ranging from pigments to photo-catalysis, solar cells to sensors [10-18]. The wider range of applications and simple preparation procedures of titania based nanotubes, nanobelts, nanowires and nanorods have gained attention in recent decades [19-22]. The higher surface-to-volume ratio of these nano-forms makes them a better choice as compared to nanoparticles. $TiO_2$ is considered as one of the promising supports in heterogeneous catalysis as well. The main attributes of titania as support include its significant band gap, reducible nature, environmental friendly, low price and crystal phase. $TiO_2$ is mainly used in photo-catalysis, electro-catalysis and thermal catalysis due to above mentioned features. $TiO_2$ is used as pure anatase, rutile or combination of both (P25). It is generally accepted that pure anatase is more active than rutile and P25 is in between the two [23].

$TiO_2$ nanotubes (TNTs) have been considered as a vital support in heterogeneous catalysis due to its unique characteristics including large specific surface area as well as pore volume, ion-exchangeability and rapid electron transport capability [24-26]. TNTs can be prepared using various techniques such as template method, anodic oxidation, sol-gel synthesis, electro-chemical synthesis and hydrothermal synthesis. Among these methods, hydrothermal synthesis has the advantage of large scale production of nanotubes with high aspect ratio as well as cation exchange capacity.

Hydrothermal synthesis is a simple process in which various parameters can be changed to control the attributes of TNTs. On the contrary, hydrothermal synthesis needs longer reaction times and concentrated NaOH. Furthermore, size uniformity and thermal stability are difficult to control in hydrothermal synthesis. The high cost and use of highly toxic hydrofluoric acid make template method and anodic oxidation less favourable in comparison with hydrothermal synthesis [24, 27-29]. According to the literature, the suitable hydrothermal treatment temperature range for TNTs preparation is 100 to 200°C [30]. Moreover, increase in hydrothermal temperature favours high yield, crystallinity and length of TNTs. Similarly, increasing hydrothermal duration favours high yield of TNTs but prolonged duration might change TNTs to nanofibers [31].

In this work, hydrothermal synthesis route is used to prepare TNTs which are later heat treated to get $TiO_2$ nanorods (TNRs). The hydrothermal treatment temperature and duration are varied from 130 to 150 ℃ and 24 to 44 h respectively. The post-drying mainly amorphous nanotubes are subjected to calcination treatment to improve their crystallinity. The calcination temperature is varied between 400 and 800 ℃. The samples are characterized using XRD, SEM and TEM.

## 4.2 Experimental

### *4.2.1 $TiO_2$ nanomaterials preparation*

The materials required to prepare $TiO_2$ nanomaterials including nanotubes and nanorods comprised the precursor which was $TiO_2$-P25, NaOH and HCl (please see Appendix A for details).

TNTs and TNRs were prepared using hydrothermal synthesis and the already established procedure [32] was followed in which 5 g of $TiO_2$-P25 was dispersed into 100 mL of 10M NaOH solution and kept under magnetic stirring for half an hour. The slurry was transferred into Teflon cups (45 mL each) of stainless steel autoclave. The slurry was subjected to hydrothermal treatment at various temperatures (130-150°C) for time durations of 24-44 h to prepare nanostructures with required aspect ratio and crystallinity for metal deposition. The samples obtained after hydrothermal treatment were washed with 0.1M HCl and DI water. The samples were subsequently dried at 120°C for 12 h followed by calcination under air at various temperatures (400-800°C) for 10 h.

### *4.2.2 Characterization techniques*

X-ray diffraction (XRD) profiles were recorded using a SuperNova Agilent technologies instrument (Cu-Kα radiation source) and all measurements were conducted at room temperature. The recordings were obtained for scanning range of 20-80° using scanning step of 0.05°. Scanning electron microscopy (SEM) and transmission electron microscopy (TEM) were performed using a JEOL 7000F FE-SEM and Philips CM200.

## 4.3 Results and Discussion

### *4.3.1 Effect of hydrothermal treatment*

Figure 4.1 displays the TEM images of TNTs prepared under autoclave treatment at a) 130°C for 48 h; b) 130°C for 72 h; c) 150°C for 24 h and d) 150°C for 44 h. The successful formation of TNTs is evident from TEM images and interestingly the change in autoclave conditions has significantly influenced the length and diameter of the resulting TNTs.

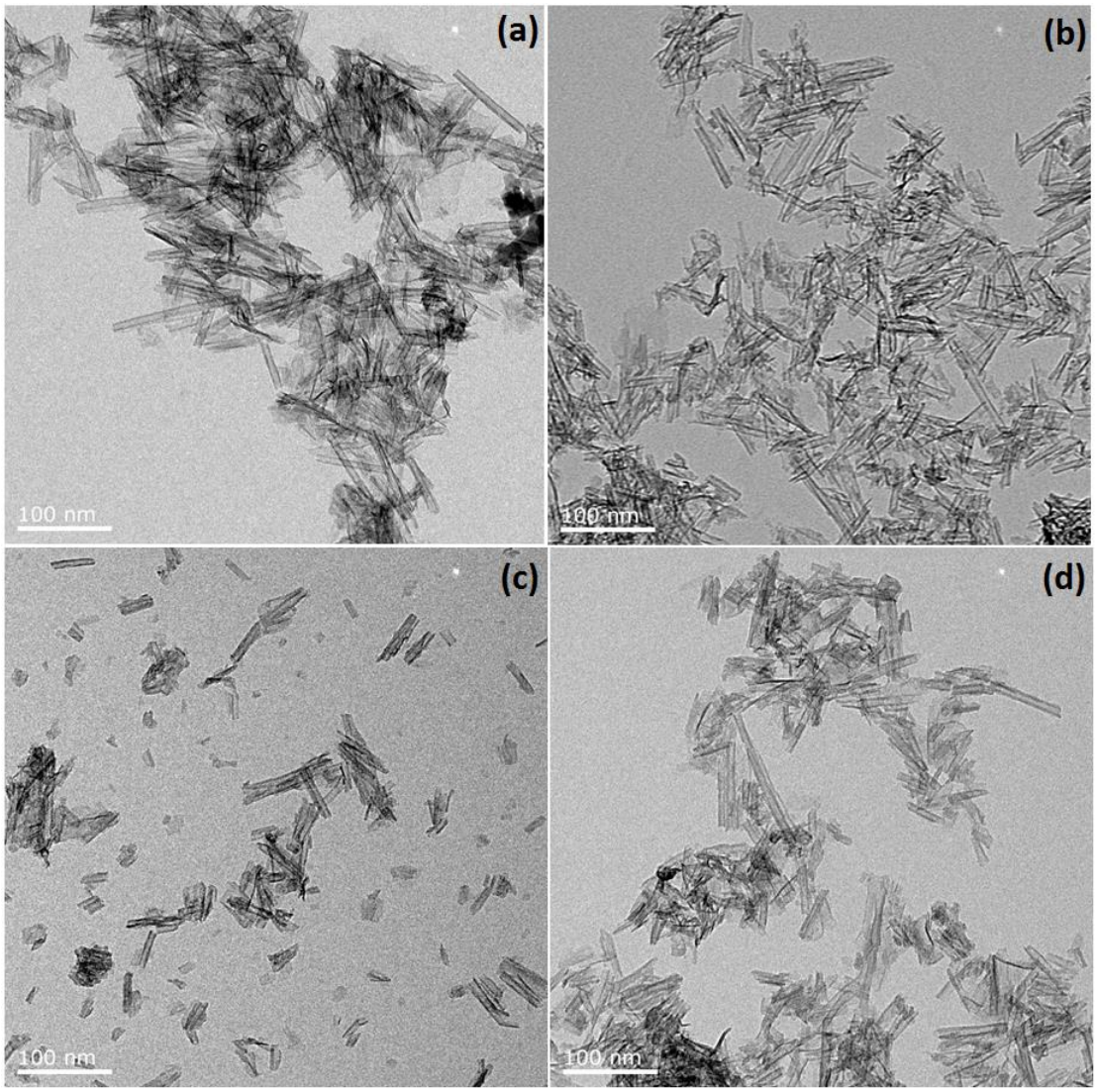


**Figure 4.1.** TEM images of TNTs treated at a) 130°C for 48 h; b) 130°C for 72 h; c) 150°C for 24 h and d) 150°C for 44 h

Figure 4.2 shows the distribution of TNTs versus length, diameter and aspect ratio. It can be clearly seen that the formation of TNTs under autoclave treatment at 150°C for 44 h exhibits nanotubes with wider range of aspect ratio. The increase in hydrothermal temperature and time caused an increment in the range of both particle size and length and thus a wide range aspect ratio TNTs were formed. It can be inferred that increase in hydrothermal duration increased the yield of TNTs. The results are in accordance with reported literature [33, 34]. Bavykin *et al*. [35] investigated the influence of various hydrothermal conditions on TNTs formation. The study of hydrothermal temperature in the range of 120 to 150°C revealed the increase in temperature produced non-hollow nanofibers. In addition, a wide distribution of diameter was observed by increasing the hydrothermal temperature. Tsai and Teng [36] also studied the effect of

hydrothermal treatment on TNTs formation and inferred the treatment temperature had a significant impact on TNTs formation and controlling the phase change from anatase to rutile. Based on the TEM results, these TNTs can be selected for next step of metal deposition as it can accommodate metal nanoparticles of various sizes.

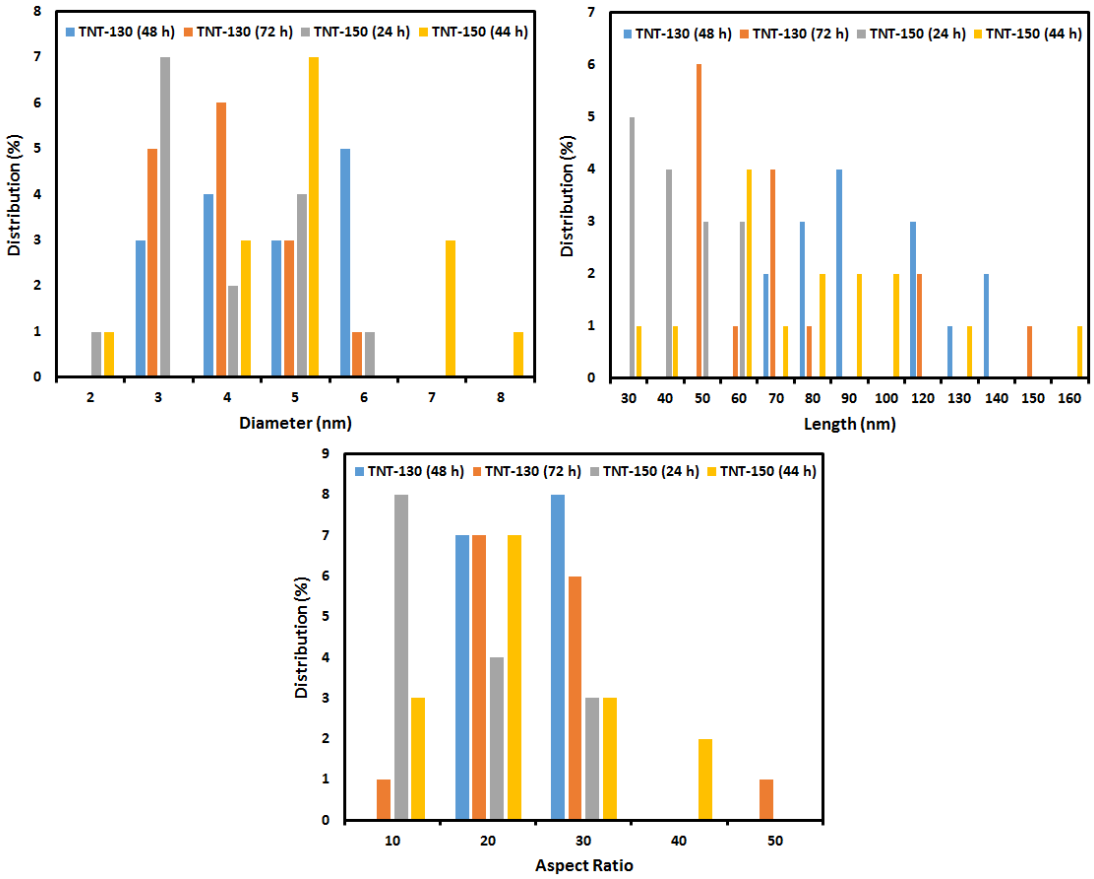


**Figure 4.2.** TNTs distribution versus diameter, length and aspect ratio

X-ray diffraction (XRD) patterns for various TNTs are shown in Figure 4.3. The diffraction patterns clearly show that TNTs obtained after drying show mainly amorphous structure and a few new peaks appeared in case of TNTs treated at 150°C for 44 h as compared to other TNTs. Moreover, a mixture of anatase, rutile and titanate phase is identified. This result suggests that the TNTs need to be heat treated to enhance the crystallinity of TNTs and to assess the role of calcination temperature on the morphology of TNTs.

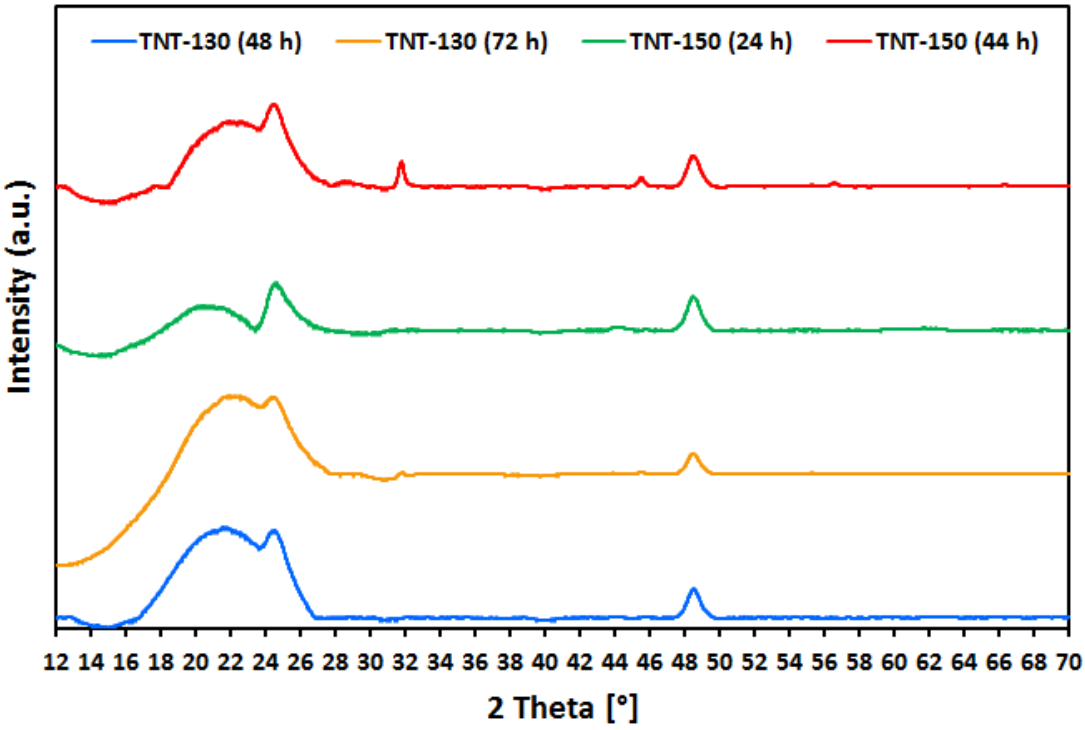


**Figure 4.3.** XRD patterns for TNTs treated under various conditions

*4.3.2 Effect of calcination temperature*

In order to improve the crystallinity of TNTs prepared, TNTs were subjected to various calcination temperatures *i.e.*, 400, 600 and 800°C. TEM images of TNTs calcined at different temperatures showed that the nanotubes obtained after drying went through reversible cycle and got converted back to nanoparticles at 400 and 600°C while titania nanorods (TNRs) with high aspect ratio were formed at 800°C as shown in Figure 4.4-4.6. A similar observation has been reported in the literature according to which calcination temperature may cause nanotubes collapse back to nanoparticles [37]. Guo *et al*. [38] synthesized TNTs using 2 g of $TiO_2$-P25 in 100 mL of 10M NaOH followed by hydrothermal treatment at 150°C for 24 h. The as-synthesized TNTs were calcined at various temperatures *i.e.*, 110, 350, 500 and 700°C. The results indicated calcination temperature had a profound impact on TNTs and TNTs calcined at 350°C started to shorten as compared to TNTs calcined at 100°C. Further increase in calcination temperature to 500°C transformed TNTs into TNRs which broke into particles at calcination temperature of 700°C. The collapse of tubular structure was assigned to loss of interlayered OH groups. Razali and his teammates [39] utilized same hydrothermal conditions as of Guo *et al*. [38] and investigated the influence of pH as well as calcination temperature on as-prepared titanate nanotubes (TTNTs). They inferred the

TTNTs with pH 12 were mainly sodium titanate nanotubes which had better thermal stability in comparison with hydrogen titanate nanotubes obtained at pH of 7. The change in calcination temperature from 300 to 700°C revealed collapse of tubular structure to nanoparticles in case of hydrogen titanate nanotubes while sodium titanate nanotubes were transformed into TNRs at calcination temperature of 700°C.

Based on the findings and discussion above, the hydrothermal conditions of 150°C for 44 h and calcination temperature of 800°C were selected for further investigation of reaction testing and role of metal deposition on TNRs obtained at above mentioned conditions.

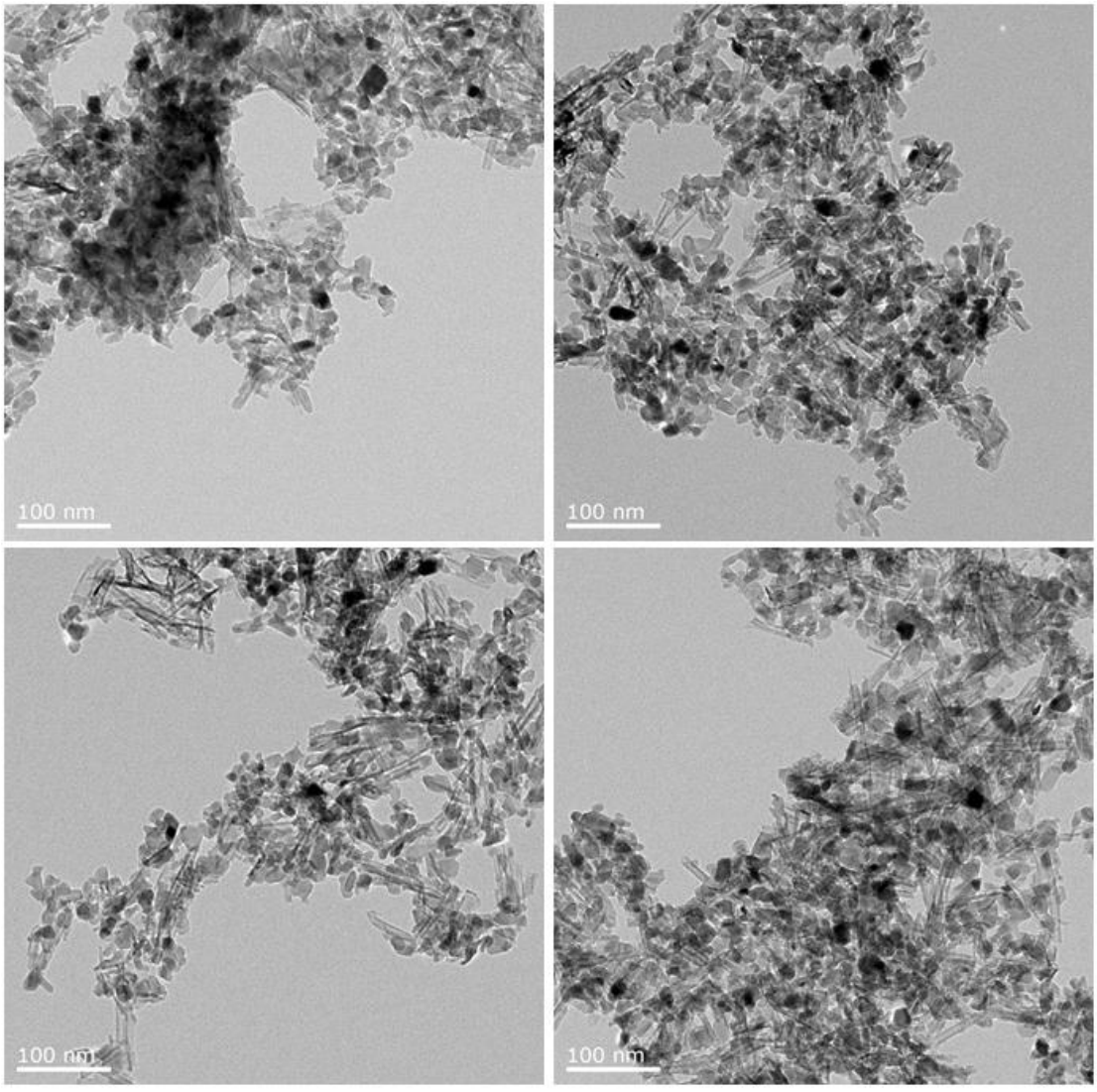


**Figure 4.4.** TEM images of TNTs calcined at 400°C

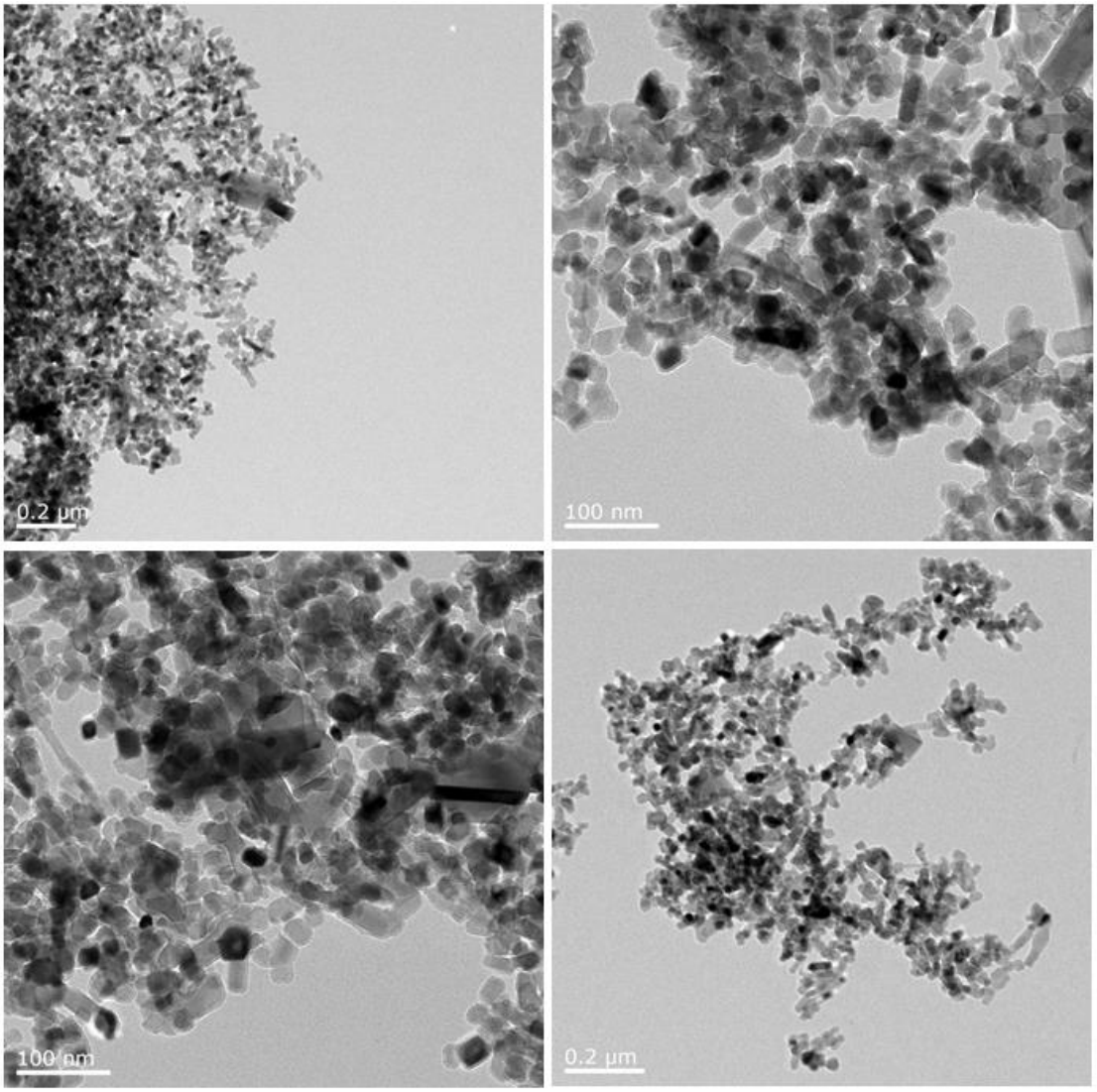


**Figure 4.5.** TEM images of TNTs calcined at 600°C

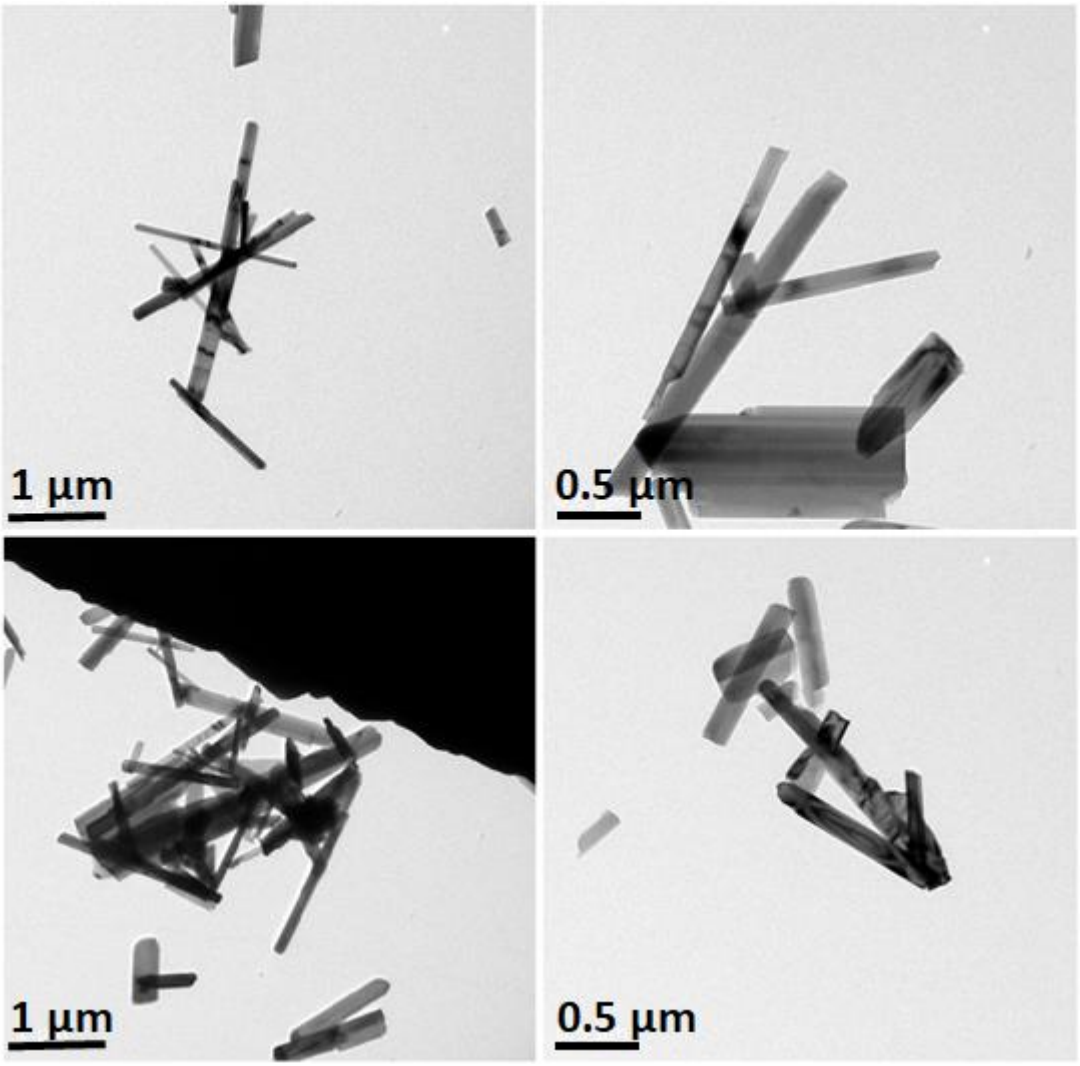


**Figure 4.6.** TEM images of TNTs calcined at 800°C

The surface morphology of TNTs calcined at 800°C was also investigated using scanning electron microscope (SEM). Figure 4.7 presents SEM images of TNTs calcined at 800°C. It can be seen that well defined TNRs with a range of aspect ratio are formed at calcination temperature of 800°C.

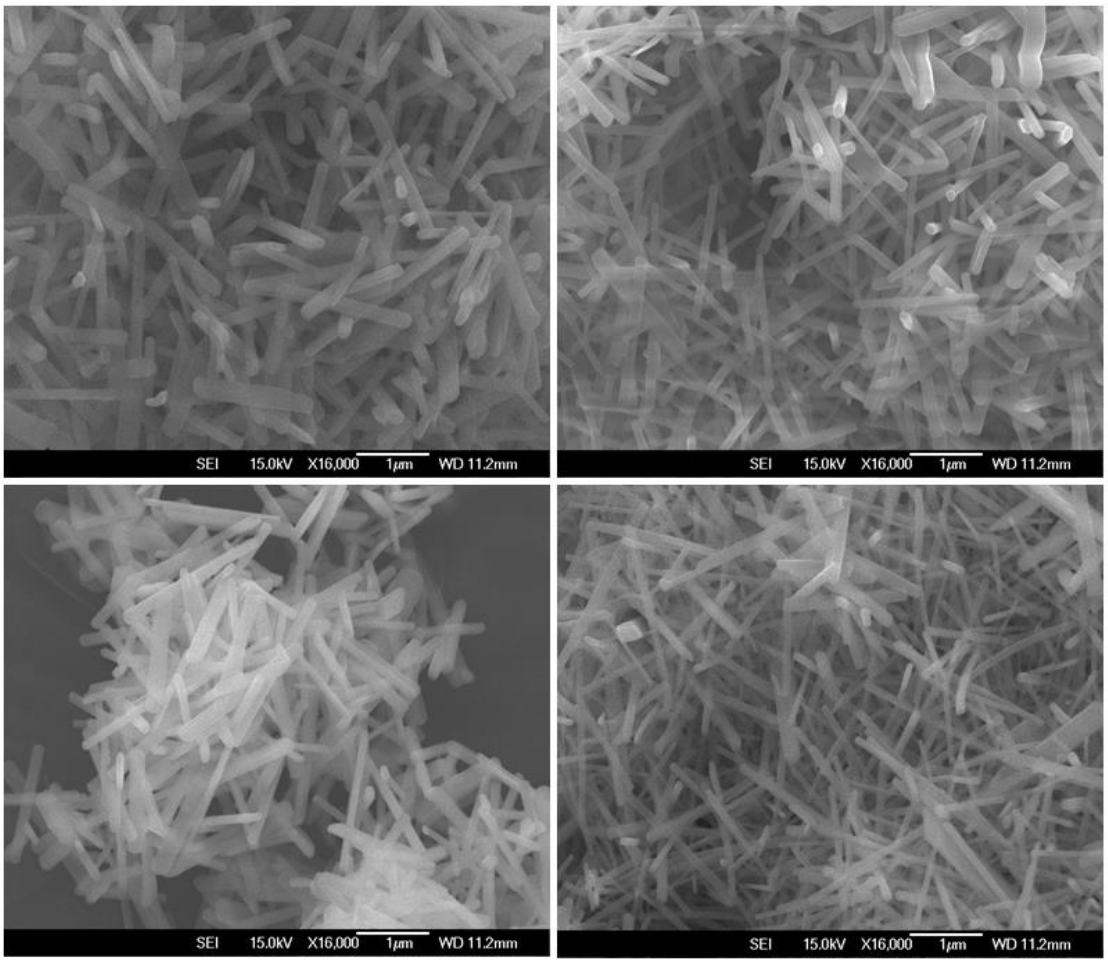


**Figure 4.7.** SEM images of TNTs calcined at 800°C

In addition to preserving the shape of nanotubes or nanorods, the other important criteria is to have a crystalline structure. XRD patterns of TNTs for different calcination temperatures are presented in Figure 4.8. It can be seen that increase in calcination temperature has a significant impact on crystalline phases of titania. Since titania P25 comprises mixture of 80% anatase and 20% rutile, increase in calcination temperature is generally expected to transform anatase into rutile. So, as calcination temperature was raised from 100 to 800°C, the diffraction peaks for anatase started to become sharp and anatase transformation into rutile was observed by increasing intensity of rutile peaks. For instance, the intensity of typical anatase diffraction peak at around 25° drops as the calcination temperature is raised at the expense of increase in the intensity of rutile peak appearing at 27.5°. The similar findings have been reported in the literature depicting phase change from anatase to rutile at higher calcination temperatures [38, 40].

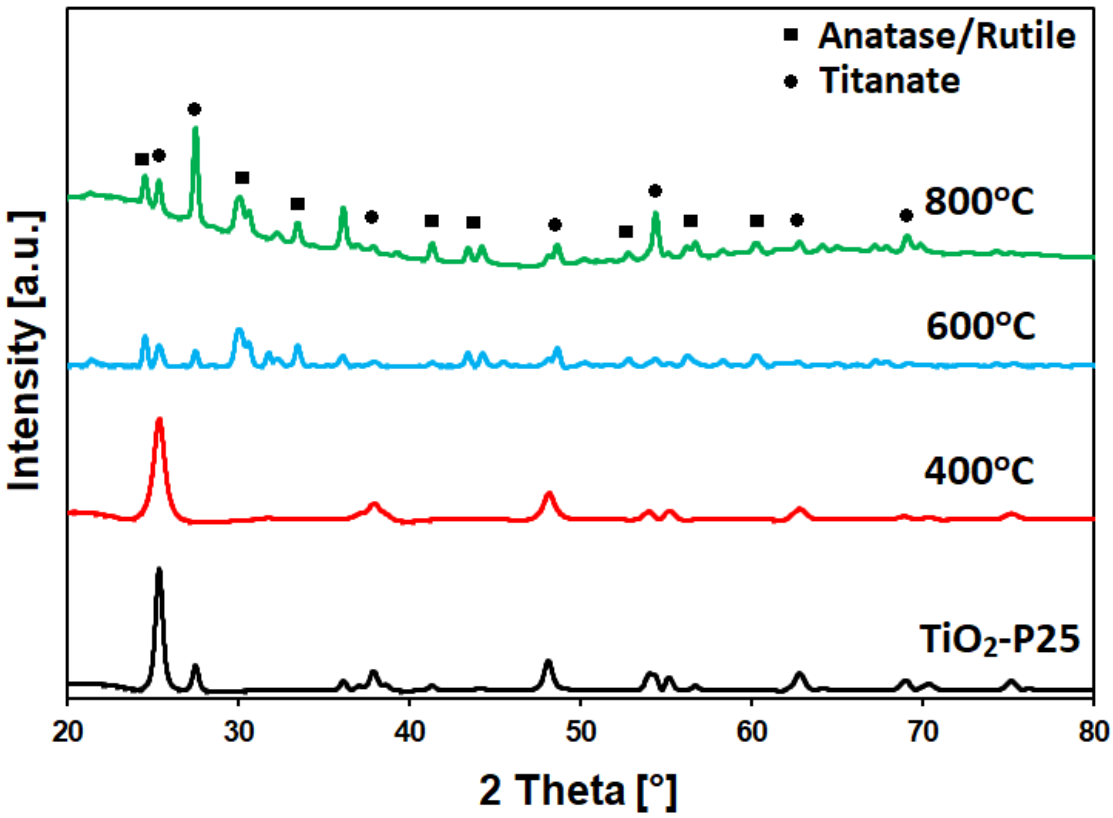


**Figure 4.8.** XRD patterns for TNTs calcined at various temperatures

### 4.4 Conclusions

The preparation of titania nanostructures including nanotubes and nanorods was successfully achieved using hydrothermal synthesis. The effect of hydrothermal treatment parameters such as time and temperature revealed that a wide range of aspect ratio can be obtained for a hydrothermal duration of 44 h at 150 ℃. The study of the effect of calcination temperature ranging from 400 to 800 ℃ showed a mix of nanotubes and particles at calcination temperatures of 400 and 600 ℃. The calcination temperature of 800 ℃ resulted in uniform titania nanorods. XRD patterns showed the transformation of anatase to rutile as calcination temperature varied between 400 and 800 ℃. The titania nanorods were chosen for anchoring the metal in the next phase of the project.

## References


[1] B. Liu, H.C. Zeng, Salt-assisted deposition of $SnO_2$ on alpha-$MoO_3$ nanorods and fabrication of polycrystalline $SnO_2$ nanotubes, J. Phys. Chem. B, 108 (2004) 5867-5874.

[2] G.T. Chandrappa, N. Steunou, S. Cassaignon, C. Bauvais, J. Livage, Hydrothermal synthesis of vanadium oxide nanotubes from $V_2O_5$ gels, Catal. Today, 78 (2003) 85-89.

[3] L. Xu, Y. Su, S. Li, Y.Q. Chen, Q.T. Zhou, S. Yin, Y. Feng, Self-assembly and hierarchical organization of $Ga_2O_3$/$In_2O_3$ nanostructures, J. Phys. Chem. B, 111 (2007) 760-766.

[4] X. Xiang, C.B. Cao, Y. Guo, H.S. Zhu, A simple method to synthesize gallium oxide nanosheets and nanobelts, Chem. Phys. Lett., 378 (2003) 660-664.

[5] R.S. Yang, Z.L. Wang, Springs, rings, and spirals of rutile-structured tin oxide nanobelts, J. Am. Chem. Soc., 128 (2006) 1466-1467.

[6] M. Law, L.E. Greene, A. Radenovic, T. Kuykendall, J. Liphardt, P.D. Yang, ZnO-$Al_2O_3$ and ZnO-$TiO_2$ core-shell nanowire dye-sensitized solar cells, J. Phys. Chem. B, 110 (2006) 22652-22663.

[7] N.H. Zhao, G.J. Wang, Y. Huang, B. Wang, B.D. Yao, Y.P. Wu, Preparation of nanowire arrays of amorphous carbon nanotube-coated single crystal $SnO_2$, Chem. Mater., 20 (2008) 2612-2614.

[8] D.W. Kim, I.S. Hwang, S.J. Kwon, H.Y. Kang, K.S. Park, Y.J. Choi, K.J. Choi, J.G. Park, Highly conductive coaxial $SnO_2$-$In_2O_3$ heterostructured nanowires for Li ion battery electrodes, Nano Lett., 7 (2007) 3041-3045.

[9] C.L. Yan, D.F. Xue, Conversion of ZnO nanorod arrays into ZnO/ZnS nanocable and ZnS nanotube arrays *via* an in situ chemistry strategy, J. Phys. Chem. B, 110 (2006) 25850-25855.

[10] E. Reck, S. Seymour, The effect of $TiO_2$ pigment on the performance of paratoluene sulphonic acid catalysed paint systems, Macromol. Symp., 187 (2002) 707-718.

[11] S.A. Yuan, W.H. Chen, S.S. Hu, Fabrication of $TiO_2$ nanoparticles/surfactant polymer complex film on glassy carbon electrode and its application to sensing trace dopamine, Mat. Sci. Eng. C, 25 (2005) 479-485.

[12] M. Zlamal, J.M. Macak, P. Schimuki, J. Krysa, Electrochemically assisted photocatalysis on self-organized $TiO_2$ nanotubes, Electrochem. Commun., 9 (2007) 2822-2826.

[13] P.D. Cozzoli, A. Kornowski, H. Weller, Low-temperature synthesis of soluble and processable organic-capped anatase $TiO_2$ nanorods, J. Am. Chem. Soc., 125 (2003) 14539-14548.

[14] G.K. Mor, O.K. Varghese, M. Paulose, K. Shankar, C.A. Grimes, A review on highly ordered, vertically oriented $TiO_2$ nanotube arrays: Fabrication, material properties, and solar energy applications, Sol. Energ. Mat. Sol. C, 90 (2006) 2011-2075.

[15] M. Gratzel, Dye-sensitized solid-state heterojunction solar cells, MRS Bull., 30 (2005) 23-27.

[16] I.A. Al-Homoudi, J.S. Thakur, R. Naik, G.W. Auner, G. Newaz, Anatase $TiO_2$ films based CO gas sensor: Film thickness, substrate and temperature effects, Appl. Surf. Sci., 253 (2007) 8607-8614.

[17] A. Wisitsoraat, A. Tuantranont, E. Comini, G. Sberveglieri, W. WIodarski, Gas sensing properties of $TiO_2$-$WO_3$ and $TiO_2$-$MO_3$ based thin film prepared by ion-assisted E-beam evaporation, IEEE Sensor, (2005) 1184-1187.

[18] G.K. Mor, M.A. Carvalho, O.K. Varghese, M.V. Pishko, C.A. Grimes, A room-temperature TiO2-nanotube hydrogen sensor able to self-clean photoactively from environmental contamination, J. Mater. Res., 19 (2004) 628-634.

[19] C.C. Tsai, H.S. Teng, Structural features of nanotubes synthesized from NaOH treatment on $TiO_2$ with different post-treatments, Chem. Mater., 18 (2006) 367-373.

[20] J. Wang, D.N. Tafen, J.P. Lewis, Z.L. Hong, A. Manivannan, M.J. Zhi, M. Li, N.Q. Wu, Origin of Photocatalytic Activity of Nitrogen-Doped $TiO_2$ Nanobelts, J. Am. Chem. Soc., 131 (2009) 12290-12297.

[21] Y. Lin, G.S. Wu, X.Y. Yuan, T. Xie, L.D. Zhang, Fabrication and optical properties of $TiO_2$ nanowire arrays made by sol-gel electrophoresis deposition into anodic alumina membranes, J. Phys. Condens. Mat., 15 (2003) 2917-2922.

[22] J. Joo, S.G. Kwon, T. Yu, M. Cho, J. Lee, J. Yoon, T. Hyeon, Large-scale synthesis of $TiO_2$ nanorods *via* nonhydrolytic sol-gel ester elimination reaction and their application to photocatalytic inactivation of E. coli, J. Phys. Chem. B, 109 (2005) 15297-15302.

[23] J. Li, G.Z. Lu, G.S. Wu, D.S. Mao, Y.L. Guo, Y.Q. Wanga, G.A. Yun, Effect of TiO2 crystal structure on the catalytic performance of $Co_3O_4/TiO_2$ catalyst for low-temperature CO oxidation, Catal. Sci. Technol., 4 (2014) 1268-1275.
[24] X.B. Chen, S. Cao, X.L. Weng, H.Q. Wang, Z.B. Wu, Effects of morphology and structure of titanate supports on the performance of ceria in selective catalytic reduction of NO, Catal. Commun., 26 (2012) 178-182.
[25] F.J. Song, Y.X. Zhao, Q. Zhong, Adsorption of carbon dioxide on amine-modified TiO2 nanotubes, J. Environ. Sci., 25 (2013) 554-560.
[26] M. Kim, S.H. Hwang, S.K. Lim, S. Kim, Effects of ion exchange and calcinations on the structure and photocatalytic activity of hydrothermally prepared titanate nanotubes, Cryst. Res. Technol., 47 (2012) 1190-1194.
[27] Y. Wu, L. Song, Y. Hu, Fabrication and Characterization of $TiO_2$ Nanotube-Epoxy Nanocomposites, Ind. Eng. Chem. Res., 50 (2011) 11988-11995.
[28] X.B. Chen, H.Q. Wang, S. Gao, Z.B. Wu, Effect of pH value on the microstructure and de$NO_x$, catalytic performance of titanate nanotubes loaded $CeO_2$, J. Colloid Interface Sci., 377 (2012) 131-136.
[29] Z.R. Tang, Y.H. Zhang, Y.J. Xu, Tuning the Optical Property and Photocatalytic Performance of Titanate Nanotube toward Selective Oxidation of Alcohols under Ambient Conditions, ACS Appl. Mater. Interfaces, 4 (2012) 1512-1520.
[30] D.S. Seo, J.K. Lee, H. Kim, Preparation of nanotube-shaped $TiO_2$ powder, J. Cryst. Growth, 229 (2001) 428-432.
[31] R.Z. Ma, K. Fukuda, T. Sasaki, M. Osada, Y. Bando, Structural features of titanate nanotubes/nanobelts revealed by Raman, X-ray absorption fine structure and electron diffraction characterizations, J. Phys. Chem. B, 109 (2005) 6210-6214.
[32] T. Kasuga, M. Hiramatsu, A. Hoson, T. Sekino, K. Niihara, Formation of titanium oxide nanotube, Langmuir, 14 (1998) 3160-3163.
[33] X.W. Xie, Y. Li, Z.Q. Liu, M. Haruta, W.J. Shen, Low-temperature oxidation of CO catalysed by $Co_3O_4$ nanorods, Nature, 458 (2009) 746-749.
[34] H.Q. Wan, Z. Wang, J. Zhu, X.W. Li, B. Liu, F. Gao, L. Dong, Y. Chen, Influence of CO pretreatment on the activities of CuO/gamma-$Al_2O_3$ catalysts in CO+$O_2$ reaction, Appl. Catal. B-Environ., 79 (2008) 254-261.
[35] D.V. Bavykin, V.N. Parmon, A.A. Lapkin, F.C. Walsh, The effect of hydrothermal conditions on the mesoporous structure of $TiO_2$ nanotubes, J. Mater. Chem., 14 (2004) 3370-3377.

[36] C.C. Tsai, H.S. Teng, Regulation of the physical characteristics of Titania nanotube aggregates synthesized from hydrothermal treatment, Chem. Mater., 16 (2004) 4352-4358.
[37] G.J. Wu, N.J. Guan, L.D. Li, Low temperature CO oxidation on Cu-$Cu_2O/TiO_2$ catalyst prepared by photodeposition, Catal. Sci. Technol., 1 (2011) 601-608.
[38] C.L. Guo, Y.Y. Wu, X. Wang, B. Yang, Effect of the support calcination temperature on selective hydrodesulfurization of $TiO_2$ nanotubes supported CoMo catalysts, J. Energy Chem., 22 (2013) 517-523.
[39] M.H. Razali, A.F.M. Noor, A.R. Mohamed, S. Sreekantan, Morphological and Structural Studies of Titanate and Titania Nanostructured Materials Obtained after Heat Treatments of Hydrothermally Produced Layered Titanate, J. Nanomater., (2012).
[40] B. Vijayan, N.M. Dimitrijevic, T. Rajh, K. Gray, Effect of Calcination Temperature on the Photocatalytic Reduction and Oxidation Processes of Hydrothermally Synthesized Titania Nanotubes, J. Phys. Chem. C, 114 (2010) 12994-13002.

# Chapter 5

# Catalytically active interfaces in titania nanorod-supported copper catalysts for CO oxidation

## 5.1 Introduction

Air quality control has become a primary concern in recent years, and the transport industry mainly generates environmentally hazardous gases, including carbon monoxide. The concept of automotive catalytic converters has had a significant impact on pollution reduction. The development of catalysts to effectively treat exhaust gas at lower temperatures has been the focus of research in recent years [1, 2]. Apart from air quality control, CO oxidation is involved in industrial chemical processes, including water gas shift, methanol synthesis, CO hydrogenation and CO oxidation by NO [3, 4]. Metal oxides, including various reducible and nonreducible oxide supports, such as ceria (CeO2), alumina (Al2O3), silica (SiO2), titanium dioxide/titania (TiO2) and zirconia (ZrO2) [1, 5-10], and multiple noble metals, including gold (Au), platinum (Pt), palladium (Pd), and silver (Ag), have been reported for CO oxidation [8, 11-14]. However, the high cost and low abundance of noble metals are limiting factors in their commercial application [6, 9, 15-17]. Moreover, because of their relative lack of thermal stability, these materials are often prone to sintering during reactions at high temperatures, which leads to the loss of surface area and a decrease in activity or change in selectivity due to disproportionate site types. Supported catalysts are able to disperse and stabilize catalytically active components on a support against sintering effectively.

Among the widely used metal oxides in heterogeneous catalysis, titania is an environmentally friendly support with distinguishing features such as nontoxicity and economic viability [18]. The morphology of the support material is found to play a pivotal role in the catalytic activity. Nanostructured supports, such as ceria nanorods, ceria nanocubes and carbon nanotubes, are reported to give excellent performance in CO oxidation [5, 6, 18]. In particular, titania nanotubes offer a high specific surface area, ion exchangeability and rapid electron transfer. High-temperature calcination of titania nanotubes results in a change in morphology to nanorods, and thus, the specific

surface area is significantly decreased. Despite the change in morphology, the ion exchangeability and electron transfer capability of the titania are still able to influence the interaction between the metal and the support, which in turn influences the catalytic performance. Camposeco et al. [19] synthesized titania nanotubes and nanoribbons with a high specific surface area by a hydrothermal technique and compared the as-synthesized titania nanotubes with titania nanocrystals for use in CO oxidation. The results revealed that the support stability, size, mesoporosity and morphology had a substantial influence on the performance. The layered and scrolled titania nanotubes demonstrated higher catalytic activity than nanorods and nanopowders, which showed insignificant activity at reaction temperatures as high as 250 °C.

The catalytic activity of a supported catalyst is influenced by various factors, such as specific surface area, type of support material, crystalline structure, metal-support interaction/interface, interaction between the probe gas and the catalyst surface, preparation method, number of available active sites, and number of reducible species [20-28]. Copper, as an active metal, plays a significant role in the carbon monoxide (CO) oxidation reaction owing to its promising features, including high activity in both the oxide and metal-only forms and relatively low cost compared with noble metals [18, 29, 30]. The study of CO oxidation over copper oxide deposited on titania nanotubes and titania nanoparticles has revealed that the titania nanotube-supported catalyst induced a strong metal-support interaction, which contributed to enhanced copper oxide dispersion over the support surface. Moreover, titania nanotubes offer a high specific surface area, and these factors significantly influence the catalytic performance of catalysts based on copper oxide deposited on nanotubular supports [18].

In a recent study by Lykaki et al. [1], surface defects in ceria-supported copper-based catalysts were explored in CO oxidation reactions. Ceria supports with different morphologies, including nanoparticles, nanocubes and nanorods, were synthesized using a hydrothermal technique. The ceria nanorods exhibited better catalytic performance than nanocubes and nanoparticles owing to the presence of more structural defects and oxygen vacancies on ceria nanorods. Hossain et al. [5] investigated the effect of the support structure on CO oxidation using silica nanospheres and ceria nanorod-supported CuOx catalysts. The reducibility of the support, the metal-support interaction and interfacial species were shown to influence the performance of the catalyst. The reduction treatment and catalytic results showed that copper deposited on

ceria nanorods, oxidized and reduced at 400 °C, exhibited CO conversions of 92 and 100%, respectively, compared with CO conversions of 68 and 72%, respectively, in the case of copper deposited on silica nanospheres. The interactions between CuOx species and the ceria nanorod surface were the main contributors to the excellent catalytic performance. The same group of researchers compared the catalytic activity between a Cu-O-Ce solid solution and CuO deposited onto ceria nanorods at various concentrations [31]. The catalysts were analyzed in oxidation-reduction cycles to probe the influence of metal-support interactions. Ceria nanorods with surface defects had strong interfacial interactions with CuO species, and the interactions caused formation of oxygen vacancies on the resulting catalyst surface.

Structural sensitivity is an important factor in CO oxidation reactions. It is assumed that CO and oxygen adsorb on the surface vacancy sites of TiO2 rather than on terraces or steps [8, 21]. Titania nanorods offer surface vacancy sites and high aspect ratios [8]. Moreover, the metal-support interface in supported catalysts is found to be the active center for the CO oxidation reaction [23]. However, detailed investigations on the synergy between titania nanorods and copper species, as well as their catalytic implications, have not been reported. Considering the impact of one-dimensional nanostructured supports in CO oxidation, the current work aims to present the role of titania nanorods prepared using hydrothermal synthesis with various copper loading in CO oxidation. The metal-support interaction, surface reducibility, surface chemisorption and surface energy of the as-synthesized catalysts were investigated to probe the catalytic viability. This work also investigates the catalytic consequences of different metal-support interfaces, as well as possible reaction mechanisms over supported and unsupported catalysts.

## 5.2 Experimental

### *5.2.1 Catalyst preparation*

For chemical details, please refer to Appendix A. Titania nanorods were synthesized using hydrothermal synthesis as reported by Kasuga *et al*. [32]. Five grams of titanium dioxide ($TiO_2$-P25) was dispersed in 100 mL of 10 M NaOH solution, and the slurry was kept under magnetic stirring for half an hour before it was transferred into an autoclave for hydrothermal treatment at 150°C for 44 h. The solid obtained was washed with 0.1 M HCl and deionized water several times to remove impurities. The solid was

filtered and dried at 120°C for 12 h and finally calcined at 800°C for 10 h to obtain titania nanorods.

The copper was deposited on titania nanorods (TNRs) using deposition-precipitation. In a typical procedure to synthesize 1 gram of 7.5 wt% copper supported catalyst, 0.235 grams of copper acetate monohydrate were dissolved in 100 mL of deionized water until a clear solution was obtained followed by the addition of 0.925 grams of the support (titania nanorods, $TiO_2$-P25, silica and alumina) into the copper-containing aqueous solution under magnetic stirring. Sodium carbonate solution (1 M) was added dropwise until a pH of 9-10 was attained. The slurry was kept under stirring for 20 h before it was centrifuged, decanted and washed three times with deionized water. The washed sample was dried at 120°C for 12 h and finally calcined at 400°C for 5 h. The similar procedure was utilized to synthesize catalysts with copper contents varying between 2.5 and 12.5 wt%. The catalysts were designated as *x*Cu-*S*, where *x* represents the copper content in wt% and *S* represents the support type (i.e, TNR = titania nanorods, $TiO_2$ = $TiO_2$-P25, $Al_2O_3$ = alumina, $SiO_2$ = silica).

### *5.2.2 Catalyst characterization*

X-ray diffraction (XRD) patterns were recorded using a Philips PW1700 X-ray diffractometer (Co-Kα radiation source). The recordings were obtained for scanning range of 20-80° using scanning step of 0.05°. MPI Jade® software was utilized for XRD data analysis. Refinement of the XRD pattern was carried out using the X'Pert Highscore Plus software. The software allows the separation of $K\alpha_1$ and $K\alpha_2$ peaks during the refinement procedure. The crystallite size was calculated exclusively based on the $K\alpha_1$ peak and applying the Scherrer equation, $K\lambda/(\beta\cos\theta)$, where $K$ is the shape factor taken as 0.89, $\lambda$ is the Co $K\alpha_1$ wavelength (1.78901 Å), $\beta$ is the full width at half maximum (FWHM in radian) at $2\theta$, and $\theta$ is the Bragg angle.

The temperature-programmed reduction with hydrogen ($H_2$-TPR), temperature-programmed desorption using CO and $O_2$ (CO-TPD and $O_2$-TPD, respectively) and CO chemisorption measurements were performed using a BELCAT II chemisorption apparatus. For these measurements, the catalyst surface was pre-treated by keeping 25-30 mg of the catalyst sample at 150 ℃ for half an hour under inert atmosphere (helium (He) flow of 30 mL/min) for $H_2$-TPR and CO chemisorption while temperature was kept at 200 ℃ for CO- and $O_2$-TPD. For $H_2$-TPR, the sample was subsequently cooled

to ambient temperature before it was heated to 500 °C at 10°C/min under analysis gas (5%$H_2$/Ar mixture) flowing at 30 mL/min. 10%CO/He (30 mL/min) and 5%$O_2$/He (30 mL/min) were injected for 1 hr followed by injection of He (30 mL/min) for 30 min to remove any remaining CO or $O_2$. Then, the sample temperature was raised to 500 °C at 10°C/min using 30 mL/min flow of He. In the case of CO chemisorption, 10%CO/He (30 mL/min) was injected in pulses until surface saturation was reached. Thermal conductivity detector (TCD) was used to monitor the outlet signal of BELCAT II. The BET surface area of the samples was measured by $N_2$ physisorption technique at 77 K by Germini VI.

The actual amount of copper in the synthesized catalyst samples was determined by inductively coupled plasma mass spectrometry (ICP-MS) (7500cx single-quad, Agilent Technologies) analysis. The samples were digested in *aqua regia* at 80°C for 2 days to ensure a complete dissolution of copper, which were then sonicated and diluted to a fixed volume. For consistency, duplicate samples were analyzed. Scanning electron microscopy (SEM) and transmission electron microscopy (TEM) were performed using a JEOL 7000F FE-SEM and Philips CM200. X-ray photoelectron spectroscopy (XPS) was performed using a Kratos Axis Ultra DLD instrument with a monochromatic Al K$\alpha$ X-ray source. Accurate quantification of the $Cu^{2+}$ and $Cu^{+}$ peak areas was carried out on the Cu $2p_{3/2}$ in accordance with the earlier report [33], where the $Cu^{2+}$ peak area ($A_{Cu2+}$) was calculated from the total peak area of the shake-up satellite peak ($A_{satellite}$) using the relationship $A_{Cu2+}$:$A_{satellite}$ = 1.89. The peak area of $Cu^{+}$ ($A_{Cu+}$) was in turn quantified from $A_{Cu+} = A_{Cu2p3/2} - A_{Cu2+}$. The technique circumvents the statistical uncertainties during the peaks deconvolution process given the close proximity between the $Cu^{2+}$ binding energy peak and that of the $Cu^{+}$.

### *5.2.3 Catalytic activity*

The CO oxidation reaction was carried out, at the temperature ranging from 100 to 240 °C, in a fixed bed tubular reactor assuming plug flow dynamic. The catalyst was placed in quartz wool, and the temperature of the catalyst bed was monitored using a k-type thermocouple. A total of 30 mg of the tested catalyst was loaded into the reactor. The reaction feed gas (20 mL/min) contained 1% CO and 10% oxygen balanced with argon was flowed over the catalyst bed. In order to eliminate the effect of external diffusion, the reaction was conducted in a differential mode at a high gas hourly space velocity

(GHSV) of 40,000 mL/h.$g_{cat}$. The products and unconverted reactants were measured by an online gas chromatograph (SRI Instruments) equipped with a flame ionization detector (FID) and a TCD. The CO conversion, rate of reaction and turnover number (TON) were calculated using the following equations:

$$CO\ Conversion\ [X_{CO}]\ (\%) = \frac{CO_{in} - CO_{out}}{CO_{in}} \times 100 \quad (5.1)$$

$$r_{CO} = \frac{F_{CO} X_{CO}}{n_{Cu}} \quad (5.2)$$

$$TON = \frac{n_{CO2}}{n_{Cu}} \quad (5.3)$$

where $F_{CO}$ is the molar flow of CO (mol/s), $X_{CO}$ is the conversion of CO, $n_{Cu}$ is the number of mole of copper in the catalyst, $r_{CO}$ is the rate of reaction in $mol_{CO}/s.mol_{Cu}$. Turnover number (TON) is the mole of $CO_2$ produced ($n_{CO2}$) per mole of copper in the catalyst.

## 5.3 Results and Discussion

### *5.3.1 Characterization of $TiO_2$ nanorods (TNR) and Cu-TNR catalysts*

Figure 5.1 shows the TEM and SEM images of the titania nanorods (TNRs), indicating that the length and diameter range from 100 nm to a few microns and 100-400 nm, respectively. The TNRs have a small surface area of approximately 15 $m^2/g$ due to the postsynthesis treatment at high temperature (800 °C). Acid washing plays a crucial role in controlling the amount of sodium, which influences the bending of titanate layers. During the washing step, the imbalance between hydrogen ($H^+$) and sodium ($Na^+$) ions on both sides of the layered titanate structure causes excess surface energy and promotes the bending of layers into a nanotubular structure [34]. Moreover, the mobilization of sodium ions during calcination at higher temperature (800 °C) causes the nanotubular structure to grow into nanorods. It can be inferred that the presence of sodium has a profound impact on the stability and morphology of the nanotubular structure formed. These observations are in agreement with previous reports that sodium plays a role in the formation of nanorods from nanotubular structures, while the absence of sodium causes nanotubular structures to break down into nanoparticles [35, 36].

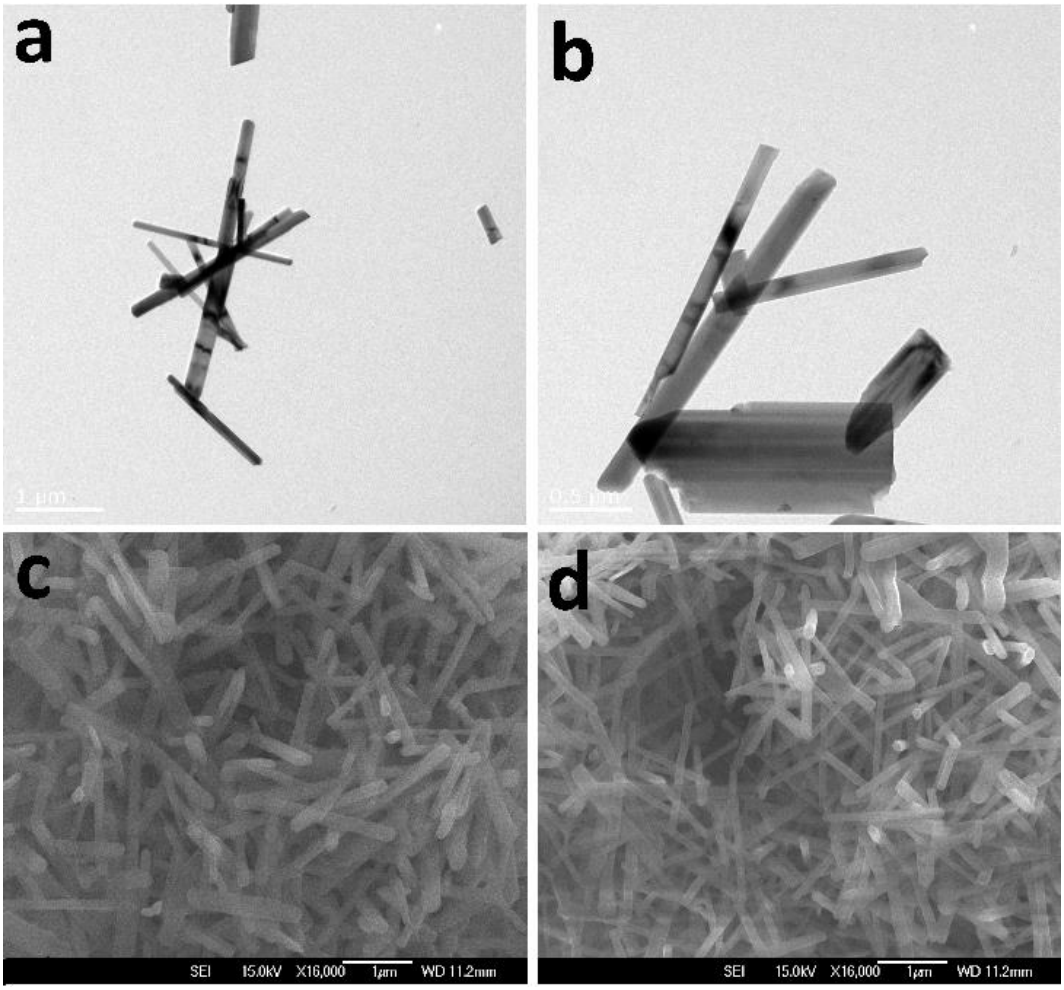


**Figure 5.1.** TEM (a & b) and SEM (c & d) images of titania nanorods. Note: scale bar of 1 µm and 0.5 µm in 1a and 1b, respectively. Scale bar of 1 µm in 1c and 1d.

Different loadings of Cu, ranging from 2.5 to 12.5 wt%, were deposited on the TNRs via deposition-precipitation. The XRD patterns in Figure 5.2a show that the Cu-loaded TNRs have similar crystalline structures with a mixture of rutile and anatase phases. It is worth noting that the main peaks associated with bulk copper oxides ($2\theta$ = 41.5 and 45.5°) are only visible as broad peaks in the Cu-TNR, inferring that the CuO exists as fine nanoparticles using the current synthesis method [37-39]. By further refinement of the spectra at the relevant region (Figure 5.2b), the Scherrer-determined size of the CuO was found to be 7, 9 and 12 nm for 5Cu-, 7.5Cu- and 10Cu-TNR, respectively. Higher Cu loading induces more coalescence during the preparation, and as such led to a systematic increase in the CuO size. $Cu_2O$ was not detected by the XRD, suggesting that they are either absent or exists as very finely dispersed species below 2 nm, which is the typical detection limit of the XRD.

The specific surface areas of Cu-TNR catalysts are also presented in Table 5.1. The specific surface areas and monolayer capacities decrease as the copper content increases, and the 7.5Cu-TNR catalyst shows a specific surface area of 14.8 $m^2/g$ and a monolayer capacity of 3.4 $cm^3/g$. The decrease in both specific surface areas and monolayer capacities with respect to copper contents concur with the increased coalescence of CuO that led to larger particle sizes at higher copper contents.

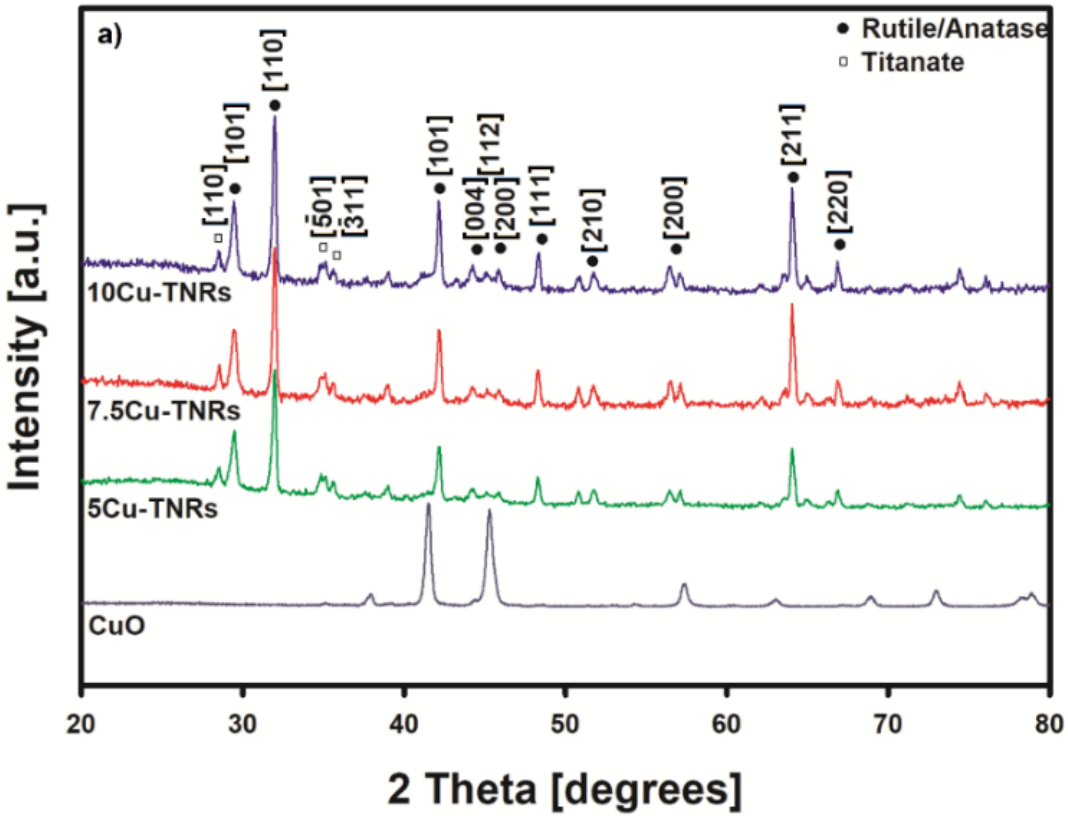

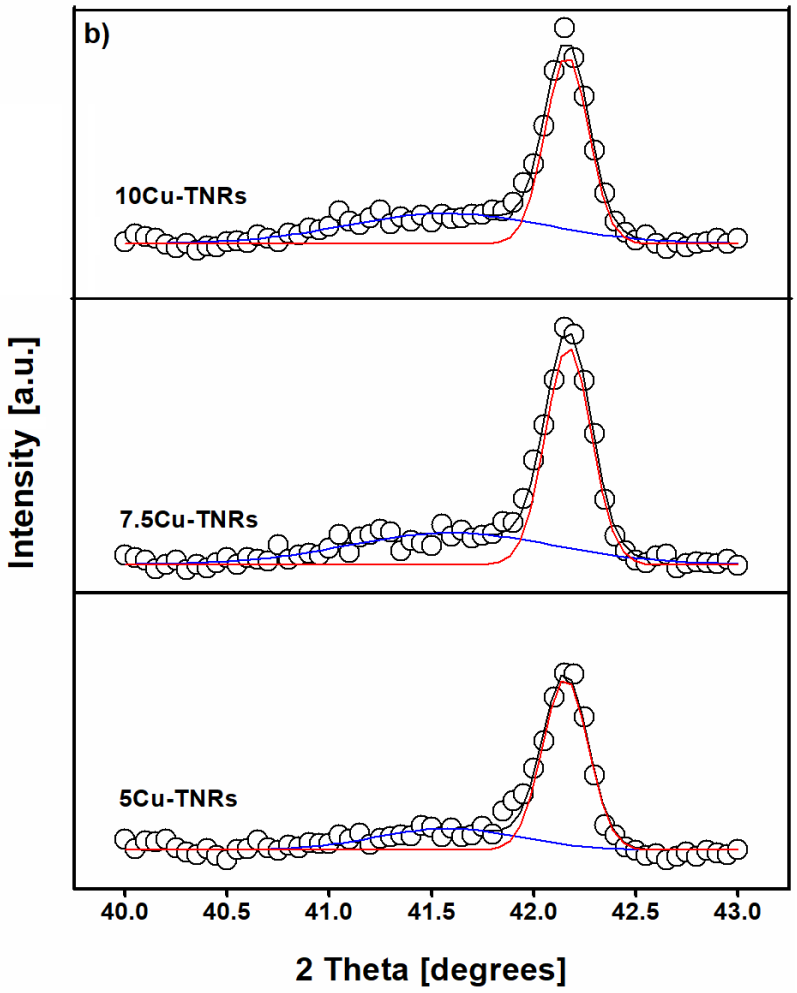


**Figure 5.2. (**a) XRD patterns of Cu-TNRs and CuO (Co Kα was used as the X-ray radiation source) and (b) refinement of the diffraction spectra in the narrow range of 40-43 degree showing the Gaussian peaks of the CuO nanoparticles (blue) and TNR (red), while the black line is the summation of the two.

*5.3.2 Surface adsorption properties of Cu-TNR*

Temperature-programmed desorption using CO (CO-TPD) and $O_2$ ($O_2$-TPD) as probe molecules was carried out to study the adsorbate-adsorbent interactions on the Cu-TNRs. The CO-TPD profiles (Figure 5.3) indicate that all the tested catalysts exhibit two distinct characteristic desorption peaks and, hence, two types of CO adsorption sites: the first in the temperature range of 60 to 200 °C (weaker CO adsorption sites) and the second in the range from 215 to 450 °C (stronger CO adsorption sites). The TNRs (without Cu metal) show adsorption peaks in the low temperature range (60-150 °C) and at approximately 390 °C, indicating that there are active sites available for CO adsorption on the bare support surface. A comparison between the bare support and

copper-deposited catalyst shows that copper deposition influences the CO adsorption capacity and that the desorption temperatures are distinctive. The CO desorption curves in Figure 3 show that the desorption peak temperature increased slightly from 100 to 105 °C and from 100 to 120 °C in the 5Cu-TNR and 10Cu-TNR catalysts, respectively, but decreased from 100 to 95 °C in the 2.5Cu-TNR and 7.5Cu-TNR catalyst compared with that of the TNR support. Moreover, Table 5.2 gives the quantitative results of CO-TPD. The area under the CO-TPD curve represents the surface coverage, which is a measure of the number of adsorption active sites. The amount of CO adsorbed increased with increasing copper content and reached a maximum adsorption of 0.231 mmol/g over 7.5Cu-TNR. Hence, a Cu loading of 7.5 wt% gave an optimum value, above which increasing the amount of Cu on the TNRs does not increase the number of CO adsorption sites. This may indicate that the Cu deposition and dispersion on the TNR surface change from a monolayer to a multilayer arrangement, as evidenced by the surface areas and monolayer capacities (Table 5.1). In addition, the desorption peaks in the high-temperature range shift from 340 to 300 °C as the Cu loading increases from 7.5 to 10 wt%. The CO adsorption strength on the strong adsorption sites decreases with increasing copper content on the Cu-TNR surface. The associated catalytic consequences of the metal-support interaction resulting from different arrangements of Cu on TNRs (i.e., monolayer vs. multilayers) will be discussed in section 5.3.5.

**Table 5.1** CO chemisorption and hydrogen consumption of Cu-TNR.

| **Catalyst** | **CO uptake ($cm^3/g$)[a]** | **Total hydrogen consumption (mmol/g)[b]** | **Degree of reduction (%)[c]** | **Specific surface area ($m^2/g$)** | **Monolayer capacity ($cm^3/g$)** |
|---|---|---|---|---|---|
| **2.5Cu-TNR** | 0.74 | 2.57 | 46.6 | 14.8 | 3.40 |
| **5Cu-TNR** | 0.86 | 0.74 | 94.2 | 13.2 | 3.03 |
| **7.5Cu-TNR** | 1.04 | 1.13 | 95.5 | 12.8 | 2.94 |
| **10Cu-TNR** | 0.61 | 0.90 | 56.9 | 10.3 | 2.36 |

[a] Measured from CO chemisorption; [b] Measured from $H_2$-TPR; [c] The ratio of $H_2$ consumed in TPR to theoretical $H_2$ required to reduce the catalyst.

CO chemisorption was conducted to estimate the CO uptake on Cu-TNR (Table 5.1). CO chemisorption results indicate that CO uptakes of 0.74, 0.86, 1.04 and 0.61 $cm^3/g$ were found for the 2.5Cu-, 5Cu-, 7.5Cu- and 10Cu-TNR catalysts, respectively,

showing the highest CO uptake for 7.5Cu-TNR. The metal particles tend to agglomerate at higher metal loadings, and therefore, a further increase in copper content to 10 wt% showed a decrease in CO uptake. These findings are consistent with previously reported results [40]. The metal contents measured using ICP-MS are given in Table 5.2.

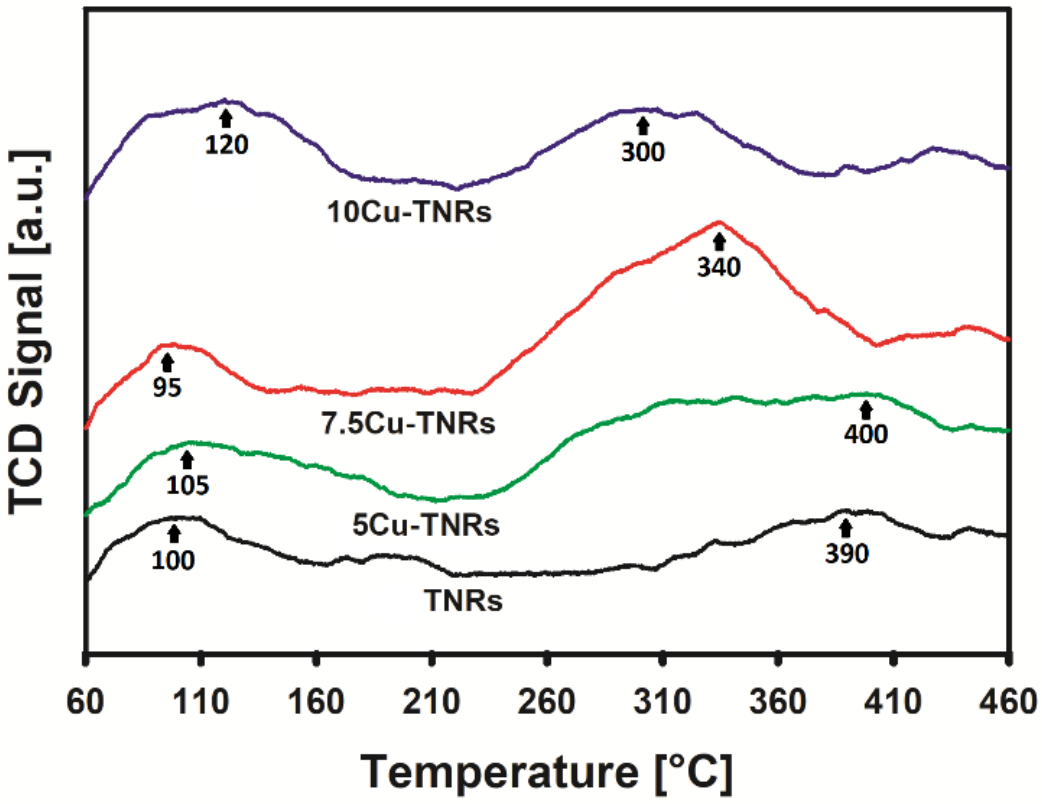


**Figure 5.3.** Temperature-programmed desorption of CO on Cu-TNR.

The oxygen desorption profiles of the copper-deposited catalysts (Figure 5.4) indicate that the Cu-TNR surface has active sites available for oxygen adsorption in addition to CO adsorption. The bare support shows only one distinct characteristic desorption peak in the temperature range between 60 °C and 160 °C (zone Z1), which can be assigned to weakly adsorbed oxygen species [41]. This single peak in Z1, however, evolves into two peaks when Cu was deposited on the TNR support, indicating the possible formation of different kinds of oxygen species on the copper-deposited catalysts. More importantly, the result indicates that additional vacant sites on both the Cu metal and interface are available for $O_2$ adsorption and that they adsorb $O_2$ more strongly than the bare support. Additional peaks in Z2, Z3 and Z4 can be observed at approximately 200 °C, 360 °C and 430 °C, respectively, and they are dependent on the Cu content. For instance, the three peaks associated with 2.5Cu-TNR in Z2, Z3 and Z4 at 200, 360 and

430 °C, respectively, shift to lower temperatures (approximately at 185 °C, 285 °C and 395 °C) when the copper content is increased to 7.5 wt% (i.e., 7.5Cu-TNR). The peak in Z2 can be ascribed to the $O_2^-$ species resulting from the $O_2$ chemically adsorbed on the surface, whereas the peaks in Z3-Z5 can be attributed to the desorption of the lattice oxygen $O^{2-}$ species formed on the surface of the catalyst [42].

Also, a new peak is observed at approximately 480 °C in Z5. An increase in Cu loading from 7.5 wt% to 10 wt% (i.e., 10Cu-TNR) shows further shifting of the peak temperatures in Z2, Z3, and Z4 (at approximately 260 °C, 340 °C and 420 °C), while the characteristic peak in Z5 shifts to 490 °C. These results provide evidence that the Cu content in TNRs affects not only the adsorption capacity of $O_2$ but also the strength and affinity of the adsorption sites to $O_2$. The latter can be critical in CO oxidation, which involves dissociative adsorption of $O_2$ as an elementary step. According to the $O_2$-TPD results, the 7.5Cu-TNR catalyst showed more prominent $O_2$ adsorption capacity and desorption at lower temperatures than the 2.5Cu- and 10Cu-TNR catalysts, as shown in Figure 5.4. These low-temperature-desorption peaks can be assigned to the oxygen species weakly bonded to the catalyst surface [43], which are the source of oxygen atoms for the oxidation reaction [42]. The results presented in Table 5.2 and Figure 5.5 show that the amounts of $O_2$ and CO adsorbed on the Cu-TNR are dependent on the Cu loading and have the same trend in which the 7.5Cu-TNR catalyst gives the highest overall adsorption capacity.

**Table 5.2** Properties and physical characteristics of Cu-TNR catalysts

| Catalyst | CO adsorbed (mmol/g)[a] | $O_2$ adsorbed (mmol/g) [b] | Position of Ti $2p_{3/2}$[c] | Position of Cu $2p_{3/2}$ [c] | Metal composition (wt%)[d] |
|---|---|---|---|---|---|
| **2.5Cu-TNR** | 0.122 | 0.040 | 459 | 933.7 | 2.45 |
| **5Cu-TNR** | 0.215 | 0.053 | 459 | 934.1 | 4.90 |
| **7.5Cu- TNR** | 0.231 | 0.077 | 458.8 | 933.7 | 7.36 |
| **10Cu-TNR** | 0.165 | 0.049 | 459 | 934.1 | 9.87 |
| **12.5Cu- TNR** | 0.099 | 0.047 | 459 | 934.1 | 12.40 |

[a] From CO-TPD; [b] From $O_2$-TPD; [c] From XPS; [d] From ICP-MS

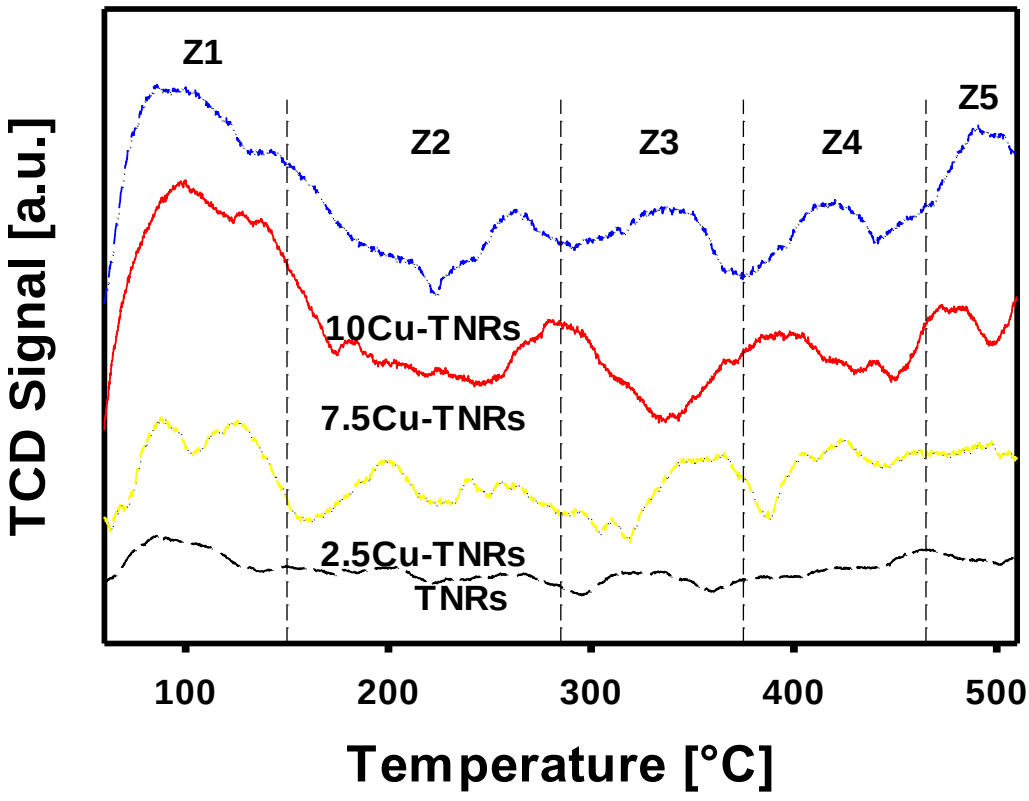


**Figure 5.4.** Temperature-programmed desorption of $O_2$ on TNR and Cu-TNR. Note: red arrows indicate peak shifts with increasing Cu loading in TNR.

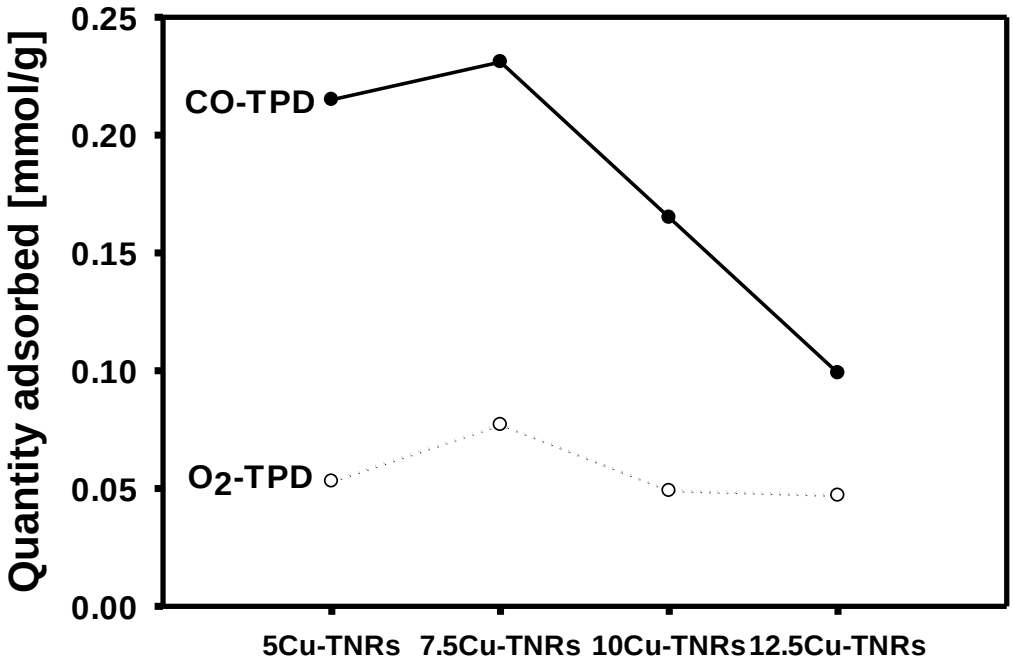


**Figure 5.5.** Comparison between Temperature-programmed desorption of CO and $O_2$ on Cu-TNR.

*5.3.3 Surface reducibility and the metal-support interactions in Cu-TNR*

Metal-support interactions, which determine the interfacial catalytic properties, are intrinsically related to the surface reducibility and were studied by using $H_2$-TPR in this work. As evident from Figure 5.6, low temperature reduction shoulder peaks with onset at ~150 °C are unique only to the Cu-TNR catalysts and are absent from the bulk CuO. These low temperature peaks were ascribed to the reduction of highly dispersed surface Cu similar to the mono- and multilayer species on TNR that are otherwise invisible to the XRD [23, 44]. This is followed by the two larger reduction peaks that correspond to the two-step reduction of CuO to $Cu_2O$ and further to $Cu^0$ [45], which in this case can be ascribed to the reduction of the CuO nanoparticles. It is interesting to note the general shift of the reduction to higher temperature from the smaller CuO (7 nm for 5Cu-TNR) to the larger size (12 nm for 10Cu-TNR) and that to the bulk CuO. This is reflective of the type and strength of interaction of the CuO as a function of particle size as well as with or without the TNR support [46-48].

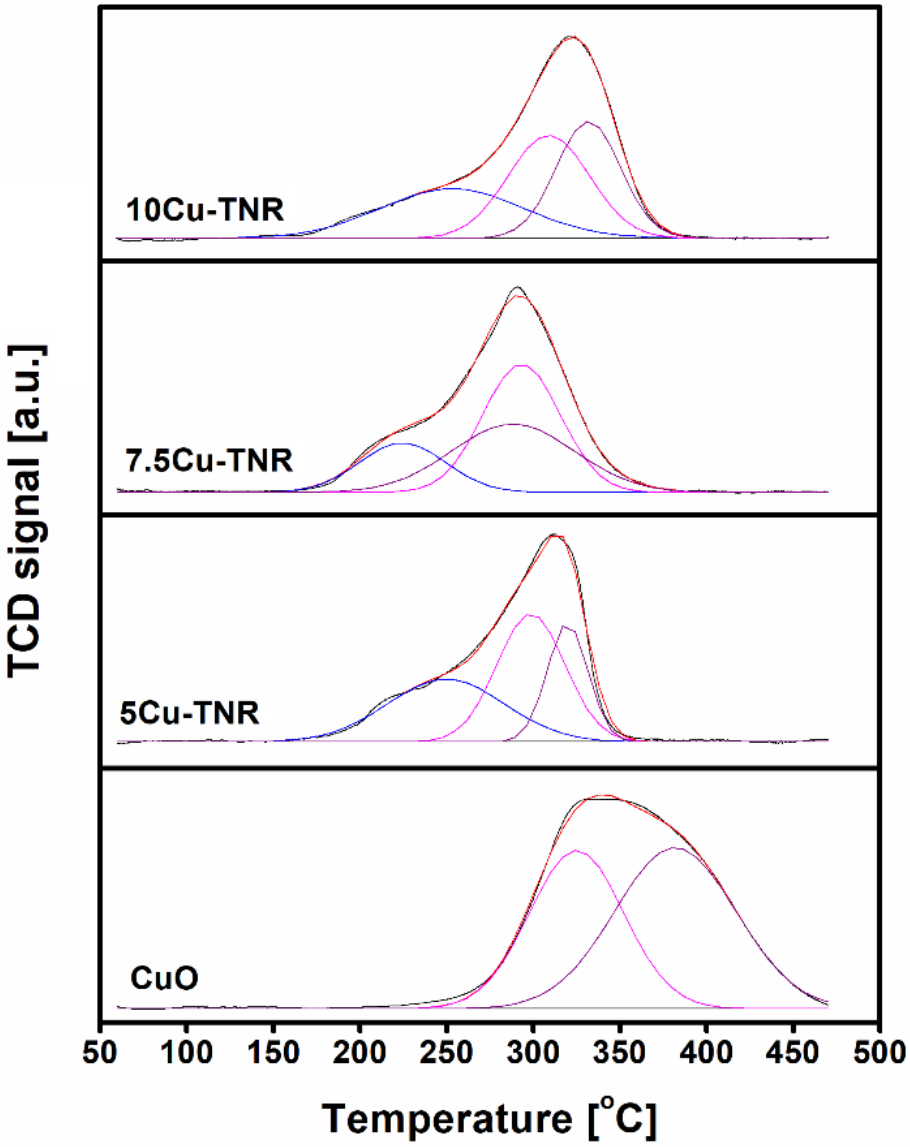


**Figure 5.6.** $H_2$-TPR profiles of reference CuO and Cu-TNR with different Cu loading.

XPS spectroscopy was used to assess the oxidation state and the electronic state of copper and titania in the catalyst based on their binding energies. Cu 2p and Ti 2p XPS spectra are shown in Figure 5.7a and 5.7b, respectively. Deconvolution of the Cu $2p_{3/2}$ peak at the binding energy range of 931 to 936 eV reveals the presence of the $Cu^{2+}$ (934.8 eV) and $Cu^{+}$ (933.0 eV) [49]. Because of the close proximity of the two peaks, direct quantification of the deconvoluted peaks is subjected to large uncertainties. Here, we adopt a more accurate approach of quantifying the shake-up satellite peaks at 940-946 eV that is unique to $Cu^{2+}$ [33]. By taking the calibrated ratio of $A_{Cu2+}$:$A_{satellite}$ = 1.89

based on the CuO standard [33] (reconfirmed with the bulk CuO sample in this study) and recalculate the amount of $Cu^{2+}$ in the Cu $2p_{3/2}$ peak, the $Cu^{2+}$ content was found to be 67, 90, 90, 97 and 97% for 2.5Cu-, 5Cu-, 7.5Cu-, 10Cu- and 12.5Cu-TNR, respectively, the remaining being $Cu^{+}$. The fact that no $Cu_2O$ was detectable by XRD, the results suggest that the $Cu^{+}$ (in coexistence with $Cu^{2+}$) must exist solely as part of the highly dispersed surface species. Nevertheless, the amount of $Cu^{+}$ species is rather minimal especially at high Cu loadings.

Two main peaks near 459 and 465 eV were attributed to Ti $2p_{3/2}$ and Ti $2p_{1/2}$, respectively (Figure 5.7b). These results are in agreement with the previously reported results in which titania peaks were found at approximately 459 and 465 eV [38, 50]. The characteristic peaks were assigned to $Ti^{4+}$ in the titania nanorods. Figure 5.8 shows the XPS O1s spectra of the copper-deposited TNR-supported catalysts. All the catalysts showed one distinct peak at approximately 530 eV and a small shoulder at approximately 535 eV. The first peak is an indication of the lattice oxygen in Ti-O bonds, while the small shoulder results from the weakly bonded (physisorbed) oxygen species [51-53]. These results corroborate the finding of the $O_2$-TPD study (Figure 5.4) that there are different oxygen species present in the Cu-TNR. In addition, the XPS results in conjunction with $H_2$-TPR and XRD, confirm the presence of highly dispersed Cu species and CuO nanoparticles (the latter increase in size with increasing Cu loadings due to weaker surface interactions).

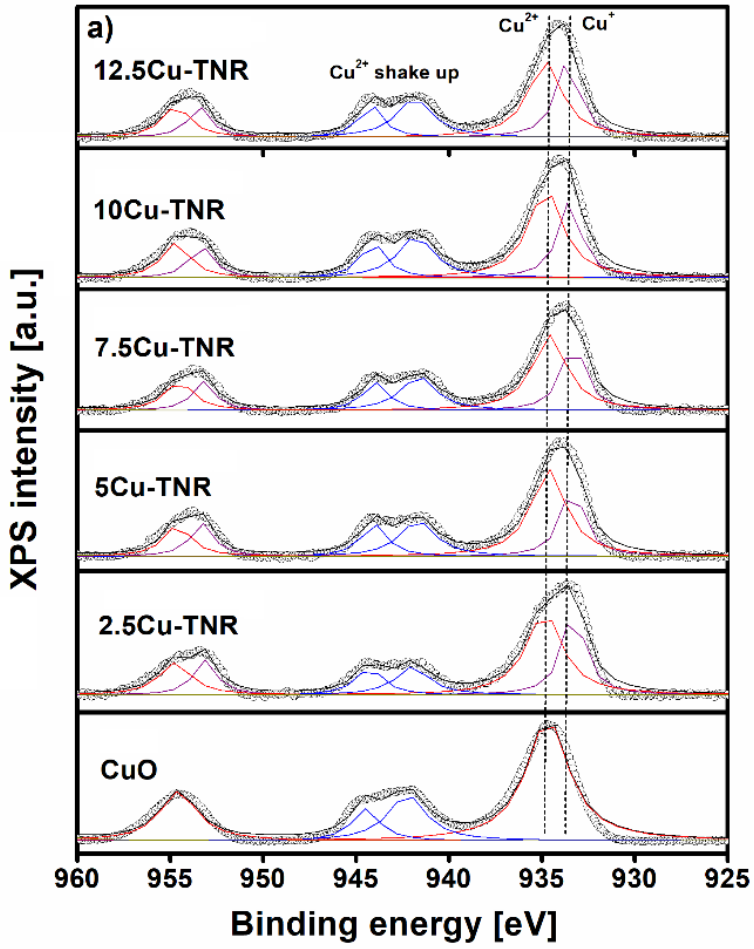
a)
12.5Cu-TNR
Cu2+ shake up
Cu2+
Cu+
10Cu-TNR
7.5Cu-TNR
5Cu-TNR
2.5Cu-TNR
CuO
XPS intensity [a.u.]
960
955
950
945
940
935
930
925
Binding energy [eV]

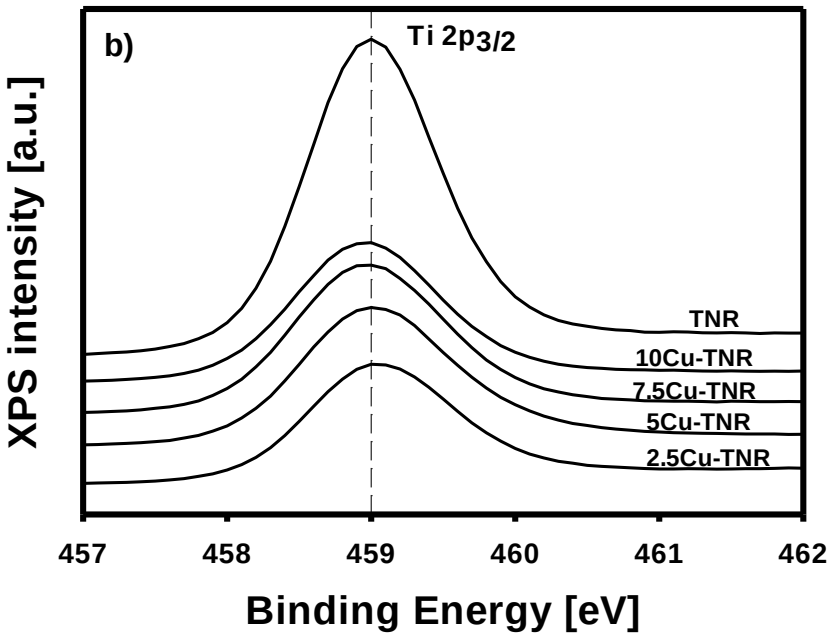


**Figure 5.7.** XPS spectra of (a) Cu 2p and (b) Ti 2p in Cu-TNR.

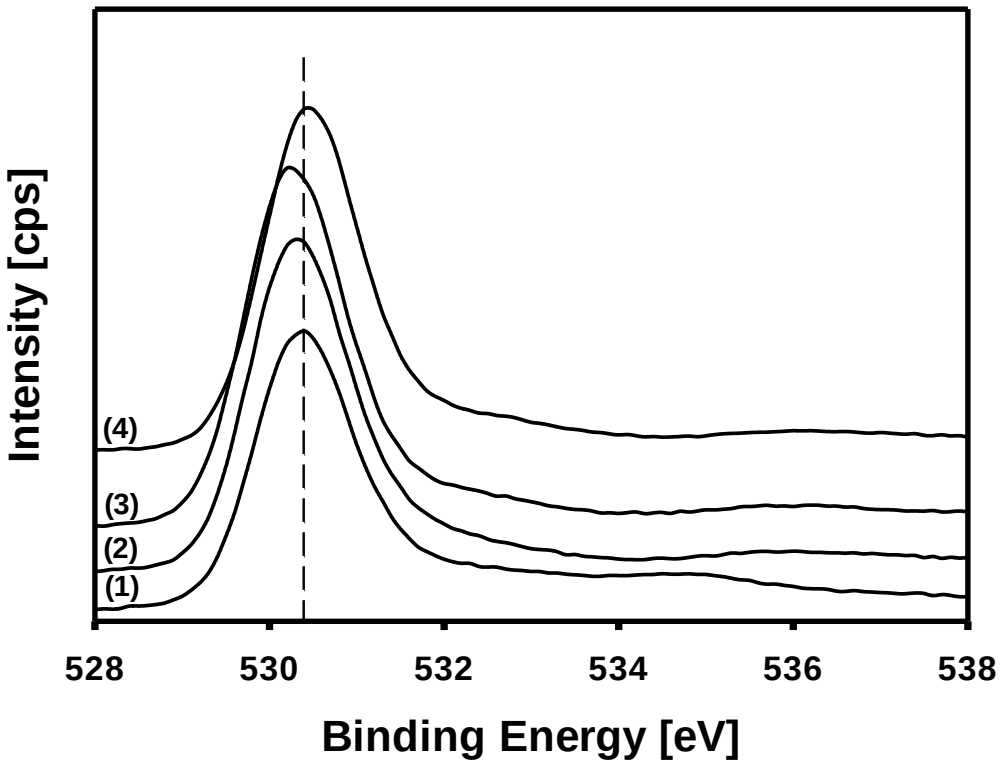


**Figure 5.8.** XPS O1s spectra of Cu-TNR: (1) 2.5Cu-TNR, (2) 5Cu-TNR, (3) 7.5Cu-TNR, (4) 10Cu-TNR.

*5.3.4 CO oxidation by Cu-TNR*

The catalytic properties of Cu-TNRs with different Cu loadings and metal-support interfaces were investigated in CO oxidation over a temperature range of 100-250 °C under atmospheric pressure (Figure 5.9). The activity profiles demonstrate the catalytic performance of unsupported and supported copper-based catalysts. CO conversion versus temperature results indicate that an increase in copper content from 2.5 to 12.5 wt% resulted in an increase in CO conversion (except an optimum with 7.5 wt% of Cu loading). For instance, at 218 ℃, CO conversions of 60, 70, 79, 57 and 39% were observed for 2.5Cu-, 5Cu-, 7.5Cu-, 10Cu- and 12.5Cu-TNR, respectively. The activity results are compared with the reported literature in Table S2 in ESM. The 2.5Cu-TNR catalyst gives a rate of $CO_2$ production per unit surface area (85.3 $\mu mol_{CO}/s.\ mol_{Cu}$) approximately eight times higher than those of the other supported Cu catalysts that involve cocatalysts or promoters, such as 5CuO-5Ce-95Ti-500 [20], $Cu_{0.08}Mn_{0.02}Zr_{0.1}Ce_{0.8}O_2$ [54] and $Cu_{70}Ti_{30}$/M-diatomite-400 [55] at 200 °C (Table 5.3).

**Table 5.3** Comparison of CO oxidations using various catalysts at 200°C.

| **Catalyst** | **CO conversion (%)** | **Rate ($\mu mol_{CO}/s.mol_{Cu}$)** | **Reference** |
|---|---|---|---|
| **5CuO-5Ce-95Ti-500** | 40 | 8.93 | [20] |
| **10CuO-5Ce-95Ti-500** | 100 | 11.1 | [20] |
| **$Cu_{0.08}Mn_{0.02}Zr_{0.1}Ce_{0.8}O_2$** | 28.5 | 5.53 | [63] |
| **$Cu_{0.1}Mn_0Zr_{0.1}Ce_{0.8}O_2$** | 30 | 4.46 | [63] |
| **$Cu_{70}Ti_{30}$/M-diatomite-400** | 95 | 6.31 | [64] |
| **$Cu_{70}Ti_{30}$/M-diatomite-500** | 90 | 5.98 | [64] |
| **2.5Cu-TNR** | 43 | 85.3 | This study |
| **5Cu-TNR** | 46 | 45.6 | This study |
| **7.5Cu-TNR** | 54 | 35.7 | This study |
| **10Cu-TNR** | 40 | 15.8 | This study |

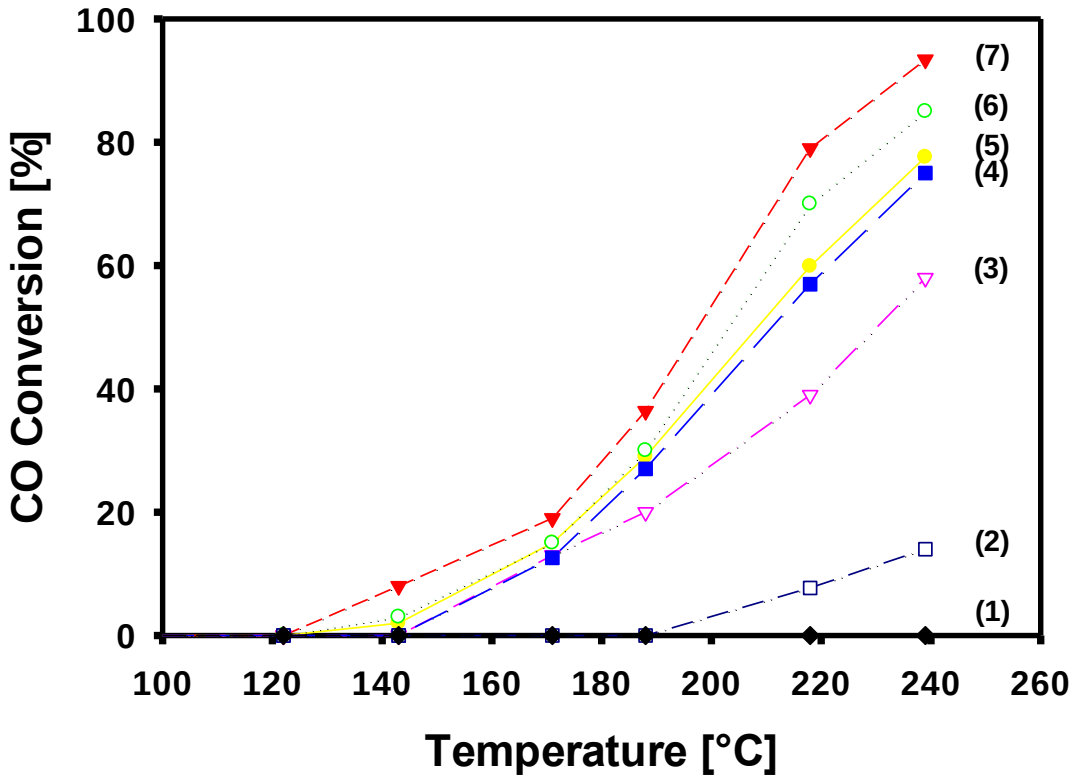


**Figure 5.9.** CO conversions at different reaction temperatures by (1) TNRs & 7.5Cu-TNR-PM, (2) CuO, (3) 12.5Cu-TNR, (4) 10Cu-TNR, (5) 2.5Cu-TNR, (6) 5Cu-TNR and (7) 7.5Cu-TNR. (Conditions: 30 mg of catalyst, a reaction mixture of 1% CO, 10% $O_2$ balanced with argon, GHSV of 40,000 ml/h.gcat)

The pure unsupported copper oxide (prepared by co-precipitating the copper precursor) and bare TNR were used as control experiments in the tested temperature range, i.e., 100-250 °C. There was no activity observed from the pure copper oxide and the bare TNR support, suggesting the importance of the metal-support interaction and the presence of active interfacial species for catalytic enhancement. To further confirm the role of interface during the reaction, 7.5 wt% CuO was physically mixed with TNRs (referred as 7.5Cu-TNR-PM) and tested for CO oxidation under the previously described reaction conditions. Interestingly, no CO conversion (shown as sample 1 in conjunction with bare support in Figure 5.9) was found for the physical mixture, which validated the hypothesis that the interfacial active sites are mainly responsible for the catalytic activity.

Since no activity was observed on the bare support, it is interpreted that the amount of CO adsorbed on the support surface played no role during the reaction, i.e., CO desorbed without interacting with the oxygen in air, and hence no $CO_2$ was produced.

This means that the surface sites associated with the low-temperature CO adsorption peak, observed in all copper-deposited catalysts (as shown in Figure 5.3), are catalytically inactive at temperatures below 145 °C. However, the interfacial active sites resulting from the metal-support interface catalyze CO oxidation significantly once an onset temperature of 145 °C is reached (Figure 5.9). In an oxygen-rich reaction environment, it is clear that the surface-chemisorbed CO produces $CO_2$ at a temperature below the higher-temperature desorption peak (i.e., 300 °C), as depicted in the previous CO-TPD results. It can be inferred that copper interactions with the titania nanorods offer an interface that converts the chemisorbed CO into $CO_2$, which was desorbed as CO in a nonoxidizing environment. This finding was further confirmed by the same reaction conditions with CO only (not shown here), and no $CO_2$ formation was observed over all catalysts. Similarly, the results of $O_2$-TPD, as shown in Figure 5.4, demonstrated that copper interactions with TNR strongly affected the oxygen adsorption capacity and thus the catalytic activity. The quantitative results in Table S1 in ESM indicate that both the $O_2$-TPD and CO-TPD results follow the same trend. The oxygen adsorption capacity was also confirmed using XPS, and the results of the O1s analysis (Figure S2 in ESM) are in agreement with those of $O_2$-TPD (Figure 5.4).

Since the amount of CO chemisorption is a measure of the interfacial active sites [56-58], the negligible amount of chemisorbed CO on the bare support (not shown here) indicates that the TNR support alone is catalytically inert to CO oxidation under the tested conditions (consistent with Figure 5.9). The CO chemisorption results (Table 5.1) indicate a strong positive dependency of the amount of chemisorbed CO on the metal content and that the maximum amount of chemisorbed CO was observed in the 7.5Cu-TNR catalyst. The interfacial active sites also facilitate $O_2$ activation, which in turn enhances catalytic activity [58].

The surface and bulk Cu species and the extent of copper interaction with the support significantly influence the CO conversion activity. The $H_2$-TPR results of the 5, 7.5 and 10Cu-TNR catalysts (as shown in Figure 5.6) indicate the presence of both highly dispersed and CuO nanoparticle species, but the number of copper species present in the bulk varied significantly among for all catalysts. The degree of reduction (defined as the ratio of hydrogen consumed in TPR to the theoretical amount of hydrogen required to completely reduce the catalyst) for all the catalysts is less than 100%. The copper species can be assumed to interact with the support in two ways, as shown in

Figure 5.10: a) well-dispersed copper species weakly interacting with the support, forming mono- and multilayer on the support surface; and b) bulk copper species forming larger copper particles and strongly interacting with the support [59-63]. At low loadings of up to 7.5 wt%, the copper species are mainly present in the form of highly dispersed Cu on the surface with small fraction of fine CuO nanoparticles, while at higher metal loadings, the copper species tend to sinter to form large nanoparticles on the surface. The extent of the metal-support interaction, surface and binding energies and transfer of electrons between the copper and titania nanorods collectively form an interface exhibiting relatively high catalytic activity for the 7.5Cu-TNR catalyst. This interpretation is supported by the $H_2$-TPR results. It can be concluded that the extent of metal-support interactions favouring a greater amount of well-dispersed $Cu^{2+}$ species layers on the interface is one of the main contributors to the excellent performance of the 7.5Cu-TNR catalyst, as shown in Figure 5.9.

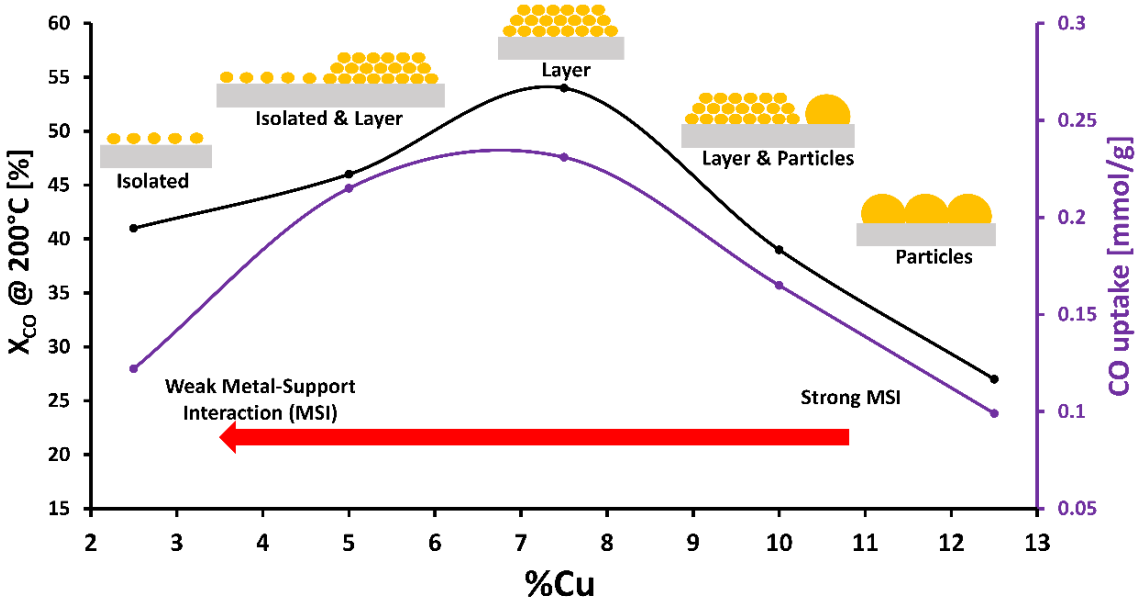


**Figure 5.10.** The schematic representation of the effect of variation in CO uptake and metal-support interaction on the CO oxidation activity of Cu-TNR catalysts.

The Arrhenius plots (Figure 5.11) indicate that the 7.5Cu-TNR catalyst has the lowest activation energy (44.7 kJ/mol) for CO oxidation compared to other Cu-TNRs. In comparison, the unsupported copper nanoparticles have an activation energy of 74.1 kJ/mol, indicating that the doping of copper over titania nanorods reduces the energy barrier. The elementary steps, especially the adsorption of reactants over the catalyst surface, define the reaction mechanism and, more importantly, the rate-determining step.

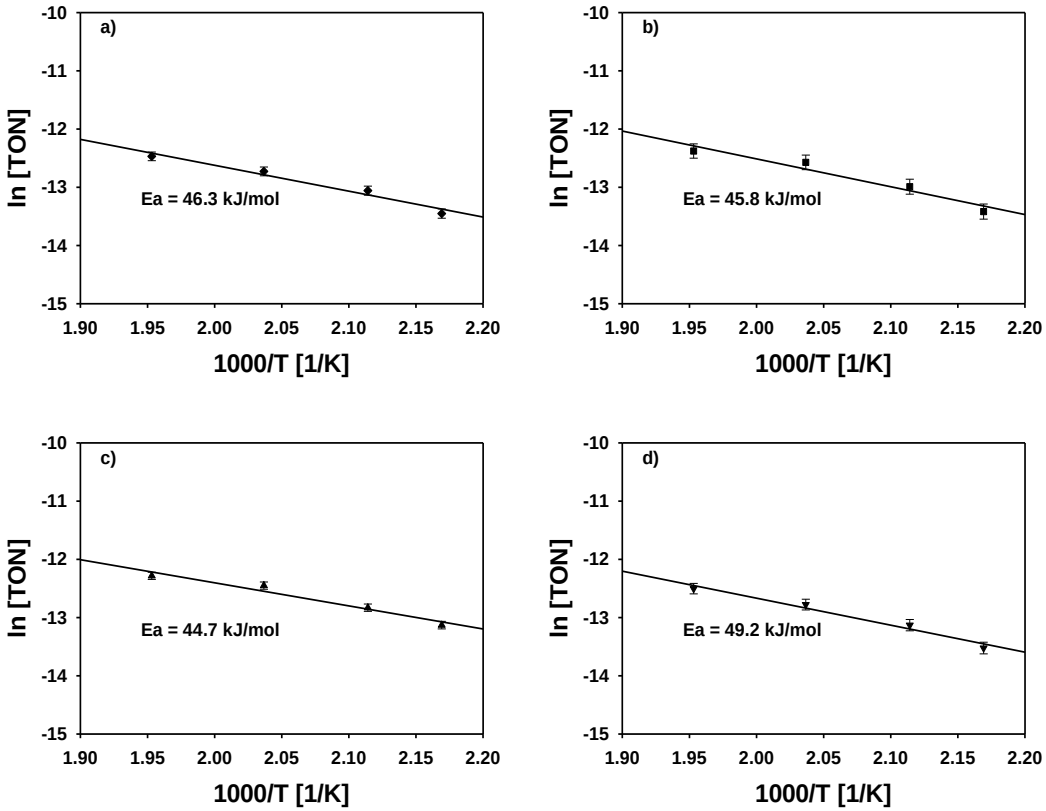


**Figure 5.11.** Arrhenius plot of CO oxidation using Cu-TNR: (a) 2.5Cu-TNR, (b) 5Cu-TNR, (c) 7.5Cu-TNR, (d) 12.5Cu-TNR.

It is generally considered that copper oxides follow the Mars-Van Krevelen (MVK) redox mechanism [60], in which CO reacts with surface lattice oxygen to produce $CO_2$, leaving behind an oxygen vacancy on the copper oxide surface. The oxygen in the gas fills out the vacancy, and this is a spontaneous reaction. The release of lattice oxygen from the copper oxide surface is the rate-determining step that provides the required oxygen for the product. The following reactions are considered [60];

$$O_2 + * \rightarrow 2O_{SL} \quad (4)$$

$$CO + O_{SL} \rightarrow CO_2 + * \quad (5)$$

where $O_{SL}$ represents surface lattice oxygen and $*$ is surface oxygen vacancy on the metal oxide surface. Metal doping on the support changes surface terrace, and thus, reactants over the new surface or metal-support interface exhibit diverse performance. Generally, for supported copper catalysts, the Langmuir-Hinshelwood (LH) mechanism is accepted, in which CO chemisorbs on the active metal site or metal-support interface,

oxygen adsorbs on the support and the adsorbed gases react to desorb $CO_2$ as the product as described in the following proposed reactions [61];

$$CO + S \rightarrow CO - S \quad (6)$$

$$O_2 + S \rightarrow O_2 - S \quad (7)$$

$$O_2 - S \rightarrow 2O - S \quad (8)$$

$$CO - S + O - S \rightarrow CO_2 + 2S \quad (9)$$

where S represents the adsorption site on the catalyst surface. In Cu-TNR catalysts, the interfacial active sites are given by the intimate contact of copper and titania nanorods, which offers adequate strength for CO and $O_2$ adsorption (in which a dissociative adsorption of $O_2$ occurs) to form $CO_2$. The $H_2$-TPR and XPS results show that $Cu^{2+}$ interacted with the titania nanorods and that the extent of the reaction varied over the range of metal contents. Consequently, it is suggested that the LH mechanism is predominant in the Cu-TNR catalysts.

The long-term stability of the best performing catalyst (7.5Cu-TNR) was evaluated at 200 ℃. Figure 5.12 shows that the catalyst exhibited a stable CO conversion over 48 h time-on-stream. This result indicates that the catalyst has potential to be used as an efficient and highly stable catalyst for medium temperature CO oxidation. The used catalysts were also characterized by XRD (Figure 5.13) after the reaction to identify any possible change in the crystalline structure. Apart from the typical anatase, rutile and titanate diffraction peaks as found in as-synthesized catalysts, an additional peak appeared at approximately 2-Theta of 35.5° can be assigned to CuO, which is associated with the sintering of copper oxide nanoparticles during the reaction. Nevertheless, the long-term activity observed for the 7.5Cu-TNR catalyst (Figure 5.12) suggests that the catalyst remained catalytically active overall despite of minor sintering.

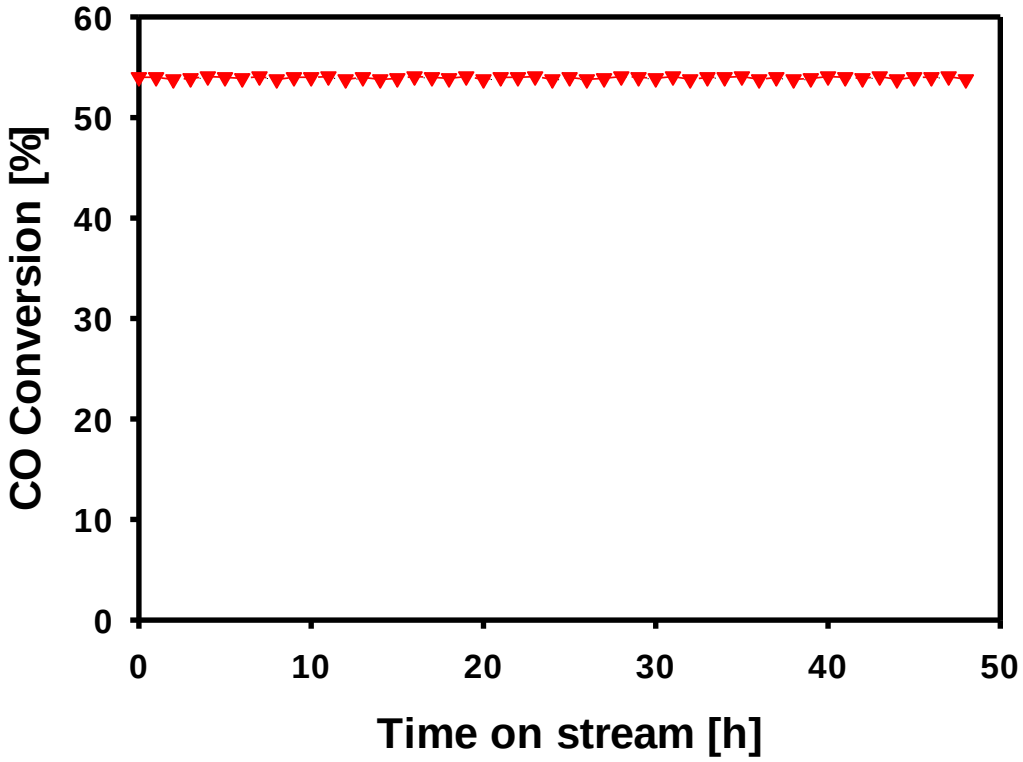


**Figure 5.12.** Long-term CO conversion achieved at 200 °C by 7.5Cu-TNR. (Conditions: 30 mg of catalyst, a reaction mixture of 1% CO, 10% $O_2$ balanced with argon, GHSV of 40,000 ml/h.gcat)

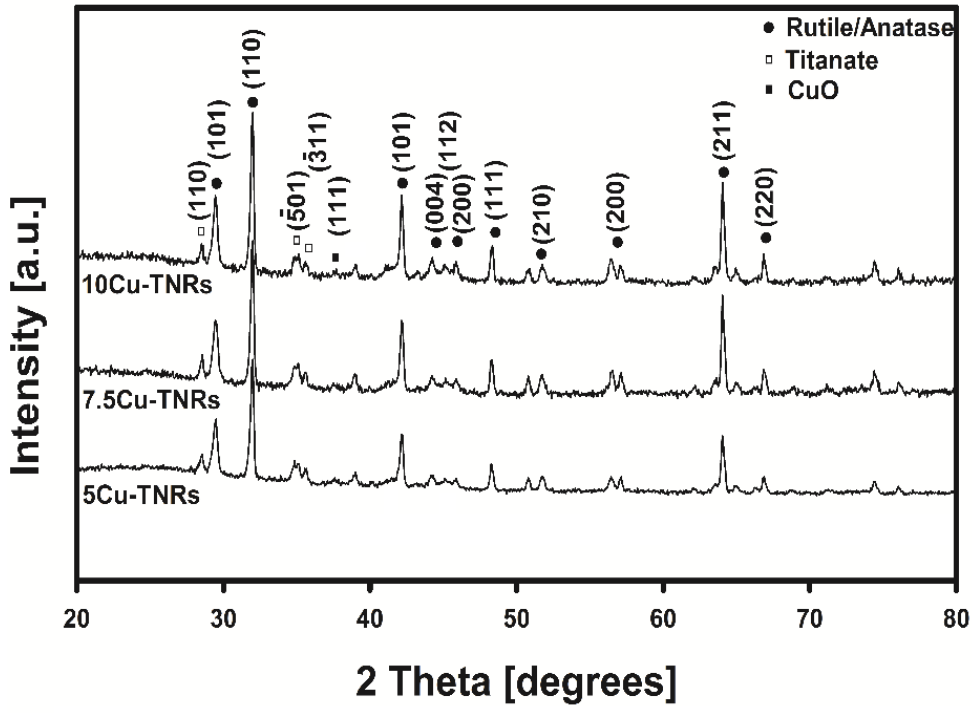


**Figure 5.13.** XRD patterns of Cu-TNRs after CO oxidation.

*5.3.5 Effect of different oxide supports*

The oxide support plays a pivotal role in controlling the interaction between metal and support, which in turn influences the catalytic performance. Therefore, various supports were investigated to exploit their role during CO oxidation. The optimal metal content, *i.e.*, 7.5 wt%, based on the catalytic performance over titania nanorods was selected for copper-based catalysts synthesis over $TiO_2$-P25, $Al_2O_3$ and $SiO_2$ support using deposition precipitation. The catalytic activities at 200°C presented diverse performance over various supports in terms of the rate of CO converted per unit copper oxide surface area per unit time (Figure 5.14).

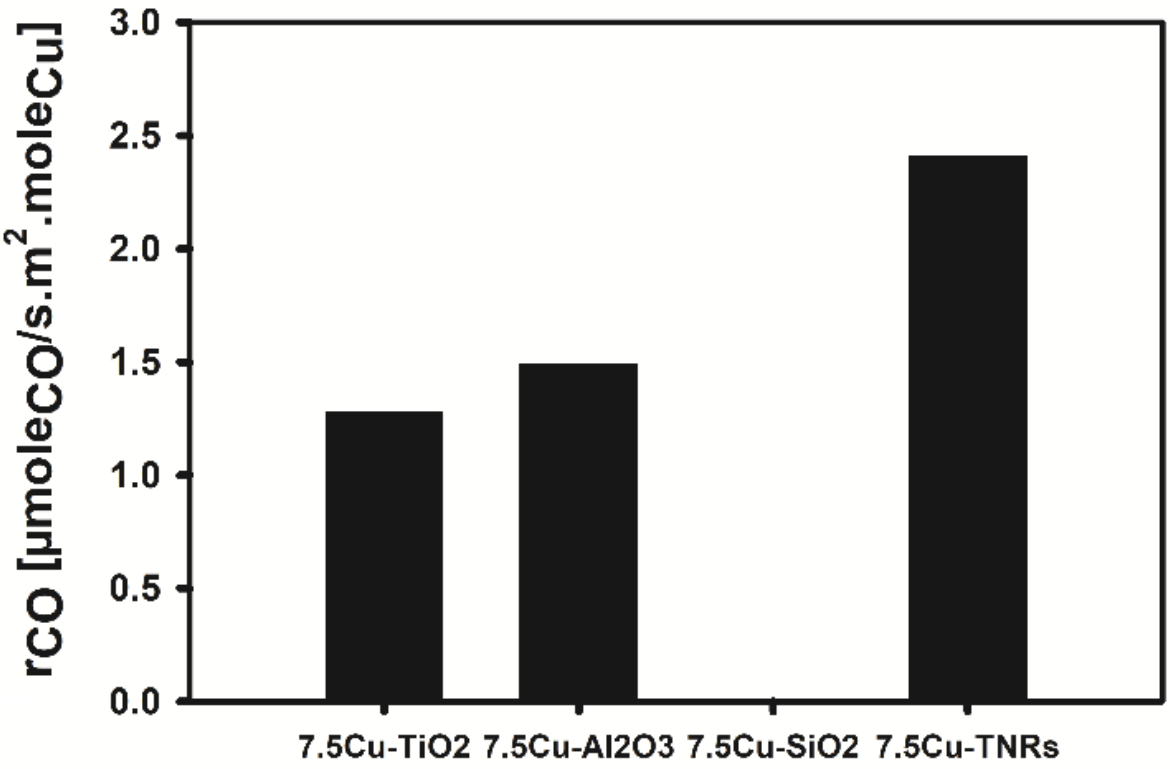


**Figure 5.14.** Measured rate of CO oxidation over different oxide-supported Cu catalysts. (Conditions: 30 mg of catalyst, a reaction mixture of 1% CO, 10% $O_2$ balanced with argon, GHSV of 40,000 mL/h.$g_{cat}$, 200°C)

While the silica-based catalyst exhibited no activity at all tested reaction temperatures, 7.5 wt% of Cu supported on alumina and $TiO_2$-P25 gave a relatively low activity compared to the TNR-based catalyst. For instance, 7.5Cu-TNR catalyst gave a CO

conversion rate of 2.41 ($\mu mol_{CO}/s.\ m^2.\ mol_{Cu}$) which is approximately twofold of 7.5Cu-$TiO_2$ (1.28 $\mu mol_{CO}/s.\ mol_{Cu}$).

The interaction between CO and the surface, characterized by the measurement of active sites *via* CO-TPD (Figure 5.15) elucidates how copper interactions with various oxide supports influence CO active sites. The alumina-supported copper catalyst showed two peaks: the first peak in the temperature range of 60-210°C, and the second peak (apparently incomplete) from 250 to 460°C. More CO was adsorbed over the alumina-supported catalyst, but the peak maxima were shifted to higher temperatures. A similar trend was observed over the $TiO_2$-P25-supported catalyst, of which the first broad peak starts at 60 and ends at 250°C, while a shoulder was observed at approximately 285°C. Clearly, more CO was adsorbed over alumina- and $TiO_2$-P25-supported catalysts, but to evaluate the number of active sites among all various supported catalysts, CO chemisorption was conducted, and the results in Table 5.4 imply that the catalyst supported on $TiO_2$-P25 possessed more sites for CO adsorption. The catalytic activity results in terms of CO converted per unit surface area show that the copper-deposited catalysts supported on TNR converted more CO per unit surface area than did the other supported catalysts. This performance can be ascribed to the presence of different types of interfaces and/or metal-support interactions among the various supported catalysts.

**Table 5.4** CO chemisorption and $H_2$ consumption of TNR- and $TiO_2$-and $Al_2O_3$-supported Cu catalysts.

| Catalyst | CO uptake ($cm^3/g$)[a] | Total $H_2$ consumption (mmol/g)[b] | Degree of reduction (%)[c] |
|---|---|---|---|
| **7.5Cu-TNR** | 1.04 | 1.13 | 95.5 |
| **7.5Cu-$TiO_2$** | 1.87 | 0.86 | 72.8 |
| **7.5Cu-$Al_2O_3$** | 0.54 | 0.64 | 54.3 |

[a] Measured from CO chemisorption; [b] Measured from $H_2$-TPR; [c] The ratio of $H_2$ consumed in TPR to theoretical $H_2$ required to reduce the catalyst.

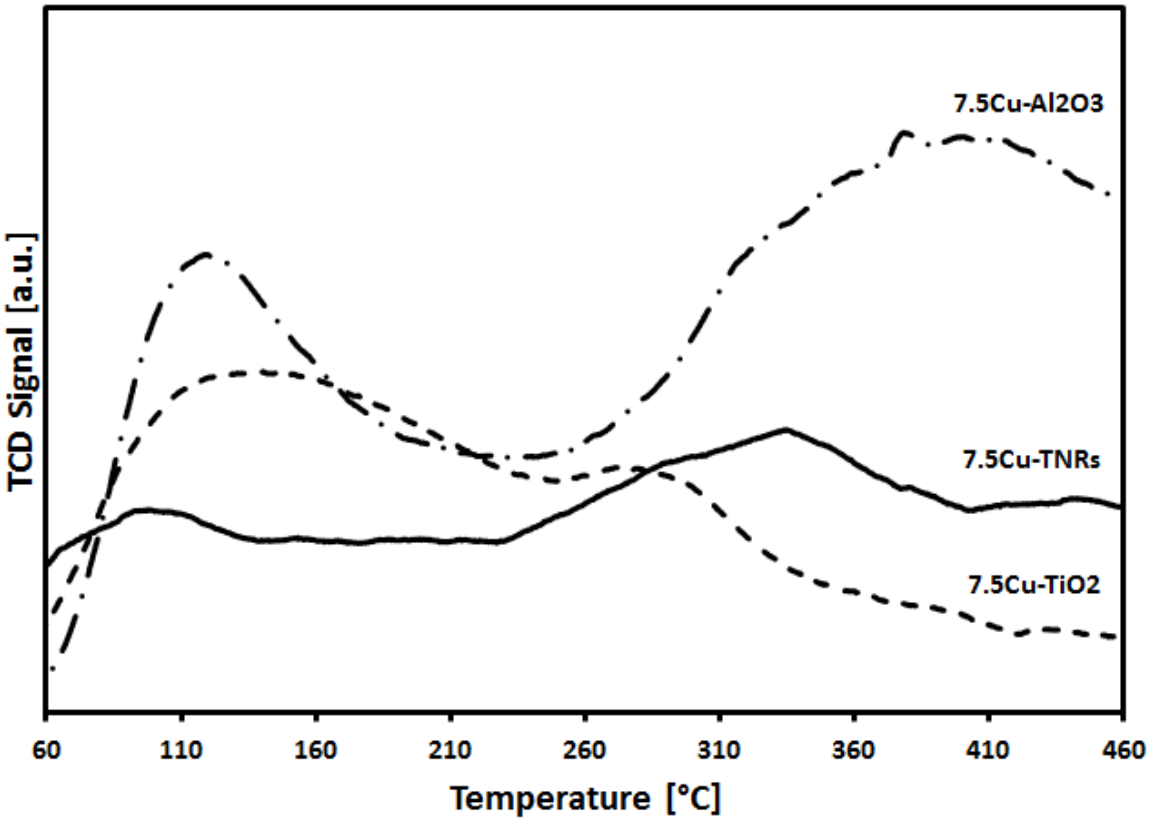


**Figure 5.15.** Temperature-programmed desorption of CO on different oxide-supported Cu catalysts.

The metal-support interactions were explored using $H_2$-TPR, and the results in Figure 5.16 clearly show that the extent of interaction varied for all supported catalysts. Since 7.5Cu-TNR catalyst has more reducible species than other catalysts, the TPR peak shifted to a lower temperature for the 7.5Cu-$TiO_2$ catalyst, exhibiting weaker interactions than other catalysts. The lower degree of reduction over the 7.5Cu-$Al_2O_3$ catalyst showed a strong metal-support interaction and the presence of $Cu^{2+}$ species is mainly in the bulk, *i.e.*, not available for hydrogen consumption. The nature of the interfacial interactions between the metal and the support determines the catalytic activity of the TNR-supported catalysts.

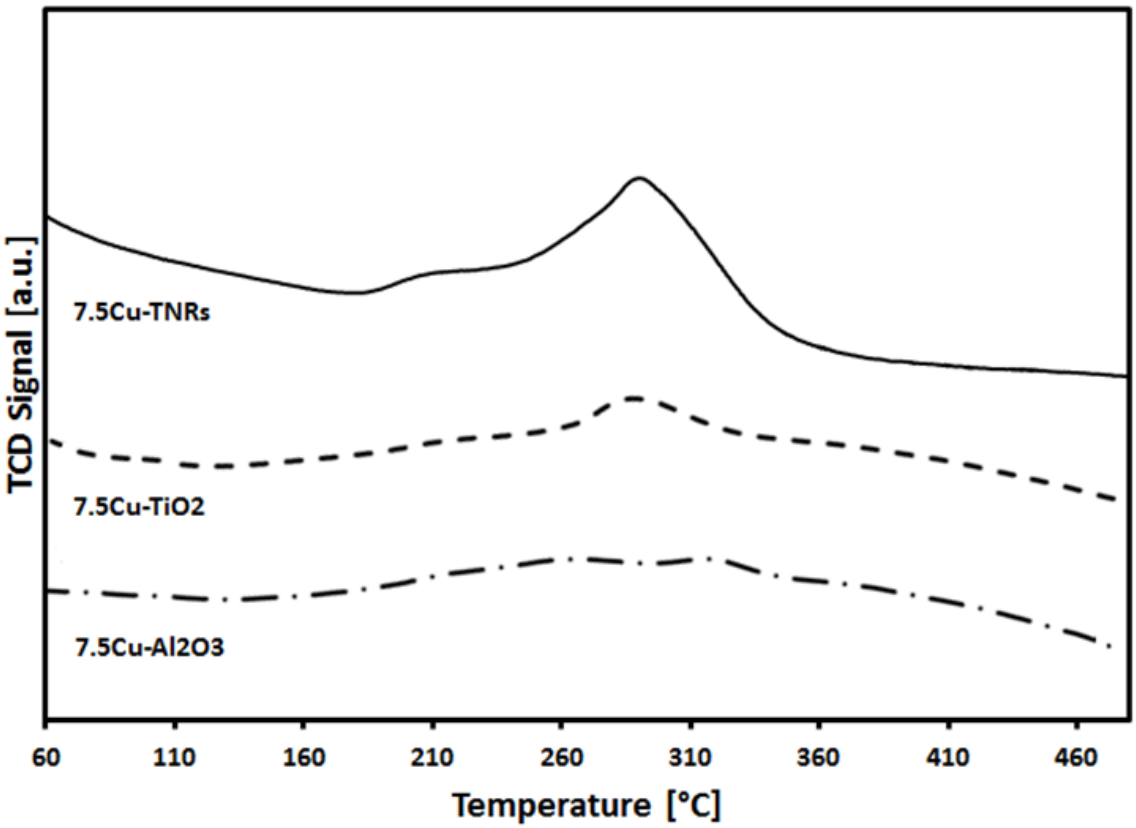


**Figure 5.16.** Temperature-programmed reduction of different oxide-supported Cu catalysts.

The apparent activation energies derived from the kinetic data for various copper-deposited catalysts (Figure 5.17) show an order of 7.5Cu-$TiO_2$ > 7.5Cu-TNR > 7.5Cu-$Al_2O_3$, indicating the nature of interfacial active sites over each supported catalyst is different. The results of the reduction profiles, activity and activation energy highlight that a suitable metal-support interaction generates interfacial sites that play a major role in controlling the activity of the resulting catalyst.

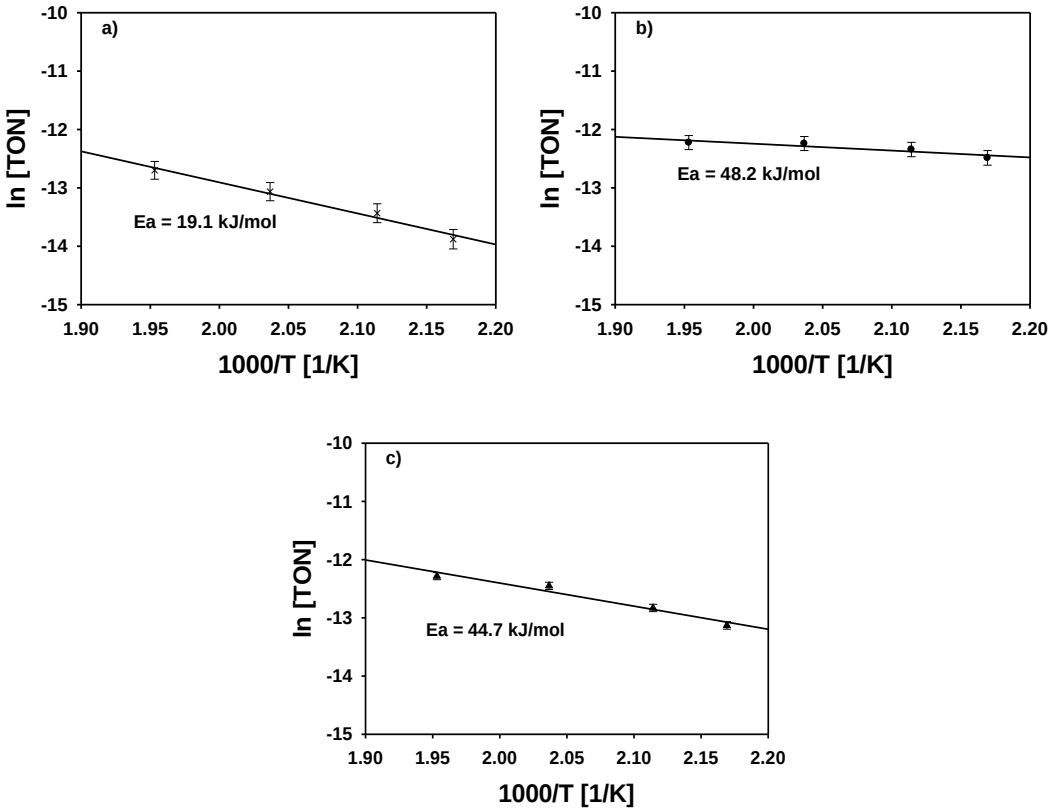


**Figure 5.17.** Arrhenius plot of CO oxidation over different oxide-supported Cu catalysts: (a) 7.5Cu-Ti, (b) 7.5Cu-Al, (c) 7.5Cu-TNR.

## 5.4 Conclusions

The catalytic consequences of the interface between copper and titania nanorods (TNRs), the degree of copper dispersion, the CO adsorption capacity and the surface/lattice oxygen sites were studied. The H2-TPR confirmed the intimate interaction between copper and TNR and thus the formation of copper-TNR interfacial active sites, as evidenced by CO chemisorption. The catalytic performance and rate of the reaction indicated that a Cu loading of 7.5 wt% on TNRs (7.5Cu-TNR) resulted in an optimum metal-support interaction, leading to interfacial active sites that are most favorable for medium-temperature CO oxidation. The reaction was found to follow the Langmuir-Hinshelwood mechanism, and a low activation energy of 44.7 kJ/mol was calculated for the 7.5Cu-TNR catalyst. The effect of various support oxides, such as titania nanoparticles ($TiO_2$-P25), alumina and silica, showed the improved performance of 7.5Cu-TNR based on the number of moles of $CO_2$ produced per mole of copper per unit surface area. The results showed that the nature of the interface resulting from copper interaction with each support played a pivotal role in the final catalytic

performance. As such, this study provides insight into advanced catalyst design that relies on the catalyst support structure and morphology, particularly for improved CO oxidation.

## References


[1] Lykaki, M.; Pachatouridou, E.; Carabineiro, S. A. C.; Iliopoulou, E.; Andriopoulou, C.; Kallithrakas-Kontos, N.; Boghosian, S.; Konsolakis, M. Ceria nanoparticles shape effects on the structural defects and surface chemistry: Implications in co oxidation by $Cu/CeO_2$ catalysts. Appl. Catal. B-Environ. 2018, 230, 18–28.

[2] Bratan, V.; Munteanu, C.; Hornoiu, C.; Vasile, A.; Papa, F.; State, R.; Preda, S.; Culita, D.; Ionescu, N. I. CO oxidation over Pd supported catalysts -in situ study of the electric and catalytic properties. Appl. Catal. B-Environ. 2017, 207, 166–173.

[3] Harzandi, A. M.; Tiwari, J. N.; Lee, H. S.; Jeon, H.; Cho, W. J.; Lee, G.; Baik, J.; Kwak, J. H.; Kim, K. S. Efficient co oxidation by 50-facet $Cu_2O$ nanocrystals coated with CuO nanoparticles. ACS Appl. Mater. Inter. 2017, 9, 2495–2499.

[4] Setvin, M.; Buchholz, M.; Hou, W. Y.; Zhang, C.; Stoger, B.; Hulva, J.; Simschitz, T.; Shi, X.; Pavelec, J.; Parkinson, G. S.; Xu, M.; Wang, Y.; Schmid, M.; Wöll, C.; Selloni, A.; Diebold, U. A multitechnique study of CO adsorption on the $TiO_2$ anatase (101) surface. J. Phys. Chem. C 2015, 119, 21044–21052.

[5] Hossain, S. T.; Almesned, Y.; Zhang, K. F.; Zell, E. T.; Bernard, D. T.; Balaz, S.; Wang, R. G. Support structure effect on co oxidation: A comparative study on $SiO_2$ nanospheres and $CeO_2$ nanorods supported $CuO_x$ catalysts. Appl. Surf. Sci. 2018, 428, 598–608.

[6] L. Baharudin, A. C. K. Y., V.B. Golovko, M.I.J. Polson, M.J. Watson CO temperature-programmed desorption of a hexameric copper hydride nanocluster catalyst supported on functionalized MWCNTs for active site characterization in a low-temperature water–gas shift reaction. Chem. Eng. J., in press, https://doi.org/10.1016/j.cej.2018.10.215.

[7] Li, D.; Chen, S. L.; You, R.; Liu, Y. X.; Yang, M.; Cao, T.; Qian, K.; Zhang, Z. H.; Tian, J.; Huang, W. X. Titania-morphology-dependent dual-perimeter-sites catalysis by $Au/TiO_2$ catalysts in low-temperature CO oxidation. J. Catal. 2018, 368, 163–171.

[8] Grunwaldt, J. D.; Baiker, A. Gold/titania interfaces and their role in carbon monoxide oxidation. J. Phys. Chem. B 1999, 103, 1002–1012.

[9] Wang, Y.; Widmann, D.; Heenemann, M.; Diemant, T.; Biskupek, J.; Schlogl, R.; Behm, R. J. The role of electronic metal-support interactions and its temperature dependence: CO adsorption and CO oxidation on $Au/TiO_2$ catalysts in the presence of $TiO_2$ bulk defects. J. Catal. 2017, 354, 46–60.

[10] Li, L. Y.; Han, W. L.; Dong, F.; Zong, L. Y.; Tang, Z. C.; Zhang, J. Y. Controlled pore size of ordered mesoporous $Al_2O_3$-supported Mn/Cu catalysts for CO oxidation. Micropor. Mesopor. Mat. 2017, 249, 1–9.

[11] Peng, S.; Lee, Y. M.; Wang, C.; Yin, H. F.; Dai, S.; Sun, S. H. A facile synthesis of monodisperse Au nanoparticles and their catalysis of CO oxidation. Nano Res. 2008, 1, 229–234.

[12] Long, B.; Tang, Y.; Li, J. New mechanistic pathways for CO oxidation catalyzed by single-atom catalysts: Supported and doped $Au_1/ThO_2$. Nano Res. 2016, 9, 3868–3880.

[13] Li, Q. L.; Xie, W.; Chen, G. Q.; Li, Y. F.; Huang, Y. J.; Chen, X. D. The behaviors of ultra-low-gold-loaded catalysts ($Au/CeO_2$) for CO oxidation in the presence of water on the catalysts. Nano Res. 2015, 8, 3075–3084.

[14] Jin, M. S.; Liu, H. Y.; Zhang, H.; Xie, Z. X.; Liu, J. Y.; Xia, Y. N. Synthesis of Pd nanocrystals enclosed by {100} facets and with sizes < 10 nm for application in CO oxidation. Nano Res. 2011, 4, 83–91.

[15] Peterson, E. J.; Delariva, A. T.; Lin, S.; Johnson, R. S.; Guo, H.; Miller, J. T.; Kwak, J. H.; Peden, C. H. F.; Kiefer, B.; Allard, L. F.; Ribeiro, F. H.; datye, A. K. Low-temperature carbon monoxide oxidation catalysed by regenerable atomically dispersed palladium on alumina. Nat. Commun. 2014, 5.

[16] Wang, K.; Cao, Y. L.; Hu, J. D.; Li, Y. Z.; Xie, J.; Jia, D. Z. Solvent-free chemical approach to synthesize various morphological $Co_3O_4$ for CO oxidation. ACS Appl. Mater. Inter. 2017, 9, 16128–16137.

[17] Najafishirtari, S.; Kokumai, T. M.; Marras, S.; Destro, P.; Prato, M.; Scarpellini, A.; Brescia, R.; Lak, A.; Pellegrino, T.; Zanchet, D.; Manna, L.; Colombo, M. Dumbbell-like $Au_{0.5}Cu_{0.5}@Fe_3O_4$ nanocrystals: Synthesis, characterization, and catalytic activity in co oxidation. ACS Appl. Mater. Inter. 2016, 8, 28624–28632.

[18] Zhu, B. L.; Zhang, X. X.; Wang, S. R.; Zhang, S. M.; Wu, S. H.; Huang, W. P. Synthesis and catalytic performance of $TiO_2$ nanotubes-supported copper oxide for low-temperature CO oxidation. Micropor. Mesopor. Mat. 2007, 102, 333–336.

[19] Camposeco, R.; Castillo, S.; Mejia, I.; Mugica, V.; Carrera, R.; Montoya, A.; Moran-Pineda, M.; Navarrete, J.; Gomez, R. Active $TiO_2$ nanotubes for CO oxidation at low temperature. Catal. Commun. 2012, 17, 81–88.

[20] Hu, L. H.; Sun, K. Q.; Peng, Q.; Xu, B. Q.; Li, Y. D. Surface active sites on $Co_3O_4$ nanobelt and nanocube model catalysts for CO oxidation. Nano Res. 2010, 3, 363–368.

[21] Shutilov, A. A.; Zenkovets, G. A.; Tsybulya, S. V.; Gavrilov, V. Y.; Kryukova, G. N. Effect of the microstructure of the supported catalysts $CuO/TiO_2$ and $CuO/(CeO_2$-$TiO_2)$ on their catalytic properties in carbon monoxide oxidation. Kinet. Catal. 2012, 53, 409–418.

[22] Paszti, Z.; Hakkel, O.; Keszthelyi, T.; Berko, A.; Balazs, N.; Bako, I.; Guczi, L. Interaction of carbon monoxide with Au(111) modified by ion bombardment: A surface spectroscopy study under elevated pressure. Langmuir 2010, 26, 16312–16324.

[23] Komova, O. V.; Simakov, A. V.; Rogov, V. A.; Kochubei, D. I.; Odegova, G. V.; Kriventsov, V. V.; Paukshtis, E. A.; Ushakov, V. A.; Sazonova, N. N.; Nikoro, T. A. Investigation of the state of copper in supported copper-titanium oxide catalysts. J. Mol. Catal. A-Chem. 2000, 161, 191–204.

[24] Lu, J. Q.; Sun, C. X.; Li, N.; Jia, A. P.; Luo, M. F. Kinetic study of CO oxidation over $CuO/MO_2$ (M = Si, Ti and Ce) catalysts. Appl. Surf. Sci. 2013, 287, 124–134.

[25] Boccuzzi, F.; Chiorino, A.; Martra, G.; Gargano, M.; Ravasio, N.; Carrozzini, B. Preparation, characterization, and activity of $Cu/TiO_2$ catalysts .1. Influence of the preparation method on the dispersion of copper in $Cu/TiO_2$. J. Catal. 1997, 165, 129–139.

[26] Zhu, H. Y.; Wu, Y.; Zhao, X.; Wan, H. Q.; Yang, L. J.; Hong, J. M.; Yu, Q.; Dong, L.; Chen, Y.; Jian, C.; Wei, J.; Xu, P. Influence of impregnation times on the dispersion of CuO on anatase. J. Mol. Catal. A-Chem. 2006, 243, 24–30.

[27] Kim, H. Y.; Liu, P. Complex catalytic behaviors of $CuTiO_x$ mixed-oxide during CO oxidation. J. Phys. Chem. C 2015, 119, 22985–22991.

[28] Chen, C. S.; Chen, T. C.; Chen, C. C.; Lai, Y. T.; You, J. H.; Chou, T. M.; Chen, C. H.; Lee, J. F. Effect of $Ti^{3+}$ on $TiO_2$-supported Cu catalysts used for CO oxidation. Langmuir 2012, 28, 9996–10006.

[29] Fahim, N. F.; Sekino, T. A novel method for synthesis of titania nanotube powders using rapid breakdown anodization. Chem. Mater. 2009, 21, 1967–1979.

[30] Goncalves, R. V.; Wojcieszak, R.; Wender, H.; Dias, C. S. B.; Vono, L. L. R.; Eberhardt, D.; Teixeira, S. R.; Rossi, L. M. Easy access to metallic copper nanoparticles with high activity and stability for CO oxidation. ACS Appl. Mater. Inter. 2015, 7, 7987–7994.

[31] Hossain, S. T.; Azeeva, E.; Zhang, K. F.; Zell, E. T.; Bernard, D. T.; Balaz, S.; Wang, R. G. A comparative study of CO oxidation over Cu-O-Ce solid solutions and $CuO/CeO_2$ nanorods catalysts. Appl. Surf. Sci. 2018, 455, 132–143.

[32] Kasuga, T.; Hiramatsu, M.; Hoson, A.; Sekino, T.; Niihara, K. Formation of titanium oxide nanotube. Langmuir 1998, 14, 3160–3163.

[33] Zhang, R.; Teoh, W. Y.; Amal, R.; Chen, B.; Kaliaguine, S. Catalytic reduction of NO by CO over Cu/CexZr1−xO2 prepared by flame synthesis. J. Catal. 2010, 272, 210–219.

[34] Zhang, S.; Peng, L. M.; Chen, Q.; Du, G. H.; Dawson, G.; Zhou, W. Z. Formation mechanism of $H_2Ti_3O_7$ nanotubes. Phys. Rev. Lett. 2003, 91.

[35] Razali, M. H.; Noor, A. F. M.; Mohamed, A. R.; Sreekantan, S. Morphological and structural studies of titanate and titania nanostructured materials obtained after heat treatments of hydrothermally produced layered titanate. J. Nanomater. 2012.

[36] Yu, X. F.; Wu, N. Z.; Xie, Y. C.; Tang, Y. Q. A monolayer dispersion study of titania-supported copper oxide. J. Mater. Chem. 2000, 10, 1629–1634.

[37] Guo, X. Z.; Huang, J.; Wang, S. R.; Wang, Y. M.; Zhang, B. L.; Wu, S. H. CuO catalysts supported on porous $TiO_2$ microspheres for low-temperature co oxidation. J. Disper. Sci. Technol. 2009, 30, 1114–1119.

[38] Tang, X. L.; Zhang, B. C.; Li, Y.; Xu, Y. D.; Xin, Q.; Shen, W. J. Carbon monoxide oxidation over $CuO/CeCO_2$ catalysts. Catal Today 2004, 93-5, 191–198.

[39] Han, M. S.; Lee, B. G.; Ahn, B. S.; Moon, D. J.; Hong, S. I. Surface properties of $CuCl_2$/AC catalysts with various Cu contents: XRD, SEM, TG/DSC and CO-TPD analyses. Appl. Surf. Sci. 2003, 211, 76–81.

[40] Xue, L.; Zhang, C. B.; He, H.; Teraoka, Y. Catalytic decomposition of $N_2O$ over $CeO_2$ promoted $Co_3O_4$ spinel catalyst. Appl. Catal. B-Environ. 2007, 75, 167–174.

[41] Merino, N. A.; Barbero, B. P.; Grange, P.; Cadus, L. E. $La_{1-x}Ca_xCoO_3$ perovskite-type oxides: Preparation, characterisation, stability, and catalytic potentiality for the total oxidation of propane. J. Catal. 2005, 231, 232–244.

[42] Meng, M.; Lin, P. Y.; Fu, Y. L. The catalytic removal of co and no over Co-Pt(Pd,Rh)/gamma-$Al_2O_3$ catalysts and their structural characterizations. Catal. Lett. 1997, 48, 213–222.

[43] Dong, L.; Tang, Y. X.; Li, B.; Zhou, L. Y.; Gong, F. Z.; He, H. X.; Sun, B. Z.; Tang, C. J.; Gao, F.; Dong, L. Influence of molar ratio and calcination temperature on the properties of $Ti_xSn_{1-x}O_2$ supporting copper oxide for co oxidation. Appl. Catal. B-Environ. 2016, 180, 451–462.

[44] Kydd, R.; Teoh, W. Y.; Wong, K.; Wang, Y.; Scott, J.; Zeng, Q. -H.; Yu, A. -B.; Zou, J.; Amal, R. Flame-Synthesized Ceria-Supported Copper Dimers for Preferential Oxidation of CO. Adv. Funct. Mater. 2009, 19, 369–377.

[45] Kydd, R.; Ferri, D.; Hug, P.; Scott, J.; Teoh, W. Y.; Amal, R. Temperature-induced evolution of reaction sites and mechanisms during preferential oxidation of CO. J. Catal. 2011, 277, 64–71.

[46] Chen, H. L.; Zhu, H. Y.; Wu, Y.; Gao, F.; Dong, L.; Zhu, J. J. Dispersion, reduction and catalytic properties of copper oxide supported on $Ce_{0.5}Zr_{0.5}O_2$ solid solution. J. Mol. Catal. A-Chem. 2006, 255, 254–259.

[47] Zimmer, P.; Tschope, A.; Birringer, R. Temperature-programmed reaction spectroscopy of ceria- and Cu/ceria-supported oxide catalyst. J. Catal. 2002, 205, 339–345.

[48] Kang, M. Y.; Yun, H. J.; Yu, S.; Kim, W.; Kim, N. D.; Yi, J. Effect of $TiO_2$ crystalline phase on CO oxidation over CuO catalysts supported on $TiO_2$. J. Mol. Catal. A-Chem. 2013, 368, 72–77.

[49] Moulder, J. F.; Stickle, W. F.; Sobol, P. E.; Bomben, K. D. Handbook of X-ray Photoelectron Spectroscopy, in: J. Chastain (Ed.), Perkin-Elmer Corporation, Eden Prairie, MN, 1992.

[50] Zhang, M.; Jin, Z. S.; Zhang, J. W.; Guo, X. Y.; Yang, H. J.; Li, W.; Wang, X. D.; Zhang, Z. J. Effect of annealing temperature on morphology, structure and photocatalytic behavior of nanotubed $H_2Ti_2O_4(OH)_2$. J. Mol. Catal. A-Chem. 2004, 217, 203–210.

[51] Feng, C. X.; Wang, Y.; Zhang, J. W.; Yu, L. G.; Li, D. L.; Yang, J. J.; Zhang, Z. J. The effect of infrared light on visible light photocatalytic activity: An intensive contrast between Pt-doped $TiO_2$ and N-doped $TiO_2$. Appl. Catal. B-Environ. 2012, 113, 61–71.

[52] Zhang, M.; Yu, X. L.; Lu, D. D.; Yang, J. J. Facile synthesis and enhanced visible light photocatalytic activity of N and Zr co-doped $TiO_2$ nanostructures from nanotubular titanic acid precursors. Nanoscale Res. Lett. 2013, 8.

[53] Ro, I.; Liu, Y. F.; Ball, M. R.; Jackson, D. H. K.; Chada, J. P.; Sener, C.; Kuech, T. F.; Madon, R. J.; Huber, G. W.; Dumesic, J. A. Role of the Cu-$ZrO_2$ interfacial sites for conversion of ethanol to ethyl acetate and synthesis of methanol from $CO_2$ and $H_2$. ACS Catal. 2016, 6, 7040–7050.

[54] Zagaynov, I. V.; Naumkin, A. V.; Grigoriev, Y. V. Perspective intermediate temperature ceria based catalysts for CO oxidation. Appl. Catal. B-Environ. 2018, 236, 171–175.

[55] Dehestaniathar, S.; Khajelakzay, M.; Ramezani-Farani, M.; Ijadpanah-Saravi, H. Modified diatomite-supported CuO-$TiO_2$ composite: Preparation, characterization and catalytic co oxidation. J. Taiwan Inst. Chem. E 2016, 58, 252–258.

[56] Ro, I.; Sener, C.; Stadelman, T. M.; Ball, M. R.; Venegas, J. M.; Burt, S. P.; Hermans, I.; Dumesic, J. A.; Huber, G. W. Measurement of intrinsic catalytic activity of Pt monometallic and Pt-$MoO_x$ interfacial sites over visible light enhanced $PtMoO_x/SiO_2$ catalyst in reverse water gas shift reaction. J. Catal. 2016, 344, 784–794.

[57] Ro, I.; Aragao, I. B.; Brentzel, Z. J.; Liu, Y. F.; Rivera-Dones, K. R.; Ball, M. R.; Zanchet, D.; Huber, G. W.; Dumesic, J. A. Intrinsic activity of interfacial sites for Pt-Fe and Pt-Mo catalysts in the hydrogenation of carbonyl groups. Appl. Catal. B-Environ. 2018, 231, 182–190.

[58] Ro, I.; Aragao, I. B.; Chada, J. P.; Liu, Y. F.; Rivera-Dones, K. R.; Ball, M. R.; Zanchet, D.; Dumesic, J. A.; Huber, G. W. The role of Pt-$Fe_xO_y$ interfacial sites for CO oxidation. J. Catal. 2018, 358, 19–26.

[59] Kikugawa, M.; Yamazaki, K.; Shinjoh, H. Characterization and catalytic activity of CuO/$TiO_2$-$ZrO_2$ for low temperature CO oxidation. Appl. Catal. A-Gen. 2017, 547, 199–204.

[60] Huang, T. J.; Tsai, D. H. CO oxidation behavior of copper and copper oxides. Catal. Lett. 2003, 87, 173–178.

[61] Wu, G. J.; Guan, N. J.; Li, L. D. Low temperature CO oxidation on Cu–$Cu_2O$/$TiO_2$ catalyst prepared by photodeposition. Catal. Sci. Technol. 2011, 1, 601–608.

[62] Sierra-Pereira, C. A.; Urquieta-Gonzalez, E. A. Reduction of NO with CO on CuO or $Fe_2O_3$ catalysts supported on $TiO_2$ in the presence of $O_2$, $SO_2$ and water steam. Fuel 2014, 118, 137–147.

[63] Chen, C. S.; You, J. H.; Lin, J. H.; Chen, Y. Y. Effect of highly dispersed active sites of Cu/$TiO_2$ catalyst on CO oxidation. Catal. Commun. 2008, 9, 2381–2385.

[64] Song, H. C.; Oh, S.; Kim, S. H.; Lee, S. W.; Moon, S. Y.; Choi, H.; Kim, S. H.; Kim, Y.; Oh, J.; Park, J. Y. The effect of the oxidation states of supported oxides on catalytic activity: CO oxidation studies on Pt/cobalt oxide, Chem. Commun. 2019, 55, 9503–9506.

[65] Loc, L. C.; Tri, N.; Cuong, H. T.; Anh, H. C.; Thoang, H. S.; Gaidai, N. A.; Agafonov, Y. A.; Lapidus, A. L. Mechanism of Carbon Monoxide Oxidation on Supported Copper Catalysts Modified with Cerium and Platinum, Kinet. Catal. 2015, 56, 774–4780.

[66] Choi, K. I.; Vannice, M. A. CO Oxidation over Pd and Cu Catalysts IV. Prereduced $Al_2O_3$-Supported Copper, J. Catal. 1991, 131,22–35.

# Chapter 6

# Cu promoted Co/TNRs catalysts for CO hydrogenation to hydrocarbons

## 6.1 Introduction

Fischer−Tropsch synthesis (FTS) is well-known process of hydrocarbon production from synthesis gas or syngas ($H_2$ + CO) [1]. Biomass, coal or natural gas are among the carbon-containing feedstock or potential sources of syngas. The hydrogen to carbon monoxide ratio and the extent of impurities vary depending upon the feedstock. For biomass or coal feedstock, $H_2$ to CO ratio also depends upon the gasification technology [2].

It is imperative to note that the FTS products quality is solely function of catalyst choice and operating conditions while syngas source feedstock does not affect the product quality. The metals that are reported to show the FTS activity are Fe, Ru, Ni and Co [3] and among these metals, only Fe and Co are commercially utilized for the FTS because they offer good trade-offs between catalyst cost, activity, stability and selectivity [4]. Although Fe is cheaper than Co and offers strong resistance to some of the poisons, Co is preferable for the production of certain hydrocarbons such as diesel. Another important aspect of Fe and Co-based catalysts is their activity towards water gas shift (WGS) reaction in which CO reacts with water to generate $CO_2$ and $H_2$. This process is important due to its impact on the $H_2$ to CO ratio during the FTS process. Co-based catalysts are less active towards WGS (except at high temperatures) and this suggests that Co-based catalysts are preferable for syngas derived from natural gas *i.e.*, rich in hydrogen [5, 6]. Biomass or coal derived syngas is hydrogen lean or CO rich and hence Fe-based catalysts are suitable for the FTS based on biomass or coal [7, 8]. However, high stability and higher selectivity of Co-based catalysts towards heavy hydrocarbons are desired properties for the FTS [9].

Co metal is usually dispersed over an oxide support and depending upon the operating conditions and catalyst properties, catalysts deactivation is observed over time. Metal agglomeration or sintering, coke or carbon formation during reaction and reoxidation

of Co metal particles are some of the deactivation mechanisms which are thoroughly discussed in [10]. The promoters are added to the metal based catalysts to enhance their activity performance and in case of the FTS process, promoters play their role in increasing activity, selectivity and stability of Co-based catalysts [11]. The textural promoter can even contribute to control Co particles sintering which is one of the main causes of deactivation [1]. Ma *et al*. [12] investigated the copper promotion over activated carbon (AC) supported 15.7 wt% Fe and 0.9 wt% K catalysts and revealed that copper addition up to 2 wt% enhanced Fe reduction but this improved reduction did not have any significant impact on the catalytic activity during the FTS process while the Cu addition influenced the product selectivity and more alcohols were produced.

Jacobs *et al*. [13] studied the effect of three promoters (Cu, Au and Ag) over 15 wt% $Co/Al_2O_3$ catalyst. The addition of smaller fractions (up to 2.7 wt%) of these promoters improved the reducibility of Co catalysts and in case of Ag and Au promoters, even active site densities were observed to be enhanced. An excessive amount of promoters proved to be detrimental because the promoters covered the Co active sites and resulted in decreased activity.

In this research work, we synthesized and compared the activities of Cu promoted Co/TNRs catalysts with the base catalyst. The Co loading is 7.5 wt% and Cu loading varied from 1.5 to 6 wt% which suggests that Cu also acts as bimetal catalyst at higher loadings. The main idea is to demonstrate the concept of how copper affects the performance of Co/TNRs catalyst as promoter and bimetal. The catalysts are characterized using XRD, CO and $H_2$-TPD and $H_2$-TPR.

## 6.2 Experimental

### *6.2.1 Catalyst preparation*

Titania nanorods (TNRs) supported copper promoted cobalt based catalysts were synthesized using desposition-precipitation method. The chemicals used include copper acetate (obtained from Sigma Aldrich®), cobalt acetate (obtained from Sigma Aldrich®), titania nanorods (TNRs) and 1M sodium carbonate ($Na_2CO_3$) solution. For 1 gram of catalyst, 0.225 grams of cobalt acetate were dissolved in deionized water and stirred until a clear solution was attained. Then, 0.925 grams of TNRs were added to

the cobalt precursors containing solution followed by dropwise addition of 1M $Na_2CO_3$ solution to maintain pH of 10. The solution was kept under magnetic stirring for 12 h followed by filtration and washing of the samples three times using deionized water. The samples were dried in oven at 120 ℃ for 12 h followed by calcination under air at 400 ℃ for 5 h. Similar procedure was adopted to synthesize Cu promoted catalysts by adding 0.0475, 0.095 and 0.19 grams of copper acetate. The Co contents were 7.5 wt% and Cu contents were varied between 1.5 and 6 wt%.

*6.2.2 Catalyst characterization*

X-ray diffraction (XRD) patterns were recorded using a Philips PW1700 X-ray diffractometer (Co-Kα radiation source). The recordings were obtained for scanning range of 20-80° using scanning step of 0.05°. MPI Jade® software was utilized for XRD data analysis.

The temperature-programmed reduction with hydrogen ($H_2$-TPR), temperature-programmed desorption using CO and $H_2$ (CO-TPD and $H_2$-TPD, respectively) were completed on a BELCAT II chemisorption apparatus. For $H_2$-TPR measurements, the catalyst surface was pre-treated by keeping 35-40 mg of the catalyst sample at 200 ℃ for half an hour under inert atmosphere (helium flow of 30 mL/min). The sample was subsequently cooled to ambient temperature before it was heated to 500 ℃ at 10°C/min under analysis gas (5%$H_2$/Ar mixture) flowing at 30 mL/min. The reduced samples were further used for CO- and $H_2$-TPD. The CO/$H_2$ adsorption was carried out at 50 ℃ using 5%$H_2$/Ar mixture (30 mL/min) and 10%CO/He mixture (30 mL/min) respectively. The desorption profiles were recorded by monitoring a thermal conductivity detector (TCD) while raising the sample temperature to 500 ℃ (10 ℃/min) using 30 mL/min helium.

*6.2.3 Catalytic activity*

The CO reduction reaction was carried out in a fixed bed tubular reactor. The catalyst was placed over glass beads, and the temperature of the catalyst bed was monitored using a k-type thermocouple. A total of 100 mg of each catalyst was loaded into the reactor and activated at 350 ℃ for 5 h using pure hydrogen at 1.5 bar prior to reaction. After completion of catalyst reduction, hydrogen was replaced with argon and temperature was decreased to reaction temperature of 240-300 ℃. The reactor was then

pressurized using argon to reach 5 bar and then the reaction feed gas (10 mL/min) containing $CO/H_2$ ratio of 2 was fed over the catalyst bed. The products and unconverted reactants were monitored by an online gas chromatograph (SRI Instruments) equipped with a flame ionization detector (FID) and a thermal conductivity detector (TCD). The CO conversion and products selectivity were calculated using the following equations:

$$CO\ Conversion\ [X_{CO}]\ (\%) = \frac{CO_{in} - CO_{out}}{CO_{in}} \times 100 \quad (6.1)$$

$$S_{Cx\%} = \frac{n_x \times nC}{CO_{in} - CO_{out}} \quad (6.2)$$

where $X_{CO}$ is the conversion of CO, $n_x$ is the number of moles of product x, $n_C$ is the number of carbon atoms in product x. The mass balance was applied based on number of moles of carbon converted into the products. The detailed experimental setup is presented in Appendix A.

## 6.3 Results and Discussion

### *6.3.1 Characterization of Cu promoted Co/TNRs catalysts*

The crystalline structure and nature of the catalyst phase is identified using powder X-ray diffraction (XRD). XRD patterns in Figure 6.1 show that the Cu-promoted Co/TNRs catalysts have similar crystalline structures with a mixture of characteristic rutile and anatase phases. It is worth noting that no characteristic peak of either Cu or Co or its oxides is observed on any of the catalysts which infers well dispersed metal particles over TNR surface [14-16].

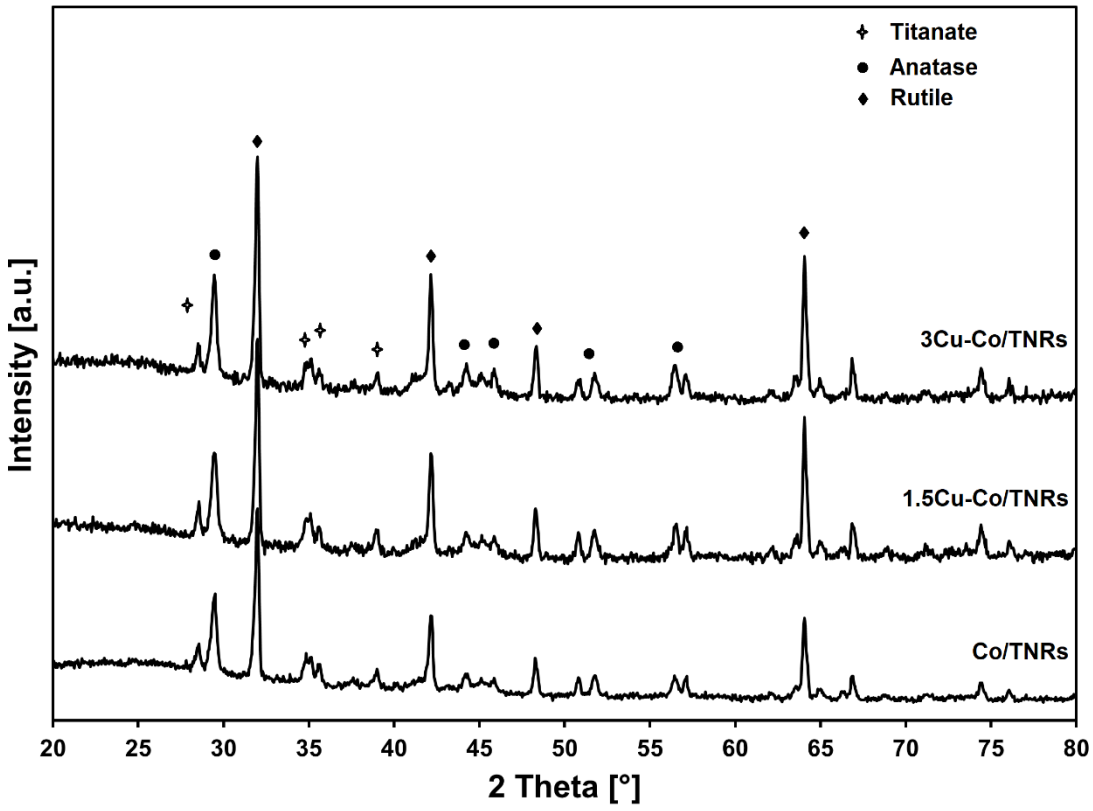


**Figure 6.1** XRD patterns of Cu promoted Co/TNRs catalysts

Temperature-programmed desorption using CO (CO-TPD) and $H_2$ ($H_2$-TPD) was carried out to gauge the interaction between probe gases and catalyst surface using BELCAT II chemisorption system. Figure 6.2 shows CO desorption profiles for Cu promoted Co/TNRs catalysts with different amounts of Cu. The desorption profiles can be divided into two regions; region I ranging from 60 to ~250 ℃ and region II between 250 and 450 ℃. A broad desorption peak is observed for all the catalysts in the region I. The peak temperatures vary for each of these catalysts which is assigned to variation in the adsorption active sites when Cu amount is changed. The desorption peak temperature increases from 110 ℃ for base Co/TNRs catalyst to 180 ℃ when smaller fraction of Cu (1.5Cu-Co/TNRs) is added. The desorption peak temperature further increases to 200 ℃ when 3 wt% Cu (3Cu-Co/TNRs) is anchored over Co/TNRs and interestingly, the desorption peak temperature drops down to 125 ℃ for 6Cu-Co/TNRs catalyst. It is generally accepted fact that CO adsorption over Cu is weaker than Co [17]; these results suggest that smaller fraction of Cu modified the Co active sites and/or the synergistic effect of two metals results in the significant rise in the peak intensity with the desorption peak shift towards higher temperature as compared with base Co/TNRs catalyst.

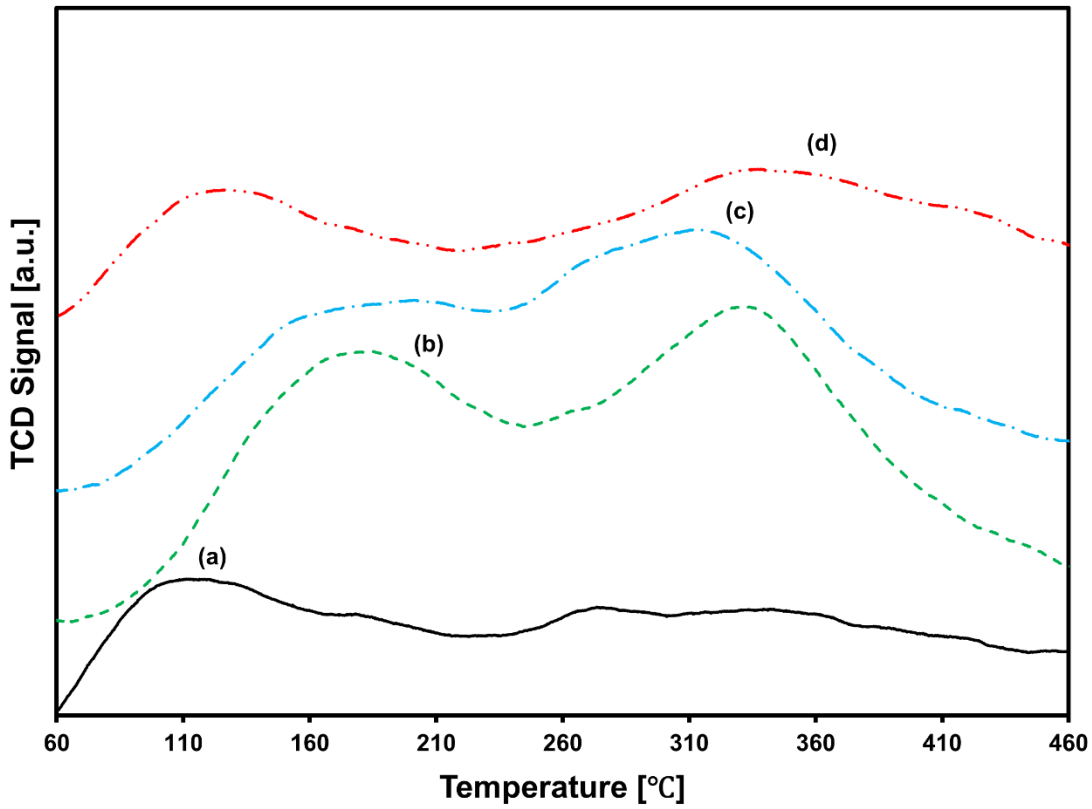


**Figure 6.2** CO-TPD profiles of Cu promoted Co/TNRs catalysts; a) Co/TNRs, b) 1.5Cu-Co/TNRs, c) 3Cu-Co/TNRs, d) 6Cu-Co/TNRs

The desorption profiles in the region II follow slightly different trend than region I. A very broad peak is observed over base Co/TNRs catalyst with temperature maxima at ~280 ℃ which shifts to higher temperature (335 ℃) after addition of Cu (1.5Cu-Co/TNRs). It is worth noting that further increase in Cu (3Cu-Co/TNRs), results in fall of the desorption peak temperature to 315 ℃ while desorption peak temperature jumps up to 340 ℃ for 6Cu-Co/TNRs catalyst. These findings are in accordance with the quantitative results given in Table 6.1 such as smaller fraction of Cu enhanced CO adsorption from 130 µmol/g over base catalyst to 480 µmol/g. CO-TPD results also suggest that smaller fraction of Cu addition did not only enhance the adsorption capacity of promoted catalysts but also the bonding between the catalyst surface and CO.

In order to gain further insight of the catalyst surface response to hydrogen adsorption, we studied $H_2$-TPD and desorption profiles are shown in Figure 6.3. The base Co/TNRs catalyst exhibits hydrogen desorption with maxima at 120, 180, 260, 345 and 425 ℃ showing various adsorption active sites over the whole temperature spectrum. The addition of Cu promoter in smaller fraction (1.5Cu-Co/TNRs) drastically modified the

adsorption active sites and a large broad peak with peak temperature of 170 ℃ is observed. In addition, two small shoulders at around 360 and 410 ℃ are also found over this catalyst. The quantity adsorbed calculated from area under the curve of Figure 6.3 is given in Table 6.1. It is obvious from the results in Table 6.1 that Cu promotion in smaller fraction results in $H_2$ adsorption of 130 µmol/g which is over three-fold the amount adsorbed over base catalyst. It is interesting to note that the catalysts with higher contents of Cu (3Cu-Co/TNRs and 6Cu-Co/TNRs) showed almost similar desorption profiles as base catalyst with slight variations in the desorption temperatures.

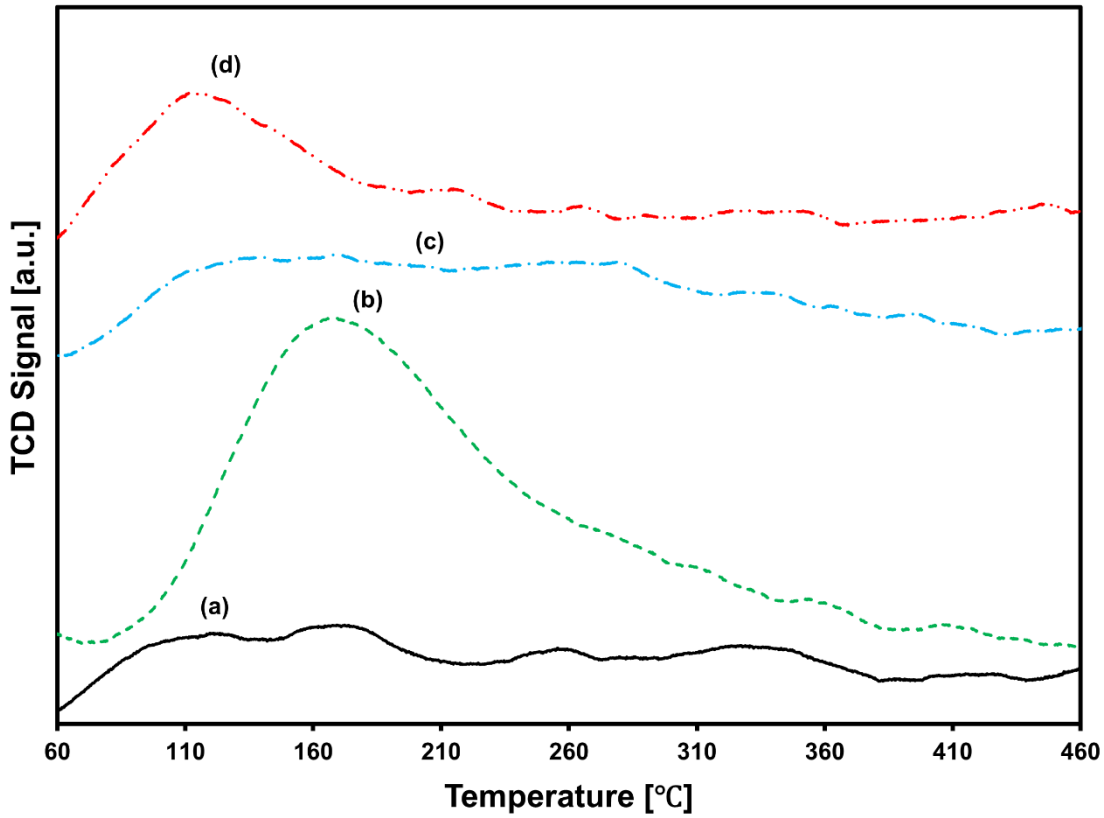


**Figure 6.3** $H_2$-TPD profiles of Cu promoted Co/TNRs catalysts; a) Co/TNRs, b) 1.5Cu-Co/TNRs, c) 3Cu-Co/TNRs, d) 6Cu-Co/TNRs

3Cu-Co/TNRs catalyst shows desorption peaks at 135, 170, 280, 345 and 400 ℃ while 6Cu-Co/TNRs catalyst displays desorption profiles at 115, 220, 265, 350 and 450 ℃. From the desorption profiles it can be inferred that Cu promoter influenced the hydrogen adsorption capacity of the catalysts and large quantities are adsorbed over the catalyst with smaller fraction of Cu (1.5Cu-Co/TNRs).

**Table 6.1** Quantitative results of CO and $O_2$ desorption

| Catalyst | CO adsorbed (µmol/g)[a] | $H_2$ adsorbed (µmol/g) [b] |
|---|---|---|
| **Co/TNRs** | 130 | 40 |
| **1.5Cu-Co/TNRs** | 480 | 130 |
| **3Cu-Co/TNRs** | 469 | 80 |
| **6Cu-Co/TNRs** | 350 | 50 |

[a] From CO-TPD; [b] From $H_2$-TPD

The extent of surface reducibility and the interactions between metal and support are important parameters in evaluating catalytic performance in heterogeneous catalysis as determined by $H_2$-TPR. The reduction profiles also provide useful information about the activation temperatures required for the reduction of metal oxides to metal form prior to the FTS reaction. The reduction profiles for the base and Cu promoted Co/TNRs catalysts are shown in Figure 6.4. The reduction of $Co_3O_4$ is reported to be complex process and generally the particle size, Co dispersion and homogeneity in the catalyst affect the Co oxides reduction [18]. Hence, the large particles weakly interacting with the support or surface oxides are easier to reduce. The reduction profiles of base Co/TNRs catalyst exhibits two reduction peaks with peak temperatures of 300 (peak I) and 405 ℃ (peak II). The explanation of the reduction of Co oxides is presented with different perspectives. From one perspective, the peak I can be assigned to the reduction of $Co_3O_4$ having weak interaction with the TNRs support. However, peak II is assigned to the reduction of $Co_3O_4$ and CoO to $Co^0$ [19]. The other perspective from the literature reports is based on the ratio of two peaks. Since the ratio of peak I to peak II is ~1/3; hence two peaks are assigned to two-step reduction of $Co_3O_4$ ($Co_3O_4 \rightarrow CoO \rightarrow Co^0$) [18, 20].

It is evident from the TPR profiles that Cu promotion significantly affected the reducibility of promoted catalysts and reduction peak temperatures over all promoted catalysts are lower than the base Co/TNRs catalyst. The Cu addition to Co/TNRs catalyst lowered the reduction peak temperatures from 300 and 405 ℃ to 245 and 335 ℃ respectively for 1.5Cu-Co/TNRs catalyst. An increase in Cu contents to 3 wt% (3Cu-Co/TNRs) lowered the reduction peak I and peak II temperatures further down to 195 and 325 ℃ respectively. The reduction temperature of peak I shifted slightly towards

right (220 ℃) while peak II reduction temperature further dropped to 315 ℃ for 6Cu-Co/TNRs catalyst. It can be inferred that Cu even present as bimetal (6Cu-Co/TNRs) enables reduction of Co oxides at temperature much lower than base catalyst. It must be noted that the peak intensities/sizes of promoted catalysts decrease with increasing Cu contents which can be assigned to coverage of Co oxide by Cu and hence loss of reducible species.

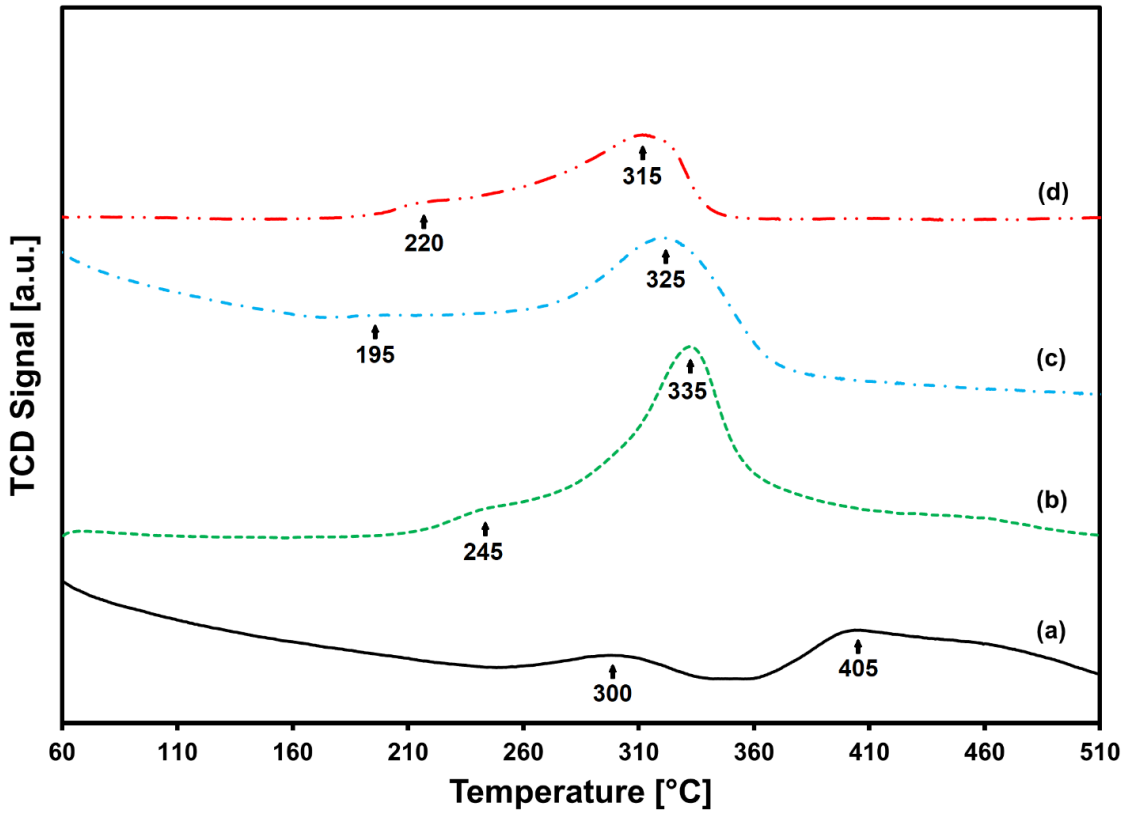


**Figure 6.4** $H_2$-TPR patterns for Cu promoted Co/TNRs catalysts; a) Co/TNRs, b) 1.5Cu-Co/TNRs, c) 3Cu-Co/TNRs, d) 6Cu-Co/TNRs

*6.3.2 FTS activity by Cu promoted Co/TNRs catalysts*

The catalytic performance of base and Cu promoted Co/TNRs catalysts for the FTS reaction at 5 bar and reaction temperatures of 240 ℃ was investigated and results of the activity and product selectivity are presented in Table 6.2 and Figure 6.5. The bare TNRs support was tested under reaction conditions and did not show any activity for the FTS reaction. The CO conversion, at 240 ℃, of base Co/TNRs catalyst is found to be 9.4% and major fractions of the products were $C_{5+}$ hydrocarbons. The Cu doping significantly influences the catalytic performance of the promoted catalysts and CO

conversion increases to 16.8% when smaller fraction of Cu (1.5 wt%) is added. The Cu promotion also affects the product selectivity, in particular, methane and $CO_2$ selectivity. It can be further observed from the FTS activity results (Table 6.2 and Figure 6.5) that 3Cu-Co/TNRs catalyst displayed significant decrease in CO conversion and further increase in Cu contents (6 wt%) exhibited detrimental CO conversions. The doping of more Cu over Co/TNRs catalyst prohibits the Co surface active sites and results in loss of catalytic activity. Based on the activity results, all the catalysts are arranged in the following order:

1.5Cu-Co/TNRs > 3Cu-Co/TNRs > Co/TNRs > 6Cu-1Co/TNRs

**Table 6.2** The FTS activity and selectivity data for base and Cu promoted Co/TNRs catalysts

| **Catalyst** | **Temperature (°C)** | **CO conv. (%)** | **$CH_4$** | **$C_2$ olefin** | **$C_2$-$C_4$ Paraffins[a]** | **$C_{5+}$[a]** | **$CO_2$** |
|---|---|---|---|---|---|---|---|
| **Co/TNRs** | 240 | 9.4 | 26.7 | 2.5 | 17.3 | 51.3 | 2.2 |
| **1.5Cu-Co/TNRs** | | 16.8 | 15.7 | 2.2 | 23.4 | 57.5 | 1.2 |
| **3Cu-Co/TNRs** | | 13.3 | 26.8 | 2.1 | 21.7 | 43.5 | 5.9 |
| **6Cu-Co/TNRs** | | 5.7 | 41.6 | - | 14.8 | 18.1 | 24.9 |
| **1.5Cu-Co/TNRs** | 300 | 25 | 32.7 | 0.6 | 21.5 | 35.7 | 9.5 |
| **3Cu-Co/TNRs** | | 19.6 | 46.1 | 0.4 | 13.5 | 16.5 | 23.5 |

Reduction: 350 °C in pure hydrogen, 6000 mL/$g_{cat.}$ h (4 h); FTS Reaction: $H_2$/CO = 2, 6000 mL/gcat. h, P = 5 bar (12 h); [a] GCMS was used to identify hydrocarbons up to C10

It is worth noting that only smaller fraction of Cu suppressed methane and $CO_2$ selectivity while anymore addition of Cu enhanced methane and $CO_2$ selectivity. Similar variations in the selectivity of paraffins and $C_{5+}$ hydrocarbons are observed over Cu promoted catalysts in comparison with the base Co/TNRs catalyst. These results can be explained by understanding the interaction of reacting gases *i.e.*, CO and $H_2$ with the

catalyst surface and their contribution towards the FTS activity before and after addition of Cu promoter.

CO dissociative adsorption is the key step in the FTS chain initiation and CO bonding with the catalyst surface also plays its role during reaction [21]. The adsorption of CO over the Co surface, at room temperature, is accepted to be non-dissociative in either linear or bridged form [22]. The linear type CO desorption occurs at 77 ℃ while bridged type CO desorbs at 167 ℃ *via* disproportionation reaction ($2CO \rightarrow C + CO_2$) [23, 24]. This suggests that the desorption profiles in region I (Figure 6.2) include both types of CO desorption. It can be inferred that this desorption peak represents bridge type CO desorption in the form of $CO_2$ due to disproportionation reaction. This would lead to the conclusion that we should observe lower $CO_2$ selectivity over promoted catalysts with higher Cu contents because these catalysts showed lower CO desorption amounts as compared with 1.5Cu-Co/TNRs catalyst. In fact, our catalytic activity results contradict this explanation.

The quantity of CO adsorbed over active metal sites depends upon the metal dispersion and adsorption stoichiometry. Additionally, CO adsorption over Cu is weaker than on Co [17]. Interestingly, smaller fraction of Cu promotes CO adsorption while higher Cu contents lead to an obvious decrease in CO adsorption (Figure 6.2 and Table 6.1). This can be explained by the fact that Cu decorates Co nanoparticles over the surface which leads to lower amount of CO adsorption over promoted catalysts with higher Cu contents [25]. On the contrary, the shift of desorption peaks to higher temperatures in case of Cu promoted catalysts shows enhanced CO bond strength which is inconsistent with weaker interaction between Cu and CO mentioned earlier. Similarly, Cu promoted catalysts show more reducibility than the base catalyst which is also inconsistent with the strong bond between CO and catalyst surface. This strong CO bonding with the Cu promoted Co/TNRs catalysts can be assigned to synergistic CO adsorption in which carbon atoms of CO adsorb on Co and oxygen atoms adsorb on Cu [26, 27]. This synergistic CO adsorption is found to be the main factor which results in increased activity of 1.5Cu-Co/TNRs catalyst. Despite the fact that FTS process is strongly dependent upon catalyst type, composition, preparation method and oxide support, similar observations are reported for Cu promoted $Co/Al_2O_3$ catalyst [28].

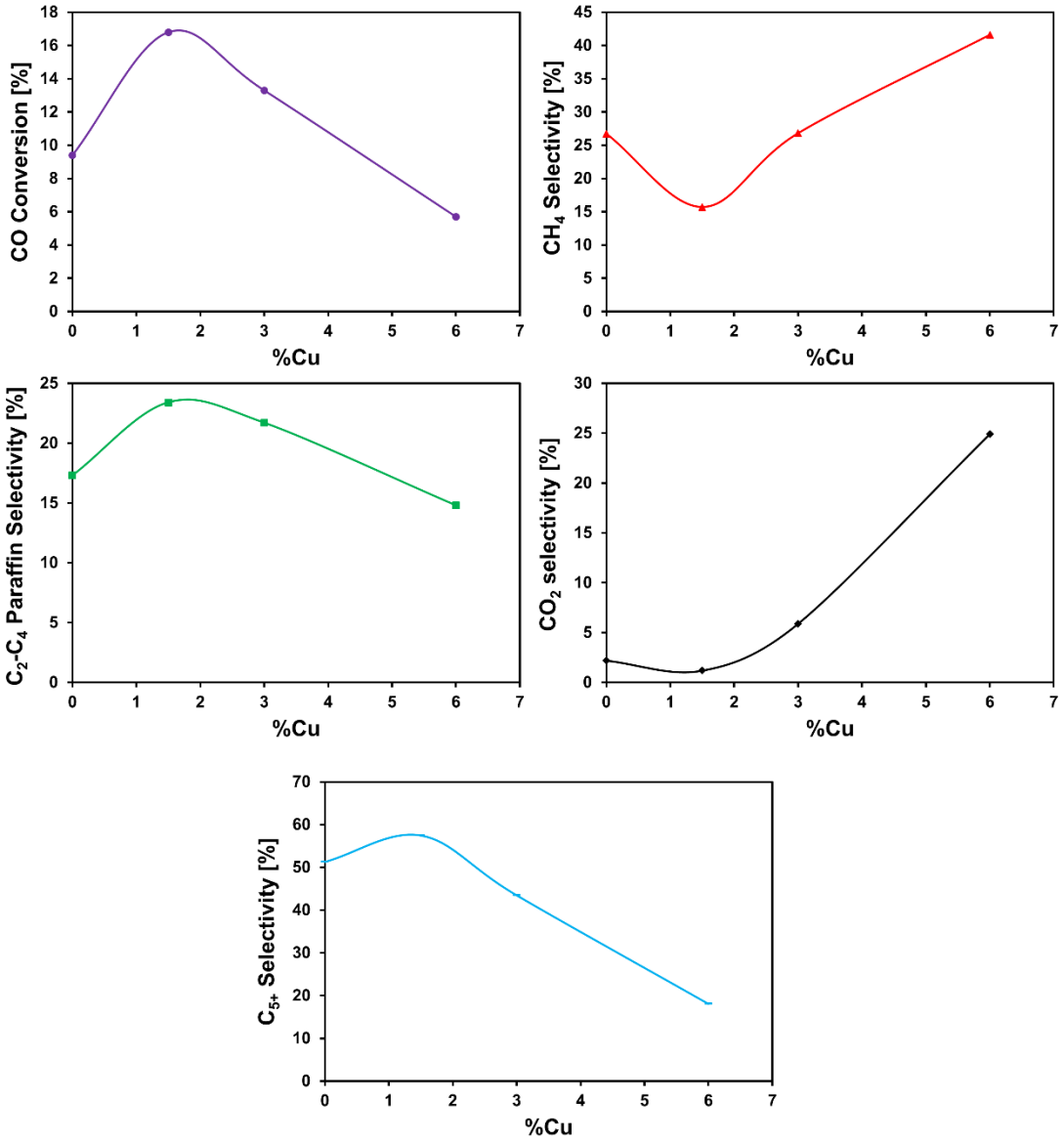


**Figure 6.5** CO conversion and product selectivity for base and Cu promoted Co/TNRs catalysts

The variations in product selectivity for Cu promoted catalysts can also be explained based on the synergistic CO adsorption and reducibility. In comparison with base Co/TNRs catalyst, the selectivity of methane and $CO_2$ is suppressed with the addition of smaller fractions of Cu (1.5Cu-Co/TNRs) which can be assigned to improved reducibility, and enhanced synergistic CO adsorption. In addition, it can be inferred that smaller fraction of Cu does not cover Co active sites rather facilitates dissociative CO adsorption [26, 27]. At fractions more than 1.5 wt%, Cu starts covering the Co active sites and thus decrease in Co active sites does not only show less CO conversion but also more formation of methane and $CO_2$. The covering of Co active sites by the Cu promoter resulting in enhanced selectivity of methane and $CO_2$ is also reported for

$Al_2O_3$ supported Co-based catalysts [13]. The water gas shift activity also contributed in the higher selectivity of methane and $CO_2$ over higher fractions of Cu [21]. It can be concluded that the catalysts with higher contents of Cu lose the synergistic effect of CO adsorption and Cu also covered the Co surface active metals which resulted in the loss of both activity and selectivity.

The best two catalysts were further tested at higher temperature (300 ℃) to investigate its effect on the catalytic activity results. The results in Table 6.2 clearly shows the increase in CO conversions and interestingly, the product selectivities are also affected at higher temperature. CO conversion increased from 16.8 and 13.3% to 25 and 19.6% for 1.5Cu-Co/TNRs and 3Cu-Co/TNRs catalysts respectively. Furthermore, high selectivities of methane and $CO_2$ are produced which suggests that both Cu and Co promote water gas shift reaction at higher temperatures [1, 29, 30].

## 6.4 Conclusions

The role of Cu promoter over Co/TNRs catalyst was investigated for the FTS reaction. The reduction profiles of Cu promoted catalysts showed that Cu doping enhanced reducibility of the resulting catalysts and thus catalyst activity. CO and $H_2$ adsorption capacities were observed to be highest for 1.5Cu-Co/TNRs catalyst which showed the highest CO conversion and $C_{5+}$ hydrocarbons selectivity at 240 ℃ and 5 bar. The increase in reaction temperature to 300 ℃ showed increase in CO conversion to 25% and 19.6% over 1.5Cu-Co/TNRs and 3Cu-Co/TNRs (29.6) catalysts respectively. The methane and $CO_2$ selectivity was found to be increase with reaction temperature in accordance with previously reported literature. The enhanced activity of 1.5Cu-Co/TNRs catalyst was associated with the synergistic mechanism of CO interaction with the catalyst surface such as carbon atoms adsorb on Co sites and oxygen adsorbs on Cu sites.

## References

[1] A.Y. Khodakov, W. Chu, P. Fongarland, Advances in the development of novel cobalt Fischer-Tropsch catalysts for synthesis of long-chain hydrocarbons and clean fuels, Chem. Rev., 107 (2007) 1692-1744.

[2] E. van Steen, M. Claeys, Fischer-Tropsch catalysts for the Biomass-to Liquid process, Chem. Eng. Technol., 31 (2008) 655-666.

[3] M.A. Vannice, Catalytic Synthesis of Hydrocarbons from $H_2$-CO Mixtures over Group-8 Metals .2. Kinetics of Methanation Reaction over Supported Metals, J. Catal., 37 (1975) 462-473.

[4] E. Iglesia, Design, synthesis, and use of cobalt-based Fischer-Tropsch synthesis catalysts, Appl. Catal. A-Gen., 161 (1997) 59-78.

[5] M.C. Marion, F. Hugues, Modification of cobalt catalyst selectivity according to Fischer-Tropsch process conditions, Stud. Surf. Sci. Catal., 167 (2007) 91-96.

[6] R. Luque, A.R. de la Osa, J.M. Campelo, A.A. Romero, J.L. Valverde, P. Sanchez, Design and development of catalysts for Biomass-To-Liquid-Fischer-Tropsch (BTL-FT) processes for biofuels production, Energy Environ. Sci., 5 (2012) 5186-5202.

[7] A. Haryanto, S.D. Fernando, L.O. Pordesimo, S. Adhikari, Upgrading of syngas derived from biomass gasification: A thermodynamic analysis, Biomass Bioenergy, 33 (2009) 882-889.

[8] M. Lualdi, S. Logdberg, F. Regali, M. Boutonnet, S. Jaras, Investigation of Mixtures of a Co-Based Catalyst and a Cu-Based Catalyst for the Fischer-Tropsch Synthesis with Bio-Syngas: The Importance of Indigenous Water, Top. Catal., 54 (2011) 977-985.

[9] B.H. Davis, Fischer-Tropsch synthesis: Comparison of performances of iron and cobalt catalysts, Ind. Eng. Chem. Res., 46 (2007) 8938-8945.

[10] N.E. Tsakoumis, M. Ronning, O. Borg, E. Rytter, A. Holmen, Deactivation of cobalt based Fischer-Tropsch catalysts: A review, Catal. Today, 154 (2010) 162-182.

[11] Morales, F. and Weckhuysen, B. M., Promotion effects in Co based Fischer-Tropsch catalysis. Catalysis, 2006, 19, 1

[12] W.P. Ma, E.L. Kugler, D.B. Dadyburjor, Promotional Effect of Copper on Activity and Selectivity to Hydrocarbons and Oxygenates for Fischer-Tropsch Synthesis over Potassium-Promoted Iron Catalysts Supported on Activated Carbon, Energy Fuel, 25 (2011) 1931-1938.

[13] G. Jacobs, M.C. Ribeiro, W.P. Ma, Y.Y. Ji, S. Khalid, P.T.A. Sumodjo, B.H. Davis, Group 11 (Cu, Ag, Au) promotion of 15%Co/$Al_2O_3$ Fischer-Tropsch synthesis catalysts, Appl. Catal. A-Gen., 361 (2009) 137-151.
[14] X.F. Yu, N.Z. Wu, Y.C. Xie, Y.Q. Tang, A monolayer dispersion study of titania-supported copper oxide, J. Mater. Chem., 10 (2000) 1629-1634.
[15] X.Z. Guo, J. Huang, S.R. Wang, Y.M. Wang, B.L. Zhang, S.H. Wu, CuO Catalysts Supported on Porous $TiO_2$ Microspheres for Low-Temperature CO Oxidation, J. Disper. Sci. Technol., 30 (2009) 1114-1119.
[16] X.L. Tang, B.C. Zhang, Y. Li, Y.D. Xu, Q. Xin, W.J. Shen, Carbon monoxide oxidation over CuO/$CeCO_2$ catalysts, Catal. Today, 93-5 (2004) 191-198.
[17] X.H. Mo, Y.T. Tsai, J. Gao, D.S. Mao, J.G. Goodwin, Effect of component interaction on the activity of Co/CuZnO for CO hydrogenation, J. Catal., 285 (2012) 208-215.
[18] B. Ernst, A. Bensaddik, L. Hilaire, P. Chaumette, A. Kiennemann, Study on a cobalt silica catalyst during reduction and Fischer-Tropsch reaction: In situ EXAFS compared to XPS and XRD, Catal. Today, 39 (1998) 329-341.
[19] P. Arnoldy, J.A. Moulijn, Temperature-Programmed Reduction of Coo/$Al_2O_3$ Catalysts, J. Catal., 93 (1985) 38-54.
[20] B.A. Sexton, A.E. Hughes, T.W. Turney, An Xps and Tpr Study of the Reduction of Promoted Cobalt Kieselguhr Fischer-Tropsch Catalysts, J. Catal., 97 (1986) 390-406.
[21] W. Chen, B. Zijlstra, I.A.W. Filot, R. Pestman, E.J.M. Hensen, Mechanism of Carbon Monoxide Dissociation on a Cobalt Fischer-Tropsch Catalyst, Chemcatchem, 10 (2018) 136-140.
[22] A.A. Tsyganenko, P.P. Mardilovich, Structure of alumina surfaces, J. Chem. Soc. Faraday Trans., 92 (1996) 4843-4852.
[23] R. Gopalakrishnan, B. Viswanathan, Temperature-Programmed Desorption and Infrared Studies on the Activation of Carbon-Monoxide on Cobalt Surfaces, J. Colloid Interface Sci., 102 (1984) 370-372.
[24] R. Gopalakrishnan, B. Viswanathan, Interaction of Co and Hydrogen on Cobalt Surfaces - a Temperature-Programmed Desorption Study, Surf. Technol., 23 (1984) 173-177.
[25] X. Mo, Y.T. Tsai, J. Gao, D. Mao, J.G. Goodwin, Effect of component interaction on the activity of Co/CuZnO for CO hydrogenation, J. Catal., 285 (2012) 208-215.

[26] S. Sitthisa, D.E. Resasco, Hydrodeoxygenation of Furfural Over Supported Metal Catalysts: A Comparative Study of Cu, Pd and Ni, Catal. Lett., 141 (2011) 784-791.
[27] B.M. Reddy, G.K. Reddy, K.N. Rao, A. Khan, I. Ganesh, Silica supported transition metal-based bimetallic catalysts for vapour phase selective hydrogenation of furfuraldehyde, J. Mol. Catal. A-Chem., 265 (2007) 276-282.
[28] S. Maity, O.O. James, B. Chowdhury, A. Auroux, Effect of copper on calcium-modified alumina-supported cobalt catalysts towards Fischer-Tropsch synthesis, Curr. Sci. India, 106 (2014) 1538-1547.
[29] M.J. Keyser, R.C. Everson, R.L. Espinoza, Fischer-Tropsch studies with cobalt-manganese oxide catalysts: Synthesis performance in a fixed bed reactor, Appl. Catal. A-Gen., 171 (1998) 99-107.
[30] M.E. Dry, The Fischer-Tropsch process: 1950-2000, Catal. Today, 71 (2002) 227-241.

# Chapter 7 Conclusions and Recommendations

## 7.1 Conclusions

In this chapter, the findings and highlights of the current research work are summarized. Furthermore, some of the recommendations for further research on this area are also suggested.

The recent developments in the spectroscopic and microscopic techniques have helped researchers to predict the performance of the catalysts. The nanostructured catalysts mainly possess features such as structure, interface and porosity. The surface structure and interface offer active sites for the reaction while reactant diffusion is controlled by porosity. Using the data obtained from these characterization techniques, the catalyst's structure and interface can be tuned to hypothesize the performance of the catalyst. This thesis is thus focused on the investigation of structure and interface of the supported catalysts. The copper nanoclusters studies are mainly based on density functional theory while real-time reaction studies are rarely found in the literature. Keeping it in mind, in the third chapter, the effect of the size of copper nanoclusters supported over $TiO_2$ was investigated. The main aim of the study was to find the size-activity threshold by varying amount of copper nanoclusters from 0.15 to 5 wt%. The catalyst characterization results indicated that the size of the copper nanoclusters influenced the properties of the catalysts such that copper dispersion decreased from 59% (0.15CT) to 5.1% (5CT) while amount of CO adsorbed increased from 0.282 mmol/g (0.15CT) to 0.503 mmol/g (5CT). The activity results showed that lower loading catalysts (0.15CT and 0.30CT) exhibited stable performance for 8 h time on stream while higher loading catalysts (0.75CT and 5CT) showed deactivation due to sintering of copper during reaction.

Considering the significance of the oxide support and in particular properties imparted by nanostructured support materials, the fourth chapter was aimed at the synthesis of titania nanorods (TNRs). The investigation of the effect of hydrothermal synthesis operating conditions such as hydrothermal temperature and duration showed that hydrothermal temperature influenced the aspect ratio of resulting nanotubes and hydrothermal duration affected the yield of nanorods. The XRD analysis showed that the nanorods were composed of mostly rutile phase.

The role of catalytically active interfaces between copper and TNRs was discussed in the fifth chapter. The deposition of copper over TNRs was carried out using deposition-precipitation method with copper varying from 2.5 to 12.5 wt%. The change in copper amount influences the metal-support interaction which in turn affects the interfacial active sites responsible for catalytic activity; this chapter was based on this hypothesis. The catalysts characterization results showed that 7.5 wt% copper loading had the highest amount of CO (0.231 mmol/g) and $O_2$ (0.77 mmol/g) adsorbed among all the catalysts. 7.5Cu-TNR catalyst also exhibited more reducibility and weaker metal-support interaction as compared with 5Cu-TNR and 10Cu-TNR catalysts. Based on the characterization results, 7.5Cu-TNR catalyst's performance was predicted to be better than the rest of the catalysts. This prediction was also based on the formation of interfacial active sites generated differently over all the catalysts. The catalytic activity results showed that 7.5Cu-TNR catalyst was found to be an optimum loading with lowest reaction temperature of 198℃ converting 50% CO into $CO_2$. This catalyst (7.5Cu-TNR) was also subjected to long term stability test at 200℃ for 40 h and no deactivation was observed. The hypothesis was later verified by characterizing the catalysts with XPS which showed binding energy of 933.7 eV for 7.5Cu-TNR catalyst as compared with binding energy of 934.7 eV for bulk CuO. The XPS peaks for $Cu^{2+}$ were de-convoluted to estimate $Cu^{+}$ contents and it was found that higher loading catalysts (10Cu-TNR and 12.5Cu-TNR) had 3% $Cu^{+}$ while 7.5Cu-TNR catalyst showed 10% $Cu^{+}$. The $Cu^{+}$ is reported to be more active than $Cu^{2+}$ and the presence of $Cu^{+}$ also influenced the interfacial active sites.

Fischer-Tropsch synthesis (FTS) is one of the promising routes to produce value-added products including hydrocarbons and oxygenates. The final chapter of the thesis was aimed at the proof of concept for the FTS reaction using Cu promoted Co/TNR catalysts. The promoters are added in the catalysts to enhance the activity and/or selectivity of the catalysts during reaction. The Cu addition to Co/TNR catalysts was predicted to influence the product selectivity. The catalyst characterization results revealed that Cu addition affected the CO and $H_2$ chemisorption of Cu promoted Co/TNR catalysts in comparison with base Co/TNR catalyst. The metal-support interaction was also influenced by the addition of Cu. Cu was added in the amount ranging from 1.5 to 6 wt% and catalytic activity results showed that addition of 1.5 wt% Cu exhibited CO conversion of 16.8% as compared with 9% CO conversion shown by

Co/TNR. As predicted, Cu promoter influenced the product selectivity and more oxygenates were produced over Cu promoted catalysts.

In conclusion this thesis was aimed to mainly study the role of the structure and the interface which was successfully investigated. This thesis provides an insight for the readers from the perspective of the real-time reaction study of copper nanoclusters and detailed investigation of the role of catalytically active interfaces between copper nanoparticles and titania nanorods.

## 7.2 Recommendations for future work

Based on the findings of this research work, we would like to suggest some recommendations to further extend this research in future:

- Copper nanoclusters are more prone to sintering and deactivation when anchored over common oxide supports. Therefore, we recommend to encapsulate these nanoclusters inside porous support such as zeolite. The encapsulation offers some promising advantages such as control over particle size growth, prohibition of metal poisoning by manipulating the pore size and obviously enhanced long term activity.
- The detailed study of mixture of nanoparticles and nanotubes during the calcination of post hydrothermal nanotubes is worth investigating to explore how these mixtures and titania phase can influence the catalytic activity.
- The intrinsic structural features of the catalyst play significant role during reaction. The investigation of the contribution of steps and kinks during the CO oxidation reaction is recommended.
- The catalytic activity tests can be further extended to investigate the selectivity of liquid products during the FTS process and the catalyst composition or bimetallic ratio can also be manipulated to direct the selectivity towards desired products.

# Appendix A

## Materials and chemicals

All materials were used without further purification. Cupric acetate (purity = 99.99%; M.W = 199.65) was purchased from Hopkin and Williams® UK, $TiO_2$-P25 was purchased from Degussa® Germany, sodium hydroxide pellets (purity = 97%; M.W = 40) and sodium carbonate (purity = 99.5%; M.W = 105.99) were purchased from Thermo Fisher Scientific® New Zealand, cobalt acetate (purity = 99.99%; M.W = 177) was purchased from Sigma Aldrich® USA.

# Appendix B

**Reactor, GC parameters and calibration**

The high pressure fixed bed reactor (FlowCAT by HEL® UK) equipped with 2 mass flow controllers (MFCs), a liquid pump, back pressure regulator and thermocouple was used for testing the FTS process while CO oxidation was tested in a customized fixed bed reactor. Figure A1 shows the schematic diagram of FlowCAT. SRI 8610C Gas Chromatograph (GC) was used for this work. The GC was equipped with thermal conductivity detector (TCD) and flame ionization detector (FID). Two columns are installed *i.e.*, 6' haysep-D and 6' molecular sieve 13x. Molecular sieve 13x column separates the permanent gases including hydrogen, air, CO, $CH_4$, while heavy hydrocarbons including $CO_2$, ethylene and ethane get separated in hayesep-D column. The GC parameters and settings are given in Table A1.

**Table A1** GC parameters and settings for CO oxidation and reduction

| **Parameter** | | **Settings** |
|---|---|---|
| TCD carrier gas | Argon | 22 psi using electronic pressure controller (ECP) corresponds to 20 ml/min |
| FID + Methanizer gases | Hydrogen | 20 psi using ECP corresponds to 25 ml/min |
| | Air | 5 psi using ECP corresponds to 5 ml/min |
| Load/Inject Valve temperature | | 70°C |
| TCD | Temperature | 150°C |
| | Gain | Low |
| FID | Temperature | 300°C |
| | Gain | High (filtered) |

The GC calibration is carried out using standard gas customized mixture purchased from BOC Limited and gas mixture composition is presented in Table A2. In order to calibrate hydrogen over a range of concentrations (in volume %), pure hydrogen was added to the standard gas mixture while argon (99.999% purity, Zero Grade) was used to dilute the gas mixture

**Table A2** Composition of standard gas mixture and corresponding retention times

| **Gas** | **Volume ratio (%)** | **Uncertainty (±%)** | **Retention time / min (TCD based)** |
|---|---|---|---|
| $H_2$ | 25 | 0.02 | 0.74 |
| CO | 34 | 0.03 | 1.16 |
| $CH_4$ | 13 | 0.03 | 1.25 |
| $CO_2$ | 19 | 0.02 | 1.65 |
| $C_2H_4$ | 4 | 0.03 | 3.03 |
| $C_2H_6$ | 1 | 0.03 | 4.37 |
| He | *Balance = 4* | 0.02 | - |

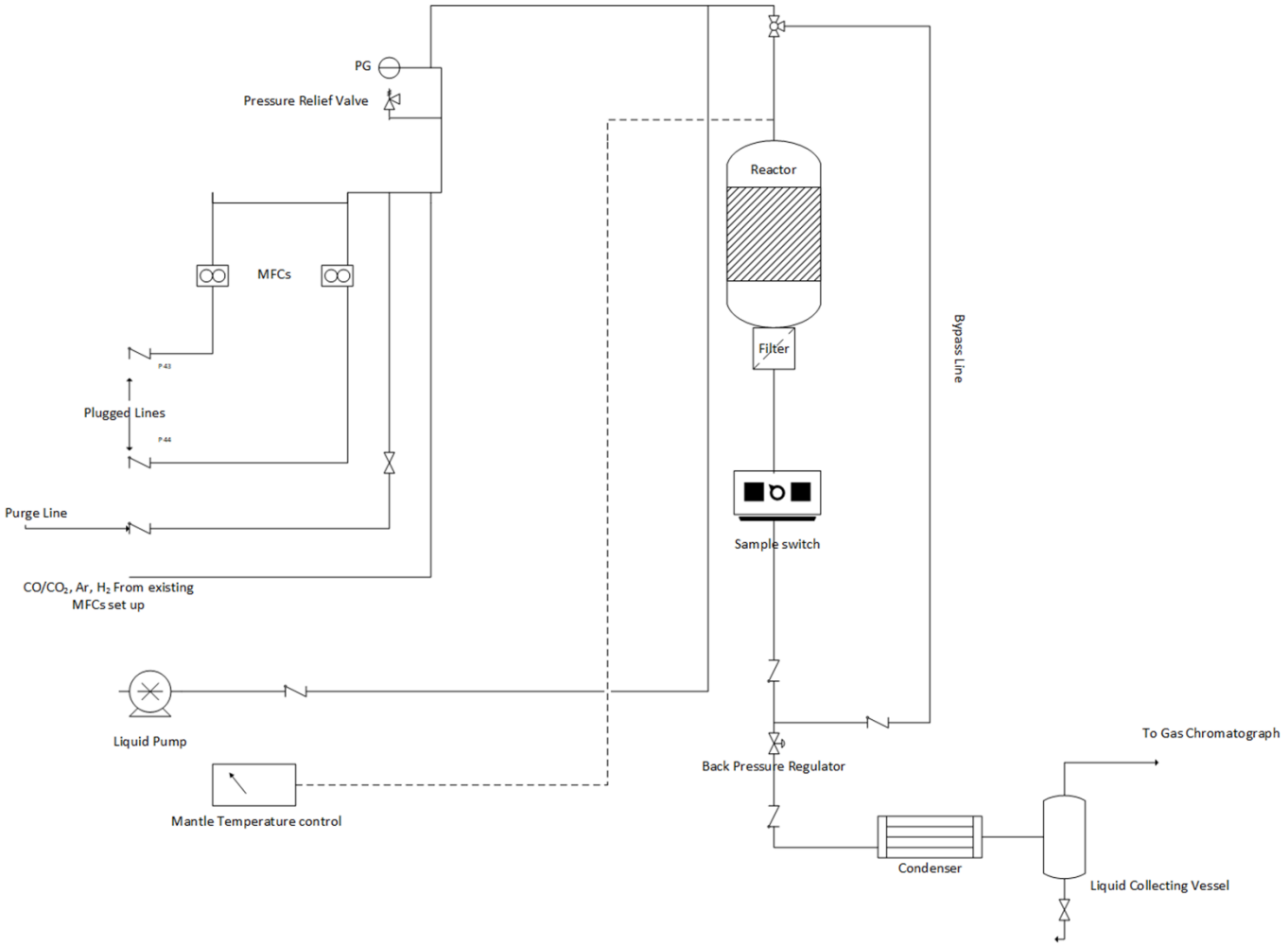


**Figure A1** Schematic diagram of fixed bed reactor (FlowCAT)

# Appendix C

**Synthesis of hexameric copper nanoclusters**

$$Cu(I)Cl \xrightarrow{PPh_3,\ THF,\ RT} [(PPh_3)_3(CuCl)_2] \xrightarrow{K-Selectride,\ THF,\ RT} [(PPh_3)CuH]_6$$

Copper(I)chloride (0.5 g, 0.005 mmol) and triphenylphosphine (1.3 g, 0.005 mol) were put in a Schlenk flask and subsequently THF (10 mL) was added. Upon stirring for 30 min a white precipitate formed. While cooling the reaction mixture in an ice bath and stirring it continuously K-Selectride (5 mL of 1.0 M in THF, 0.005 mol) was added slowly through syringe. The mixture turned dark red. The ice bath was removed and the mixture was stirred for one hour. The resulting dark red solution was filtered and washed with THF (2 × 5 mL). Under vacuum the filtrate was reduced to 50 % of its initial volume and stored in the freezer for several days. After 24 hours the product started to crystallize as dark red plates (yield: 62 %).

X-ray quality crystals: the solution was layered with the same quantity of hexanes:

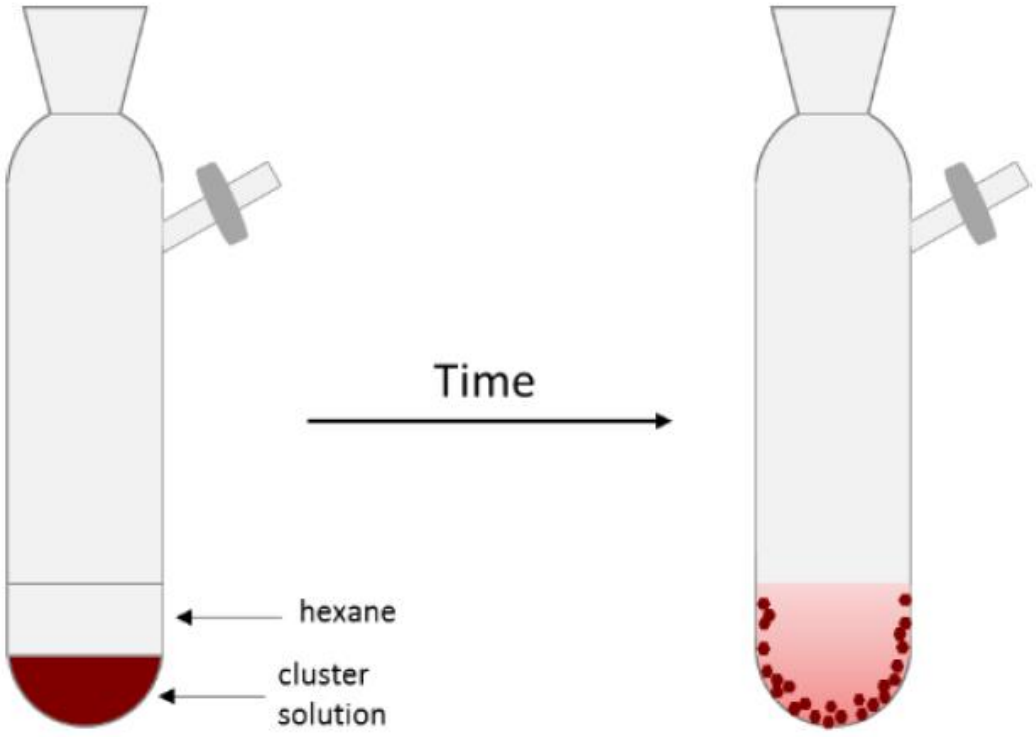

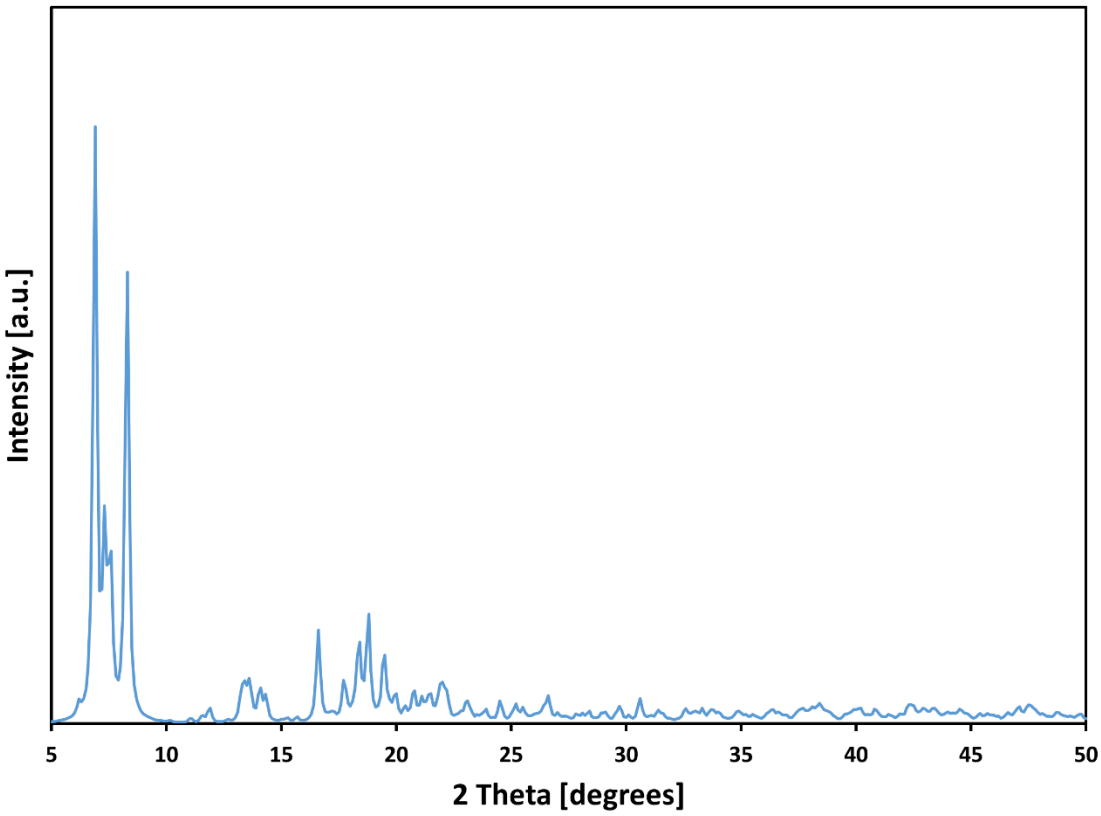


**Figure A2** PXRD patterns of copper nanoclusters

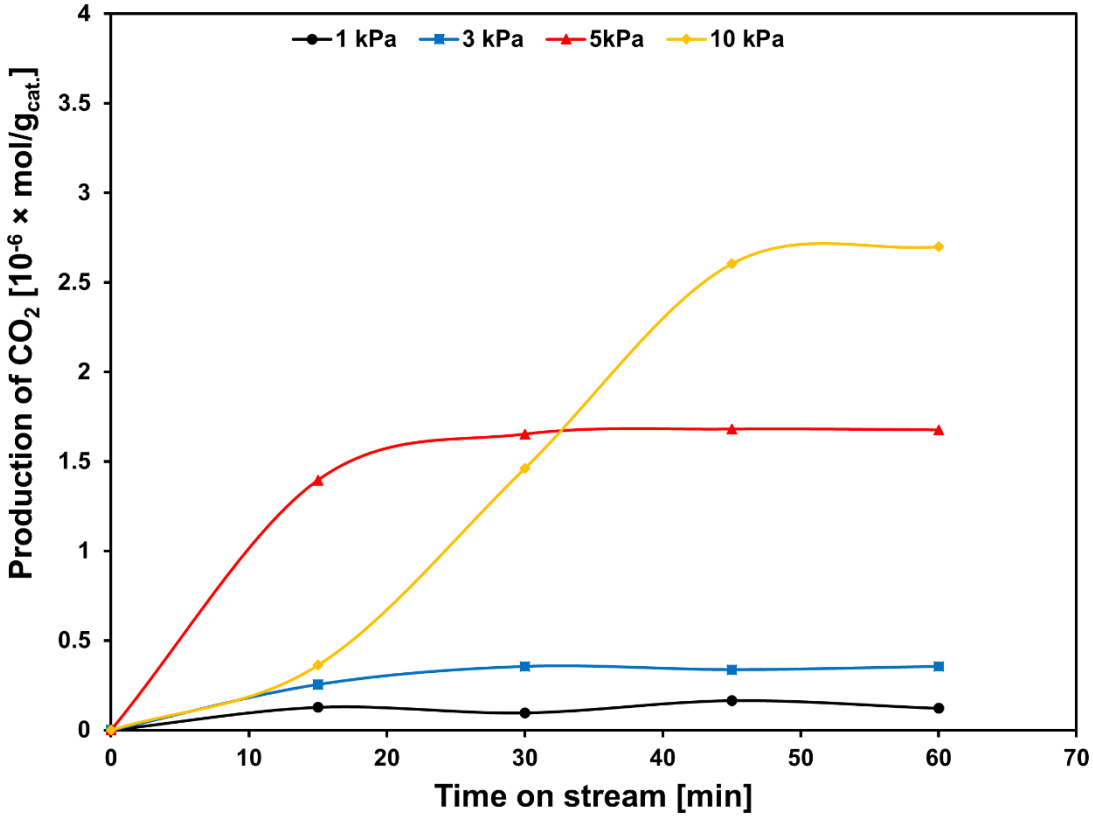


**Figure A3** Production of $CO_2$ versus time for 0.15CT catalyst [$P_{CO}$ = 1-10 kPa; $P_{O2}$ =10 kPa]

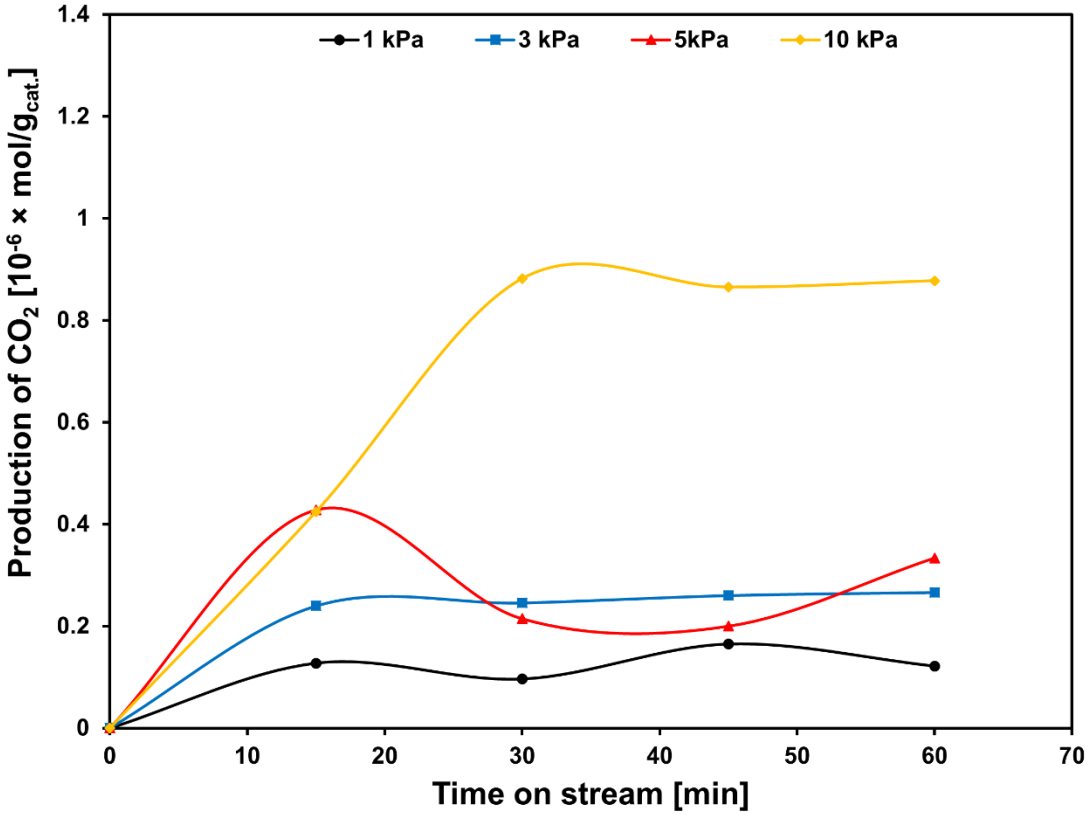


**Figure A4** Production of $CO_2$ versus time for 0.75CT catalyst [$P_{CO}$ = 1-10 kPa; $P_{O2}$ =10 kPa]

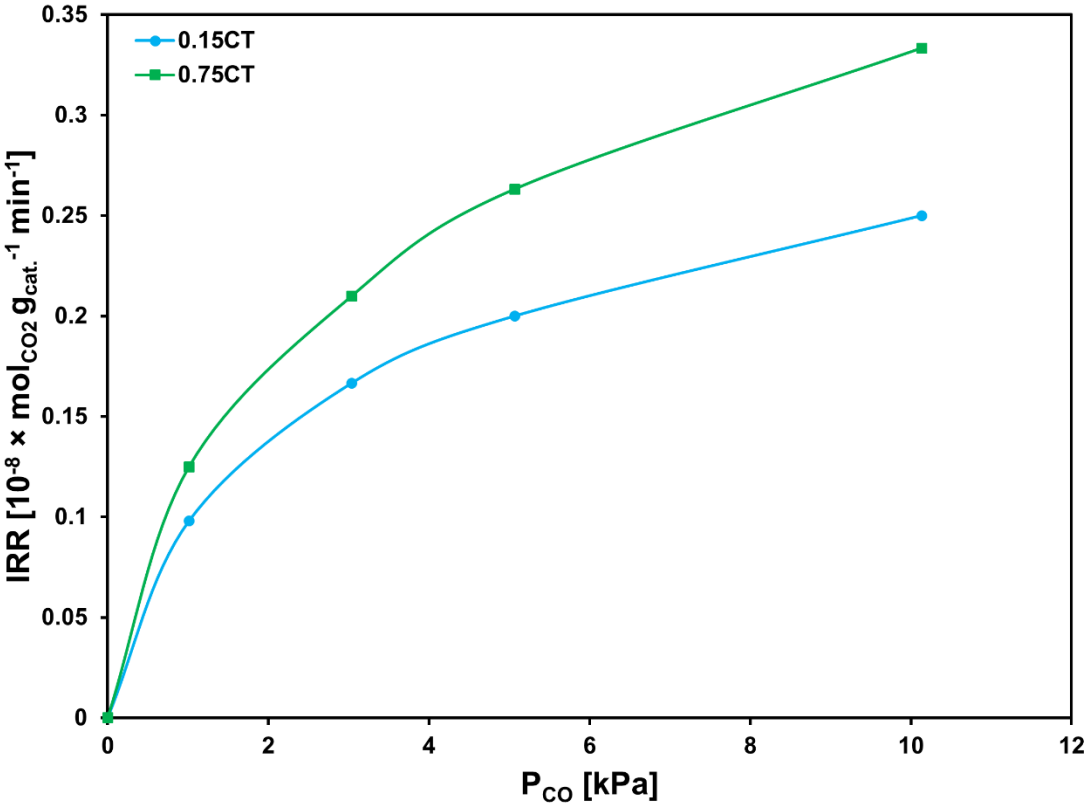


**Figure A5** IRR versus $P_{CO}$ for 0.15CT and 0.75CT catalysts

# Appendix D

## Copyrights permissions for chapter 2

### Royal Society of Chemistry - License Terms and Conditions

| | |
|---|---|
| Order Date | 25-Nov-2019 |
| Order license ID | 1005445-1 |
| ISSN | 2046-2069 |
| Type of Use | Republish in a thesis/dissertation |
| Publisher | RSC Publishing |
| Portion | Chart/graph/table/figure |

#### LICENSED CONTENT

| | | | |
|---|---|---|---|
| Publication Title | RSC advances | Rightsholder | Royal Society of Chemistry |
| Date | 01/01/2011 | Publication Type | e-Journal |
| Language | English | URL | http://pubs.rsc.org/en/Journals/JournalIssues/RA |
| Country | United Kingdom of Great Britain and Northern Ireland | | |

#### REQUEST DETAILS

| | | | |
|---|---|---|---|
| Portion Type | Chart/graph/table/figure | Distribution | Worldwide |
| Number of charts / graphs / tables / figures requested | 1 | Translation | Original language of publication |
| Format (select all that apply) | Electronic | Copies for the disabled? | No |
| Who will republish the content? | Author of requested content | Minor editing privileges? | No |
| Duration of Use | Life of current edition | Incidental promotional use? | No |
| Lifetime Unit Quantity | Up to 14,999 | Currency | USD |
| Rights Requested | Main product | | |

#### NEW WORK DETAILS

| | | | |
|---|---|---|---|
| Title | Nanostructured catalytic architectures for CO oxidation and reduction | Institution name | University of Canterbury |
| | | Expected presentation date | 2020-01-31 |
| Instructor name | Wasim Khan | | |

#### ADDITIONAL DETAILS

| | | | |
|---|---|---|---|
| Order reference number | N/A | The requesting person / organization to appear on the license | Wasim Khan/University of Canterbury |

#### REUSE CONTENT DETAILS

| | | | |
|---|---|---|---|
| Title, description or numeric reference of the portion(s) | Fig. 6 | Title of the article/chapter the portion is from | High aspect ratio TiO2 nanowires tailored in concentrated HCl hydrothermal condition for photoelectrochemical water splitting |
| Editor of portion(s) | N/A | | |
| Volume of serial or monograph | 5 | | |

SPRINGER NATURE LICENSE
TERMS AND CONDITIONS

Nov 24, 2019

---

This Agreement between Mr. Wasim Khan ("You") and Springer Nature ("Springer Nature") consists of your license details and the terms and conditions provided by Springer Nature and Copyright Clearance Center.

| | |
|---|---|
| License Number | 4698601148907 |
| License date | Oct 30, 2019 |
| Licensed Content Publisher | Springer Nature |
| Licensed Content Publication | Rendiconti Lincei |
| Licensed Content Title | Development of a Fischer-Tropsch catalyst: From laboratory to commercial scale demonstration |
| Licensed Content Author | Carlo Perego |
| Licensed Content Date | Jan 1, 2007 |
| Licensed Content Volume | 18 |
| Licensed Content Issue | 4 |
| Type of Use | Thesis/Dissertation |
| Requestor type | academic/university or research institute |
| Format | electronic |
| Portion | figures/tables/illustrations |

| | |
|---|---|
| Number of figures/tables/illustrations | 1 |
| Will you be translating? | no |
| Circulation/distribution | 500 - 999 |
| Author of this Springer Nature content | no |
| Title | Nanostructured catalytic architectures for CO oxidation and reduction |
| Institution name | University of Canterbury Christchurch New Zealand |
| Expected presentation date | Jan 2020 |
| Portions | Figure 4 |
| Requestor Location | Mr. Wasim Khan<br>Office 204 CAPE<br>University of Canterbury<br><br>Christchurch, Canterbury 8140<br>New Zealand<br>Attn: Mr. Wasim Khan |
| Total | 0.00 USD |